INFORMATION TO USERS

This manuscript has been reproduced from the microfilm master. UMI films the text directly from the original or copy submitted. Thus, some thesis and dissertation copies are in typewriter face, while others may be from any type of computer printer.

The quality of this reproduction is dependent upon the quality of the copy submitted. Broken or indistinct print, colored or poor quality illustrations and photographs, print bleedthrough, substandard margins, and improper alignment can adversely affect reproduction.

In the unlikely event that the author did not send UMI a complete manuscript and there are missing pages, these will be noted. Also, if unauthorized copyright material had to be removed, a note will indicate the deletion.

Oversize materials (e.g., maps, drawings, charts) are reproduced by sectioning the original, beginning at the upper left-hand corner and continuing from left to right in equal sections with small overlaps. Each original is also photographed in one exposure and is included in reduced form at the back of the book.

Photographs included in the original manuscript have been reproduced xerographically in this copy. Higher quality 6" x 9" black and white photographic prints are available for any photographs or illustrations appearing in this copy for an additional charge. Contact UMI directly to order.

UMI

A Bell & Howell Information Company
300 North Zeeb Road, Ann Arbor MI 48106-1346 USA
313/761-4700 800/521-0600

Reproduced with permission of the copyright owner. Further reproduction prohibited without permission.

PLASMA PROPERTIES AND HEATING AT THE ANODE OF A 1 kW ARCJET USING ELECTROSTATIC PROBES

BY

NICHOLAS TILIAKOS

B.S., Cornell University, 1990
M.S., University of Illinois, 1993

THESIS

Submitted in partial fulfillment of the requirements
for the degree of Doctor of Philosophy in
Aeronautical and Astronautical Engineering
in the Graduate College of the
University of Illinois at Urbana-Champaign, 1997

Urbana, Illinois

UMI Number: 9812790

UMI
300 North Zeeb Road
Ann Arbor, MI 48103

UNIVERSITY OF ILLINOIS AT URBANA-CHAMPAIGN

THE GRADUATE COLLEGE

MAY 9, 1997
(date)

WE HEREBY RECOMMEND THAT THE THESIS BY

NICHOLAS TILIAKOS

ENTITLED PLASMA PROPERTIES AND HEATING AT THE ANODE OF A 1 kW ARCJET USING ELECTROSTATIC PROBES

BE ACCEPTED IN PARTIAL FULFILLMENT OF THE REQUIREMENTS FOR

THE DEGREE OF DOCTOR OF PHILOSOPHY

Rodney L. Burton
Director of Thesis Research

W. C. Solomon
Head of Department

Committee on Final Examination†

Rodney L. Burton Chairperson

Mark J. Kushner

Lee H. Sentman

Herman Krier

† Required for doctor's degree but not for master's.

0-517

Abstract

There has been a renewed interest in the potential of electric propulsion to significantly increase spacecraft mission capabilities and lower launch costs. Electrothermal arcjet thrusters have now matured to the point where they are competitive with chemical propulsion systems for satellite stationkeeping, maneuvering and orbital transfer. As a result, research in this field has been fueled by the current boom in the global satellite telecommunications and computer industries. Future space mission scenarios will require an increase in the capabilities of space propulsion systems, in particular arcjet thrusters and an increase in their performance envelope. To approach these engine requirements more expeditiously, numerical arcjet models have been designed. However, these models require validation through experimentation and application of various diagnostic techniques. Of particular importance to improving arcjet design is understanding the physics of the internal nozzle flow-field.

In this investigation, electrostatic micro-probes were used to measure floating and anode sheath potential, current density, electron number density, electron temperature and anode heating distributions in the near-anode region of a 1 kW electrothermal arcjet thruster. The objectives of this experimental investigation were to: (1) understand what controls arc attachment in a low power arcjet, i.e., to understand how the arc attachment region is affected by the propellant flow rate and the arcjet operating current; (2) probe the anode boundary layer making plasma property measurements for several arc currents (7.8-10.6 A), $N_2 + 2H_2$ propellant flow rates (40-60 mg/s) and specific energies (18.8-27.4 MJ/kg); (3) verify azimuthal current symmetry; (4) understand what affects anode heating, a critical thruster lifetime issue; and (5) provide experimental data for numerical arcjet models, in particular the Megli-Krier-Burton (MKB) arcjet model developed at the University of Illinois.

All of the above objectives were met through the design, fabrication and implementation of fourteen electrostatic micro-probes, of sizes ranging from 0.170 mm to 0.43 mm in diameter. The probes were positioned at various axial and azimuthal locations in the engine nozzle. A technique for cleaning and implementing these probes was developed. Two configurations were used: flush-mounted planar probes and cylindrical probes extended 0.10-0.30 mm into the plasma flow.

Obtaining plasma property data in the near-anode region of an arcjet thruster is important for validating arcjet models. This is because many numerical models do not accurately and self-consistently solve Ohm's Law coupled with the full Navier-Stokes and Maxwell's equations. In addition to this shortcoming, some models assume thermal equilibrium near the anode or artificially force the arc to attach in the supersonic region. Consequently these models cannot realistically simulate the current and voltage distributions, which are coupled with the anode heating. This is important because, to improve arcjet design and performance for advanced space missions, the thruster must perform under very high anode thermal loading, i.e., specific energy.

The main results of this investigation are: (1) electrostatic micro-probes can successfully be used in the harsh environment of an arcjet; (2) under all conditions tested the plasma is highly non-equilibrium in the near-anode region; (3) azimuthal current symmetry exists for most operating conditions; (4) the propellant flow rate affects the location of maximum anode sheath potential, current density, and anode heating more than the arc current; (5) the anode sheath potential is always positive and varies from 8-17 V depending on thruster operating conditions; (6) the fraction of anode heating varies from 18-24% over the range of specific energies tested; and (7) based on an energy loss factor of $\delta = 1200$, reasonable correlation between the experimental data and the MKB model was found.

Dedication

This work is proudly dedicated to my parents, Theologos and Helen Tiliakos whose love and support for their children has no bounds.

In loving memory of my grandmother, Anna Pappas.

Acknowledgments

This work would not have been possible without the concern, guidance and assistance from many individuals.

I am greatly indebted to my advisor, Professor Rodney L. Burton, for his insights, advice and support throughout my graduate career. Not only was his expertise in electric propulsion invaluable, but his tremendous practical experience was especially helpful for the successful completion of this work. His enthusiasm, sense of humor, and positive attitude were also greatly appreciated because many times during the course of this endeavor things did not always work so smoothly in the laboratory.

I would also like to acknowledge the professors on my Ph.D. committee for their advice and guidance. I am grateful to Prof. Herman Krier, who, as co-director of this research, provided many illuminating ideas and contributions, not to mention his delightful personality and uncanny ability to transform complex engineering ideas into simple analogies one can easily understand. I would also like to acknowledge Prof. Sentman, whose meticulous teaching skills have benefited me enormously; my knowledge of plasma diagnostics would definitely have been incomplete without the guidance of Prof. Kushner.

I have also benefited from the technical help of the following people: Prof. D. Ruzic of the Nuclear Engineering Department, J. Frizzell of the Mechanical Engineering Electronics Shop for consultation concerning the diagnostics set-up and use of electronics equipment; P. Kurath and J. Williams for instruction on producing photomicrographs; W. Johnson, K. Elam and D. Foley of the Theoretical and Applied Mechanics machine shop for fabricating the HD-18 thruster; Dr. R. Myers of Primex Aerospace for his advice regarding probe cleaning techniques and T. Haag of the NASA-Lewis Research Center for his numerous suggestions pertaining to arcjet operation.

Support for this work was provided by the United States Air Force Office of Scientific Research and their AASERT program under contracts F49620-92-J-0448 and -0280. The program director is Dr. Mitat Birkan. Additionally, the teaching assistantship support from the Department of Aeronautical and Astronautical Engineering is greatly appreciated.

Throughout the course of my research, I was given the opportunity to work with many outstanding individuals to whom I owe much gratitude. I would like to thank my office-mates Dr. G. Willmes and S. Bushman for helping me out in the laboratory and patiently listening to my raving about my favorite N.Y. sports teams. To past and present members of the Electric Propulsion Group: many thanks to Dr. S. Bufton and Dr. T. Megli for numerous helpful discussions and assistance in the laboratory; many thanks to Mike Wilson, whose vast knowledge of everyday life has improved my Trivial Pursuit game. I also greatly appreciate the friendship of Prof. Yen, whose personal experiences and stories have provided delightful conversations.

My stay here in the Midwest has been memorable, thanks to the special friendship of many people. They also include: S. Dimitrakis, the "Espresso Royale" crowd, M. Doyle, R. Foelsche, S. Gordon, D. Jenkins, D. Liolos, J. Otto, T. Roberts, K. Smith, and K. Walker.

I owe much gratitude to my uncle Manny Pappas (a.k.a. "G.T."), once a New Yorker but now a Chicago native, for always being there for me; your interesting philosophy and outlook on life has definitely rubbed off on me.

I am most indebted to my parents, Theologos and Helen Tiliakos and to my brother Michael. Without their love and support none of this work would have been as fun or worthwhile. To them I owe everything and from them I learned everything that is important in life. Without their hard work and dedication I never would have been in a position to attain my goals. Throughout my life my family has made me aware of how proud they are of me... well, I owe them much and cannot describe how proud I am of them.

Table of Contents

List of Symbols

A_p	Geometric probe collection area [m^2]
A_{eff}	Effective probe collection area [m^2]
$A_{Post\text{-}Test}$	Post-test probe geometric area [m^2]
c	Fraction of damaged Al_2O_3 tip
c_e	Most probable electron thermal speed [m/s]
C_p	Probe capacitance [nF or pF], specific heat [J/kg-°K]
d_h	Probe hole diameter [mm]
D_p	Probe diameter [mm]
D	Damkohler number, diffusion coefficient [m^2/s]
e	Electronic charge [Coulomb]
E	Electric field [V/mm]
I	Current [A]
I_d	Displacement current [A]
I_e,I_i	Electron/ion current [mA]
I_{sp}	Specific impulse [sec]
j	Current density [A/cm^2]
k	Boltzmann constant [J/°K]
Kn	Knudsen number
L_{arc}	Region of arc attachment [mm]
L_{ext}	Probe extension length [mm]
$\bar{L}$	Average probe exposure length [mm]
$\dot{m}$	N_2+2H_2 Propellant mass flow rate [mg/sec]
m_e	Electron mass [kg]
M_i	Reduced ion(N^+, H^+) mass [kg]]
n_r	Number density of species r [m^{-3}]
Oh	Ohmic heating [W/mm^3]

P	Power [W], pressure [Pa]
Q_a	Total electron power deposition into anode [W]
Q_{rs}	Elastic momentum transfer cross section for species r,s [m^2]
q_e	Anode heating due to electrons [W/cm^2]
r_p	Probe radius [mm]
R_e	Flow Reynolds number
R_E	Electric Reynolds number
R_s	Shunt resistor [Ω]
$T_{es,\ is}$	Electron /ion temperature at pre-sheath/plasma edge [°K]
T_o	Initial probe temperature, before biasing [°K]
Δt_{cln}	Probe cleaning duration [sec]
u	Velocity for particles entering probe sheath [m/s]
u_R	Uncertainty in results
V	Voltage [V]
V_{cln}	Probe cleaning voltage [V]
v_f	Plasma flow velocity [m/s]
W	Anode tungsten material work function [eV]

Greek Symbols

α	Degree of collisionality or λ_D / r_p or Eq. (3.49)
α_{ioniz}	Degree of ionization
β	Recombination coefficient [m^3/s]
γ	Reduction factor for I_e, Eq. (3.49)
δ	Energy loss factor
ε_i	Ionization potential, [eV]
ε_i	Permitivity constant [F/m]

ε	Probe "exposure" factor, Sec. 2.3.3.
λ_{rs}	Mean free path [μm]
λ_s	Sheath thickness [μm]
λ_D	Debye length [μm]
μ_r	Mobility of species r [A^2s/kg]
ν	Collision frequency [sec^{-1}]
$\bar{\Omega}^{(1,1)}_{e-i}$	Heavy particle collision integral [m^2]
ρ	Density of tungsten [kg/m^3]
ρW	Resistivity of tungsten [Ω -m]
σ	Electrical conductivity [Ω-m]$^{-1}$
τl	End-effect parameter
ϕ	Potential [V]
$\bar{\phi}_s$	Weighted anode sheath potential [V]
ϕ_{eq}	Equivalent anode sheath potential [V]
χ	Nondimensional probe voltage

Subscripts

a	Anode
arc	Pertaining to the arcjet
e,i	Electron/ion
e-sat, i-sat	Electron/ion saturation values
o	Bulk plasma quantity
s	Sheath
th	Random thermal value
f	Floating

p	Probe, pre-sheath
pre	Pre-sheath
pl	Plasma bulk flow
B	Bohm value

1. INTRODUCTION AND BACKGROUND

1.1 Electric Propulsion

Electric propulsion is a form of advanced space propulsion that utilizes electrical energy to create a 10,000-20,000 °K plasma, which is then expanded through a supersonic nozzle generating thrust, with exhaust velocities up to 10,000 m/s. The available thrust from today's electric thrusters is relatively small, .005-1N, compared to chemical rockets [Sutton, 1992] so that electric propulsion engines can only be used in space.

Electric thrusters are used for satellite on-orbit maneuvering, North-South (N-S) and East-West (E-W) stationkeeping (NSSK, EWSK) of geosynchronous (GEO) communications satellites and drag make-up for low earth orbit (LEO) satellites, [Butler, *et al.,* 1996]. Four MR-508 hydrazine augmented arcjets have currently served two years of a twelve year NSSK mission on the Telstar 401 satellite, now on orbit [Wilbur, *et al.,* 1991; Pollard, *et al.,* 1993].

Advances in electronics, materials and electric propulsion related technologies have brought a renewed interest in the potential of this technology to significantly increasing spacecraft mission capabilities and lowering launch costs, [Wilbur, *et al.,* 1991]. The main advantage of electric propulsion thrusters over chemical rockets is their higher specific impulse, I_{sp}. The I_{sp} for electric propulsion thrusters is ~ 450-2000 s compared with I_{sp} ~400 s for chemical engines. The specific impulse is a measure of the total thrust impulse per unit weight of propellant, [Sutton, 1992]. Therefore, since $(I_{sp})_{E.P.} > (I_{sp})_{chem}$, electric propulsion thrusters utilize their propellant more efficiently, translating into weight savings for a given spacecraft velocity change, ΔV [Wilbur, *et al.,* 1991]. This performance advantage can enhance the spacecraft's capabilities in several ways: (1) a smaller launch vehicle can be used, leading to a large reduction in launch costs, (2) the spacecraft's useful payload mass can be increased, enhancing for example, a science mission and extending its lifetime, (3) the trip time necessary for on-orbit spacecraft repositioning can be decreased [Sackheim, *et al.*, 1993], and (4) can possibly lead to interplanetary travel in shorter time periods [Wilbur, *et al.*, 1991].

The upper I_{sp} limit for chemical rockets is due to the finite amount of chemical energy that can be extracted from the propellant. In contrast, the attraction of electric propulsion is that theoretically, there is no upper limit on I_{sp} since any amount of electrical energy can be added to a given quantity of mass [Hill *et al.*, 1992].

The three classes of electric propulsion are: (1) *electrostatic*, in which heavy positive ions are accelerated in an electric field, providing $I_{sp} \sim 1000$-2000 s, e.g. an ion thruster; (2) *electrothermal*, where the propellant is electrically heated by an arc discharge (arcjet) or by heat transfer from a resistive element or wall (resistojet); and (3) *electromagnetic*, in which the plasma is accelerated primarily by a self-induced or an applied magnetic field generating a Lorentz force, $\mathbf{j} \times \mathbf{B}$, e.g. a magnetoplasmadynamic (MPD) thruster.

Unfortunately, electric propulsion also has some limitations compared with other propulsion technologies [Wilbur, *et al.*, 1991]. For example, for arcjet thruster lifetime issues, the present day technology is limited by the ability of the anode (nozzle) to handle the high thermal fluxes associated with operation at high specific energies, $P/\dot{m} \geq 80$ MJ/kg. Due to the intolerably high heat loads many prototype thrusters fail during extended life tests [Butler, *et al.*, 1996]. Other problems include: cathode erosion leading to arc attachment instabilities; possible spacecraft contamination and telemetry interference due to plasma plume effects; and frozen flow losses resulting in decreased thruster efficiency and performance.

The physics of these devices is complicated due to the highly coupled non-equilibrium gas dynamics and plasmadynamics of a supersonic chemically reacting viscous flow. Recently, numerical models [Butler, *et al.*, 1993, 1994; Miller, *et al.*, 1996; Megli, *at al.*, 1996; Babu, *et al.*, 1996; and Burtner, *et al.*, 1996] are beginning to shed light on the complex arcjet physics.

It is obvious from the above discussion that more research in electric propulsion is required to bring this exciting and challenging technology to full maturity.

1.1.1 The Present Status of Electric Propulsion: Arcjet Thruster Research

Electrothermal arcjet thrusters have matured to the point where they are now competitive with chemical propulsion systems for satellite station-keeping. However, fundamental research is still required to understand the physics of these thrusters. Specifically, an understanding of current attachment, anode heating and arc operating modes is lacking. These issues are relevant to improving arcjet thruster efficiency, performance and lifetime.

Much research has been done with electrothermal thrusters, both theoretical and experimental, with a major effort focused on understanding the physics of these devices. Various numerical models [Butler, *et al.*, 1993, 1994; Miller, *et al.*, 1996] have been formulated to simulate the arcjet physics, but only recently has a model been developed that self-consistently solves Ohm's law and accounts for chemical and thermal nonequilibrium effects throughout the flowfield [Megli, 1995; Megli, *et al.*, 1996]. This model, referred to as the Megli-Krier-Burton (MKB) model, is presently being developed and improved at the University of Illinois.

Our understanding of the near-field exit plane region of arcjets has received much attention and recently thorough experimental data has been obtained and compared with the MKB model [Bufton, 1996]. However, there appears to be a dearth of plasma property data in the anode boundary layer of an arcjet. This is believed to be due to the harsh environment of the arcjet nozzle interior. Investigating this region is required in order to understand the near anode physics, relevant to arc attachment and anode heating.

Preliminary experiments [Tiliakos *et. al.*, 1996] implementing single Langmuir probes flush mounted in the anode wall of a HD-18 tungsten alloy [Mi-Tech Metals Inc.] thruster have provided electron temperature and number density data at the plasma/pre-sheath edge, T_{es} and n_{es} respectively, anode current density j_a, floating potential ϕ_f, and anode sheath potential ϕ_s.

Any attempts at improving the efficiency and performance of arcjet thrusters is ultimately related to understanding the fundamental anode energy input and loss mechanisms. The input electrical energy heats the propellant, in particular it leads to the dissociation and ionization of the propellant, producing charged particles that carry the current density and hence the energy. This energy input goes into heating the electrodes (i.e., anode thermal losses), frozen flow losses (dissociation/ionization, electronic excitation, molecular vibration and rotation), radiation, random thermal energy and most importantly into useful thrust [Hoskins, *et al.*, 1993].

In the following sections a brief description of the arcjet physics is presented, followed by a literature review and a summary of the research objectives.

1.1.2 Overview of Key Arcjet Physics

A power processing unit (PPU) is used to generate an electrical arc between the cathode and anode. To initiate arc breakdown a high voltage pulse, ~O(4 kV), is used to eject electrons from the 2 % thoriated tungsten (ThW) cathode by enhanced electric field emission [Tilley, 1993]. The cathode also emits electrons as a result of ion bombardment and the Schottky effect [Tilley, 1993]. Since these "primary" electrons carry with them a high thermal energy, electron emission from the cathode serves to keep it relatively cool, ~ 3700 °K.

The simulated hydrazine, $N_2 + 2H_2$, propellant is injected into the plenum chamber, at a temperature of ~300 °K, via an injector disk with a tangential swirl to provide arc stability and to reduce heat transfer to the upstream anode surfaces [Butler, *et al.*, 1996]. The gas dynamic forces propel the arc through the constrictor (about 0.25 mm long), into the supersonic region, as shown in Fig. 1.1, attaching in a diffuse, "umbrella-like" fashion along the anode. The propellant gas merges with the arc, in a complicated and continuous process [Butler, *et al.*, 1996].

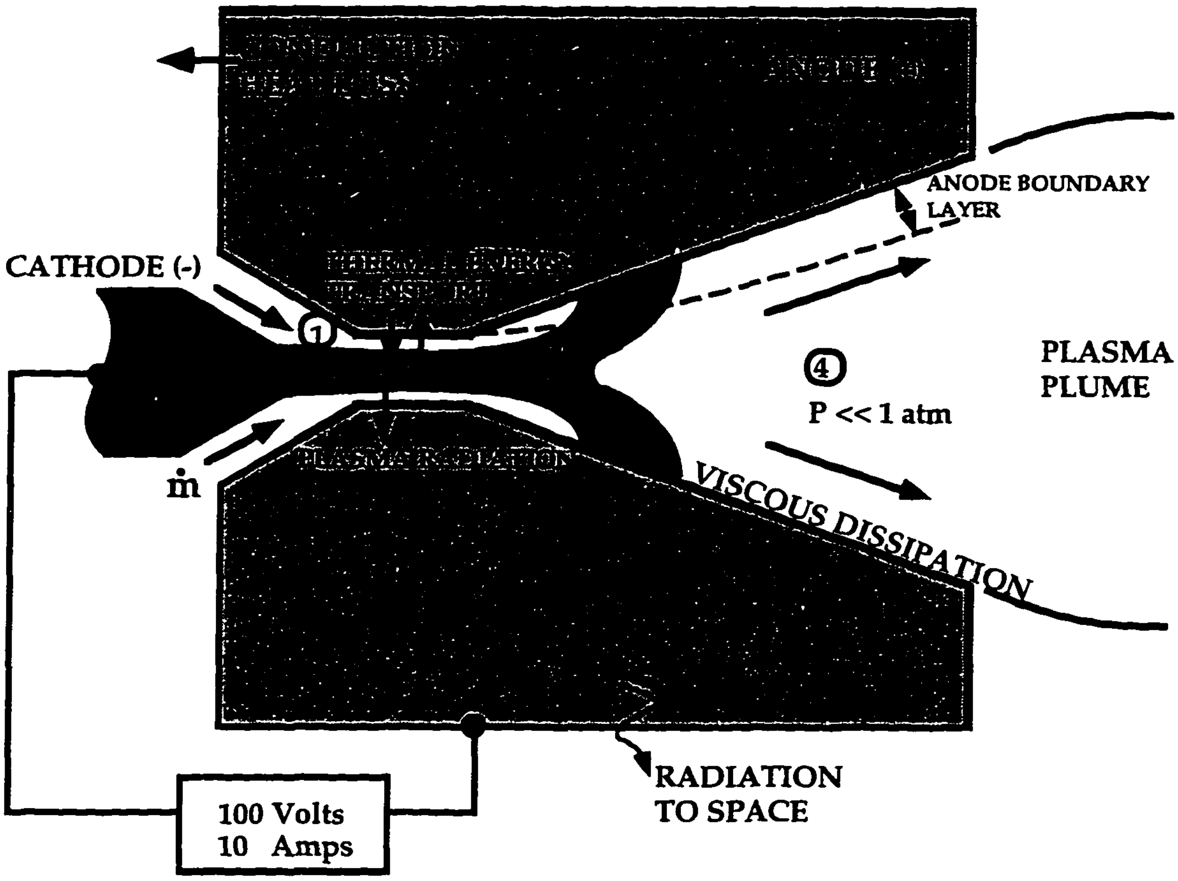

Fig. 1.1 Schematic of a typical electrothermal arcjet thruster showing the various regions of interest and the relevant heat transfer mechanisms. [Parts of this schematic are reproduced from Butler, *et al.*, 1996].

The arc is transported by the mobile electrons and gas dynamic forces through the constrictor, to the anode surface. On their way to the anode the primary electrons collide with the N, H atoms and N_2, H_2 molecules. These electron-impact interactions lead to dissociation and ionization of the constituent species, creating more electrons in an "avalanche" effect.

Figure 1.1 shows a schematic of four different zones of arcjet physics, summarized as follows:

(1) Zone 1 (**Near-Cathode Region**): the main activity in this region is "the dissipation of electrical energy via collisions of electrons with the neutral and ionized propellant"[Butler, *et al.*, 1996]. Ion bombardment of the cathode also occurs, producing more electrons in the arc discharge. Upon start-up, the cathode absorbs an enormous heat loading that melts the tip (see Appendix I for photomicrographs of cathode erosion) and evaporates some of the thorium. The arc traverses along the cathode surface, eventually settling into an arc attachment area ~O(10^{-8} m^2). The arc is comprised mostly of electrons that travel through the propellant to the anode, continually decelerated by collisions with the ions, neutrals and molecules and also continually accelerated by the applied resistive electric field in the bulk plasma, E_{pl} [Butler, *et al.*, 1996].

(2) Zone 2 (**Constrictor**): In this region the arc passes through the constrictor aided by the electric field and gas dynamic forces. The constrictor serves to minimize arc instabilities [Wilbur, *et al.*, 1991], constricting the arc and maintaining a cool gas layer near the walls. During the electron particle collisions, the electrons transfer some of their energy to the heavy particles thus raising the heavy particle temperature and the bulk gas temperature in the process [Butler, *et al.*, 1996]. The arc occupies the centerline region of the constrictor, with a relatively cooler layer of gas along the constrictor walls, ~T_a ~ 1400°K. The electron temperature along the constrictor centerline is about 20,000 °K. Thermodynamic equilibrium exists between the electrons and heavy particles here because of the high collisional coupling between the species due to the high arc intensity.

(3) Zone 3 (**Supersonic Region**): This region is characterized by a rapid gas dynamic expansion of the plasma and by decreasing resistive electric field strengths. As a result, thermal energy exchange between the electrons and heavy particles drastically decreases [Butler, *et al.*, 1996]. Inside the arc core,

near the thruster centerline, there are still sufficient interparticle collisions so that $T_e \sim T_{gas}$, [Megli, 1995; Miller, *et al.*, 1996]. Due to the large radial gradients in n_e and T_e, electrons diffuse to the anode wall, providing a finite conductivity σ so that the arc can attach to the anode surface.

A typical low power arcjet nozzle is on the order of 1 cm in length. With particle speeds between 5-10 km/sec the charged particle residence time ($\sim 10^{-6}$ sec) is much smaller than the recombination time. As a result, the flow is in chemical nonequilibrium, leading to large frozen flow losses and a decrease in arcjet performance. This means that a significant portion of the energy devoted to dissociating and ionizing the propellant is lost, i.e. is frozen and therefore not available for conversion into directed kinetic energy and thrust. The low pressures in the arcjet nozzle (<< 1 atm) contribute to low recombination rates, and consequently high frozen flow losses. There is also thermal nonequilibrium, $T_e \neq T_i, T_{gas}$, vibrational and rotational non-equilibrium in the nozzle. Other factors that limit arcjet performance include: thermal losses to the anode due to ohmic heating, current attachment, convection and radiation to the wall [Hoskins, *et al.*, 1993]; wall friction losses in the nozzle due to large viscous and thermal boundary layer growth; nonuniform profile losses, electrode erosion and arcjet instabilities. The nozzle flow is highly viscous, with flow Reynolds number ~O(1000-1500), based on the constrictor diameter.

To achieve high specific impulse and thrust efficiency, the specific energy , $P/\dot{m}$ = input electrical power divided by propellant mass flow rate, must be increased. However, when the maximum specific energy is reached the anode becomes detrimentally affected by the high heat fluxes associated with these energies, e.g. high thermal loading, leading to material erosion. Therefore, improvement of arcjet performance for all power levels relies heavily on understanding the interaction between the plasma and the anode wall, and anode heating [Hoskins, *et al.*, 1993].

In both the constrictor and nozzle regions, energy transport from the plasma to the walls is a strong function of the electron number density and temperature distributions. Non-equilibrium processes determine the spatial variation in current attachment and anode heating. Such processes dominate in the thick boundary layer, so that measurements of local n_{es} and T_{es} inside the boundary layer will be helpful in understanding the current attachment and energy deposition between the plasma and the anode. The distributions of current density, electric field and voltage are poorly understood; they are also strongly coupled to the n_{es} and T_{es} distributions near the anode.

Due to the thick viscous and thermal boundary layers present in the nozzle, the plasma core flow and boundary layer processes are also coupled. The volumetric ohmic heating j^2/σ, determines where the energy is deposited, which in turn determines the electrical conductivity $\sigma(n_{es}, T_{es})$. This electrical conductivity distribution then prescribes the voltage and current distributions, which affect the arc attachment and the thermal losses to the anode.

1.2 Literature Review

A brief literature review is presented in two separate sections. First, a description of some previous electrostatic probe research with arcjets and other devices is documented, followed by a review of some recent arcjet internal diagnostics work using spectroscopic methods and other techniques and previous research relevant to this investigation.

1.2.1 Previous Electrostatic Probe Research

Electrostatic probes refer to a type of Langmuir probe used when the flow Knudsen number, $Kn < 1$. Langmuir probes have been a powerful means of plasma diagnostics since the early 1920's, when the method was first developed and implemented by Irving Langmuir [Langmuir, *et al.*, 1923, 1924, 1926]. Electrostatic probes have recently been used in magnetoplasmadynamic thrusters[Soulas, *et al.*, 1993; Gallimore, *et al.*, 1993] and arcjet plumes[Carney *et al.*, 1989] as a diagnostic. Much experimental work has been done in studying arcjet plume properties [Carney, *et al.*, 1989; Burton, *et al.*, 1996] but until recently relatively little work has been performed to obtain plasma properties within the arcjet nozzle, where the arc behavior governs thruster performance.

Soulas and Myers [Soulas *et al.*, 1993] measured the anode energy deposition of a low pressure free burning arc using calorimetry and a single Langmuir probe. Their experimental results showed that anode power deposition decreased with increasing anode surface pressure up to 6.7 Pa then became insensitive to pressure. Anode power deposition was dominated by electrons with the anode fall voltage contributing over half of the anode power, a result obtained in this work as well. The results of Soulas *et al.*, [1993] results also showed that anode power deposition can be reduced by operating at higher anode pressures, reducing the arc current and applied magnetic field strengths and having the magnetic flux lines intercept the anode.

Gallimore *et al.*, [1993] used an array of thermocouples, floating and triple electrostatic probes to measure the anode heat flux and anode fall voltage in a multimegawatt self-field quasisteady magnetoplasmadynamic thruster, using argon and helium as propellants. Anode fall voltages varied from 4-50 V and anode power fractions reached as high as 70% with helium at 150 kW and 50% with argon at 1.9 MW. Anode power fractions were found to depend heavily on propellant flow rates, and above 2.5 MW the anode power fraction decreased monotonically with increasing thruster power.

Several authors have also used the classical Langmuir probe to study the characteristics of the arcjet exhaust plume. Plume studies are important because of the plume's potential impact on the satellite electrical systems due to electromagnetic interference or its adverse environmental effects on communications and telemetry. Carney *et al.*, [1989] used electrostatic single probes of cylindrical and spherical geometry to measure electron number densities, ~O(1-3x10^9/cm^3) and electron temperatures between 4600-8100 °K, in the plume of a 1 kW arcjet. Their results showed that the exhaust is slightly ionized, ~1% with local plasma potentials near facility ground.

Several other recent exhaust plume research using electrostatic probe diagnostics include: Kim *et al.*, [1996] obtained ion current density and electron number density profiles in the near-field plume of a 1.35 kW stationary plasma thruster (SPT-100) using a single cylindrical Langmuir probe; Sankovic [1990] measured electron number densities and temperatures in the near field plume of a 1 kW simulated hydrazine arcjet thruster using cylindrical and spherical single electrostatic probes; Keefer *et al.*, [1996] used a cylindrical probe in the plasma exhaust plume of a 15 cm three grid xenon ion thruster; Bufton *et al.* [1996] used single, triple and quadrupole electrostatic probe techniques at the exit plane of a 1 kW NASA-Lewis arcjet thruster; the quadrupole electrostatic probe, originally developed by Burton, *et al.* [1993] and DelMedico [1992], was also used in the exhaust plume of an MPD thruster.

Electrostatic probes have also been used in supersonic and hypersonic flows. Tan [1973] studied the utility of a cylindrical Langmuir probe transverse to a plasma flow, both theoretically and experimentally. In combination with electron temperature and density data from a complimentary cylindrical probe aligned with the flow, the transverse probe can yield ion Mach number data and local flow velocity. Jakubowski [1972] measured the response of cylindrical probes at various angles of incidence in a low density hypersonic argon plasma and found that the ion current does depend on the angle of incidence. Segall *et al.*, [1973] experimentally and theoretically investigated the current-voltage characteristics of cylindrical probes in a high velocity collisionless plasma flow. Segall *et al.*, [1973] concluded that cylindrical Langmuir probes transverse to the high velocity plasma flow may be used as reliable diagnostics tools.

The utility of electrostatic probes is not limited to cylindrical and spherical geometries only. Flush-mounted electrostatic probes have been used: for analyzing the properties in a hypersonic flowfield, e.g. on re-entry space vehicles and interplanetary probes for analyzing atmospheric particle densities and temperatures [Hayes, *et al.*, 1973]; and for obtaining ion density profiles in the boundary layers of supersonic flow of partially ionized shock-heated air over a flat plate, [Bredfeldt, *et al.*, 1967; Boyer, *et al.*, 1972 and Russo *et al.*, 1972; Tseng *et al.*, 1971].

Based on the above discussion, the utility of Langmuir and electrostatic probes of various geometries and configurations is quite extensive.

1.2.2 Previous Arcjet Nozzle Interior Diagnostics Research

The first experimental investigations of the nozzle region of a low power arcjet have been conducted at the NASA-Lewis Research Center. Zube *et. al* [1992] performed emission spectroscopy of the plasma flow inside the nozzle of a 1 kW hydrazine arcjet. Several 0.25 mm holes were drilled into the diverging section of the nozzle, providing optical access to the internal flow. Measurements included atomic electron excitation, vibrational and rotational temperatures for the expanding plasma using the relative line intensity techniques. However, no data were obtained inside the constrictor region and the closest data point was 2.4 mm downstream of the constrictor.

Investigations of plasma conditions inside the nozzle and constrictor have been performed on low and medium power arcjets [Zube, *et al.*, 1992; Zube, *et al.*, 1993 and Glocker, *et al.*, 1992]. Experiments were performed where drilled holes [Zube, *et al.*, 1992] or a quartz window[Glocker, *et al.*, 1992] were used to obtain spectroscopic access inside the nozzle. Radial and axial profiles of H_2 excitation temperature, electron density and atomic hydrogen density in the arcjet were measured.

Emission spectroscopy has been the main diagnostic used for internal probing of the arcjet. Investigations that have obtained measurements of plasma conditions inside the constrictor have been performed on medium power arcjets (5-20 kW), [Zube, *et al.*, 1993; Glocker, *et al.*, 1992]. In the work of Zube *et.al* [1993] the constrictor had a 2 mm radial hole in it covered by a quartz window, providing optical access to the central arc region. Spectroscopic measurements included radial profiles of H_2 excitation temperature, electron density and atomic hydrogen density in the constrictor. However, due to problems with line width determination near the walls only the data from the inner 60-70 % of the constrictor diameter gave reliable results, [Zube, *et al.*, 1993].

Other internal diagnostics work includes that of Hargus *et al.* [1994] who performed internal emission spectroscopy measurements in the nozzle expansion region of a 26 kW ammonia arcjet. Three optical access ports were equally spaced along the nozzle wall. Atomic and ionic excitation temperatures of H and NII were obtained as well as electron number densities.

Curran *et al.* [1990] studied arc energy deposition in the segmented anode of a 1-2 kW arcjet, the nature of arc attachment, and its effects on performance characteristics of the device. The current distribution to five anode segments, separated with boron nitride spacers, was individually measured as well as floating potential and anode fall voltage. Also, the arc was forced to attach to a particular region along the anode by electrically isolating various segments. The current was found to attach diffusely to the anode, with more than 50% of the input power to the arcjet added in the diverging section of the nozzle. The axial current density distribution was also dependent on the mass flow rate and was found to decrease significantly as the flow expanded through the nozzle, consistent with the Zube and Myers [1992] result of electron number density.

The question of current symmetry in high power thrusters has been addressed by Harris *et al.*,[1992] who studied the temporal behavior of dc arcs on a water-cooled radially-segmented 30 kW arcjet anode with N_2 propellant.

The copper anode was divided into four equal radial segments that were electrically isolated with aluminum oxide gaskets. The current distribution in each segment was measured as a function of total current and mass flow rate. Harris *et al.*, [1992] found that for the range of arc currents considered, 100-250 A, the current distribution in the segmented anode is generally asymmetric.

1.3 Research Objectives and Motivation

The goal of this research is to improve our understanding of arc attachment and anode heating processes in the boundary layer of a low power (1 kW) arcjet thruster operating on simulated hydrazine, $N_2 + 2H_2$. An experimental investigation of the anode boundary layer was conducted using electrostatic micro-probes. The standard 1 kW NASA-Lewis arcjet design was modified to accommodate fourteen micro-probes in the anode body and to facilitate the heat transfer analysis in the MKB model. Several parameter studies were conducted including: varying the arcjet operating current, $7.8 \leq I_{arc} \leq 10.6$ A; the $N_2 + 2H_2$ propellant flow rate, $40 \leq \dot{m} \leq 60$ mg/s; and the position of the micro-probes, i.e. flush probe ($L_{ext} = 0$ mm) and cylindrical probe ($L_{ext} = 0.1$, or 0.25-0.3 mm) configurations.

The main objectives of this experimental study were to: (1) understand what affects arc attachment in a modified low power arcjet; (2) investigate the anode boundary layer region and obtain data for various plasma properties, e.g. ϕ_f, ϕ_s, j_a, T_{es} and n_{es} for different arcjet operating conditions; (3) verify azimuthal current symmetry; (4) understand what affects anode heating; and (5) provide experimental data that will assist the numerical arcjet modeling community to more accurately predict and calculate the current and voltage distributions in an arcjet. These objectives were achieved through the design, fabrication and implementation of an array of fourteen electrostatic micro-probes positioned at various axial and azimuthal locations in the anode.

In the following sections the motivation for studying and the importance of the above objectives is addressed.

1.3.1 Arc Attachment Physics

Understanding the near-anode physics is relevant to determining the transition between diffuse and constricted modes of arc attachment [Self, *et al.*, 1983]. Operation of an anode in a constricted mode leads to large ohmic heating, $O_h = j_a^2/\sigma$ and therefore detrimental anode heating q_e and erosion, thus limiting the electrode lifetime and decreasing thruster performance. A knowledge of the current density distribution along the anode will provide detailed information on the anode heating and the non-equilibrium physics in the near-anode region, essential information for numerical models attempting to realistically simulate arcjet flows. Anode heating, a critical life-limiting factor for high performance arcjets [Lichon, *et al.*, 1996], is determined by the physics of arc attachment [Meeks, *et al.*, 1993].

In order for arcjet thrusters to operate at significantly higher specific energies $P/\dot{m}$, required to perform more ambitious space missions and on-orbit tasks, the processes which occur at the plasma-anode boundary must be better understood and predicted [Butler, *et al.*, 1996].

Understanding where the arc attaches and what thruster parameters affect this, e.g. flow rate, arcjet operating current, material issues, etc., is also related to predicting electrothermal instabilities in the near-anode region. For example, the area on the anode of high current density may be an overheated region which may cause higher electrical conductivity in that area, thereby allowing more current to attach there, further overheating the surface and leading to thermal runaway, [Birkan, 1996].

1.3.2 Anode Energy Deposition

Understanding the plasma physics and dynamics of arc attachment is related to the plasma-anode energy transfer mechanisms [Butler, *et al.*, 1996]. For models to realistically predict the anode heat flux distribution, accurate calculations of the current distribution along the anode are required, [Martinez-Sanchez, *et al.*, 1996].

Since electrode erosion, in particular anode erosion, determines the lifetime of the engine, measurements of the anode heating distribution are required to improve our understanding of what affects the energy transfer to the anode. This is crucial to improving thruster performance and lifetime at the higher specific energies required for future space missions [Birkan, 1996; Butler, *et al.*, 1996].

1.3.3 Azimuthal Current Symmetry

Accurate and self-consistent simulation of the arcjet thermophysics is very complicated. The gas dynamics, governed by the Navier-Stokes equations, are highly coupled to the plasmadynamics, governed by Maxwell's Equations along with various dissociation and ionization reactions. In addition, due to the high speed, chemically reacting nature of the plasma flow, various degrees of chemical and thermal non-equilibrium exist.

To simplify the set of governing equations, most numerical models *assume* that azimuthal symmetry exists, e.g. azimuthal current symmetry, reducing the equations to two-dimensional in character. However, related to the arc attachment problem is the issue of whether the azimuthal symmetry assumption is valid [Martinez-Sanchez, *et al.*, 1996]. The question of azimuthal symmetry is also related to the question of arc attachment stability. If the arc is asymmetric, then there is the possibility of preferential arc attachment, and then an intense, perhaps constricted arc spot would significantly erode and overheat a region of the anode, leading to thermal runaway as described earlier, [Birkan, 1996].

1.3.4 Numerical Model Validation

Present numerical arcjet models cannot accurately and self-consistently predict the electron number densities, electron temperature, current distributions, and therefore ohmic heating, along the anode. As a result, artificial restrictions are placed on the electrical conductivity in order to simulate the arc attachment [Rhodes, *et al.*, 1990; Butler, *et al.*, 1993; Miller, *et al.*, 1993]. A fully coupled, self-consistent approach where j_a^2/σ is calculated, without any a priori assumptions on the electrical conductivity, is currently being pursued by our research group with the development of the MKB code.

A major objective of this research is to obtain direct measurements of plasma properties in the anode boundary layer, a region that models have traditionally had difficulty simulating the physics. It is the intention of this work to provide this necessary model validation so that future advanced arcjet thrusters can be designed more efficiently and expeditiously with a realistic model.

1.3.5 Plasma Properties in the Anode Sheath

The main reason why the majority of numerical models have difficulty accurately predicting arc attachment is that the near-anode non-equilibrium physics is not correctly simulated. Many models assumed a single fluid species temperature, so that the requisite level of electron number density and electrical conductivity near the anode was not met, making arc attachment impossible. These models have therefore had to impose artificial conductivity floors in order to achieve arc attachment [Butler, *et al.*, 1993]. However, once this artificial limit is imposed the model loses its ability to predict the current distribution along the anode since there is no self-consistent coupling with Ohm's Law. Other models artificially insulated the constrictor, forcing the arc to attach downstream in the supersonic region, [Miller, *et al.*, 1993].

Models that impose such limitations on electrical conductivity will not accurately predict arc attachment and therefore anode heating, the critical issue for improving arcjet lifetime and performance. Therefore, experimental data of electrical conductivity would help these models realistically simulate arc attachment and anode heating.

From the above discussion we see that understanding the physics in the near-anode region, especially arc attachment and anode heating, is required to improve thruster design and numerical arcjet model predictions. To accomplish the objectives outlined earlier, an experiment was designed to implement electrostatic micro-probes. It is the intention of this work is to provide numerical arcjet modelers with relevant data to assist in the validation of their models.

In the following sections the techniques, procedures and data analysis methods are outlined, followed by a presentation of the key results and conclusions.

2. EXPERIMENTAL APPROACH AND SET-UP

2.1 University of Illinois Arcjet Thruster

For this study a 1 kW thruster was fabricated with similar dimensions to the standard NASA-Lewis 1 kW thruster [Curran *et al.*, 1992]. The University of Illinois thruster operates nominally at a flow rate of 50 mg/s, an arcjet current of 10 amps and arcjet voltage of 110 volts, using simulated hydrazine, a gaseous mixture of $N_2 + 2H_2$, as propellant. Implementing this design allows direct comparison of the data obtained in this study with previous experiments that have used the standard NASA-Lewis 1 kW thruster. A description of the UIUC thruster geometry and its operation is presented below.

2.1.1 Thruster Geometry and Operation

A schematic of the thruster used in this work is shown in Fig. 2.1, and a photograph is shown in Fig. 2.2; the NASA 1 kW nozzle is shown in Fig. 2.3 for comparison. The converging cone half angle is 30°, while the diverging section is 20° half angle. The constrictor diameter 0.63 mm and length 0.25 mm were kept identical to the NASA thruster. The exit plane diameter is 9.52 mm, providing an area ratio of 225:1. The major difference with the NASA design was elimination of the anode insert and associated seal and implementation of a single-piece thruster body. Use of a monolithic body facilitates modeling of the anode heat transfer, as well as placement of an array of fourteen electrostatic micro-probes at various axial and azimuthal locations in the anode wall, Figs. 2.1-2.2.

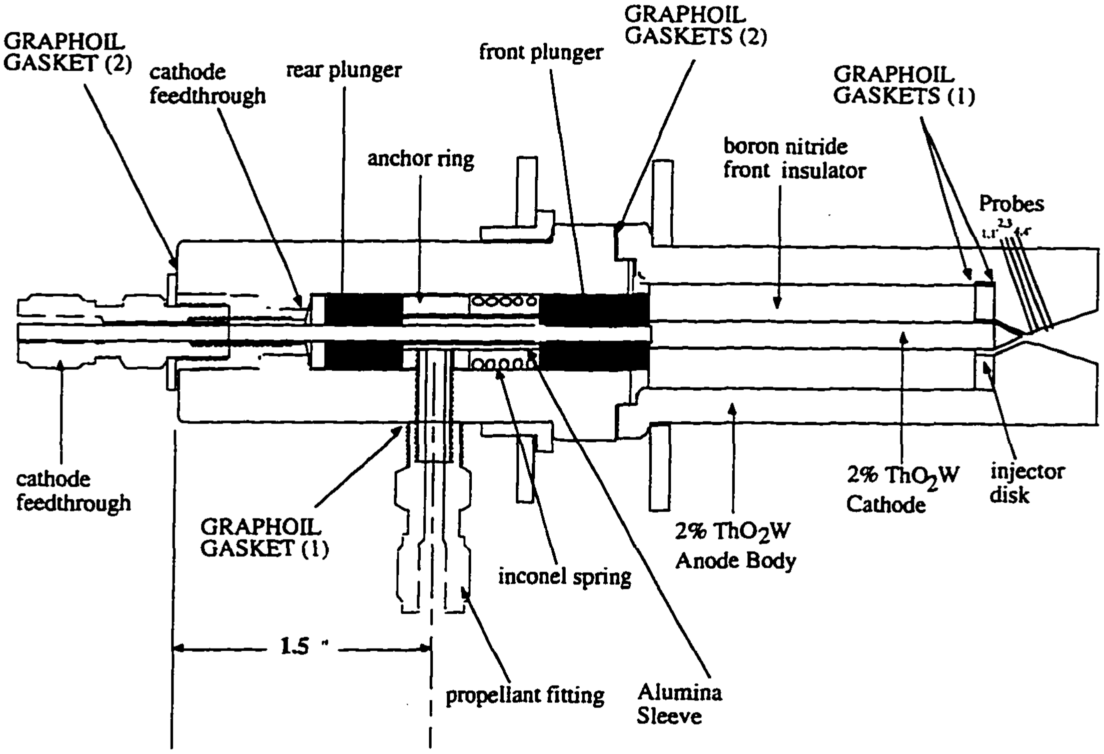

Fig. 2.1 Cross-sectional view of 1 kW UIUC thruster used in this work. Notice the monolithic anode body, compared with the NASA-Lewis arcjet, Fig. 2.3.

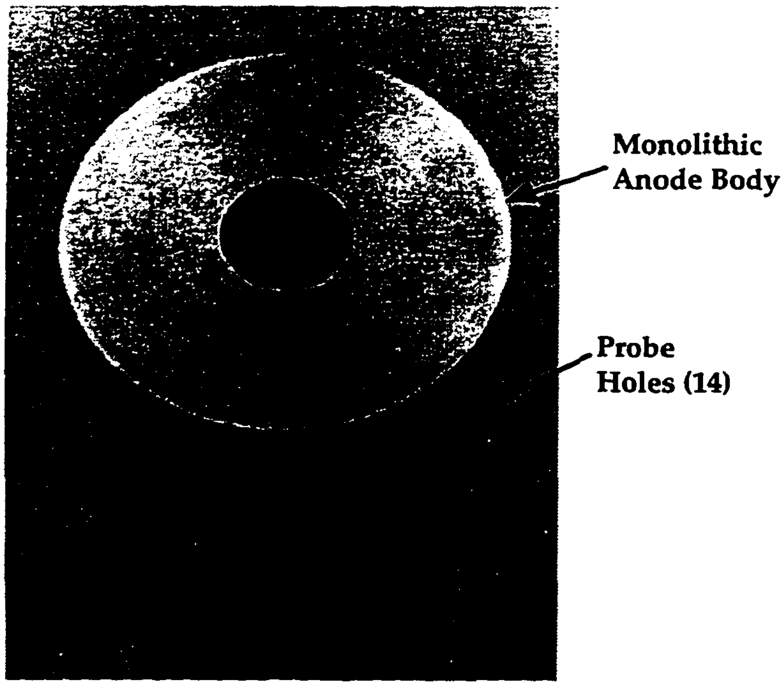

Fig. 2.2 Photograph of the 2% thoriated tungsten nozzle tested in this investigation. Notice the array of probe holes for housing the electrostatic micro-probes.

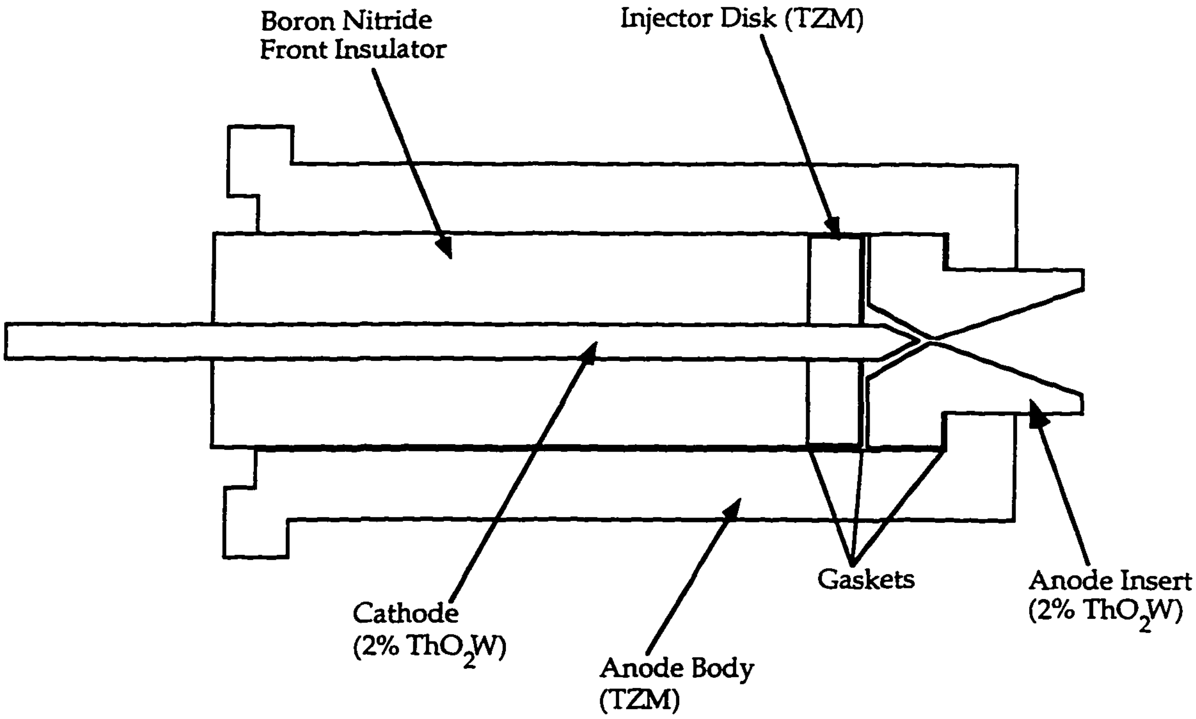

Fig. 2.3 Cross-sectional view of the standard 1 kW NASA-Lewis arcjet thruster showing the anode insert.

The probe numbers designate the axial distance, in mm, from the constrictor exit; e.g. probe 1 is positioned 1 mm downstream of the constrictor exit. Probes 1, 4, 7, 10 and probes 1', 4', 7' and 10' are at the same axial location, but separated 180°. This set of eight probes provides information on current symmetry.

The arcjet nozzle (anode) was fabricated from 2% thoriated tungsten (ThO$_2$W) material. The cathode was also fabricated from 2% ThO$_2$W and has a 30° half-angle tip. It is 3.18 mm in diameter at the rear of the arcjet, stepping up to 4.77 mm at the thruster head. The cathode gap is set to 0.60 mm ± 0.13 mm. This arc gap was set by first forcing the cathode tip in contact with the anode and then retracting the cathode 0.838 mm. The cathode feedthrough is then securely tightened until the arc gap is 0.597 mm.

The thruster is seated on a mount inside a 1.5 m^3 vacuum tank, with a background pressure range of 0.1-0.2 Torr for flow rates between 40-60 mg/sec.

The simulated hydrazine propellant flow rate is varied between 40 and 60 mg/sec, controlled by two Unit mass flow controllers, [Unit Instruments, Inc.]. For nozzle surface temperature measurements a chromel-alumel type K thermocouple is located at 45° and 9.4 mm from the exit plane. The thermocouple has a radiation shield covering it, made of a stainless steel sheet, covering it, thus providing a more accurate measurement of the anode surface temperature, T_{noz}.

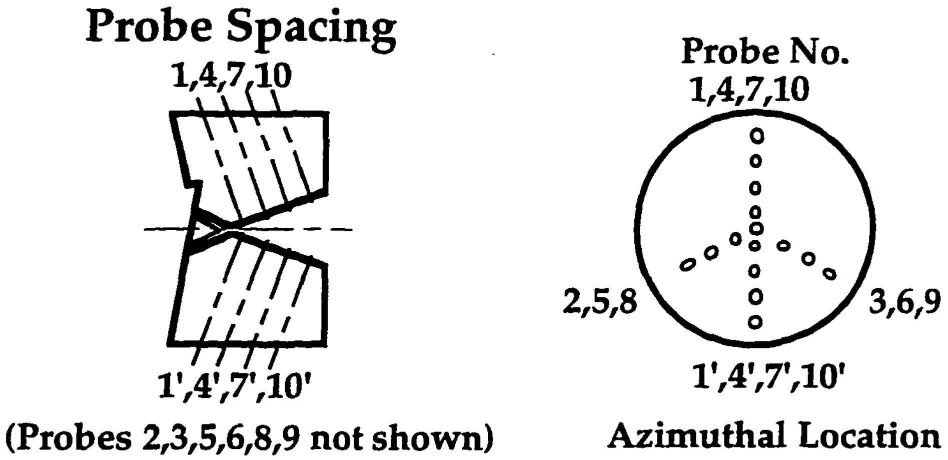

Fig. 2.4 Shown above is a schematic of the array of 14 electrostatic microprobes located at various axial and azimuthal locations. Probes 1,4,7,10 and 1',4',7'10' are used to verify current symmetry.

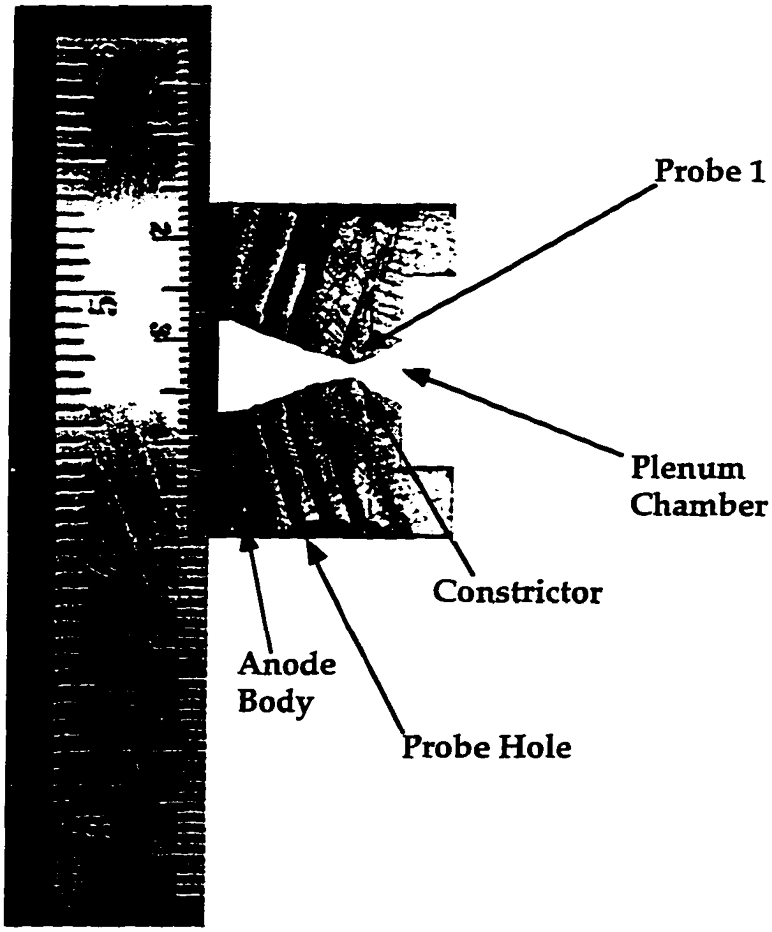

Fig. 2.5 A close-up view of the nozzle cross-section from a 1 kW thruster made from a HD-18 tungsten alloy. The photo shows eight of the fourteen probe channels that house the probes. The internal volume of the supersonic region is ~ 0.6 cm^3.

The gaseous propellant mixture, $N_2 + 2H_2$, is premixed and injected into the propellant feedthrough, making its way through the narrow passages of the boron nitride front insulator and anode housing. The front insulator has a concentric hole 4.7 mm in diameter, that centers the cathode within the plenum chamber. The dimensions of this hole are critical; a cathode misalignment of 0.05-0.08 mm has been found to lead to arc instabilities, start-up problems, asymmetric arc attachment and possible constrictor erosion. Longitudinal grooves machined into the outer surface of the front insulator allow the propellant to remain in contact with the hot anode body, thus being regeneratively heated, before injection into the arc [Curran, *et al.*, 1992]. The gaseous propellant is then introduced into the subsonic region via a molybdenum injector disk, serving mainly to impart a tangential swirl to the propellant stream. This azimuthal component is achieved by two holes 0.51 mm in diameter located 180° apart and tangential to the hole through which the cathode passes. Graphite foil gaskets 0.0025 mm thick are used to seal interfaces from the vacuum environment outside the thruster.

The UIUC thruster is operated with the anode electrically grounded to facility ground and the cathode nominally operating at -110 volts. This is done mainly for safety reasons, as well as for minimizing the introduction of electrical noise to the probe signals, since they are embedded in the anode wall.

Power is provided to the thruster by a power processing unit (PPU), which was supplied by the NASA Lewis Research Center. The operator sets the arcjet operating current I_{arc} from the PPU, and the thruster voltage, V_{arc} is determined by the arcjet plasma impedance, nominally 10 Ω, and the propellant mass flow rate $\dot{m}$. As a result of the switching nature of the PPU electronics, I_{arc} has an ac ripple type waveform. This ripple has a frequency of 15-20 kHz, resulting in arc current fluctuations that are ± 8% about the mean [Bufton, 1996].

Once the operator sets both the PPU to the desired operating arc current I_{arc} and the propellant flow controllers to the desired $\dot{m}$, the arcjet thruster is ready for testing. The PPU is turned on, sending a 4 kV pulse to the cathode and initiating ignition; the high voltage pulse is then turned off and the PPU is set to the "RUN" mode, where the voltage drops down to about $100 \leq V_{arc} <$ 125 V. The plasma plume is observed to flicker slightly as the arc traverses along the electrode surfaces, stabilizing after a few seconds, resulting in a steady plume. At this point the nozzle surface temperature T_{noz}, increases dramatically, Fig. 2.6, to its steady state operating temperature.

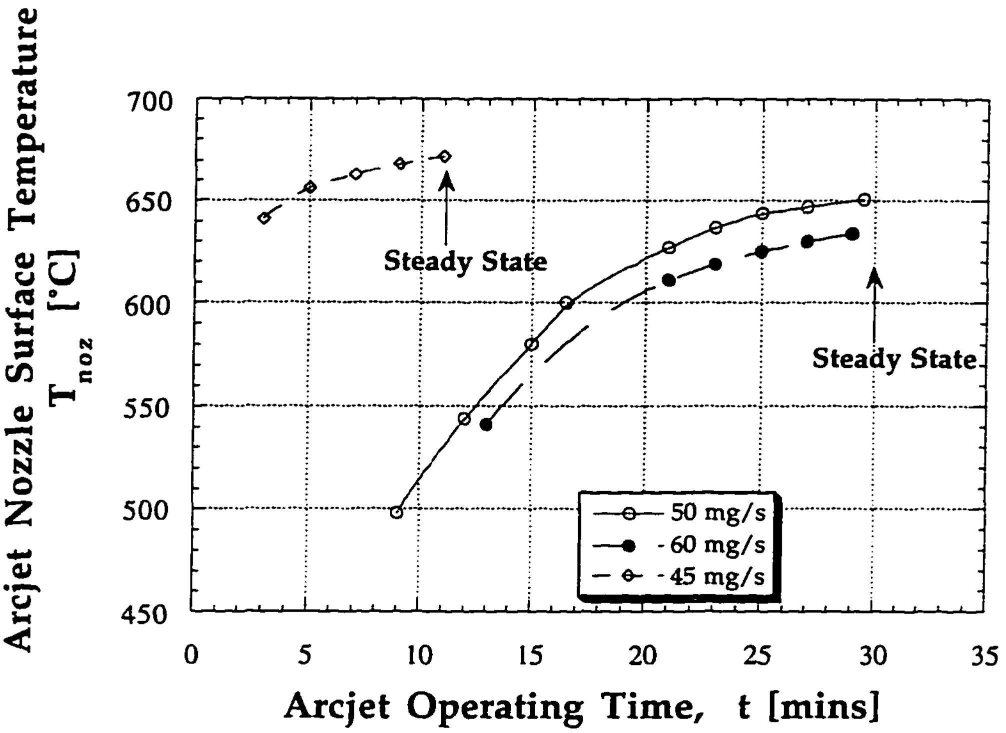

Fig. 2.6 Shown above is the nozzle surface temperature as a function of arcjet run time. For $\dot{m}$ = 50, 60 mg/s the thruster reaches a steady state temperature of ~ 650 °C after about 30 minutes; for $\dot{m}$ = 45 mg/s the steady state temperature of ~ 675°C is attained after 11 minutes.

Since the arcjet is a negative impedance device, as I_{arc} increases, for a fixed propellant flow rate, V_{arc} decreases, Fig. 2.7. This is because as I_{arc} increases more energy is input into the plasma so that T_e increases. As Iarc increases the plasma resistivity decreases. Because the plasma resistivity decreases faster than I_{arc} increases, it follows that V_{arc} also decreases with increasing I_{arc}. Figure 2.7 shows the voltage-current data for various flow rates for both the NASA-Lewis 1 kW arcjet and the UIUC thruster tested in this work.

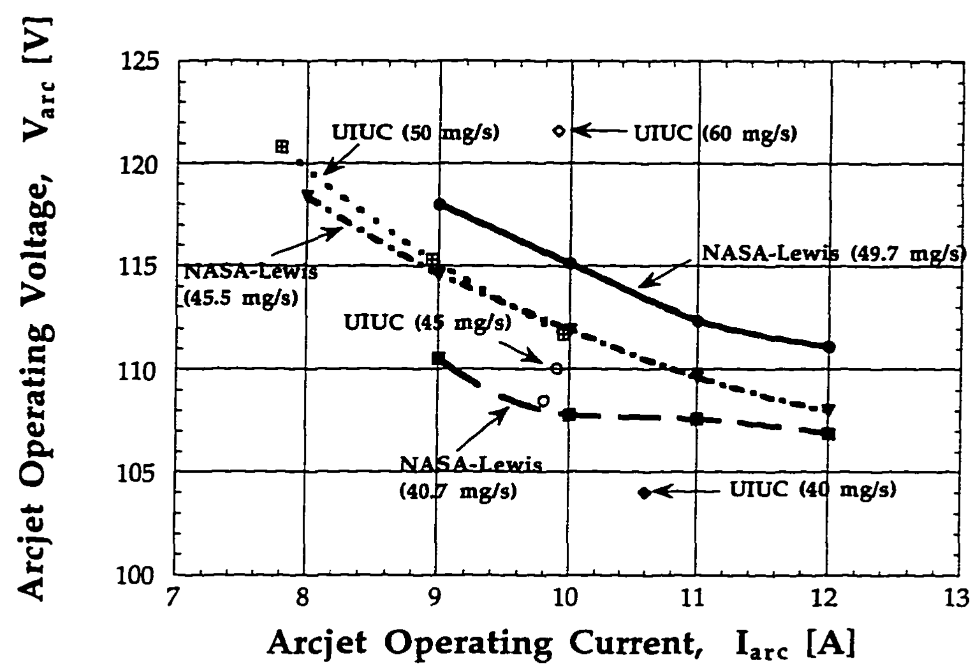

Fig. 2.7 The negative impedance character of the arcjet is displayed above for various $N_2 + 2H_2$ propellant flow rates. Experimental data is shown for both the NASA-Lewis 1 kW arcjet and the UIUC thruster.

2.2 Experimental Apparatus and Facilities

All of the experimental data presented in this work were obtained using the apparatus available in the Electric Propulsion Laboratory at the University of Illinois at Urbana-Champaign. A brief description of each of the relevant equipment is presented in the following sections.

2.2.1 Vacuum and Propellant Supply Systems

In order to simulate the space environment in which electrothermal arcjets are used, the thruster was operated in a 1 m diameter x 1.5 m long vacuum tank. The tank was maintained under vacuum conditions by a 2500 cfm Roots blower, backed by a second 1300 cfm Roots blower and two 150 cfm mechanical displacement pumps, [Bufton, 1996]. With no propellant flow, the pumping system can maintain a pressure of 2 mTorr in the 1.5 m^3 tank volume. During steady state arcjet operation, the tank pressure is nominally between 0.1-0.2 Torr for the propellant flow rates used in this study.

The arcjet thruster is mounted inside a stainless steel 5-way cross, as shown in Fig. 2.8. The thruster rests on a mount attached to a G-10 composite plate, bolted to one flange of the cross. The exhaust plume flows into the tank, through the opposite flange. Two other access ports of the cross are 6" diameter x 0.5" thick quartz windows, allowing visual inspection of the thruster and the probes during operation. The remaining port of the 5-way cross is connected to the vacuum pumping system.

Fig. 2.8 The arcjet thruster is mounted inside a stainless steel 5-way cross attachment to a 1.5 m^3 vacuum tank, as shown above, in a side view. The arcjet mounting plate houses the various diagnostic feedthroughs.

The propellant utilized in this study was a gaseous mixture of nitrogen, N_2 and hydrogen, H_2. In order to simulate the decomposed hydrazine (N_2H_4) propellant used onboard satellites, a molar mixture of 2/3 hydrogen and 1/3 nitrogen, $N_2 + 2H_2$, was used. The mass flow rate for N_2 is then 7.0 times that for H_2. This mixture was supplied by nitrogen and hydrogen industrial gas cylinders, each with 99.95% purity. The nitrogen gas supply was located adjacent to the propellant flow controllers in the laboratory, while the hydrogen gas, for safety reasons, was located in a remote "tank farm" and metered into the laboratory through high pressure copper lines. The laboratory is also equipped with hydrogen alarms, which automatically shut off the hydrogen supply via a solenoid when activated.

The $N_2 + 2H_2$ propellant flow rate can be varied between 40 and 90 mg/sec and is controlled by two Unit Instruments, Inc., mass flow controllers. The hydrogen gas was metered by a model UFC-1510A mass flow controller, with a maximum capacity of 10 SLM, or about 15 mg/s of H_2. Similarly, the nitrogen gas was metered by a model UFC-1500A controller, with a maximum capacity of 5 SLM, or about 80 mg/s of N_2 [Bufton, 1996].

Calibration of the flow controllers is performed periodically to insure minimal drift during the experiments. This is accomplished by implementing the ideal gas law, using a small tank with a known volume, and monitoring the gas temperature in the tank with a type K thermocouple. The procedure involves timing a certain pressure rise in the tank ΔP, and monitoring the gas temperature in the tank during this pressure rise. Since the temperature in the tank varied by no more than a few degrees during the calibration, an average temperature is used to calculate the gas flow rate, $\dot{m}$:

$$\dot{m} = \frac{dm}{dt} = \frac{V_t \Delta P}{R\left(T_{avg}\right)\Delta t} \qquad (2.1)$$

where V_t is the calibration tank volume (17080 cm^3), R is the gas constant for the particular gas being calibrated, T_{avg} is the average gas temperature during the calibration procedure, and ΔP is the pressure rise being monitored during the time interval Δt. With this method, the mass flow rates of the N_2, H_2 gases supplied to the thruster were known to within ± 2%, [Bufton, 1996]. For a specified propellant flow rate, the individual flow rates for the H_2 and N_2 gases are dialed into the controller as a percentage of the total capacity of that controller. Once the individual propellant flow rates are set, the total propellant ṁ to the thruster is kept constant during the experiment by feedback loops built into the flow controllers. The thruster mass flow rates used in this study, including the separate % amounts of N_2 and H_2 gas, are shown below in Table 2.1, with the calibration curves for H2 and N2 shown in Figs. 2.9 and 2.10, respectively.

Table 2.1 Summary of the flow controller settings for the $N_2 + 2H_2$ propellant mass flow rates used in this work.

Total ṁ (mg/s)	ṁ of H_2 (mg/s)	H_2 Flow Controller (%)	ṁ of N_2 (mg/s)	N_2 Flow Controller (%)
40	5.0	33.6	35.0	46.2
45	5.6	37.6	39.4	51.9
50	6.2	41.7	43.7	57.7
60	7.5	49.8	52.5	69.1

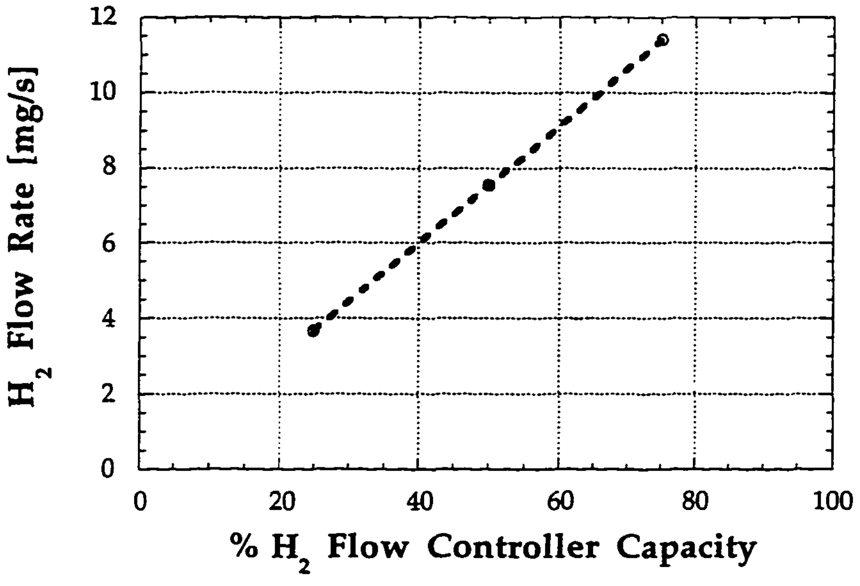

Fig. 2.9 Shown above is the calibration curve for the hydrogen flow controller.

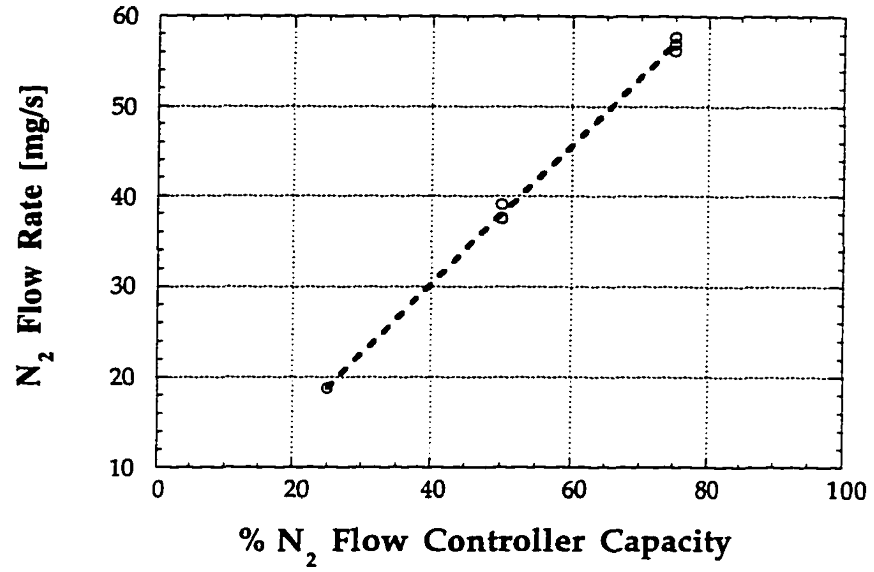

Fig. 2.10 Shown above is the calibration curve for the nitrogen flow controller.

2.2.2 Data Acquisition Equipment

The data obtained in this experiment is in the form of probe voltage signals, which are recorded using a SOLTEC, Inc. ADA-FE-08R four-channel digitizing oscilloscope. This oscilloscope has a maximum sampling rate of 10 MHz with a maximum storage capacity of up to 64K samples on each of the four channels. The floating potential data was sampled at a rate of 333 Hz for 16,384 samples and the V-I data was sampled at 1.67 kHz for 32,768 samples. To determine whether high frequency components were overlooked at the 333 Hz sampling rate during the ϕ_f measurements, a test was conducted where ϕ_f data was obtained for probe 2 at a sampling rate of 10 kHz. It was found that the ϕ_f was fairly constant with time and was within the experimental error of the ϕ_f data obtained at 333 Hz.

Prior to probe biasing, each probe was sequentially cleaned via ion bombardment, (Sec. 2.4.2) using a -160 V signal from a Hewlett-Packard Model 895A power supply, with a maximum output of -320 V and 1.5 A.

Each of the probes was then sequentially biased with multiple sinusoidal waveforms using a Wavetek Model 147 HF sweep and function generator. The output of the function generator was set to a ± 2.44 volt peak-to-peak 10 Hz pulse, and fed into a 9:1 gain noninverting operational amplifier circuit powered by a LM675T high power op-amp, which prevented over-loading the function generator output signal. The op-amp circuit supplied each probe with a ± 22.4 volt peak-to-peak signal.

The probe current was obtained by measuring the potential drop across a low inductance 2% shunt resistor, $R_s = 103.7\ \Omega$. This was the maximum resistor value used without overloading the function generator current output, while still providing a reasonable S/N (signal-to-noise) ratio. A 0.1% 9.4 μF capacitor network was used across R_s for noise filtering. The probe voltage was determined from the function generator output and was corrected for the potential drop across R_s during the data reduction.

The probes were individually biased and cleaned through a probe controller unit, (see Fig. 2.11). This unit housed: the shunt resistor to measure the probe current; capacitors; a jumper cable and several switches for individual control of each probe in the nozzle; and push buttons for probe cleaning, biasing and triggering signals. A jumper cable was used for protecting the circuitry from inadvertently sending large voltage signals back to the function generator input, which would damage the device. The signal inputs to the controller unit are: (1) the probe biasing signal from the op-amp/function generator combination; (2) the probe cleaning signal from the HP Model 895A power supply; (3) the 6 Vdc triggering signal used to gate the function generator output; and (4) the arcjet operating current and voltage signals.

The signal outputs from the probe controller unit to the oscilloscope are: (1) probe biasing voltage, (2) potential drop across R_s, (3) arcjet operating voltage and (4) arcjet operating current. The voltage signal to Channel 1 of the oscilloscope was reduced with a 5:1 voltage divider, to protect the oscilloscope from any high probe cleaning signals. These signals were recorded on an IBM 286 computer via an IEEE-488 bus, which connected the SOLTEC oscilloscope to the computer. At each of the channel inputs to the oscilloscope a .086 μF capacitor was used in parallel with the oscilloscope input impedance to provide additional noise filtering of the probe signals. These capacitors were only required when obtaining floating potential data.

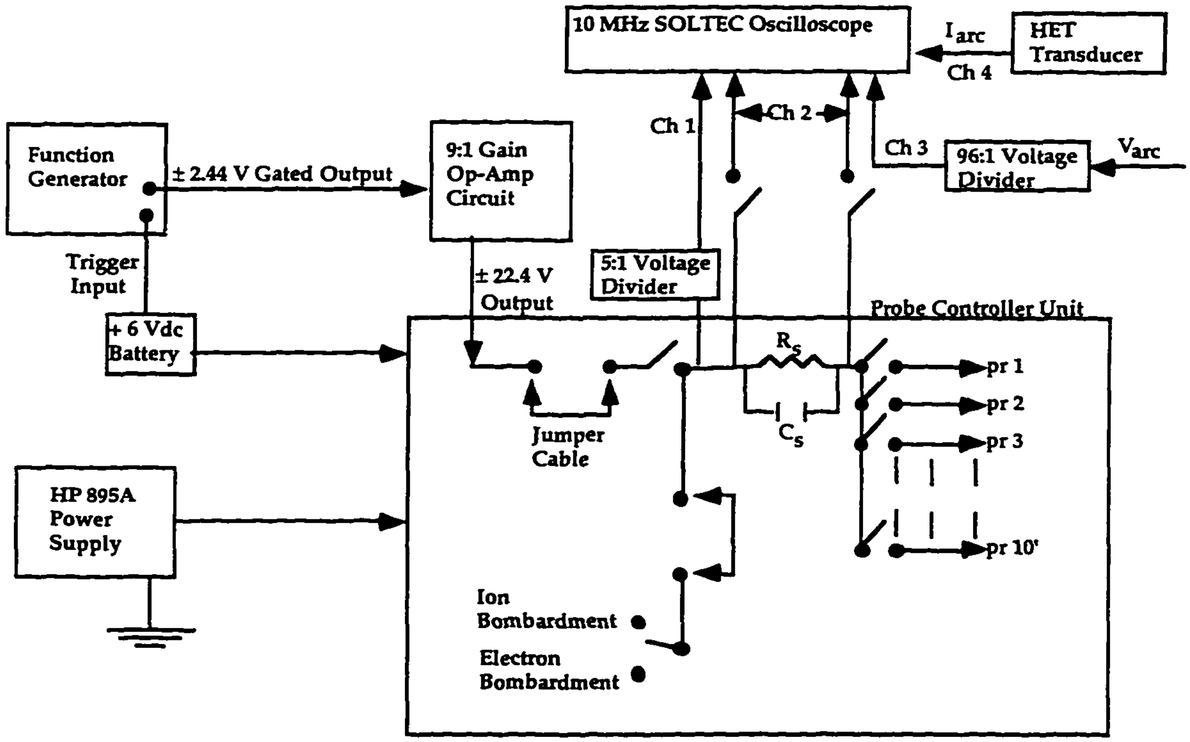

Fig. 2.11 Schematic of diagnostics set-up and data acquisition equipment. The probe controller unit houses the probe selection switches, the shunt resistor, capacitor, a jumper cable and probe cleaning switches.

The arcjet was powered by a NASA-Lewis power processing unit (PPU). The PPU is a pulse width modulated power supply with rapid current regulation. It has an open circuit voltage of 175 Vdc and a maximum current output of about 11 A. To initiate arc breakdown, the PPU has a circuit which provides a 4 kV pulse at 1 Hz until arc ignition is acquired. After arc breakdown, the main power supply circuitry then sustains the arc, and the pulse circuit stops, [Curran, *et al.*, 1992]. The user specifies the amount of arc current I_{arc} as an input, with the thruster voltage, V_{arc} determined by the plasma impedance, ~10 Ω. The design of the PPU electronics is such that there is an inherent ac ripple associated with the arcjet supply current. The PPU ripple, as determined by Bufton [1996], has a frequency of 15-20 kHz, resulting in I_{arc} variations that are ± 8 % about the mean.

The arcjet operating voltage was measured with a voltage probe attached to the cathode feedthrough. To obtain a tolerable signal level for the oscilloscope, a 96:1 voltage divider was placed in parallel with the arcjet.

The arcjet operating current was measured by a Hall-effect current sensor. The Hall-effect transducer (HET) was a LEM USA, Inc. model LTA 100P 1:1000 current transformer, which produced an output of 1 mA for each amp of current passing through the transducer coil. The HET output current was measured by obtaining the voltage drop due to the current across a 34.6 Ω shunt resistor. To obtain reasonable output signals, five turns of the arcjet current lead wire were looped through the current transformer. The conversion for the arcjet operating current was $I_{arc} = 5.78 \times V_{out}$, where V_{out} is the voltage drop across the 34.6 Ω shunt resistor, [Bufton, 1996].

For nozzle surface temperature measurements a radiation-shielded chromel-alumel type K thermocouple was located at 45° and 9.4 mm from the exit plane.

2.3 Electrostatic Single Probe Diagnostic Technique

Much of the recent internal nozzle diagnostics work has been done using spectroscopic methods, [Zube, *et al.*, 1992, 1993; Glocker, *et al.*, 1992; Hargus, *et al.*, 1994; Cappelli *et al.*, 1994]. Although these techniques are attractive because they are relatively non-intrusive, they can be expensive and difficult to set-up and implement in the laboratory. Electrostatic probes have recently been used in magnetoplasmadynamic thrusters [Soulas, *et al.*, 1993; Gallimore, *et al.*, 1993; Burton, *et al.*, 1993] and arcjet plumes [Carney, *et al.*, 1989] as a diagnostic. They are relatively simple in design and provide a convenient method of obtaining local plasma properties at the probe pre-sheath edge, e.g. electron number density n_{es}, electron temperature T_{es} and current density j_a. Such local measurements will help validate numerical model predictions near the anode and guide these models to more accurately describe the near-anode physics, important for understanding arc attachment physics and anode heating.

The electrostatic micro-probes used in this research are a type of Langmuir probe. The descriptive term "electrostatic" essentially refers to a diagnostic that measures the properties of a *continuum* plasma [Chung, *et al.*, 1975], whereas Langmuir probes refer to diagnostics in a *rarefied* plasma. Langmuir probes were first invented by Irving Langmuir in the 1920's, for studying the plasma in an arc discharge tube, [Langmuir, *et al.*, 1923, 1924, 1926] Since then these probes have been used in a wide variety of applications, from studying the physics of high energy fusion devices such as tokamaks to studying the boundary layer of a hypersonic vehicle during reentry [Boyer, *et al.*, 1972; Bredfeldt, *et al.*, 1967; Hayes, *et al.*, 1973].

In this work electrostatic micro-probes are utilized to study the anode boundary layer of a 1 kW arcjet thruster, providing information on local current density j_a, floating and sheath potentials ϕ_f and ϕ_s, electron temperature at the pre-sheath/plasma edge, T_{es}, and electron number density at the pre-sheath/plasma edge n_{es}. Although this technique may seem physically intrusive, it is later shown that with careful implementation and interpretation of data, electrostatic micro-probes can provide detailed information about important local plasma properties in the anode sheath, where much of the complex arcjet thruster plasmaphysics occurs. This fact, combined with the low cost and relatively simple maintenance of the probes and their implementation, makes them attractive for internal arcjet boundary layer diagnostics research.

Two types of probe geometries are used in this study. A cylindrical probe extending into the plasma flow an amount $0.1 \leq L_{ext} \leq 0.3$ mm and a flush-mounted planar probe, $L_{ext} = 0.0$ mm, flush with the interior anode wall. Each probe geometry will provide the relevant plasma properties mentioned above. The cylindrical probes are used in order to obtain the plasma properties within 0.25-0.30 mm of the anode at each of the 14 axial and azimuthal locations.

2.3.1 Probe Sizing and Geometry

From Fig. 2.5 it is obvious that the arcjet nozzle dimensions are very small. The constrictor diameter is 0.64 mm, while the exit diameter is 9.6 mm. The nozzle radius at probe 1 is 0.68 mm, and at probe 10 it is 3.96 mm. This geometry places obvious constraints on the probe's size. The probe radius r_p, must be minimized to avoid any induced disturbances to the plasma flow, placing an upper limit on r_p. However, because of the intense plasma heating, especially within the first 3 mm of the constrictor exit, the probe must have a large enough thermal mass to avoid melting, thereby placing a lower limit on r_p. The probe must also be large enough to collect a measurable amount of current, but small enough to avoid perturbing the plasma as well.

Probe heating and thermionic emission effects also require consideration. Calculations are made based on an approximate heat transfer analysis that neglects plasma radiation and convective heating effects to the probe. If a balance is attained between the power deposited into the probe due to the current collection and the thermal heat capacity of the probe, then an estimate of the final probe temperature is given as:

$$T_p(\Delta t) = T_o + \left[\frac{I_p^2\rho_w}{\rho C_p\left(A_p\right)^2}\right]\Delta t \qquad (2.2)$$

where T_o is the initial probe temperature, before the probe is biased positive or negative; I_p is equal to the maximum electron current collected during a typical test, approximately 25 mA; ρ_w is the resistivity of the tungsten probe ($5.6\text{x}10^{-8}$ Ω-m); ρ is the density of tungsten ($1.93\text{x}10^5$ kg/m^3); C_p is the specific heat of tungsten (162 J/kg °K), A_p is the geometric probe area and Δt =0.1 sec is the period of one sinusoidal pulse to the probe. Before the biasing potential is applied, T_o is estimated as the gas temperature along the anode, $T_{gas}=T_a=1400$°K, since the probe and the plasma are in direct contact and therefore in thermal equilibrium.

For conservative calculations of r_p = .08 and 0.21 mm, for a probe bias of 0.1 sec (10 Hz function generator frequency) the probe's temperature rise, given by the second term in Eq. (2.2), is ~O(.01-1 °K) for I_p = 20-200 mA. This is a negligible amount, so that the limiting factor on the probe integrity is the gas temperature, not the probe temperature rise during biasing. Therefore where the probe is placed in the plasma flow determines its survivability. Even for the cylindrical probe placement of 0.25-0.3 mm into the flow, $(T_{gas})_{avg}$ ~ 1600 °K, so that the probe integrity is not compromised, since the melting temperature of tungsten is 3700 °K.

A small probe radius is also required to minimize perturbation effects to the plasma flow around a cylindrical probe that extends away from the anode wall. Depending on the sheath thickness, a small probe may have a large sheath-field fringing effect, thereby artificially increasing its collection area and perturbing the space-charge potential field near the probe, (See Fig. 3.7, Sec. 3.2.2). If the ratio of the sheath thickness λ_s, to the probe radius r_p is << 1 then the sheath fringing field has negligible effect. To assess the field-fringing effect $\lambda_{s,e}$ is calculated, since the sheath area for electron collection is required for evaluating j_a. As shown in Fig. 2.12, for $(r_p)_{1,1'}$ = 0.085 mm and

$(r_p)_{2\text{-}10'}$=0.20 mm, so that $\lambda_{s,e}/r_p < O(1)$, i.e. negligible sheath-edge effects. It is also desirable to operate the probe in a thin collisionless sheath regime, simplifying the data analysis. To satisfy this condition, $r_p/\lambda_D >> 1$ and $\lambda_{rs} >> \lambda_s$, where λ_{rs} is the mean free path for collisions between species r and s, Sec. 3.2.1.

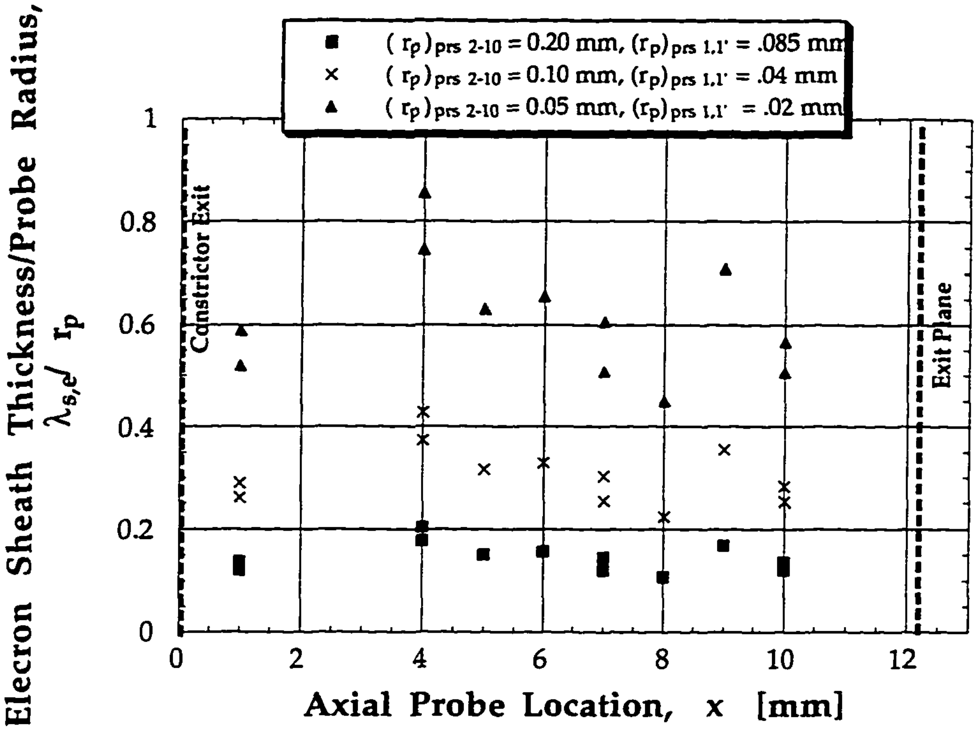

Fig. 2.12 The electron sheath thickness normalized by the probe radius vs x for three different probe radii. The ratio of $\lambda_{s,e}/r_p$ is a measure of sheath-edge effects, which are minimized if $\lambda_{s,e}/r_p < 1$.

Another constraint on the probe size is the probe hole diameter d_h, which houses the tungsten probe wire, the alumina (Al_2O_3) tubing that surrounds the probe and the stainless steel tubing that protects the Al_2O_3. It is desirable to minimize d_h : (1) to prevent any possible adverse affects the presence of the hole may have on arc attachment (due to sharp edges), and on the fluid dynamics, i.e. flow separation, especially near the constrictor exit; and (2) to place more probes inside the anode.

Preliminary results from the MKB (Megli-Krier-Burton) numerical arcjet model [Megli, *et al.*, 1996], suggested that the region of maximum current density was within 1 mm of the constrictor exit. Based on this finding, the probe holes were sized to 0.94 mm for a nominal alumina tubing O.D. of 0.79-0.86 mm. This dimension on d_h would position probes 1 and 1', 1 mm axially downstream of the constrictor exit with a lateral distance of about 0.58 mm between the constrictor exit and the edge of the probe hole. This was the closest possible location to the constrictor that a hole can be machined without compromising the integrity of the nozzle throat and minimizing any flow disturbances in that region.

Another concern with regards to sizing the probe is generation of displacement currents in the coaxial probe wire-Al_2O_3 configuration. The tungsten wire, surrounded by a cylindrical dielectric, can essentially be considered a capacitor. A displacement current I_d is created in the gap of a capacitor due to changing electric fields inside the Al_2O_3-probe wire configuration; therefore $I_d = \varepsilon_o d\Phi_E /dt$ where Φ_E is the electric field flux given as: $\Phi_E = E^*A$, where A is the area of the capacitor gap.

The probe-plasma system can be modeled as an electrical circuit with the plasma providing a path to ground. The probe-Al_2O_3 configuration is described by a probe resistance R_p and a capacitor C_p to ground. In this circuit, only I_p can be measured by the 2% shunt resistor $R_s = 103.7\ \Omega$. Consideration must be made to avoid capacitative effects, i.e. the generation of relatively large displacement currents I_d, that may dominate I_p, leading to spurious results.

In order to compare the magnitude of the displacement current I_D, with the probe current I_p, the ratio of the displacement current to the probe current is calculated. An order of magnitude analysis shows that for a probe length of 1 cm and an average biasing voltage of 10 V at a frequency of 10 Hz, the ratio $I_D/I_p \sim 2\text{x}10^{-6}$ for the minimum probe current of ~ 1 mA. Therefore, the generation of displacement currents in the Al_2O_3-probe wire configuration is not a concern.

The capacitive impedance is $Z_c = (1/2\pi f C_p)$, where f is the function generator frequency. For probes 1 and 1′, $C_p = 0.10$ nF and for a biasing frequency of 10 Hz, $Z_c = 160$ MΩ; for probes 2-10′, C_p=20.5 pF and for a biasing frequency of 10 Hz, $Z_c = 800$ MΩ. Since $Z_c >> R_s$, if any displacement current were generated in the probe-Al_2O_3 configuration it would flow through R_s and therefore be measured as the total probe current, I_p. However, even if any I_d were generated this current is much less than I_p, as discussed above.

In summary, the various constraints that dictate the probe size are:

(1) the value of r_p/λ_D required by a particular probe theory, e.g. collisionless thin sheath, or collisional thick sheath; Sec. 3.2. As a general rule the probe dimension should be very much smaller than the characteristics dimensions of the plasma being studied, [Swift, *et al.*, 1969]. As mentioned earlier, to minimize sheath-edge effects the quantity $\lambda_{s,e}/ r_p << 1$.

(2) if there are any gradients in the plasma properties near the anode, the probe dimensions should be such that no appreciable change in the plasma parameter exists over a distance of ~ 100 r_p. For low pressure plasmas this requirement can be satisfied when the mean free path between electrons and ions is much greater than r_p, but still much less than the plasma dimension, [Swift, *et al.*, 1969]; mean free path calculations show that this is indeed the case with the mean free path for electron-H+ collisions varies between 1-6 mm, a value much larger than r_p.

(3) minimize r_p to prevent large carrier drain to the probe and flow disturbances.

(4) probe size should be large enough to avoid melting, thermionic emission effects and achieve a reasonable signal/noise ratio, i.e. collect a measurable amount of current.

(5) the probe dimensions should be of such size so as to minimize any unwanted capacitative effects the probe wire/Al_2O_3 combination may induce.

Based on the above analysis and requirements, the size selected for probes is presented in Table 2.2. The total number of probes selected was fourteen; this maximizes the resolution of plasma property axial profile data. Both planar (flush-mounted) and cylindrical probe geometries were used to probe the anode boundary layer.

Table 2.2 The probe specifications for diameter of the tungsten wire, alumina (Al_2O_3) tubing and probe hole dimensions.

Probe	D_p (mm)	Al_2O_3 O. D. (mm)	d_h(mm)
1, 1′	0.15-0.18	0.58	0.68
2-10′	0.41-0.43	0.86	0.94

The probe dimensions listed in Table 2.2 satisfy the five criterion discussed earlier.

2.3.2 Probe Fabrication

The electrostatic micro-probes 2-10′ are made from 0.43 mm diameter 99.95% pure tungsten wire, surrounded by an alumina (Al_2O_3) insulator tubing with an average O.D. = 0.86 mm and I.D = 0.51 mm and inserted into a Type 304 stainless steel tube, I.D. = 1.22 mm. For probes 1,1′ 0.17 mm diameter tungsten wire is used, surrounded by an Al_2O_3 tubing with an average O.D. = 0.58 mm and I.D. = 0.20 mm and inserted into a Type 304 stainless steel tubing with I.D. = 0.81 mm. Alumina (99.8% Al_2O_3) was selected as the insulator for the tungsten probe wire because: (1) it has a high volume resistivity of $\geq 10^{12}$ Ω-m at 300 °K for 99.8% Al_2O_3 and a volume resistivity of 10^6 Ω-m at 1300 ° K for 96% Al_2O_3,[Vesuvius McDanel, 1991]; (2) it has a relatively high dielectric strength, 320 V/Mil [Vesuvius McDanel, 1991]; (3) it has a maximum temperature of use of 2200 °K which is >> T_a ($T_a \sim 1400$ °K); and (4) the required sizes for the insulator tubing were readily available with alumina as the material.

The tungsten probe wire and alumina tubing are held in place with high temperature (2500 °K) zirconia adhesive. The probe wire is inserted into the alumina, with its tip extended at various extension lengths L_{ext}, from the tubing edge, Fig. 2.13.

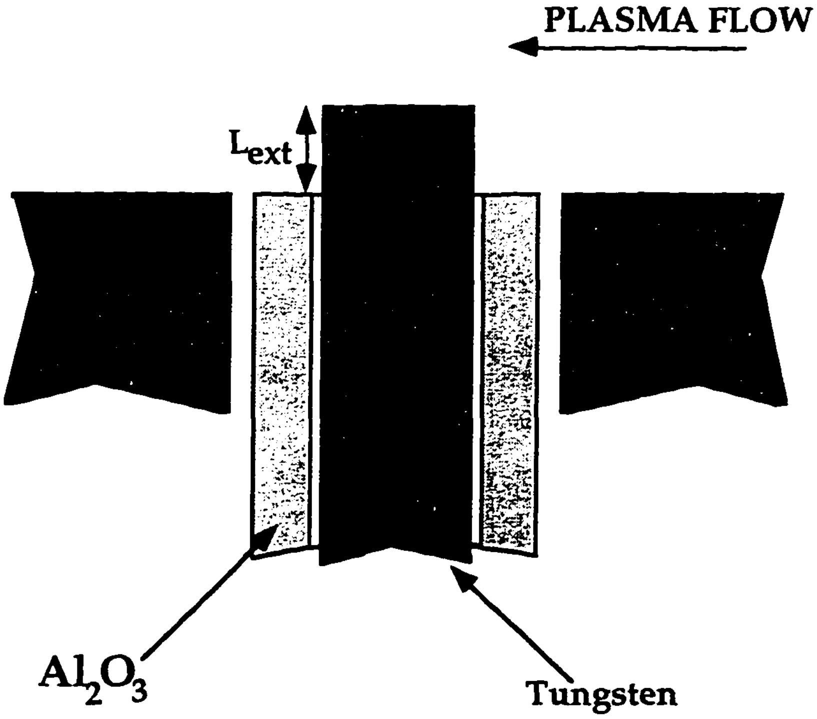

Fig. 2.13 Shown above is a drawing to scale of the tungsten probe-Al_2O_3 configuration inside the anode. The probe tip extension is varied between ~0.0 and 0.3 mm into the plasma flow. The probe diameter, Al_2O_3 size and probe hole diameter specifications are shown in Table 2.2.

The extension length L_{ext}, is measured before and after testing with a high power microscope/camera set-up. A gap is intentionally allowed between the probe wire and the Al_2O_3 edge, to prevent contact with any sputtered probe material that may have deposited onto the alumina tubing edge. Any contact between sputtered material on the tubing edge and the probe leads to uncertainty in the probe collection area.

Tungsten was selected for the probe material because of its high melting point, 3680 °K, and high work function, 4.55 eV [Goodfellow, *et al.*, 1995] giving low electron emission. During probe fabrication it was important that both the probe and Al_2O_3 tip be made as flat as possible through repeated sanding, eliminating any rough edges from the surface.

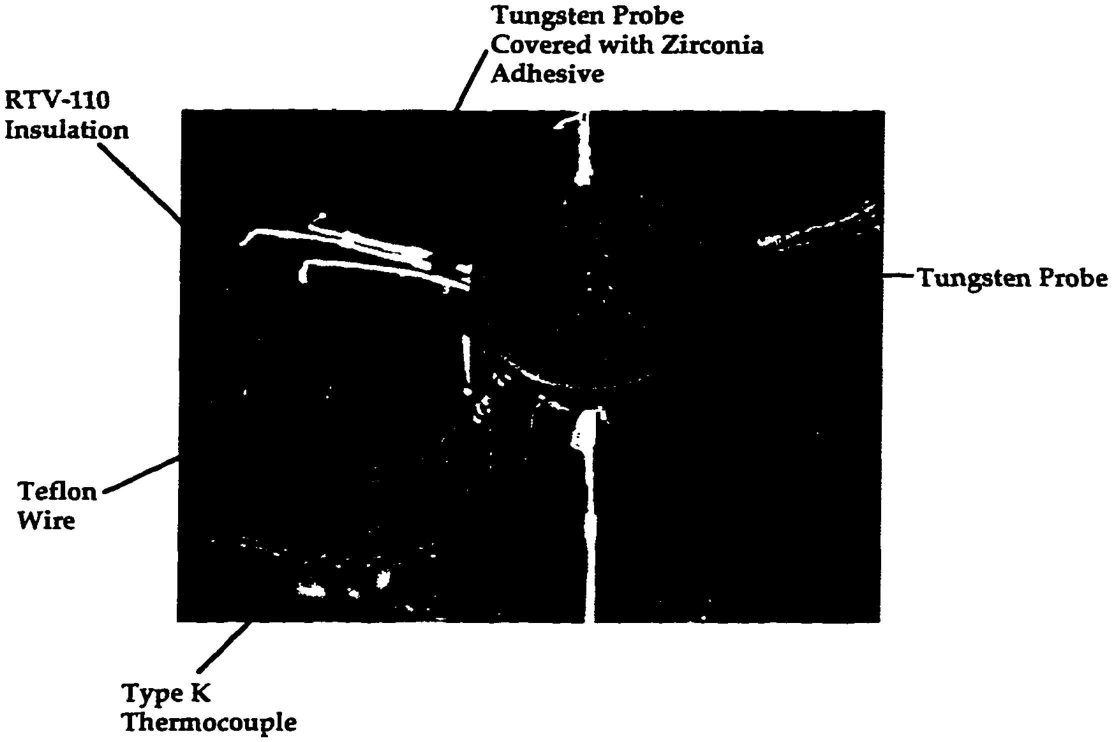

Fig. 2.14 A photograph of the monolithic thruster body, with the probes shown in position. The white spots on the nozzle interior surface are the Al_2O_3 tubing with the tungsten probe wire positioned inside. Teflon wires are shown attached to gold plated miniature connectors to the probe wires.

The tungsten wire/Al_2O_3 configuration was then carefully placed inside a stainless steel tubing, which was then glued into the grounded anode. The edge of the alumina was flush with the internal anode surface, so that only the tungsten probe tip was allowed to extend into the plasma flow. The ends of the probe wires were each soldered to gold plated miniature connectors and were then mated to Teflon wires mounted to two vacuum connectors. All connections were covered with RTV 110 [General Electric Co.], an electrically insulating adhesive, Fig. 2.14.

After each test, the probes are removed from the anode and their surface condition is inspected and their diameter is measured again. Post-test photomicrographs are only taken for the cylindrical probes to assess L_{ext}. Also the electrical conductivity of each probe is checked with a multimeter. The probes are then cleaned with repeated sanding to remove foreign deposits that may have accumulated during the experiment, and re-used. New alumina tubing may also be used for the probes depending on their post-test condition.

2.3.3 Measurement of Probe Collection Area

Whether the probes are planar, i.e. flush-mounted, or cylindrical, determining their geometric area is complicated if the alumina tubing is damaged, exposing an unknown collection area. If Al_2O_3 damage occurred it was almost exclusively to probes 1,1' and 2, since they are in the region of maximum current density. This damage is mainly cracking or tip vaporization of the Al_2O_3 tubing due to the intense heating and thermal stresses encountered by these probes.

Cracking or vaporization of the Al_2O_3 exposes an unknown probe area to the plasma flow, adding to the uncertainty in the A_p calculation, and therefore the current density measurement. Figure 2.15 a-d shows the various scenarios of Al_2O_3 damage that have been observed.

Based on the scenarios depicted in Fig. 2.15a-d, the post-test geometric probe area is given as:

$$A_{Post-Test} = \frac{\pi D_p^2}{4} + \varepsilon \pi D_p \left(\bar{L}c + L_{ext}\right) \qquad (2.3)$$

where D_p is the probe diameter, L_{ext} is the probe extension length from the anode, and $\bar{L}$ is an average probe exposure length due to the Al_2O_3 cracking. The variable c is an estimate of the fraction of Al_2O_3 tip cracked and varies from 0-1 and ε is a probe "exposure factor", where $\varepsilon = 0$ refers to a flush-mounted probe and $\varepsilon = 1$ refers to the probe when it is not flush with the alumina and is exposed to the plasma flow, either intentionally or if damage occurs to the alumina tip, Fig. 2.15b and c or if the alumina recedes into the probe hole, Fig. 2.15d.

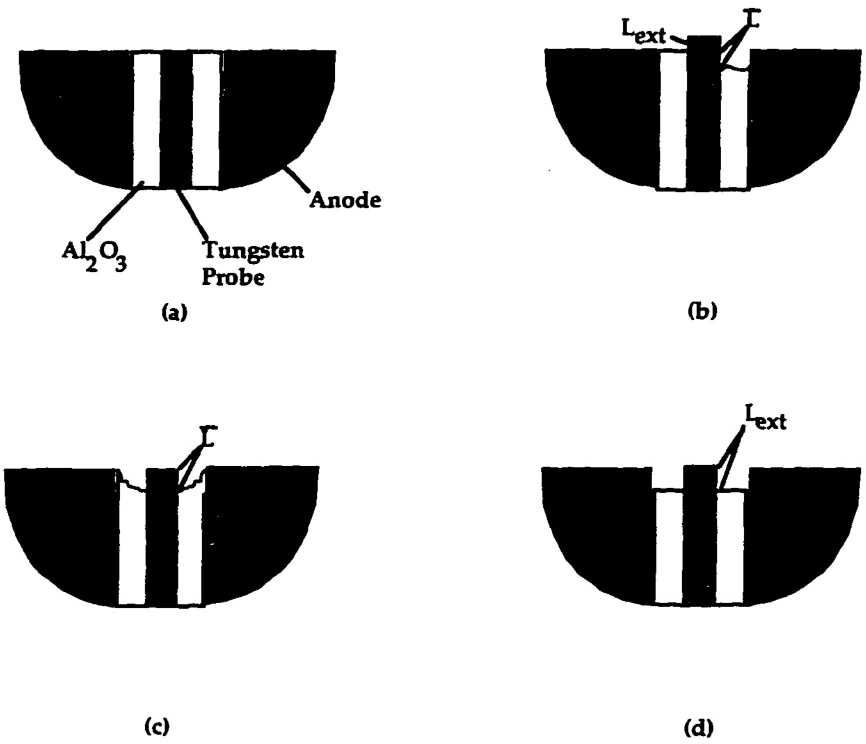

Fig. 2.15 Schematic of the various configurations of the Al_2O_3 tubing, exposing probe wire to current collection. Case (a) is when the probe is flush-mounted; case (b) is when a cylindrical probe is used, with part of the Al_2O_3 tip cracked; case (c) is when the flush probe is used with part of the Al_2O_3 tip cracked; and case (d) is when the flush or cylindrical probe is used, but the Al_2O_3 tubing has receded into the probe hole. Cases (b) and (c) only occurred occasionally to probes 1, 1′ and 2. The probe extension length is given by L_{ext}.

The factors c and ε make Eq. (2.3) a general expression for the geometric probe area. Equation (2.3) provides an approximate calculation of the geometric probe area; if the Al_2O_3 is not cracked and there is no exposure to the flow then only the first term in Eq. (2.3) provides the area. The values of D_p, L_{ext} and $\bar{L}$ in Eq. (2.3) are the post-test values, and the values for c and L are best estimates based on post-test visual observations of each probe with a magnifying lens.

Effect of Sheath On Probe Collection Area

In order to obtain accurate measurements of probe current density j_a, the probe's current collection area must be accurately calculated. The probe current collection area does not only include the geometric area of the probe A_p, but may also require accounting for the probe sheath area, A_s. This is particularly true if the probe bias is very high, in which case the probe sheath may extend enough into the boundary layer so that convection effects must be included in the analysis of the probe characteristic, [Hayes *et al.*, 1973; Clements, *et al.*, 1971], Sec. 3.2.3.

If the probe sheath thickness λ_s, is thick compared with the probe radius r_p, and larger than the boundary layer near the anode δ, then the sheath will intercept convected plasma particles and may collect them depending on their energy and the magnitude of the probe bias, [Clements, *et al.*, 1971]. It is therefore important to calculate the sheath thickness at all locations in the nozzle and compare this with the boundary layer thickness, Section 3.2.2.

When the sheath thickness is comparable to the probe dimensions, then the sheath is termed thick and the probe's collection area is appreciably different from the probe's actual physical area. A sheath is classified as thin if the ratio of the probe radius, r_p, to the Debye length λ_D, is much larger than 1. Also, if the ion saturation current $I_{i\text{-}sat}$, is constant and independent of a negative probe bias potential, then sheath convection effects are negligible since the sheath is thin, Sec. 3.2 and the probe collection area is assumed equal to the geometric probe area. Under certain conditions the ion saturation current may be dependent on the probe bias; this is because the sheath thickness increases as the probe potential is made more negative, leading to an increase in the sheath area and the overall effective probe collection area, A_{eff}. The dependence of λ_s and therefore sheath area, on the probe bias is determined by calculating the probe sheath thickness for significantly negative bias, i.e. an ion sheath surrounding the probe.

To provide accurate measurements of the probe geometric collection area, photomicrographs are made of all fourteen probes prior to and following testing. Figure 2.14 shows a photomicrograph of probe 2 before testing. The side view gives the extension length L_{ext} and diameter of the probe, D_p. A typical average value of the geometric area of the flush probe, except probes 1,1′, is 1.84 x 10^{-7} m^2 ± 6%, with an average diameter of 0.42 m m ± 1%.

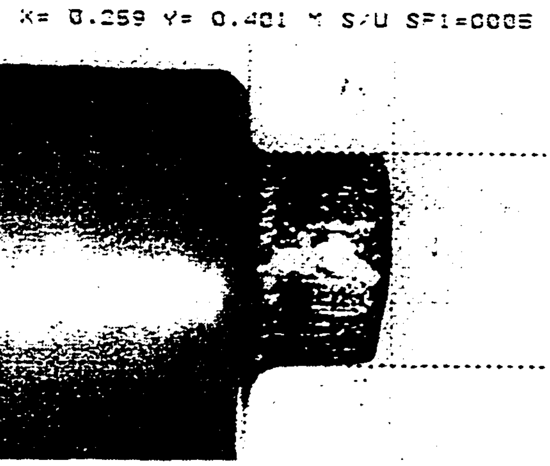

Fig. 2.14 Photomicrograph of probe 2, before a series of experiments, taken with a high power microscope/camera set-up. The side view provides L_{ext} and the probe diameter D_p, in mm.

2.3.4 Electrostatic Probe Operation and Experimental Procedure

All fourteen micro-probes are located in the anode housing at 10 axial and 4 azimuthal locations. One end of each probe is *in situ*, exposed to the plasma flow. The other end of the probe wire is soldered to a gold plated miniature connector which mates with Teflon wires mounted to two hermetically sealed vacuum connectors. Two 8 conductor twisted pair shielded Belden cables extend from the vacuum connectors to a probe diagnostics controller unit, from which BNC cables then carry the probe signals to 4 differential input channels of a 10 MHz digital SOLTEC® oscilloscope. The probe controller unit (Sec. 2.2.2) is an integral part of the diagnostics set-up, because it allows individual control over which probes are turned on or off in the nozzle and which probe cleaning techniques, i.e. ion bombardment and/or electron bombardment, are implemented.

Plasma properties, ϕ_f, ϕ_s, n_{es}, T_{es} and j_a are derived from the probe V-I characteristic, obtained by biasing the probe with a function generator and measuring the probe current, I_p with a current sensing shunt resistor R_S = 103.7 Ω ± 2%. The function generator is also used in a continuous mode, supplying a wavetrain of sinusoidal signals to the probes. The function generator frequency is kept at 10 Hz to avoid distortions in the probe V-I characteristics, as well as unwanted voltage drops across the low inductance shunt resistor located inside the probe controller unit.

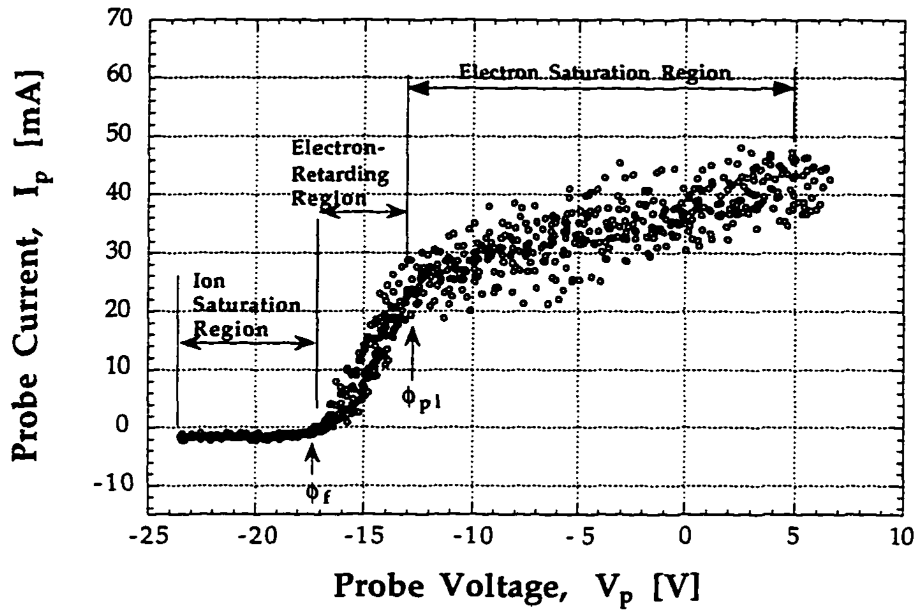

Fig. 2.15 A typical probe V-I characteristic.

A probe characteristic, a plot of probe current I_p as a function of probe voltage V_p, is obtained by biasing the probe with a sinusoidal voltage signal and measuring the collected current. Figure 2.15 shows a typical probe V-I characteristic. The potential at which the electron-retarding region diverges from linearity is referred to as the plasma potential ϕ_{pl} and the potential where the probe current becomes zero is the floating potential ϕ_f.

Sections of the V-I curve include: (a) the electron-saturation region, where only electrons are collected for $V_p \geq \phi_{pl}$ and the probe is surrounded by an electron sheath, (b) the electron-retarding region where some ions and energetic electrons are collected for $\phi_f \leq V_p \leq \phi_{pl}$, and (c) the ion-saturation region, where only ions are collected for $V_p < \phi_f$, and the probe is surrounded by an ion sheath. Further details on the information that can be extracted from the probe V-I curve are described in Sec. 3.3.

Prior to each experiment the probes are visually inspected for erosion and checked for continuity in the circuit. The arcjet is started at 50 mg/sec and 10 A taking about 25-30 minutes to achieve a steady state temperature of ~ 900 °K. The probes are cleaned about 30 seconds before they are sinusoidally biased and are also cleaned approximately every 2-3 minutes. The probes are cleaned via ion bombardment, Sec. 2.4, with one to two -160 V square wave pulses, for a cleaning duration time of about 0.15 sec.

After each probe is individually and sequentially cleaned the oscilloscope is armed and triggered as floating potential data ϕ_f is obtained by sequentially switching through all fourteen probes in increasing and decreasing order. This is done to verify reproducibility and to monitor any hysteresis in the data. The ϕ_f data is obtained with the function generator isolated from the circuit with a switch, Fig. 2.11. Similarly, the probe V-I characteristics are obtained by first cleaning the probes then sequentially switching and biasing the probes in increasing and decreasing order. The floating potential data is sampled at a rate of 333 Hz for 16,384 samples and the V-I data is sampled at 1.67 kHz for 32,768 samples. Data is obtained throughout the arcjet warm-up period and through steady state operation. Once all the data is obtained at a given experimental condition, either the flow rate or the arcjet operating current is then varied and the above procedures are repeated. Because the a.c. ripple on the arcjet current waveform is ~ 16 kHz [Bufton, 1996] and since the probes are biased at 10 Hz, the ϕ_f, ϕ_s, j_a, n_{es}, and T_{es} data are actually average values.

2.3.5 Experimental Considerations

The utility of electrostatic probes depends on the experiment performed. For example, in time varying plasma devices, such as pulsed arcjets, a rapid method for obtaining a probe V-I would be required. In this work, the plasma properties are obtained during steady state operation of a d.c. arcjet, so that rapid acquisition of the probe V-I is not a concern, though the probe biasing time should be kept minimal to avoid over-heating the probe.

In this research, it has been found that if the probes are biased at frequencies of 1-10 Hz the V-I curves for *clean* probes are very reproducible. However, for probe biasing frequencies ≥ 100 Hz distortions in the V-I curves are observed. These distortions are mainly in the form of relatively large hysteresis loops in the electron-retarding portion of the probe characteristic, making calculation of the electron temperature highly suspect. Sankovic [1990] observed similar sweep rate effects on the probe characteristic for probes situated in the exhaust plume of a 1 kW arcjet biased at frequencies of 100 Hz and 1 kHz. Therefore, to minimize the effects of high sweep rate, the probe biasing frequency was kept at 10 Hz for all the experiments conducted.

2.4 Probe Cleaning

Though the Langmuir probe is a fairly simple device, there are some complications associated with its implementation. Some of these include: (1) contamination of the probe's surface due to the formation of impurity layers; (2) change of probe area due to sputtering or melting of probe material in intense discharges; (3) temporal variation of the probe's effective work function during the measurement period [Szuszczewicz *et al.*, 1975]; (4) secondary electron emission; (5) plasma perturbation due to the presence of the probe, discussed further in Sec. 3.5; and (6) thermionic emission from the probe surface. Problems (4)-(6), are discussed in Sec. 3.5; issues (1)-(3) can be potential problems, but are solvable, as addressed below.

In the following sections an account is given of how probe contamination affects the V-I characteristic, a brief description of various cleaning methods, and a description of the cleaning technique used in this work.

2.4.1 Electrode Surface Contamination

Contamination of a probe's surface can greatly distort the V-I characteristic, leading to large errors in the measurement of electron temperature and electron number density, as well as underestimation of the current densities [Thomas, *et al.*, 1971]. Probe contamination has been documented in different types of plasmas such as: glow discharges [Thomas, *et al.*, 1971], rf discharges [Mosburg, *et al.*, 1983], and magnetrons [Bell *et al.*, 1988].

The causes of electrode surface contamination are not always readily identifiable, but contributions may come from the coating of sputtered material onto the probe surface from other solids in the system; the probe contaminant could also be a metallic oxide of the probe material, [Clements *et al.*, 1978]. The Al_2O_3 tubing could also be coated with material that sputtered off the probe surface, potentially increasing the probe collection area. In this work, there have been some instances where the alumina sleeve tip vaporizes, depositing its material on probes directly downstream. Consequently, the contaminated probe characteristic, Fig. 2.16, produces erroneous results for j_a, T_{es}, n_{es}, ϕ_f and ϕ_s.

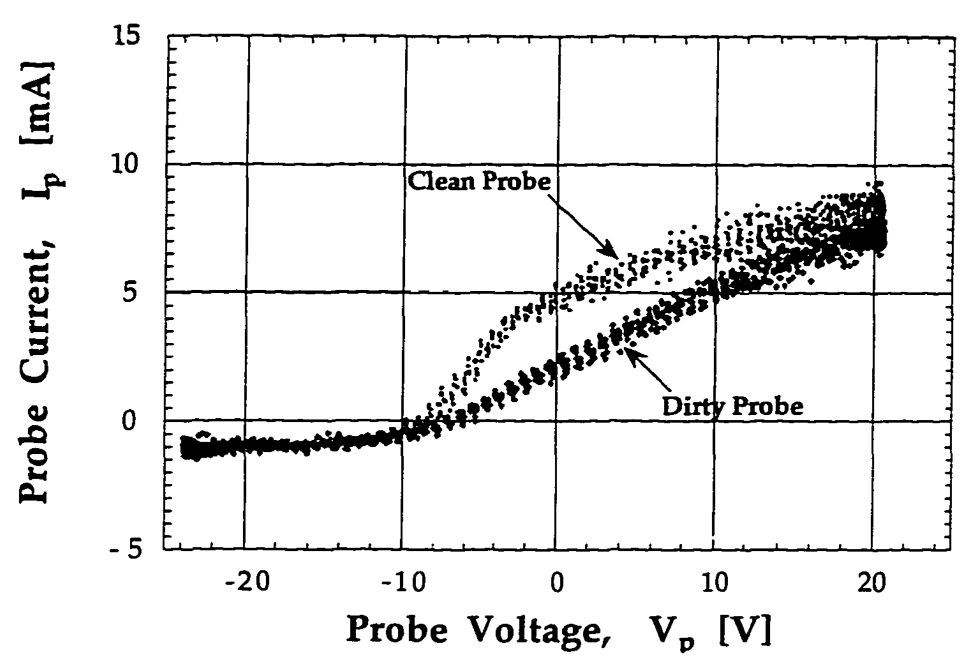

Fig. 2.16 A comparison of a V-I characteristic from a clean probe (10′) and a contaminated probe (10). Notice the shallower slope of the electron-retarding region ($-9\text{ V} \le V_p < 0\text{ V}$) for the contaminated probe and the absence of the distinctive "knee" in the curve, seen in the clean probe. The curves are based on experimental flush probe data for $\dot{m} = 50$ mg/s and 8.9 A.

Figure 2.16 shows a comparison of the V-I characteristics for a clean probe (probe 10′) and a dirty probe (probe 10). Notice the shallower slope of the electron-retarding region for the contaminated probe. This leads to an erroneous T_{es} which is about 1.5 times larger than T_{es} obtained from the clean probe.

Another contribution to electrode contamination may come from the absorption of gases and vapors from the surrounding plasma. The insulating layer of contaminant provides an additional resistance R_c, and capacitance C_c to the probe circuit. When the probe is biased with a potential V_p, the collected charged particles will flow to the contaminated surface and charge up the associated capacitance C_c and alter the surface layer by bombardment [Winters, *et al.*, 1974]. These conditions shift the probe bias to a different value than is actually applied and alter the collected current. The contaminating layers may not remain uniform during the probe biasing sweep. Consequently, electrode surface contamination leads to alterations in the probe's V-I characteristic in the form of hysteresis loops and abnormally shallow slope of the transition region, implying higher electron temperatures, Figs. 2.16-2.17.

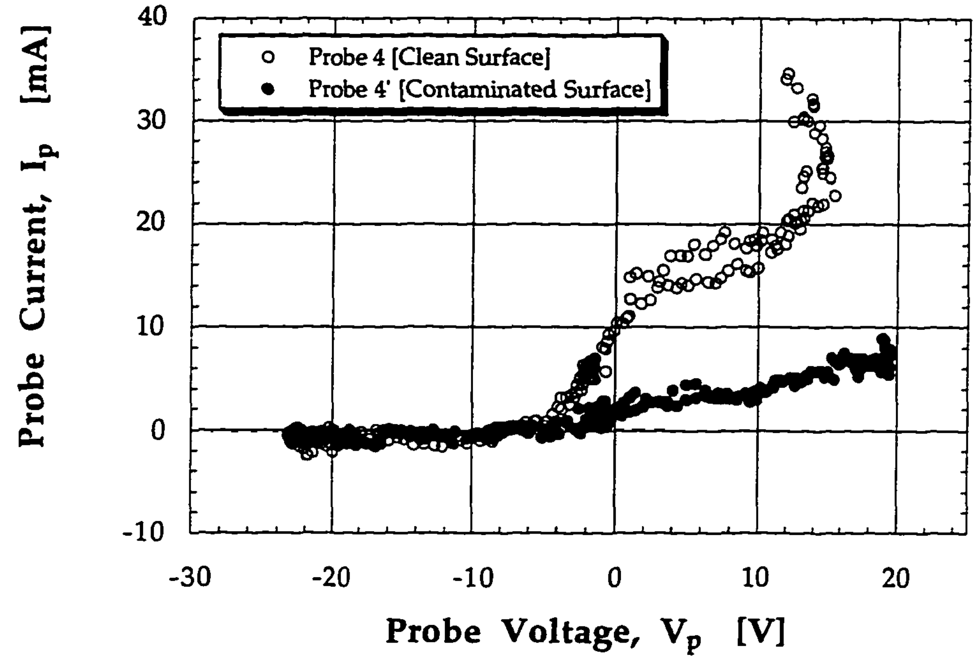

Fig. 2.17 Comparison of a probe characteristic for a clean probe (probe 4) and a contaminated probe (probe 4'). Contamination has a effect on the slope of the transition region, $-4 \le V_p \le 4$ V, and the value of I_a.

In this work, the main contributor to contamination of the probe surface was due to vaporization of the alumina surrounding the tungsten probe wire and subsequent deposition of this material onto the probe itself and others downstream, (Fig. 2.18), though the alumina material can withstand temperatures up to about 2200 °K. Figure 2.18 shows a comparison of a clean and contaminated probe. Notice the dark gray contaminants on the probe surface, contributing to a dirty and uneven surface layer.

When vaporization/thermal cracking of the alumina tip occurred, it was mainly limited to probes 1, 1′, 2. For probes located at x ≥ 4 mm Al_2O_3 vaporization of the probe tip was rarely observed. Unfortunately, damage to the probe insulator material, i.e. cracking and vaporization of the tip, also contributed to the uncertainty in the probe collection area. The effect of this uncertainty on the data analysis is discussed in Sec. 3.6. Attempts were made to minimize the insulator vaporization by receding the Al_2O_3 tip slightly, ~ O(0.05-0.10) mm into the probe hole. However, this also contributed to uncertainty in the probe collection area as well as in the probe position in the anode boundary layer. Therefore this procedure was abandoned in favor of flush-mounting the alumina tubing with the anode wall.

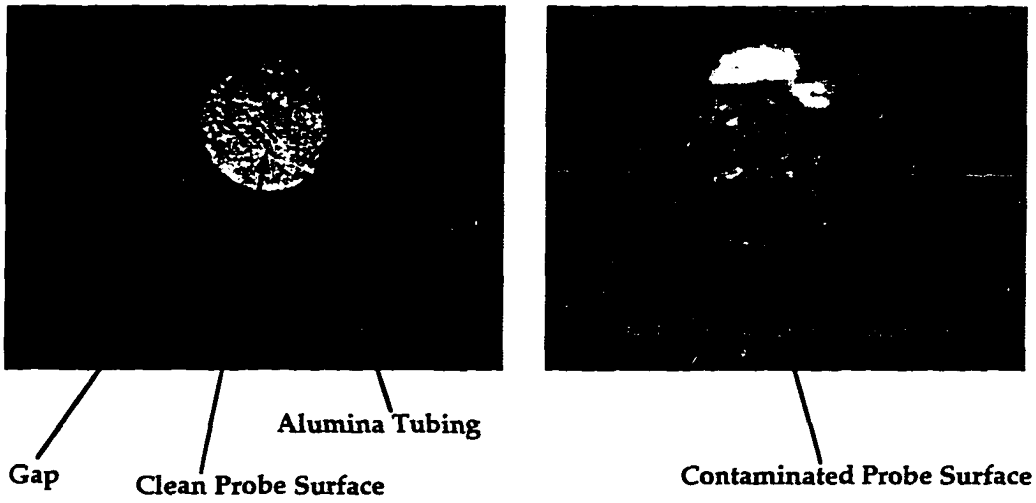

Fig. 2.18 Photomicrograph of a clean and contaminated probe, showing the effects of contamination on the probe surface condition. The contamination was predominantly the result of Al_2O_3 vaporization and subsequent deposition of this material onto the probe surface.

The effect of probe contamination is also evidenced in a semilog plot of electron current versus probe voltage; as contamination of the probe increases the "rounding of the knee" becomes more profound [Thomas *et al.*, 1971; Waymouth, 1959]. This rounding of the "knee" is also the result of plasma noise, [Hershkowitz, 1989]. This phenomena is clearly shown in Fig. 2.16

where the knee for the clean probe is relatively sharp and distinctive, compared with the noticeable absence of the knee for the contaminated probe.

Another condition which can affect the actual probe voltage is variation of the probe surface work function, sometimes called the patch effect [Swift, *et al.*, 1969]. The probe surface condition can change so rapidly that its work function may vary as the V-I characteristic is recorded; this is especially true when a static, point by point biasing technique is used [Wehner, *et al.*, 1952]. In this work the probes are biased sinusoidally, obtaining all the V-I data points simultaneously, thus minimizing probe heating effects and variation of the probe material's work function.

The probe material is 99.95% pure tungsten, with a work function of 4.5 eV [Schott, 1968; Goodfellow, *et al.*, 1995]. The probe work function is affected by adsorption of impurities and evaporation and sputtering from the probe. A changing probe work function leads to: (1) a shallower slope of the electron-retardation region, as is the case with contaminant layers on the probe; and (2) hysteresis in the probe characteristic and therefore a shifting of the "knee" along the voltage axis. This shifting in voltage may correspond to an amount approximately equal to the work function of the probe material [Wehner, *et al.*, 1952].

A varying probe work function also affects the reliability of plasma potential data in low voltage discharges and leads to the collection of electrons at different regions of the probe characteristic with a different probe work function, which may lead to an erroneous measurement of the plasma electron velocity distribution [Wehner, *et al.*, 1952], and consequently an incorrect value for T_{es}. This results in a non-Maxwellian electron velocity distribution, so that the electron-retarding region, on a semilog plot of I_e versus V_p, is not linear. In this research, for clean probes, the electron retarding region is linear so that the probe work function is assumed constant during the measurement period. This is accomplished by using ion bombardment for probe cleaning which, according to Waymouth [1959] helps maintain a constant probe work function.

2.4.2 Probe Cleaning Method Used in This Study

Many different types of probe cleaning methods exist. For example, probes can be cleaned by: (1) electron bombardment, where the probe is biased at a positive potential, leading to vaporization of the contaminants; (2) ion bombardment, where the probe is maintained at a large negative potential, imparting sufficient energy to the ions to sputter off the probe contaminants; (3) a combination of methods (1) and (2), first employing electron bombardment, allowing the probe to "cool" down sufficiently and then implementing ion bombardment [Thomas *et al.*, 1971] ; and (4) various pulsed probe techniques, where high speed circuitry is used to pulse the probe [Waymouth, 1959; Szuszczewicz *et al.*, 1975, and Holmes *et al.*, 1975].

Techniques (1) and (2) can be operated in a continuous mode or a pulsed mode. The advantage of electron bombardment is that it only requires a few volts positive, with respect to the plasma potential. However, the disadvantages of using electron bombardment are that the probe surface is usually heated to a very high temperature, possibly damaging the probe or leading to thermionic emission, which can be a serious source of error when interpreting the V-I characteristic, [Chang *et al.*, 1970]. Similarly, ion bombardment can lead to sputtering of the probe's material onto the Al_2O_3 edge making it conductive and drastically changing the probe's effective collection area.

Probe cleaning is dependent on the type of experiment performed. In near-field 1 kW arcjet plume studies by Sankovic *et al.*, [1990] the electrostatic probes were cleaned by electron emission, while being biased at +100 V. In this case the electron emission technique was used because of the advantage of visually monitoring the probe as it was being cleaned in the plume.

As mentioned in Sec. 2.4.1 probe contamination can also occur through coating of the alumina tubing with conductive material that may have sputtered off the probe surface. This can artificially increase the probe collection area if the material comes into contact with the probe. In a worst case scenario, the probe could become electrically "shorted" to some other electrode in the system [Clements *et al.*, 1978], such as the anode. To prevent this from happening: (1) the probe cleaning duration time is kept below 1 second to minimize probe heating, and melting or sputtering of the probe; and (2) there is a gap between the probe surface and the inner diameter of the alumina, Al_2O_3, tube, to minimize the chance of contact between the probe and any sputtered material on the Al_2O_3 surface edge, Fig. 2.18.

Probe cleaning by electron bombardment was not employed in this research because the electron current drawn would be intolerably large and would therefore damage the probes. Also, since the probes were embedded inside the thruster anode, i.e. in situ, visual inspection of the probe heating as it was being cleaned was impossible. Because of the above reasons, the probes were cleaned using a pulsed ion bombardment technique. To minimize the amount of probe current collected during the cleaning process, the probes were *individually* and *sequentially* cleaned with 1-2 square-wave pulses of -160 V, with a duration time of about Δt_{cln}=0.15 sec. This was done to prevent probe melting and thermionic emission during the cleaning. Minimizing Δt_{cln} was achieved by manually triggering a push-button switch, which, on average, provided Δt_{cln}~ 0.15 sec.

It was initially believed that the best approach to maintaining clean probes throughout the experiment was to have the probes continuously cleaned by ion bombardment, until it was time to apply the sinusoidal biasing potential. However, when this was done the probes collected too much current, ~0.1-.5 A, and on some occasions would burn out the shunt resistor; this approach was quickly abandoned in favor of the pulsed technique described above.

A probe cleaning study was conducted in which the following parameters were varied and their effects on the probe V-I characteristic were monitored: (1) probe cleaning duration time, Δt_{cln} (Fig. 2.19); (2) number of cleaning pulses, (Fig. 2.20); (3) magnitude of cleaning signal V_{cln}; and (4) probe diameter. The probe cleaning procedure that was used served mainly to maintain the original clean state of a probe, but once a probe was contaminated in situ it was very difficult to clean. This cleaning technique was found to be independent of Δt_{cln}, V_{cln}, the number of cleaning pulses and the probe diameter.

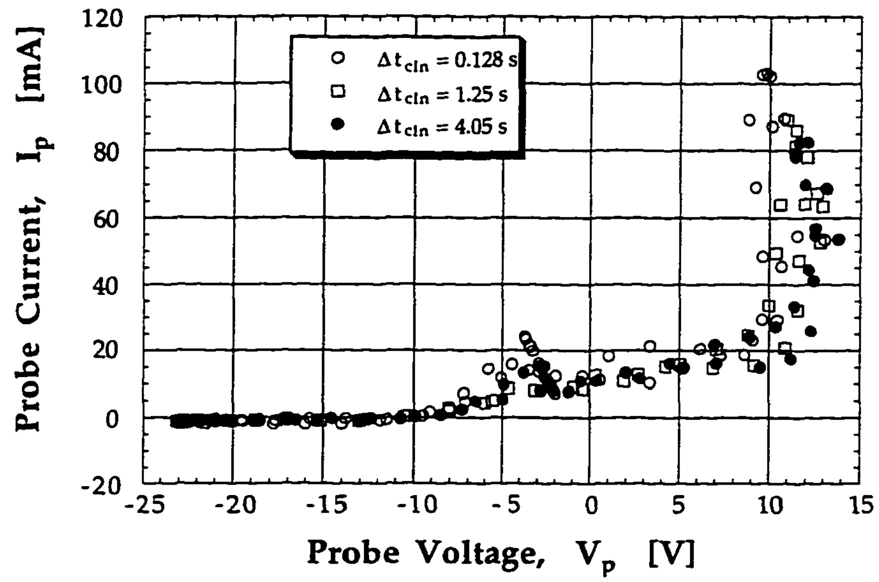

Fig. 2.19 Shown above is the probe 3 V-I characteristic for three different probe cleaning duration times, Δt_{cln}. The probe was cleaned using the pulsed ion bombardment technique, described in the text. There are negligibly small differences in the data for Δt_{cln} = 0.128 s, 1.25 s or 4.05 s.

Deciding whether a probe V-I characteristic is spurious due to probe contamination effects can be deceptive. For example, there have been instances where a probe V-I curve would exhibit some roundness in the knee,

Fig. 2.16, yet post-test observations of the probe surface showed that it was fairly clean.

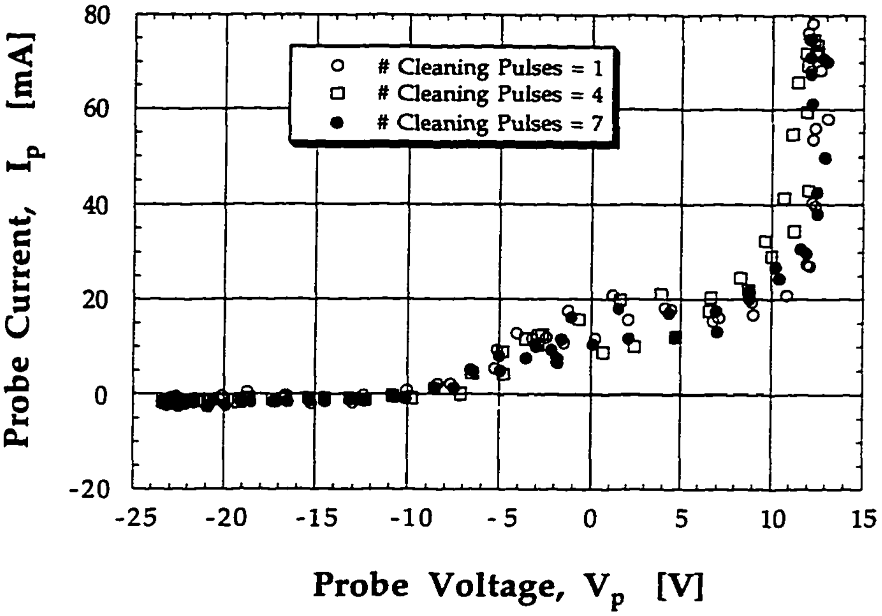

Fig. 2.20 Shown above is the probe 3 characteristic for 1, 4, and 7 cleaning pulses. The probe was cleaned using the pulsed ion bombardment technique at -160 V, for $\Delta t_{cln} \cong 1\text{-}2$ s. All three cleaning pulses produce a similar probe characteristic.

According to [Thomas *et al.*, 1971] the "rounding of the knee" "is too qualitative to serve as an indicator of contamination." Based on the observations made during this investigation it appears that "rounding of the knee" almost always occurs if a probe is contaminated; however, the converse was found to not always be true. This is what makes probe contamination effects particularly insidious.

The greatest probability for probe contamination to occur is: (1) within the first 1-2 minutes of arcjet start-up since the arc is still traversing the anode surface, before attaining a steady Varc; and (2) if the probes collect too much current during cleaning causing melting or vaporization of the Al_2O_3 tip.

Another observation made about probe contamination is that some probes were found to be contaminated yet their V-I characteristics exhibited no major hysteresis loop. This is believed to be due to the stabilization of the probe's contaminated surface during the experiment. On another occasion the V-I characteristic of a clean probe did exhibit some hysteresis in the electron-retarding region. Whether a probe was indeed contaminated was based solely on post-test visual inspection of all the probes tested. During the data analysis every effort was made to present data from "clean" probes. Therefore, data from probes that were severely dirty, e.g. Fig. 2.18, were not included in the analysis. However, some probes were found to have relatively clean surfaces, with some light discoloration patterns ("rainbow-like" in appearance). For the most part, data from these probes was included in this work, unless otherwise noted.

3. ELECTROSTATIC PROBE THEORY

3.1 Sheath Physics

When a plasma is in contact with a biased surface such as an electrode or wall, a non-neutral region develops between the plasma and that surface. This non-neutral region is called a sheath, which is an electrical boundary layer on the order of several Debye lengths (λ_D) wide, where space-charge effects dominate, i.e. $n_e \neq n_i$, resulting in large sheath electric fields, E_{sh}. The Debye length is defined as $\lambda_D = (\varepsilon_o k T_{es}/n_{es} e^2)^{1/2}$. The Debye length is the distance over which quasi-neutrality breaks down, so that for distances less than λ_D, $n_e \neq n_i$.

Understanding the sheath physics is related to: (1) anode heating and therefore anode erosion; and (2) arc attachment, i.e. constricted versus diffuse mode, [Self, *et al.*, 1983; Cappelli, *et al.*, 1992].

In the following sections a brief description of sheath fundamentals and anode sheath physics is presented.

3.1.1 Sheath Fundamentals

The plasma conditions in the sheath depend on whether it has a positive or negative potential drop, which in turn is dependent on whether $j_{th,e} > j_a$ or $j_{th,e} < j_a$, where $j_{th,e}=(1/4)en_{es}c_{es}$, the electron random thermal current density and c_{es} is the most probable thermal speed of electrons given as $c_{es}= (8kT_{es}/\pi m_e)^{1/2}$.

Figure 3.1 shows the pre-sheath and sheath regions for a negative potential fall, i.e. $j_{th,e} > j_a$, near the anode and a positive potential fall. A negative potential fall sheath is referred to as an electron repelling sheath, whereas a positive potential fall is an electron attracting sheath, Sec. 3.1.2.

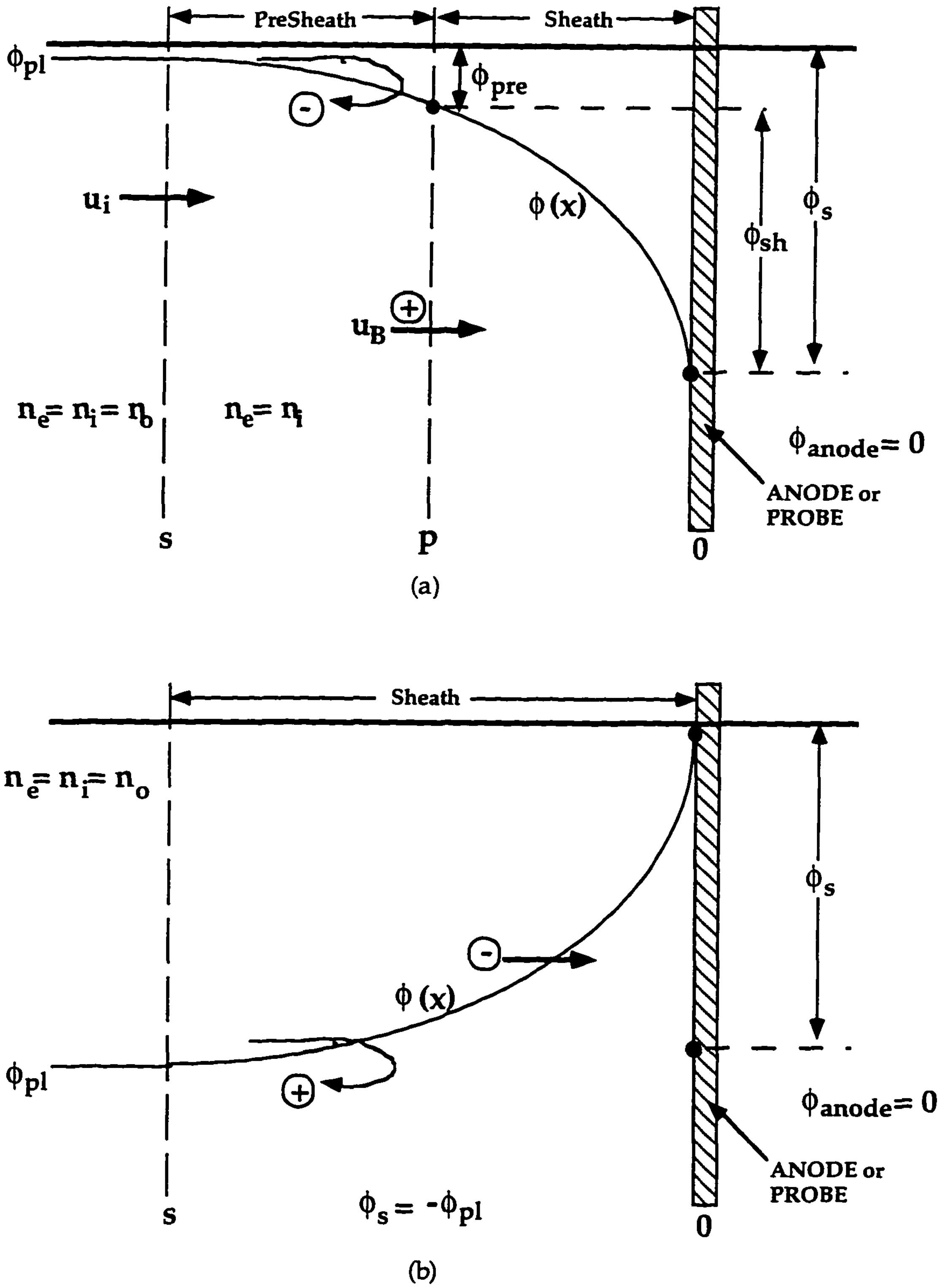

Fig. 3.1 Shown above are schematics of: (a) an electron-repelling (i.e. ion) sheath; and (b) electron-attracting sheath near the anode. For the electron-repelling sheath a pre-sheath layer exists, providing a smooth transition from the quasi-neutral plasma to the non-neutral sheath region near the anode.

The purpose of a sheath is to set up a potential to contain the more mobile charged species in the plasma, allowing the flow of charged carriers to the wall to be balanced. The pre-sheath is a transition layer between the quasi-neutral plasma and the sheath, providing a smooth transition and matching the boundary conditions between the two regions. Inside the sheath $n_e \neq n_i \neq n_o$; inside the anode pre-sheath $n_e = n_i \neq n_o$; and in the bulk plasma $n_e = n_i = n_o$. Depending on the sign of the sheath potential n_e can be greater than or less than n_i inside the sheath. For a negative anode potential fall the pre-sheath serves to provide the ions with a directed velocity at the sheath edge, known as the Bohm velocity, u_B given by [Bohm, 1949; Allen *et al.*, 1957]:

$$u_B = \sqrt{\frac{kT_{es}}{M_i}} \tag{3.1}$$

where k is Boltzmann's constant, T_{es} is the electron temperature at the pre-sheath/plasma edge and M_i is the ion reduced mass for the hydrazine propellant given by $M_i = \frac{m_{H^+} m_{N^+}}{m_{H^+} + m_{N^+}}$.

Equation (3.1) is the ion velocity required at the sheath/pre-sheath interface for an electron repelling sheath, with a collisionless pre-sheath. The Bohm velocity is different for a collisional pre-sheath, Sec. 3.4.

The Bohm velocity is required to satisfy Poisson's equation and ion continuity for a negative sheath potential. To provide the ions with the requisite kinetic energy the pre-sheath has a small but finite electric field, so that the pre-sheath potential drop is [Lieberman *et al.*, 1994]:

$$\phi_{pre} = -\frac{kT_{es}}{2e} \tag{3.2}$$

In the ion sheath of Fig. 3.1a the electrons are repelled with only the most energetic electrons reaching the anode. The thickness of the sheath/pre-sheath combination can be several Debye lengths, i.e. λ_s~5-10λ_D where λ_s is the sheath thickness, Sec. 3.2.2.

The potential drop across the sheath depends on the degree of collisionality, $\alpha=\lambda_s/\lambda_{rs}$. The analysis for collisionless sheaths is relatively straightforward and is presented in Sec. 3.3. Before a sheath analysis is made a classification of the probe sheath collisionality must first be addressed.

3.1.2 Electron-Attracting vs Electron-Repelling Sheaths

One of the major contributions to anode heating is the electron power deposition in the anode sheath, as shown in Eq. (3.3) for a collisionless electron-repelling thin sheath [Merinov, *et al.*, 1976; Diamant, 1995]:

$$q_e = j_a\left[2kT_{es}/e + W\right] \tag{3.3}$$

It should be noted that in the work of Merinov, *et al.*, [1976] , the *total* anode heating for an electron repelling sheath also includes a term due to ion heating, given as $q_i = j_{th,i}[\phi_s + \varepsilon_i - W + 2k\Delta T_i/e]$, where ε_i is the ionization energy of the gas, $j_{th,i}$ is the ion random thermal current density and ΔT_i is the difference between the gas temperature and the ion temperature. However, since $T_i \ll T_e$ and $j_{th,i} \ll j_{th,e}$, the contribution of the ions to the total anode heating is negligible when compared with the electron contribution.

For a collisionless electron-attracting thin sheath, the anode heating is [Oberth, 1970]:

$$q_e = j_a\left[5kT_{es}/2e + \phi_s + W\right] \tag{3.4}$$

where ablation, thermionic emission, Joule heating of the anode, convection and radiation from the plasma are neglected. In Eqs. (3.3) and (3.4), $j_a > 0$ is the current density leaving the anode, ϕ_s is the anode sheath potential, where $\phi_s > 0$ for an electron-attracting sheath and $\phi_s < 0$ for an electron-repelling sheath, T_{es} is the electron temperature at the sheath/pre-sheath edge, and $W = 3.7$ eV is an average value for the work function of the 2% thoriated tungsten anode, [Goodfellow, *et al.*, 1995]. For an electron-attracting sheath $j \cong j_{th,e}$ [Vainberg, *et* *al.*, 1978] and for an electron-repelling sheath $j \cong j_{th,e} \exp[-|e\phi_s|/kT_{es}]$ [Merinov, *et al.*, 1976] , where the electron thermal current density is $j_{th,e} = en_{es}(kT_{es}/2\pi m_e)^{1/2}$.

There has been some confusion in the literature over the coefficient of the electron thermal energy term in Eqs. (3.3) and (3.4), [Merinov, *et al.*, 1976; Oberth, 1970]. For an electron-repelling sheath Eq. (3.3) is derived [Diamant, 1995] by integrating the electron kinetic energy flux over a Maxwellian distribution, with a lower limit of integration on the electron perpendicular velocity of $(2e\phi_s/m_e)^{1/2}$. Also, the perpendicular electron velocity entering the sheath is shifted by $(2e\phi_s/m_e)^{1/2}$; this is included in the Maxwellian distribution function, which, when integrated over three dimensions leads to Eq. (3.3). The term $j_a\phi_s$ cancels out in the integration, leaving only $j_a 2kT_{es}/e$ in the evaluation.

For an electron-attracting sheath the electron kinetic energy flux is integrated over an anisotropic Maxwellian distribution, in which the electron perpendicular velocity is shifted by its drift velocity, j/en_{es}, [Oberth, 1970]. The 5/2 factor results because all electrons in the Maxwellian distribution, not just those with velocities greater than $(2e\phi_s/m_e)^{1/2}$ enter the sheath and strike the anode.

Theoretical work focusing on the interaction of the sheath with the plasma bulk flow has shed some light on the physics of arc attachment [Meeks, *et al.*, 1993; Dinulescu, *et al.*, 1980; Cappelli, 1992], but there have been no supporting experimental data on sheath characteristics for arcjets.

The probe V-I characteristic and resulting plasma properties yield three independent approaches for calculating the total anode sheath potential ϕ_s, [Tiliakos, *et al.*, 1996]:

(1) The anode sheath potential is determined from the plasma potential at the "knee" of the characteristic from $\phi_s = -\phi_p$.

(2) The anode sheath potential is determined from j_a and $j_{th,e}$. For electron-repelling sheaths, which occur at low values of j_a and high $j_{th,e}$, the anode current balance can be written [Merinov *et al.*, 1976]:

$$j = j_{th,e}\exp\left[-\left|e\phi_S\right|/kT_{es}\right] - j_{emit} - j_{th,i} \qquad (3.5)$$

where $j_{th,e}$ and $j_{th,i}$ are the electron and ion random thermal current densities and j_{emit} is the current density of electrons thermionically emitted from the anode. For $T_i \approx T_a \leq 1400$ °K, the ion and emitted-electron contributions can be neglected, giving for the potential drop of an electron-repelling sheath [Tiliakos *et al.*, 1996]:

$$\phi_S = \left(\frac{kT_{es}}{e}\right)\ln\left[\frac{j_a}{j_{th,e}}\right] < 0 \qquad (3.6)$$

Deriving n_{es}, T_{es}, j_a and $j_{th,e}$ from the probe characteristic, ϕ_s can be calculated from Eq. (3.6).

(3) The anode sheath potential is determined from the floating potential, [Chen, 1965]. The current density to a probe at a potential V_p is:

$$j_p = j_{th}\exp\left[e\left(V_p - \phi_{pl}\right)/kT_{es}\right] - j_{th,i} \qquad (3.7)$$

where $j_{th,i}$ is given by the Bohm current, [Chen, 1965; Allen *et al.*, 1957]. For $j_p = 0$ at $V_p = \phi_f$, with $\phi_s = -\phi_{pl}$, Eq. (3.7) gives:

$$\phi_S = -\phi_f + \frac{kT_{es}}{e}\left\{\ln(0.61) + \ln\left[\sqrt{\frac{2\pi m_e}{M_i}}\right]\right\} \qquad (3.8)$$

The first term in brackets comes from the Bohm criterion for the pre-sheath voltage of $\phi_{pre} = -kT_{es}/2e$ (Sec. 3.1.1), if the ion current density is the Bohm current density: $j_B = en_{es}\exp\left[\frac{-e}{kT_{es}}\left(\frac{kT_{es}}{2e}\right)\right]u_B = en_{es}(0.61)u_B$, where u_B is the Bohm velocity, Eq. (3.1).

3.2 Probe-Sheath Classification

A sheath always develops between a plasma and an electrode. When the electrode or probe is biased through a range of positive and negative potentials it attracts charged particles and a plot of probe current I_p versus probe biasing voltage V_p, a probe characteristic, is obtained. The magnitude of the probe current depends: (1) on the sheath size and events in the sheath, e.g. collisions and ionization reactions; and (2) the probe surface condition, e.g. contamination, thermionic emission of probe material, sputtering, etc. Interpretation of the probe characteristic depends on the sheath collisionality, $\alpha \equiv \lambda_S/\lambda_{rS}$, i.e. number of collisions in the sheath. If there are no collisions in the sheath, then obtaining n_{es} and T_{es} from the characteristic is relatively straightforward and the Laframboise method can be used [Laframboise, 1966], providing a convenient analytical approach to the data analysis, Section 3.3.2.

If sheath collisionality is significant, i.e. $\alpha >> 1$, then interpreting the probe characteristic is more complex, and an analytical approach may not be readily available. Assessing sheath collisionality is done by calculating and comparing various length scales, such as Debye length λ_D, probe radius r_p and various charged particle mean free paths, λ_{rs}. Also, the sheath thickness must be calculated and compared with λ_{rs} and r_p. Since analysis of the probe characteristic is dependent on sheath collisionality, a review of the conditions for probe sheath classification and the magnitude of various length scales is presented in the following sections.

3.2.1 Length Scales

The collision regime of a probe sheath depends on the following length scales: the sheath thickness λ_s, Debye length λ_D, probe radius r_p and the charged particle mean free path λ_{rs}, given by:

$$\lambda_{rs} = \frac{1}{n_r Q_{rs}} \tag{3.9}$$

where n_r is the number density of species r and Q_{rs} is the elastic momentum transfer cross section between colliding partners r and s.

The length scale regimes of probe operation are presented in Table 3.1, [Chung *et al.*, 1974]. The Knudsen number is defined as the ratio of a relevant mean free path and the probe radius, $Kn \equiv \lambda_{rs}/r_p$. The condition Kn >> 1 does not necessarily represent the collisionless condition; the sheath may or may not be collisional depending on the relative magnitudes of λ_{rs} and λ_D. Likewise, the condition Kn<<1 represents the case where the probes are always collisional with respect to the continuum gas flow, and the sheath may or may not be collisional, depending on the relative magnitudes of λ_{rs} and λ_D, [Chung *et al.*, 1975]. There are also several transitional domains, e.g. Kn~O(1), $\lambda_D \sim \lambda_{rs}$ and $r_p \sim \lambda_D$. The double transitional case means that $r_p \sim \lambda$ and Kn ~ 1, and the transitional sheath refers to $\lambda_D \sim \lambda$.

Table 3.1 Probe-sheath classification regimes for a classical Langmuir probe and an electrostatic probe.

Knudsen Number	$\lambda_{rs}, r_p, \lambda_D$	**Classification**
>> 1 (Classical Langmuir Probe)	$\lambda_{rs} >> r_p >> \lambda_D$	collisionless thin sheath
	$\lambda_{rs} >> \lambda_D >> r_p$	orbital limit-thick sheath
	$\lambda_D >> \lambda_{rs} >> r_p$	collisional thick sheath
<< 1 (Electrostatic Probe)	$r_p >> \lambda_D >> \lambda_{rs}$	collisional thin sheath
	$\lambda_D >> r_p >> \lambda_{rs}$	collisional thick sheath
	$r_p >> \lambda_{rs} >> \lambda_D$	collisionless thin sheath
~O(1)	$\lambda_D \sim \lambda_{rs}$	transitional sheath
	$r_p \sim \lambda_D \sim O(1)$	transitional sheath

The criteria listed in Table 3.1 for probe sheath classification are assessed for all fourteen probes. The MKB arcjet model [Megli, *et al.*, 1996] was used to obtain values for $n_{H^+}, n_H, n_{H_2}, n_{N^+}, n_N, n_{N_2}$ along the anode wall at r = 0 mm, for simulated hydrazine propellant, for the nominal conditions of $\dot{m}$ = 50 mg/sec and I_{arc} = 10 A. These values were then used to calculate the mean free path and Debye length at each probe location, for 31 separate reactions. Table 3.2 shows comparisons of the Debye length and the relevant mean free path for electron and ion particle collection for each probe, based on experimental values of n_{es} and T_{es}. The relevant mean free paths are selected based on the largest collision frequency between collected particles and molecules in the sheath, providing the smallest λ_{rs}, i.e. a conservative comparison between λ_{rs}, r_p and λ_D. The collision frequencies for the 31 separate reactions were calculated with the cross-sectional data used in the MKB model, [Megli, 1995; Spencer *et al.*, 1976].

Table 3.2 Comparisons of the relevant mean free path lengths and probe radii are presented for probe-sheath classification, based on the MKB model [Megli, 1995] and experimental results for nominal arcjet conditions n_{es}, T_{es} for $\dot{m}$ = 50 mg/sec and I_{arc} = 9.8 A, using flush probes. Note that the electron-H_2 mean free path for probe 2 was based on T_{es} calculated from the potential data, Sec. 4.2.5.

Probe #	r_p [μm]	$\lambda_{H^+\text{-}H_2}$ [μm]	$\lambda_{e\text{-}H_2}$ [μm]	λ_D [μm]
1	82	1.4	12	3.9
1′	85	1.4	15	5.3
2	211	3.8	28	5.9
3	210	9.1	169	8.7
4	210	14	114	4.3
4′	213	14	114	6.5
5	211	22	191	7.8
6	210	27	222	6.8

Table 3.2. (Continued)

Probe #	r_p [μm]	$\lambda_{H^+-H_2}$ [μm]	λ_{e-H_2} [μm]	λ_D [μm]
7	211	42	340	6.0
7′	214	42	344	7.2
8	212	52	435	6.9
9	212	66	526	9.5
10	213	83	656	7.8
10'	213	83	656	9.0

Table 3.3 Knudsen number and r_p/λ_D calculations for ion and electron collection, based on the MKB model [Megli, 1995] and flush probe results for $\dot{m}$ = 50 mg/sec and I_{arc} = 9.8 A.

Probe #	Kn# (e- collec.)	Kn# (ion collec.)	r_p/λ_D
1	.14	.02	21
1′	.17	.02	16
2	.13	.02	21
3	.80	.04	24
4	.53	.07	48
4′	.53	.07	33
5	.91	.10	27
6	1.1	.13	31
7	1.6	.20	35
7′	1.6	.20	30
8	2.1	.25	30
9	2.5	.31	22
10	3.1	.39	27
10′	3.1	.39	24

It was determined from the mean free path calculations that electron-H_2 collisions are dominant when the probe is collecting electrons and H+-H_2 collisions are dominant for ion collection. Figure 3.2 shows a graphical comparison between r_p, $\lambda_{e\text{-}H_2}$, $\lambda_{H^+\text{-}H_2}$ and λ_D at each probe location. For probes 1-6, the Knudsen number for electrons Kn_e, is less than 1, i.e. continuum electrostatic probe, while $Kn_e > 1$ for probes 6-10′, i.e. classical Langmuir probe. For ion collection, the Knudsen number for ions Kn_i, is less than 1 at all probe locations, i.e. a continuum electrostatic probe.

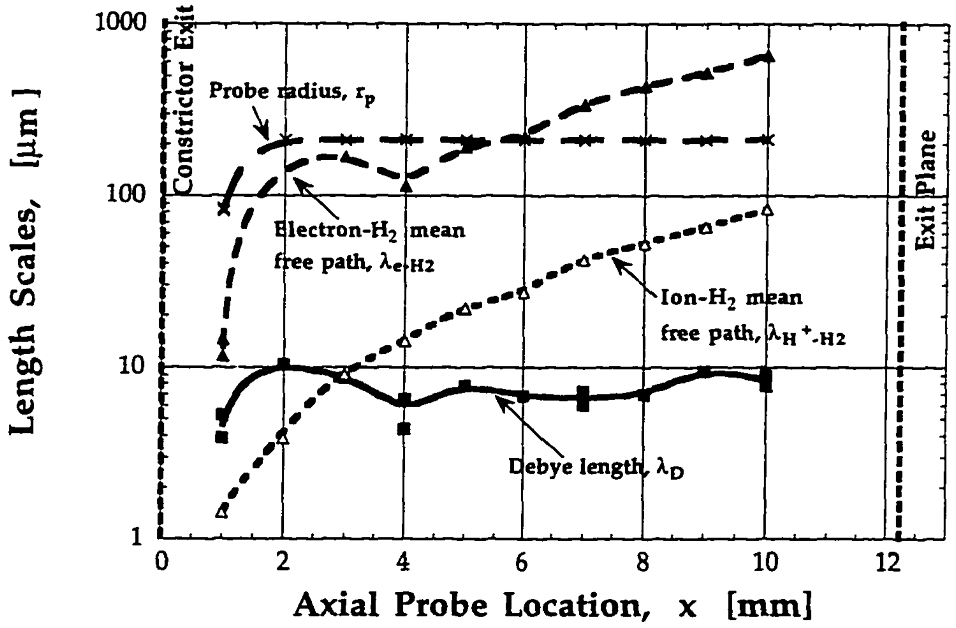

Fig. 3.2 Graphical comparison between various relevant length scales required for probe-sheath classification. Calculations are based on the MKB model [Megli, 1995] and experimental results for n_{es}, T_{es} for $\dot{m}$ = 50 mg/sec and I_{arc} = 9.8 A, using flush probes.

Using the results from Tables 3.1 and 3.2 and Fig. 3.2 the probe sheath collisionality, i.e. thin or thick, collisionless or collisional probe sheath can now be assessed. The results are summarized in Fig. 3.3.

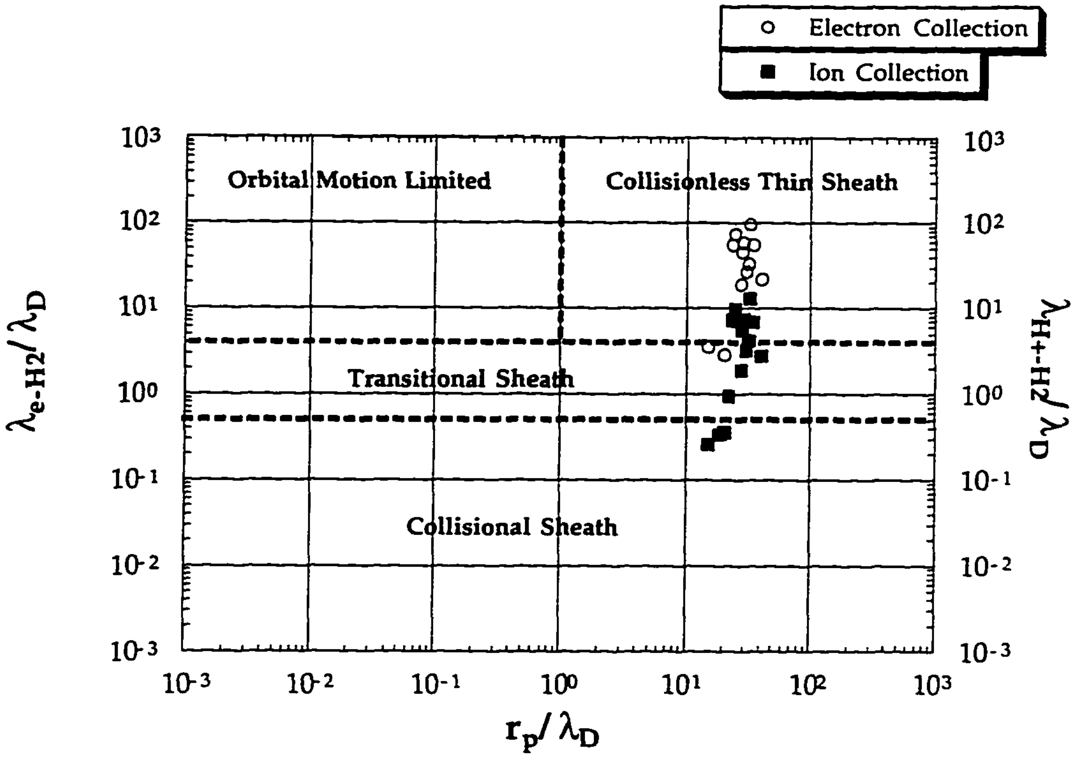

Fig. 3.3 Graphical representation of the various probe-sheath classification regimes. Calculations are based on the MKB model [Megli, 1995] and experimental results for n_{es}, T_{es} for $\dot{m}$ = 50 mg/sec and I_{arc} = 9.8 A, using flush probes.

Based on the calculations of r_p, mean free paths for electron-H_2 molecule and hydrogen ion-H_2 molecule interactions, and λ_D (Fig. 3.3) for ion collection: probes 1, 1' and 2 have a thin, highly collisional sheath; probes 3-6 have a transitional thin sheath; and the remaining probes have thin collisionless sheaths. For electron collection probes 1-3 have a transitional thin sheath and probes 4-10' have a thin collisionless sheath. A transitional sheath is borderline between the collisionless and collisional cases.

To further classify the sheath collisionality, an assessment of the sheath size is now required, followed by methods for interpreting the characteristic for each of the probe conditions.

3.2.2 Sheath Size

A comparison of the sheath size, λ_s with r_p, λ_{e-H_2} and $\lambda_{H^+-H_2}$ is required to assess probe-sheath collisionality, which directly affects how the probe V-I characteristic is interpreted.

Knowledge of the relative size of λ_s, in relation to r_p, is also important for determining sheath-edge effects and calculating the sheath area, A_s. The sheath area is required, in addition to the physical probe area A_p to derive the current density at zero volts j_a, given by:

$$j_a = \frac{I_a}{A_{eff}} \tag{3.10}$$

where I_a is the probe current when $V_p = 0.0 \pm 0.1$ V, and A_{eff} is the effective probe collection area:

$$A_{eff} = A_s + A_p = \overline{R}A_p \tag{3.11}$$

where $\overline{R} \equiv A_{eff}/A_p$ is defined by the following empirical formula, for a flush probe and for $\lambda_s/r_p < 1$, [Tseng, *et al.*, 1970; Tseng, 1969]:

$$\overline{R} \equiv \frac{A_{eff}}{A_p} \cong 1 + \left(\frac{\lambda_s}{r_p}\right)^2 + \frac{1}{3}\left(\frac{\lambda_s}{r_p}\right)\left[1 - 0.92\left(\frac{\lambda_s}{r_p}\right)\right] \tag{3.12}$$

Substituting Eq. (3.12) into Eq. (3.11), the sheath area becomes: $A_s = A_p\left(\overline{R} - 1\right)$. For a cylindrical probe, [Ruzic, 1994]:

$$\overline{R} \equiv \frac{A_{eff}}{A_p} = 1 + \left(\frac{\lambda_s}{r_p}\right) \tag{3.13}$$

The sheath size may also increase with probe potential, depending on the probe geometry. If a probe is biased highly negative or positive with respect to the plasma potential, the sheath may increase in thickness to the point where it becomes as large as the viscous boundary layer, i.e., thick sheath. When this happens, the probe electric field is perturbing the plasma and the sheath will intercept free streaming charged particles, so that convection effects must be accounted for when calculating I_p or I_i [Clements, *et al.*, 1971; Smy, 1976], discussed further in Sec. 3.2.3. If the sheath thickness increases with probe potential the probe would collect more current, depending on the probe geometry so that electron saturation is never reached. Thus, the probe characteristic can tell us qualitatively, whether the sheath is thin or thick. This is shown in Fig. 3.4, where, for an ideal planar probe, the sheath collection area remains constant as the probe bias increases, so that the electron saturation region plateaus.

For a planar probe, the sheath thickness may increase, but the same flux is collected since the cross-sectional collection area remains unchanged, [Ruzic, 1994; Kushner, 1997]. Thus, true electron saturation is only obtained with an infinitely large planar probe, or if $r_p >> \lambda_s$. For cylindrical or spherical probes the volume intercepted by the sheath continues to grow and therefore the collected electron-saturation current increases, [Ruzic, 1994].

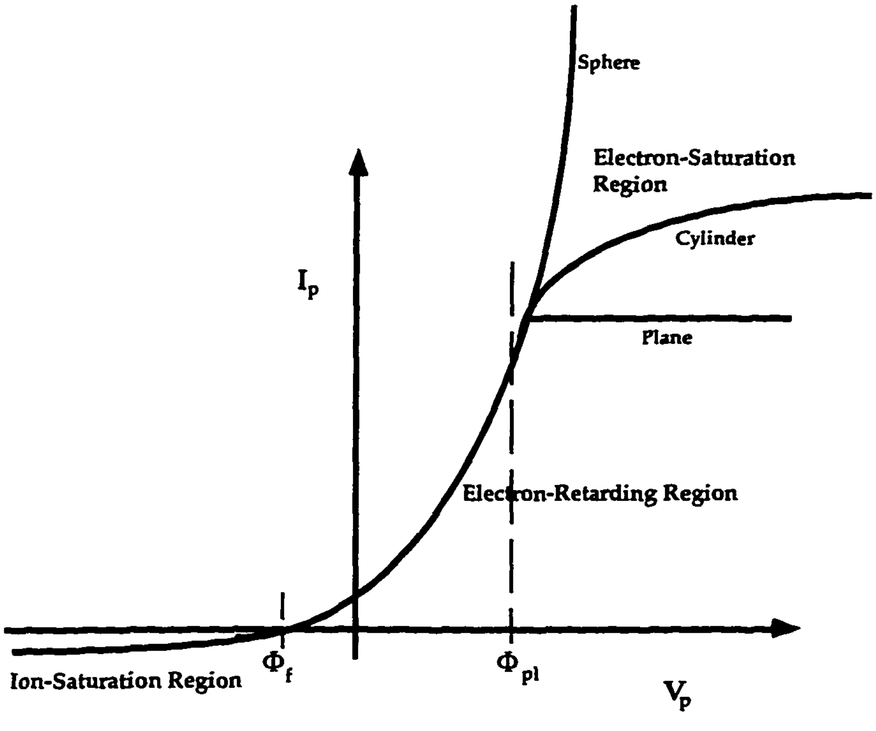

Fig. 3.4 Shown above are the ideal V-I characteristics for probes of planar, cylindrical and spherical geometry [Ref: Herskowitz, 1989] .

Figure 3.5 shows an experimentally determined probe V-I characteristic. Comparison of Figs. 3.4-3.5 shows that the flush probe does not saturate for $V_p > \phi_{pl}$ because of a slight increase in the sheath thickness with probe voltage and the probe sheath-edge effects, during electron collection. The accumulation of data points for the cylindrical probe between -11 V $\leq V_p \leq$ -7 V is a consequence of the (non-zero) negative offset of the function generator output signal just before the sinusoidal pulse occurs. This non-zero offset leads to a finite voltage drop across R_s and a measurable current, as displayed in Fig. 3.5.

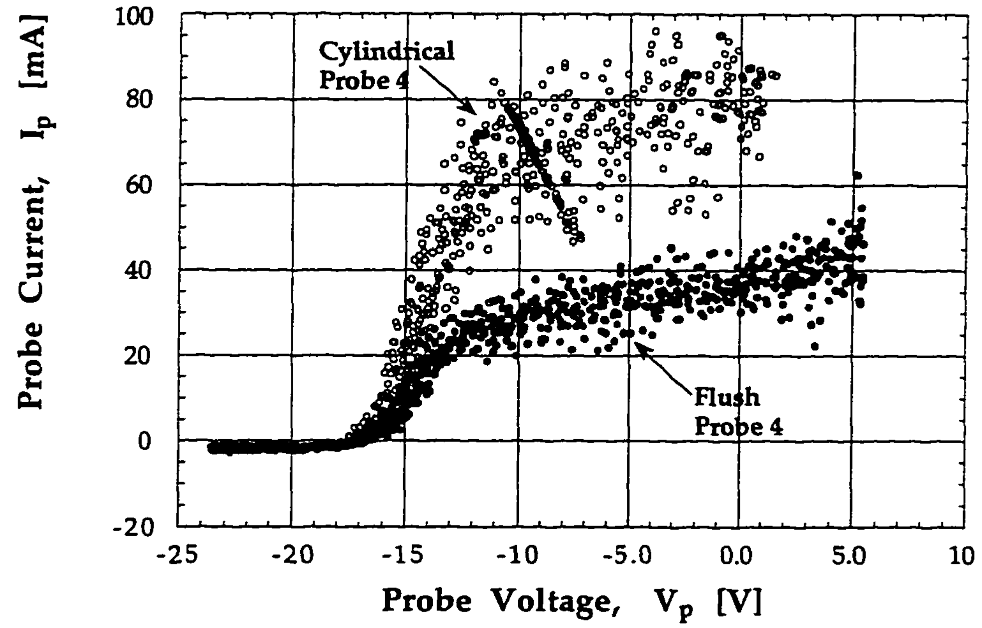

Fig. 3.5 Shown above are the experimental characteristics at x = 4 mm, for a planar flush-mounted probe and a cylindrical probe. The experimental conditions are for $\dot{m}$ = 50 mg/sec and I_{arc} = 9.9 A.

For all probes the plasma potential is negative, so that the current at V_p = 0.0 V is in the electron saturation region, Fig. 3.6. The electron saturation region increases slightly with probe biasing potential, as compared with an ideal planar probe, Fig. 3.4. This suggests that the sheath thickness for electron collection $\lambda_{s,e}$ is dependent on the probe potential. This dependence of $\lambda_{s,e}$ on V_p is also a function of sheath collisionality, and is derived below.

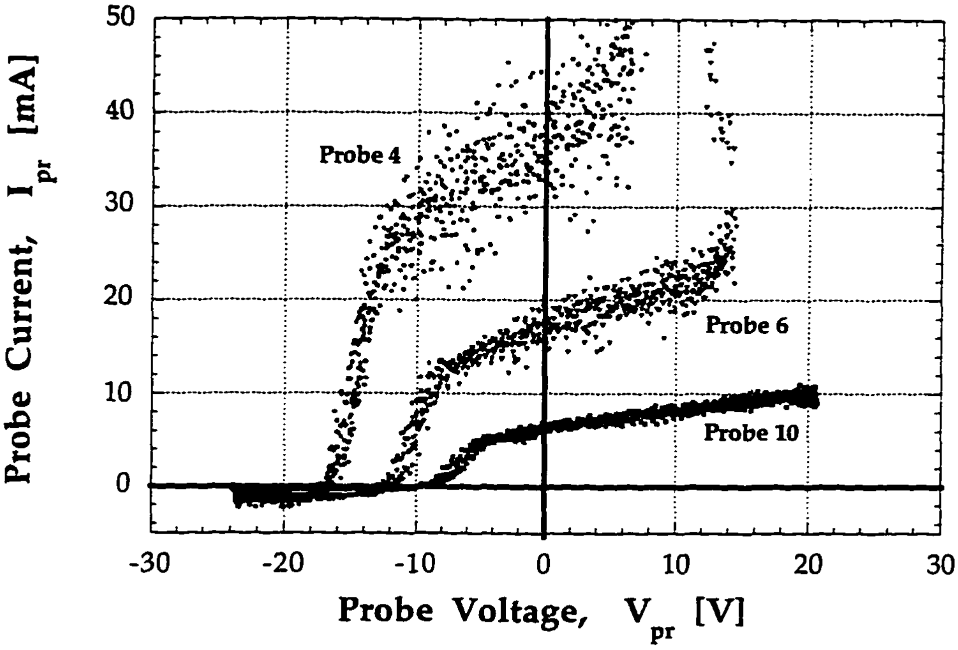

Fig. 3.6 Typical experimental V-I characteristics for flush probes 4, 6, and 10, showing that $\phi_{pi} < 0$ throughout the anode boundary layer, with the current at zero volts I_a, located in the electron saturation region. The experimental conditions are for $\dot{m} = 50$ mg/sec and $I_{arc} = 9.8$ A.

For a thin collisionless electron sheath, an expression is derived for $\lambda_{s,e}$, starting with Poisson's equation:

$$\nabla^2\phi(r) = -\frac{e}{\varepsilon_o}[n_i(r) - n_e(r)] \tag{3.14}$$

where r is the radial distance perpendicular to the probe surface. The following assumptions are made: (1) the electrons are in thermal equilibrium with each other; (2) the electron drift is neglected; (3) inertial, magnetic and collisional forces are neglected; and (4) $n_i(r) \sim 0$, i.e. the sheath is predominantly electron attracting. With these assumptions, the electron species momentum equation then reduces to the Boltzmann relation for electrons:

$$n_e(r) = n_{es}\exp\left[\frac{e\phi(r)}{kT_{es}}\right] \tag{3.15}$$

where $\phi(r)$ is the potential distribution in the sheath. Substituting Eq. (3.15) into Eq. (3.14), and applying assumption (4), Poisson's equation becomes:

$$\frac{d^2\phi(r)}{dr^2} = \frac{e}{\varepsilon_o} n_{es}\exp\left[\frac{e\phi(r)}{kT_{es}}\right] \tag{3.16}$$

Multiplying Eq. (3.16) by $d\phi(r)/dr$ and integrating from $\phi = V_p = 0$ to $\phi = \phi_{pl}$, the electron *collisionless* sheath thickness at zero volts is:

$$\lambda_{s,e} = |\phi_{pl}|\left[\frac{2en_{es}T_{es}(eV)}{\varepsilon_o}\left\{1 - \exp\left[\phi_{pl}/T_{es}(eV)\right]\right\}\right]^{-1/2} \tag{3.17}$$

where n_{es} and T_{es} are the electron number density and electron temperature at the plasma/pre-sheath edge, respectively. Once the electron sheath thickness at zero volts is known, the effective probe collection area is calculated from Eqs. (3.11) and (3.12), and the current density is derived from Eq. (3.10). Equations (3.11) and (3.12) are used to assess the sheath size effects on the effective probe collection area, with n_{es} and T_{es} obtained from experimental data.

Typical results for $\lambda_{s,e}/r_p$ and $\overline{R}$ are shown in Fig. 3.7. The effective probe area at zero volts is fairly constant throughout the anode boundary layer. For all fourteen probes the sheath contributes at most ~ 10% increase in A_{eff} and $\lambda_{s,e}/r_p$ is at most 0.20. The ratio $\lambda_{s,e}/r_p$ is a measure of sheath edge effects, i.e. the sheath-fringing electric field effect on current collection; since $\lambda_{s,e}/r_p << 1$ sheath-edge effects are considered negligible.

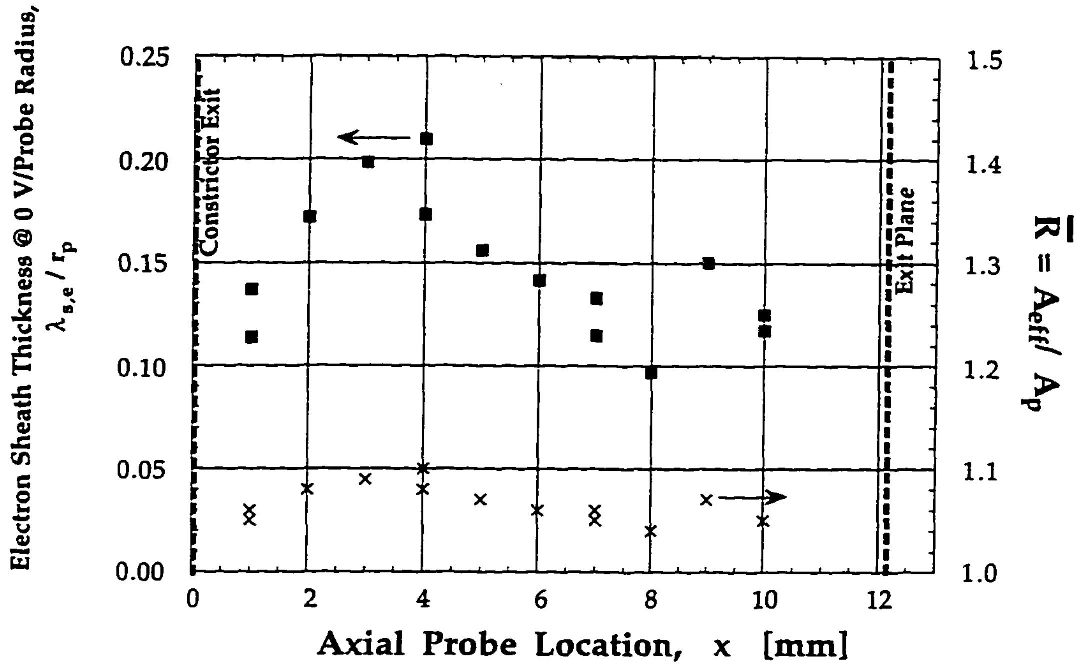

Fig. 3.7 The normalized electron sheath thickness at zero volts $\lambda_{s,e}/r_p$ is shown at all probe locations. Also shown is the ratio of effective probe collection area to the geometric probe area, $\bar{R}$, These results are based on the experimental conditions of $\dot{m} = 50$ mg/sec and $I_{arc} = 9.8$ A, for the flush probe configuration and numerical results from the MKB model.

If the probe dimensions are too small with respect to the sheath thickness, i.e. $\lambda_{s,e}/r_p \gg 1$, then the probe fringing electric field causes large perturbations to the potential distribution around the probe, increasing the effective probe collection area, Fig. 3.8. If this is not considered during the data reduction the j_a data may be overestimated by only including the geometric probe area, and not accounting for the large sheath area.

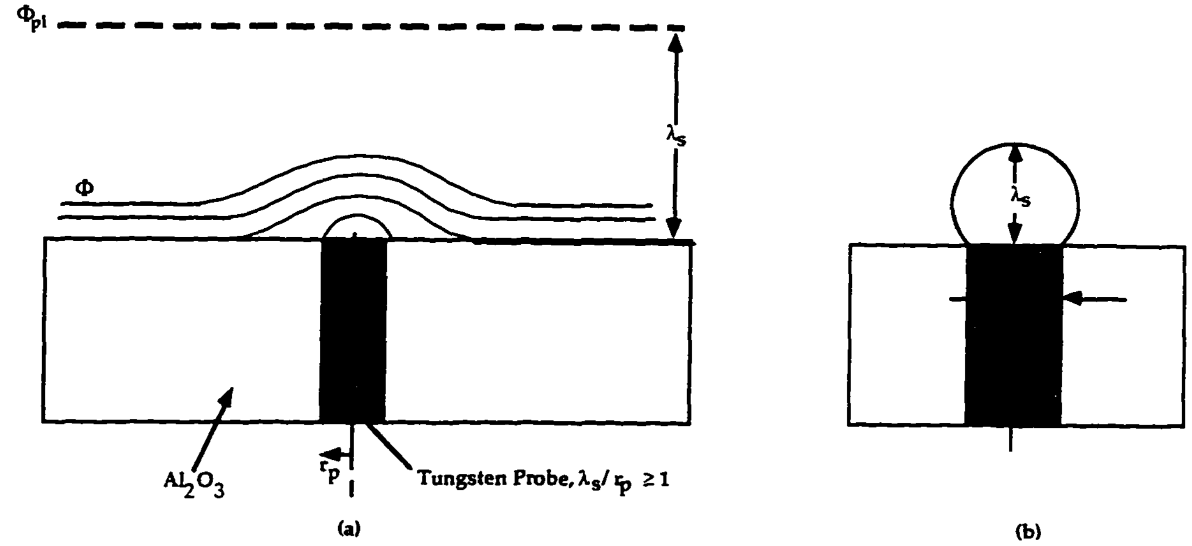

Fig. 3.8 The above schematics show: (a) the field-fringing effects of a small probe surrounded by a relatively thick sheath and its effects on the potential distribution close to the probe surface; and (b) the planar probe area is modeled as a spherical cap above the flat surface, which is a function of λ_s/r_p, Eq. (3.12) in the text, [Tseng *et al.*, 1970; Tseng, 1969] .

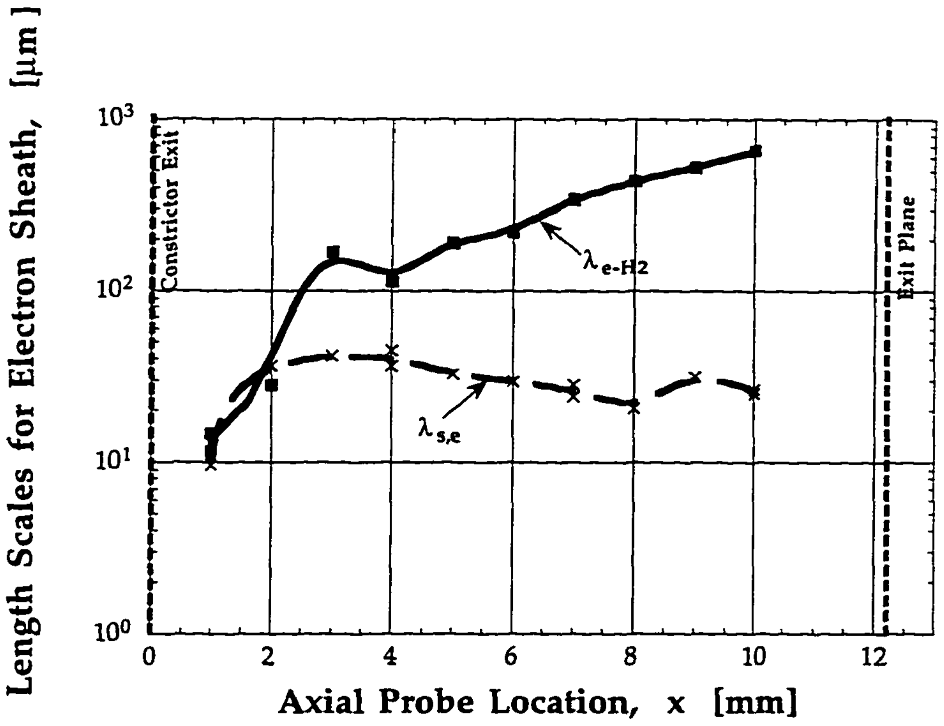

Fig. 3.9 A comparison between the sheath thickness for electron collection and the electron-H_2 mean free path is made to assess the sheath collisionality. Calculations are based on experimental flush probe data values for n_{es}, T_{es} for $\dot{m}$ = 50 mg/sec and I_{arc} = 9.8 A and numerical results from the MKB model.

Equations (3.12) and (3.17) are used to assess the sheath size effects on the effective probe collection area, with n_{es} and T_{es} (eV) based on experimental data. As shown in Fig. 3.9, at probe locations $x \leq 2$ mm, $\lambda_{s,e} > \lambda_{e\text{-}H_2}$ so that the sheath is marginally collisional for electron collection. For this situation if T_{es} is derived assuming a collisionless sheath, then this value for electron temperature represents an upper bound to the actual electron temperature.

For a collisional electron sheath, the sheath thickness as a function of probe potential is derived with the following assumptions: (1) no inelastic collisions in the sheath; (2) $n_i(r) \sim 0$, i.e. electron sheath only; (3) 1-D sheath; (4) no magnetic fields; and (5) the sheath is thin enough with respect to r_p so that $T_e(r)$ and $j_e(r)$ are approximately constant but $T_e \neq T_{i,gas}$. The electron continuity equation becomes:

$$\frac{d}{dr}[n_e(r)u_e(r)] = 0 \tag{3.18}$$

The electron species momentum equation gives:

$$m_e n_e(r)u_e(r)\frac{du_e(r)}{dr} = en_e(r)E_r(r) - \frac{dp_e(r)}{dr} - m_e n_e(r)\nu_{m,e}u_e(r) \tag{3.19}$$

where $p_e(r)$ is the electron pressure in the radial direction, $E_r(r)$ is the radial electric field and $\nu_{m,e}$ is the elastic momentum collision frequency between electrons and H_2 molecules. An order of magnitude analysis of each term in Eq. (3.19) shows that the inertial and electron pressure gradient terms may be neglected, especially for probes 1-3. This reduces the electron momentum equation to an equation for $u_e(r)$:

$$u_e(r) = \frac{-e}{m_e\nu_{e-H_2}}\frac{d\phi(r)}{dr} = -\mu_e\frac{d\phi(r)}{dr} \tag{3.20}$$

where μ_e is the electron mobility defined as $\mu_e \equiv \dfrac{e}{m_e\nu_{e-H_2}}$, and e is the electronic charge 1.6×10^{-19} Coul.

From the electron continuity equation, Eq. (3.18), n_{es} is represented in terms of the electron flux at the probe surface, i.e. the electron current density j_p, assuming that $u_e >> u$, where u_e is the electron velocity and u is the bulk plasma velocity. The electron continuity equation then reduces to:

$$n_e(r_s) = n_{es} = \frac{j_p}{eu_e(r_s)} \tag{3.21}$$

Substituting Eq. (3.20) into Eq. (3.21):

$$n_{es} = \frac{j_p}{eu_e(r_s)} = j_p\left[-\frac{\mu_e}{e}\frac{d\phi(r)}{dr}\right] \tag{3.22}$$

Assuming $n_i(r) \sim 0$ for an electron sheath, Eq. (3.22) is combined with Poisson's equation, Eq. (3.14), to give:

$$\left(-\mu_e\frac{d\phi(r)}{dr}\right)\frac{d^2\phi(r)}{dr^2} = \frac{j_p}{\varepsilon_o} \tag{3.23}$$

Making the substitution $a=d\phi(r)/dr$ and $da/dr = d^2\phi(r)/dr^2$ Eq. (3.23) is integrated from the sheath edge, r_s where $E_r(r_s)=d\phi(r_s)/dr = a(r_s)\sim 0$, to the probe surface where $a(r_p)=d\phi(r_p)/dr = -E_r(r_p) = -(\phi_s-V_p)/\lambda_{s,e}$. Also, using the assumption that j_p = constant provides the approximate thickness for a *collisional* electron sheath:

$$\lambda_{s,e} = \left[\frac{0.5\varepsilon_o\mu_e\left(\phi_s - V_p\right)^2}{j_p}\right]^{1/3} \tag{3.24}$$

where $\phi_s = -\phi_{pl}$. Equation (3.24) is applicable for $V_p > \phi_{pl}$ and can also be rearranged to obtain a V-I relation:

$$j_p = \frac{I_p}{A_p} = \left[\frac{\varepsilon_o\mu_e\left(\phi_s - V_p\right)^2\overline{R}\left(\lambda_{s,e}, r_p\right)}{2\lambda_{s,e}^3}\right] \tag{3.25}$$

Equation (3.24) was used to obtain the collisional electron sheath thickness for probes 1-3, while Eq. (3.17) was used to calculate the collisionless electron sheath thickness for probes 4 -10′, with the results shown in Fig. 3.9. As discussed later in the data analysis, Sec. 3.3, it is assumed that the electron sheath is collisionless at all probe locations.

The ion sheath thickness as a function of probe bias is also important for assessing sheath collisionality. The ion current is required to calculate the electron current, I_e, since $I_e = I_p - I_i$.

For a collisionless ion sheath, the ion sheath thickness, $\lambda_{s,i}$ is derived analogous to $\lambda_{s,e}$ starting with Poisson's equation and assuming that $n_e(r) \sim 0$. The ion current density is given by the Bohm current, $j_B = en_{es}\,(kT_{es}/M_i)^{1/2}$ so that the collisionless ion sheath thickness is [Ruzic, 1994]:

$$\lambda_{s,i} = (1.02\lambda_D)\left[\sqrt{\frac{-e\left(V_p - \phi_{pl}\right)}{kT_{es}}} - \frac{1}{\sqrt{2}}\right]\left[\sqrt{\frac{-e\left(V_p - \phi_{pl}\right)}{kT_{es}}} + \sqrt{2}\right] \qquad (3.26)$$

For a collisional ion sheath, the thickness is approximated from [Lieberman, 1994]:

$$\lambda_{s,i} = \left[\frac{9}{8}\frac{\varepsilon_o \mu_i V_p^2 A_p}{I_{i,sat}}\right]^{1/3} \qquad (3.27)$$

Equation (3.27) is the collisional form of the Child's Law for a planar, space-charge limited, mobility-controlled sheath and for highly negative probes, $V_p << \phi_{pl}$. For the derivation of Eq. (3.27) it was assumed that the ion elastic collision frequency and the ion mobility are independent of ion velocity. The ion sheath thickness is evaluated at $V_p = -24$ V.

An alternate method for calculating the ion collisional sheath thickness is to use the results of the Sheridan ion sheath model [Sheridan, *et al.*, 1991]. This model describes the effects of ion collisionality on the ion sheath as a function of various degrees of collisionality, α. Numerical solutions were obtained to the ion species momentum and Poisson equations, for collisional models assuming a constant mean free path or a constant ion mobility in the sheath. A graphical solution for the nondimensional ion sheath thickness, $d = \lambda_{s,i}/\lambda_D$, was derived. If the collision parameter, $\alpha \equiv \lambda_D/\lambda_{rs}$, and the nondimensional probe potential, $\chi \equiv -e\phi_p/kT_{es}$, are known, then d and therefore $\lambda_{s,i}$ are found, [Sheridan, *et al.*, 1991].

Both Eq. (3.27) and the numerical results of the [Sheridan *et al.*, 1991] model were used to calculate the ion collisional sheath thickness and compare with $\lambda_{H^+-H_2}$, as shown in Fig. 3.10.

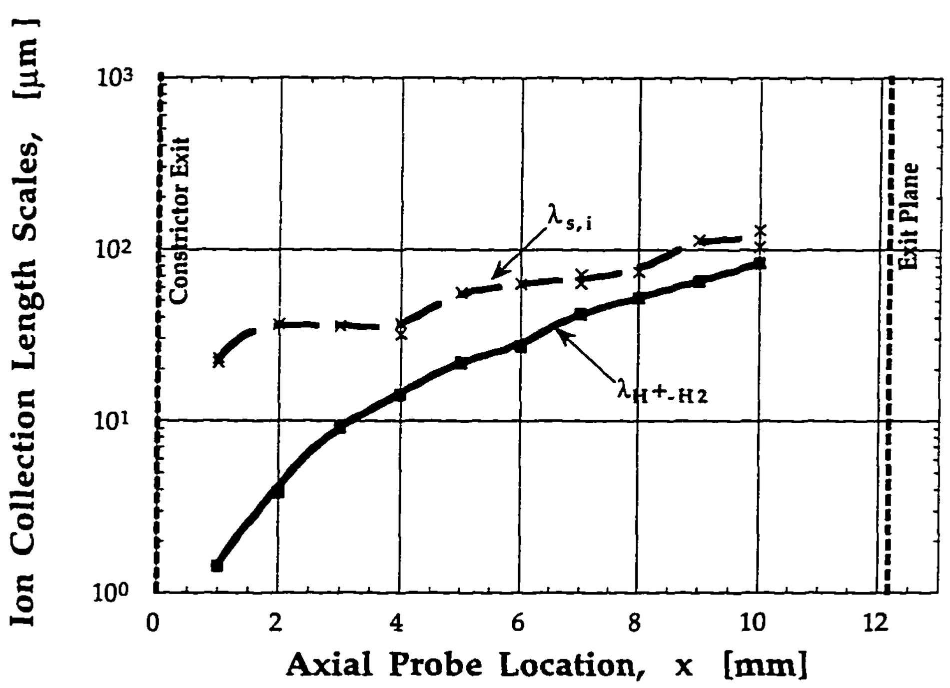

Fig. 3.10 A comparison between the sheath thickness for ion collection and the H^+-H_2 mean free path is made to assess the ion sheath collisionality. Calculations are based on flush probe results for n_{es}, T_{es} for $\dot{m} = 50$ mg/sec and $I_{arc} = 9.8$ A, and numerical results from the MKB model. The ions are collisional in the sheath at all probe locations.

The collisionless and collisional ion sheath thickness calculations show that $\lambda_{s,i} > \lambda_{H+-H2}$ at all probe locations, so that for ion collection the sheath is collisional. The degree of ion sheath collisionality, $\alpha = \lambda_{s,i}/\lambda_{H+-H2}$, varies from highly collisional at probes 1,1′ (about 15 collisions in the ion sheath) to moderately collisional at probes 10, 10′, (about 1 collision) as shown in Fig. 3.11. For electron collection the electron sheath is moderately collisional at probes 1, 1′ (~ 1 collision) and for x > 1 mm, the probe electron sheath is collisionless (<< 1 collision); therefore, the electron sheath is considered collisionless at all probe locations. For both ion and electron collection, the probe sheath collisionality is largest near the constrictor and sharply decreases as the flow expands through the nozzle.

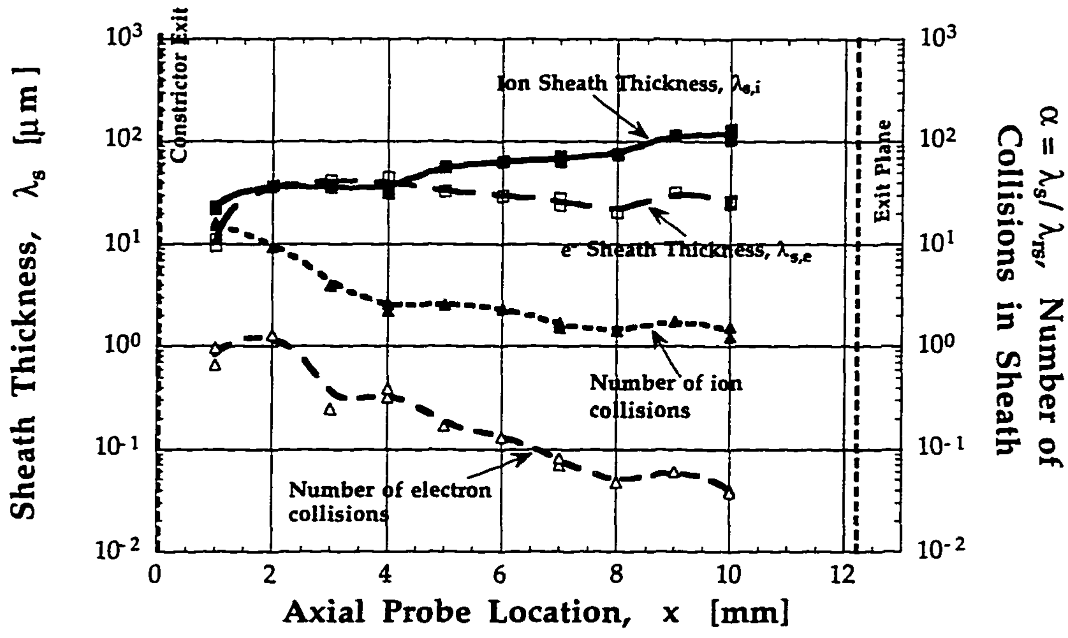

Fig. 3.11 A plot of the ion sheath thickness, collisionless electron sheath thickness and number of H_2 molecule collisions at all probe locations. Calculations are based on flush probe data for n_{es}, T_{es} for $\dot{m}$ = 50 mg/sec and I_{arc} = 9.8 A and numerical results from the MKB model.

In summary, for ion collection probes 1-4 are highly collisional and probes 5-10′ are moderately collisional. For electron collection all the probes are relatively collisionless. For both ion and electron collection the sheath surrounding the probe is thin since $r_p >> \lambda_D$.

With the calculations of the sheath thickness and collisionality assessment complete, the final classification required before the data is analyzed is to establish the probe operational regime, i.e. sheath-convection or diffusion-limited probe current. As mentioned earlier, when the probe is biased highly positive or negative the sheath may increase in size, intercepting convecting charged particles from the plasma flow. In this case the probe operates in the "sheath-convection" regime, which occurs when the electric Reynolds number, $R_E >>1$ (see Sec. 3.2.3) so that convection effects are important in the sheath analysis; similarly, if $R_E << 1$ then the probe current is diffusion limited. These issues are defined and addressed in the following section.

3.2.3 Regimes of Probe Operation

Langmuir probes are relatively simple in design and implementation. However, interpretation of their results may not be straightforward, especially if the probe sheath is collisional, or sheath-edge effects are significant with possible complications including probe cooling and recombination effects.

To analyze the probe data properly, the sheath for all fourteen probes was classified. The analysis in Secs. 3.2.1 and 3.2.2 showed that the sheath is thin with respect to r_p at all locations, but is moderately collisional for electron collection for probes 1,1′ and collisionless for probes 2-10′. The ion sheath is highly collisional for probes 1-3, e.g. 5-16 collisions as shown in Fig. 3.11 and moderately collisional for probes 4-10′, with about 1-3 collisions in the sheath. Before the probe V-I characteristic is analyzed, the probe operational regime must be assessed, so that an appropriate theory is applied for analyzing the ion current at all voltages, $I_i(V_p)$. Once $I_i(V_p)$ is known, then

$I_e(V_p)$ can be calculated; a plot of $\ln(I_e)$ versus V_p provides the electron temperature, T_{es}.

These probe operating regimes include low and high pressure plasmas, ~O(1 atm), stationary versus flowing plasmas and diffusion versus sheath-convection modes. Each of these regimes will be evaluated for each of the fourteen probes in the anode boundary layer, for the nominal arcjet operating conditions of $\dot{m} = 50$ mg/sec and $I_{arc} = 9.8$ A.

An important nondimensional quantity in studying plasma flows past an electrode, e.g. a Langmuir probe, is the electric Reynolds number, R_E, defined as:

$$R_E = \left(\frac{v_f 2r_p}{\mu_i \frac{kT_{es}}{e}} \right) = R_e Sc_i \tag{3.28}$$

where v_f is the plasma flow velocity, and μ_i is the ion mobility (A^2s/kg), at the sheath edge. The electric Reynolds number is also defined as the product of the flow Reynolds number R_e and the ion Schmidt number, Sc_i, given by: $Sc_i \equiv v_{m,i}/D_i$, where $v_{m,i}$ is the elastic momentum transfer collision frequency and D_i is the ion diffusion coefficient. The electric Reynolds number relates the ion ambipolar diffusion velocity to the plasma flow velocity at the sheath edge. In order for the ambipolar diffusion velocity to exceed the flow velocity, $R_E << 1$; for this case the plasma surrounding the probe can be considered stationary.

A general theory for weakly ionized flow about an arbitrary solid body was developed by Lam [1964]. The electrical response of the body was calculated as a function of the flow properties. Lam formulated a governing set of equations that included Poisson's equation and the species momentum equations, which were nondimensionalized to include R_E for $T_{es} \neq T_i$. In order to make the equations tractable, $T_{es} = T_i$ is *assumed*, so that Poisson's equation is combined with the species conservation equations to give:

$$2\frac{\partial^2 n_i}{\partial \eta^2} - \left(u\frac{\partial n_i}{\partial x} + vR_E^{1/2}\frac{\partial n_i}{\partial \eta}\right) = R_E\alpha^2\frac{\partial}{\partial \eta}\left(\frac{\partial \chi}{\partial \eta}\frac{\partial^2 \chi}{\partial \eta^2} + \frac{\partial^3 \chi}{\partial \eta^3}\right) \qquad (3.29)$$

The first term in Eq. (3.29) represents a diffusion current and is of order $O(1/\eta^2)$, where $\eta = y\sqrt{R_E}$, a nondimensional y-coordinate, perpendicular to the probe's surface; the second term is a convection current, of order O[1]; and the third term is of order $O(R_e\alpha^2\chi^2/\eta^4)$ and represents the ion current driven by the sheath electric fields; $\alpha \equiv \lambda_D/r_p$, $\chi \equiv e\phi/kT_{es}$. The electric Reynolds number in combination with the nondimensional Debye length and probe potential, provides the following distinct probe operating regimes, [Smy, 1976]:

(1) If $R_E\alpha^2\chi^2 << 1$ then the third term in Eq. (3.29) is negligible, so that the ion current is dominated by diffusion and convection and sheath effects may be ignored. Sheath effects refer to the influence of the sheath electric fields to the particle motions and trajectories around the probe. This mode of probe operation is referred to as the *diffusion-convection* regime. This regime is characterized by a thin sheath with respect to the thermal and viscous boundary layers, so that the ion saturation current is constant with increasingly negative probe potential.

(2) If $R_E\alpha^2\chi^2 >> 1$, then the first term in Eq. (3.29) is neglected and the ion current is determined by convection and sheath effects. For this regime the ion sheath is thick, on the order of the boundary layer thickness, so that true ion saturation is not attained. This is a consequence of the ion sheath thickness increasing with probe potential, thus intercepting more free streaming ions at the boundary layer interface, δ. This is particularly true if the probe bias χ is very high, in which case the probe sheath may extend enough into the boundary layer, Fig. 3.12, so that convection effects must be included in the analysis of the probe characteristic, [Hayes *et al.*, 1973; Clements, *et al.*, 1971].

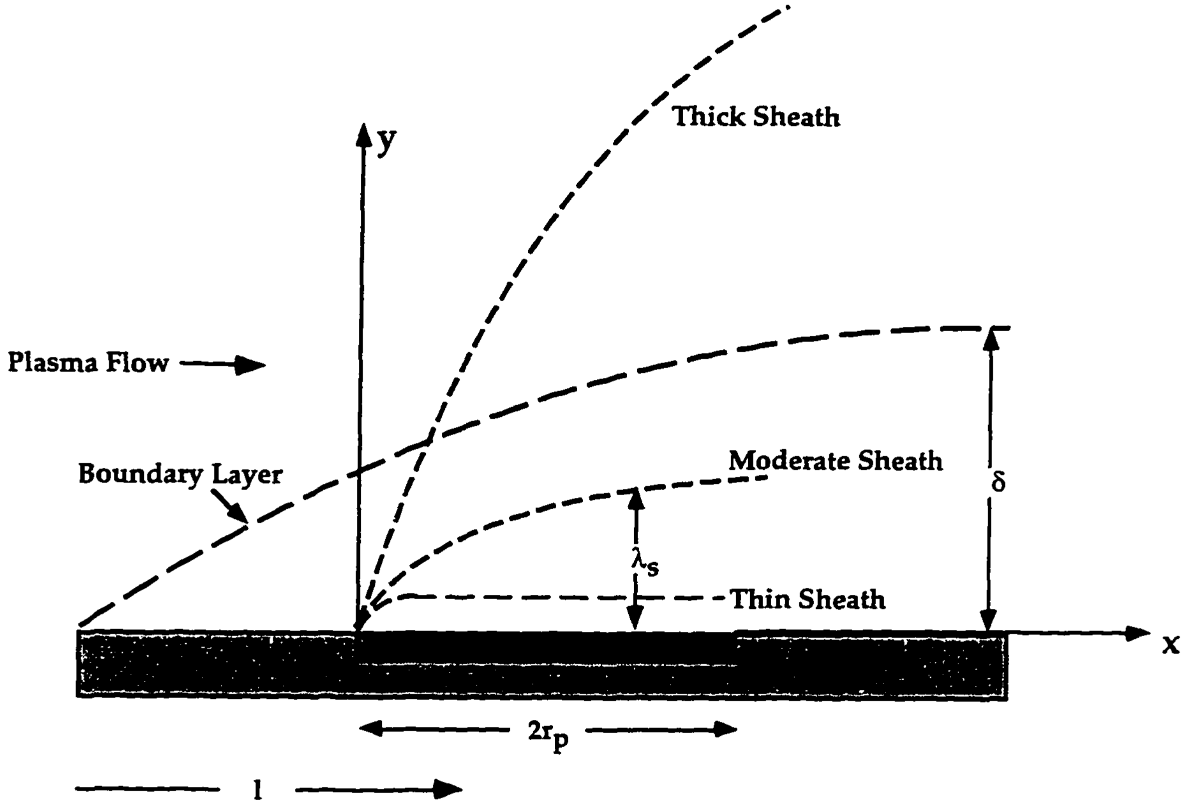

Fig. 3.12 Schematic of various probe sheath sizes λ_s, and how they relate to the boundary layer thickness, δ [Clements, *et al.*, 1971].

In the regime where $R_E\alpha^2\chi^2 >> 1$, the sheath is thick compared with the boundary layers and all ions which are convected into the sheath eventually reach the probe, effectively increasing the ion current to the probe. In addition to $R_E\alpha^2\chi^2 >> 1$, if $R_E\alpha^2 < 1$, then all the ions convected into the sheath are directed to the probe by the sheath electric field E_{sh}; this is called the *sheath-convection* regime. If $R_E\alpha^2 > 1$, then the sheath electric fields are only strong enough to divert a portion of the ions convected into the sheath to the probe; this is referred to as the *E field-convection* regime, [Sonin, 1967].

As $R_E\alpha^2\chi^2$ becomes larger than 1, the sheath thickness approaches the size of the ionization diffusion region or electric boundary layer, [Smy, 1976]. A further increase in $R_E\alpha^2\chi^2$ by increasing the negative probe potential, causes the sheath to expand, displacing the diffusion layer further into the bulk plasma. If $R_E\alpha^2 < 1$, all ions in the sheath are driven to the probe by the sheath electric field and therefore as the sheath expands the ion probe current will increase with probe potential. To support this current the diffusion layer becomes thinner and in the limit of $R_E\alpha^2\chi^2 >> 1$, i.e. thick sheaths, it is the sheath thickness that effectively determines the probe current, [Smy, 1976].

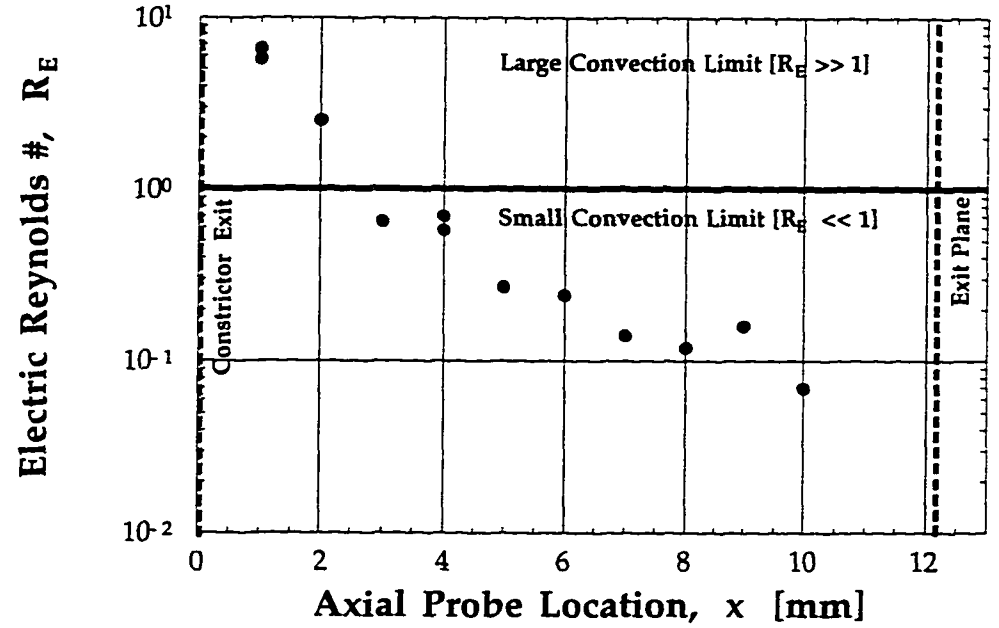

Fig. 3.13 The electric Reynolds number calculations at all probe locations, based on experimental flush probe n_{es}, T_{es} data for $\dot{m} = 50$ mg/s and $I_{arc} = 9.8$ A and data from the MKB model. The regime $R_E >> 1$ represents the large convection limit while $R_E << 1$ is the small convection limit.

Experimental flush probe data, for the nominal conditions of $\dot{m} = 50$ mg/sec, $I_{arc} = 9.8$ A, are used to assess the mode of operation for each probe. In calculating R_E, the plasma flow velocity at the sheath edge and the ion mobility are calculated from the MKB numerical arcjet model, Chapter 7. The R_E calculations are presented in Fig. 3.13; $R_E << 1$ for probes 3-10′, while $R_E > 1$ for probes 1,1′ and 2. However, the experimental data for the ion saturation current of probes 1, 1′, and 2 is constant with increasing probe bias, implying that the ion sheath is thin and convection effects may be neglected. The ion current in a collisional sheath is usually small and is not greatly affected by the probe voltage, [Ruzic, 1997]. Figure 3.14 shows that $R_E\alpha^2\chi^2 < 1$ at all probe locations, so that all probes are operating in the diffusion-convection regime for ion collection with a thin ion sheath.

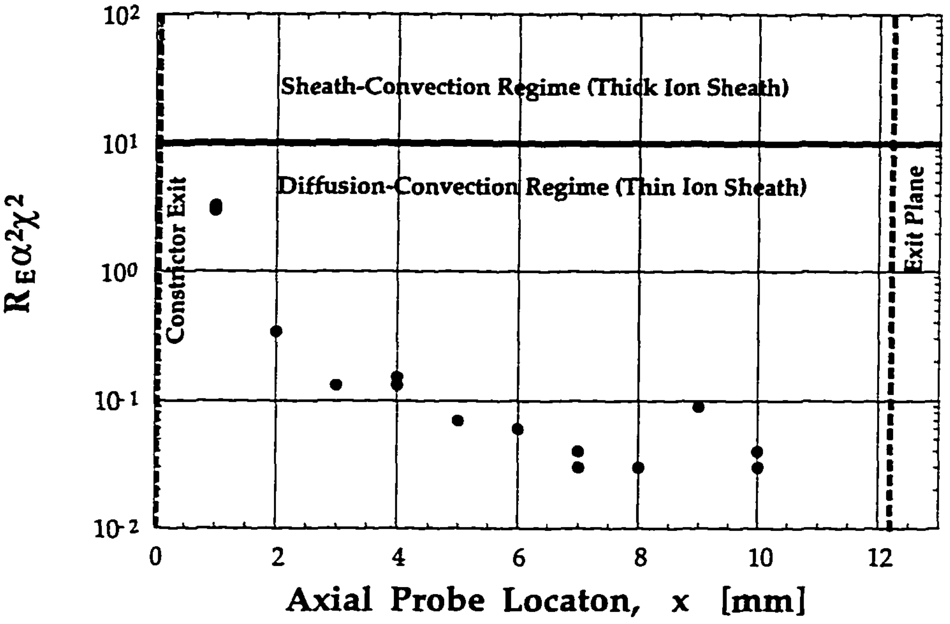

Fig. 3.14 The parameter $R_e\alpha^2\chi^2$ is evaluated at all probe locations. It is calculated based on experimental flush probe data for n_{es} and T_{es} for $\dot{m}$ = 50 mg/s, I_{arc} = 9.8 A and numerical data from the MKB model.

Interpretation of the probe data also depends on whether the probes are immersed in a stationary or a flowing plasma. The plasma surrounding the probe can be considered stationary if $R_E < 1$, and flowing if $R_E > 1$. Figure 3.13 suggests that for probes 1-2 the plasma is considered flowing, and for probes 3-10′ it is "stationary". However, these calculations are based on numerical results for the plasma flow velocity at approximate sheath edges. Though the plasma near the probe surface is flowing, convection effects do not dominate the particle flux to the probes, since the plasma flow velocity v_f is relatively low, ~$O(10^3$ m/s) compared with the species thermal velocity, $O(10^3$-10^4 m/s) in the anode sheath layer.

Other factors requiring consideration when assessing the operational regime of Langmuir probes are chemical reactions and heat transfer effects in the vicinity of the probe. In the bulk plasma arc core, i.e. on the arc centerline, recombination and ionization balance, providing an equilibrium ionization density of n_e. Near the probe this equilibrium is disturbed if the plasma ionization and temperature are artificially decreased by sheath, diffusion and heat-conduction processes, [Smy, 1976]. A nondimensional parameter that relates the probe current due to recombination effects, $I_R \sim (r_p)^3 \beta (n_e)^2 e$ to the thin sheath diffusion current is the Damkohler number D, [Carrier, *et al.*, 1970] defined as:

$$D \equiv \frac{r_p^2 \beta n_{es}}{\left(\mu_i \frac{kT_{es}}{e}\right)} \tag{3.30}$$

where β is the recombination coefficient (m^3/sec), given as: $\beta = (3.4 \times 10^{-28}) n_{es} (T_{es}/1000)^{-4.5}$, [Mitchner, *et al.*, 1973]. The Damkohler number also represents the degree of thermal and chemical nonequilibrium, e.g. for $D << 1$, the flow is considered chemically frozen and for $D >> 1$, the flow is in equilibrium, [Chung, *et al.*, 1975]. For the nominal case of 50 mg/s, 9.8 A the Damkohler number is less than 1, so that the plasma flow in the near-anode region can be considered to be chemically frozen.

There may be cooling effects near the probe, associated with its presence in the plasma. Plasma cooling in the probe vicinity may result in a net reduction in probe current due to recombination and induced temperature gradients. According to the work of [Chung, *et al.*, 1975] recombination effects will be significant if $D/R_E > 1$. This is a comparison of the recombination time, $1/\beta n_e$, with the flow time, r_p/v_f. Figure 3.15 shows that $D/R_E << 1$ at all probe locations so that recombination effects near the probe can be neglected.

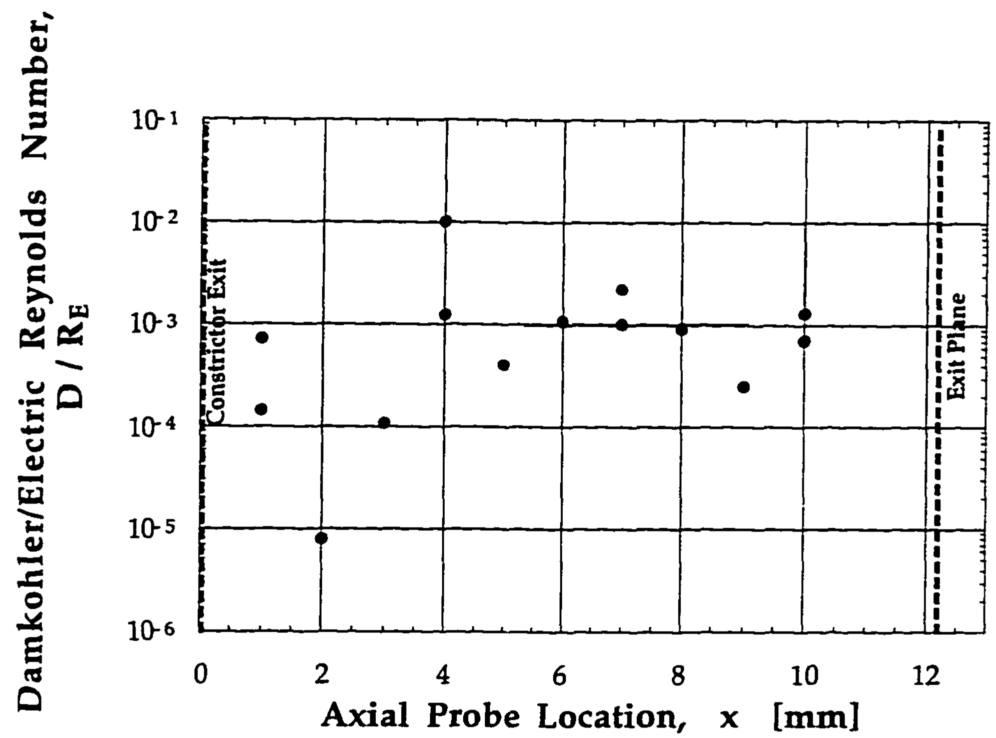

Fig. 3.15 The ratio of Damkohler number D to electric Reynolds number R_E, is calculated at all probe locations. If D/R_E is << 1 then recombination effects near the probe are not significant. These results are based on experimental flush probe data for n_{es} and T_{es} for $\dot{m} = 50$ mg/s, $I_{arc} = 9.8$ A and numerical data from the MKB model.

For probe cooling the temperature difference between the plasma and the probe produces a layer of cold gas around the probe, of thickness $O[r_p/\sqrt{R_E}]$, [Smy, 1976]. For $R_E\alpha^2\chi^2 >> 1$, the sheath-convection regime, only a small portion of the sheath, not including the sheath edge, will be cooled. In this case temperature effects will not influence the number density and electron temperature measurements. The effect of cooling near the probe is to "compress the velocity, ionization and temperature profiles towards the probe, leaving the ionization and heat fluxes to the probe unchanged," [Smy, 1976]. To minimize cooling effects, a characteristic time defined as v_f/r_p should be larger than 10^4 sec^{-1}, [Smy, 1976]. As shown in Fig. 3.16 this criterion is satisfied at all probe locations, so that probe cooling and thermal effects are negligible.

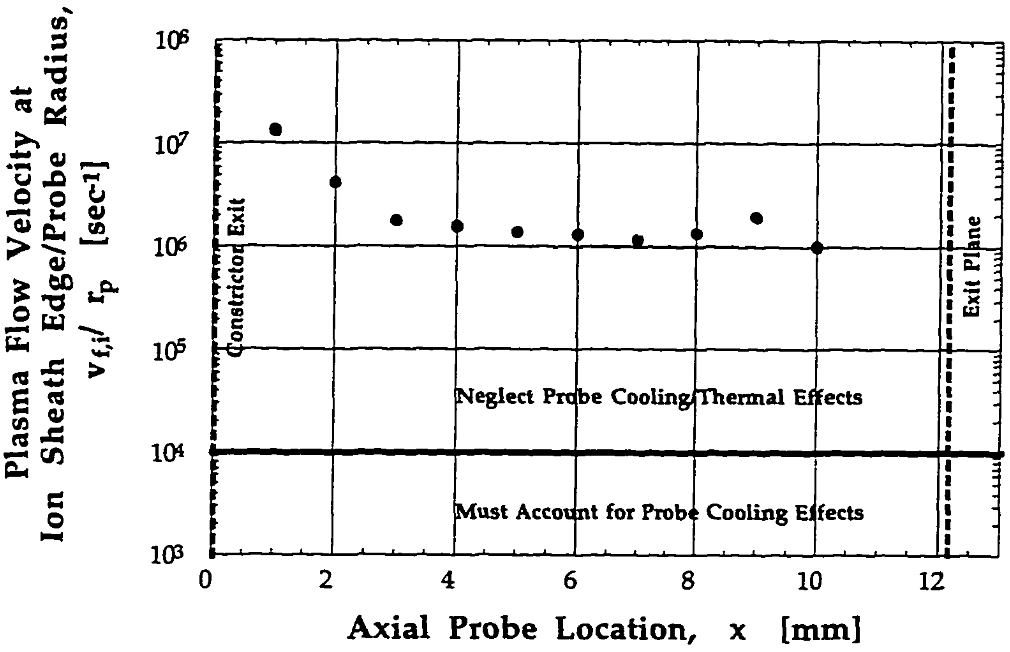

Fig. 3.16 At all probe locations probe cooling and thermal effects are negligible since the ratio of plasma flow velocity to probe radius is > 10^4 sec^{-1}, [Smy, 1976].

It is apparent from the preceding discussion that, although electrostatic probes are simple devices, their implementation and interpretation can be involved. For convenience, the regimes of probe operation described earlier are delineated in Fig. 3.17. In Fig. 3.17 the regime of probe operation for this work is shown as the shaded area, i.e. Zone I. In Zone I, the diffusion-convection regime, there are negligible recombination and negligible probe cooling effects near the probe which is surrounded by a thin collisional ion sheath and a thin collisionless electron sheath. The various zones of operation are summarized as follows, [Smy, 1976]:

(a) Zone I: Diffusion-convection, ($R_E\alpha^2\chi^2 < 1$, $D < 1$).

(b) Zone II: Sheath-recombination, [$D > 1$ ($R_E\alpha^2\chi^2 < 1$), $D > R_E$ ($R_E\alpha^2\chi^2 > 1$)].

(c) Zone III: Sheath-convection, ($R_E\alpha^2\chi^2 > 1$, $D < R_E$).

(d) Zone IV: Electric Field convection, ($R_E\alpha^2 > 1$).

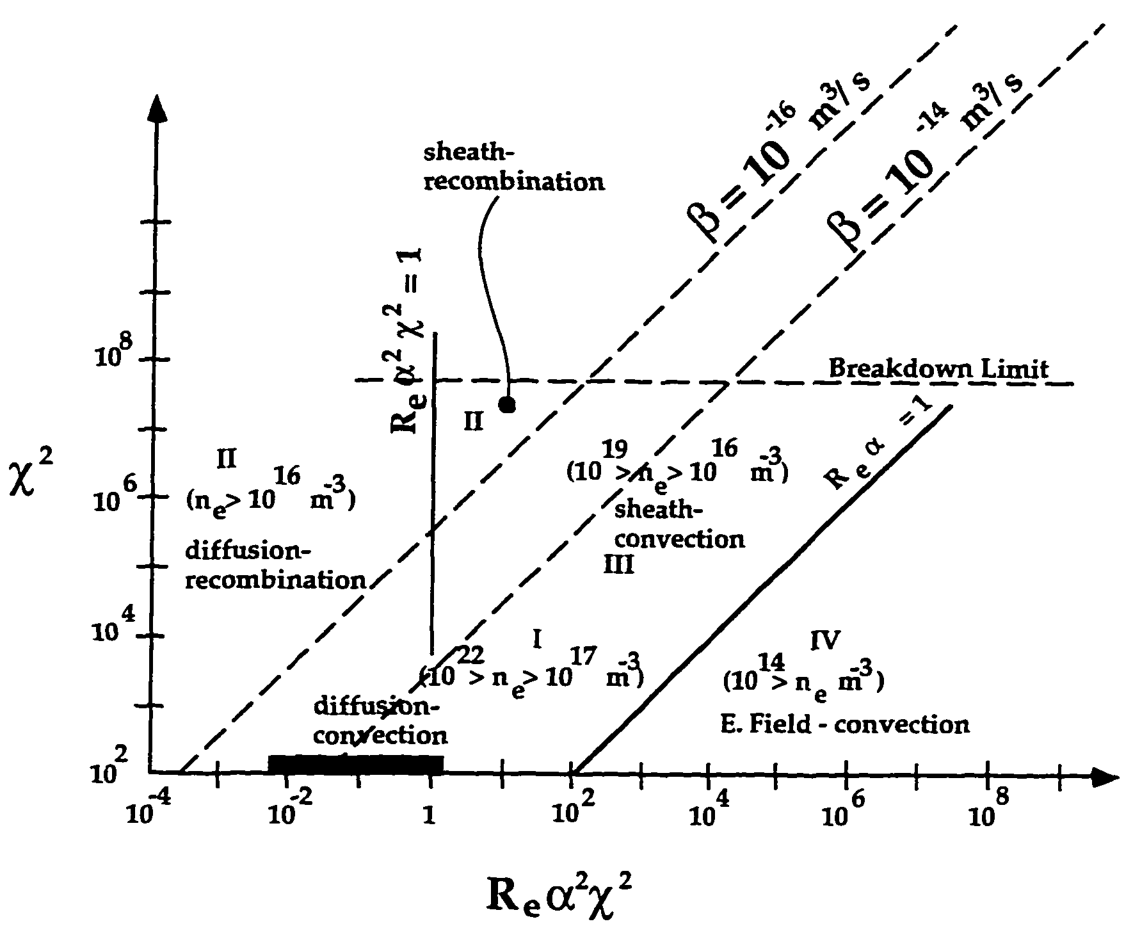

Fig. 3.17 This schematic of χ^2 vs $R_E\alpha^2\chi^2$ delineates the various regimes of probe operation in flowing plasmas, discussed in the text. The criterion for each regime is $1 \leq v_f \leq 100$ m/s, $0.2 \leq r_p \leq 2$ mm, and $\mu_i \sim .002$ As^2/kg; these criterion apply only for the flush probe configuration. This figure was reproduced from Smy [1976]. The shaded region represents the probe operation regime for this work.

In Fig. 3.17, the dotted line represents an upper limit to probe operation, noted as 'sheath breakdown', which occurs when the large electric fields within the convection driven sheath become sufficiently high to generate dielectric breakdown in the gas [Clements, *et al.*, 1973], or to promote field emission from the probe [Mikoshiba *et al.*, 1973; Hoppman, 1968; Smy, 1976]. Of all the operating regimes depicted in Fig. 3.17, the recombination regime, $R_E\alpha^2\chi^2 < 1$, is the most complicated one to analyze since both cooling and recombination effects introduce considerable complexities into the sheath equations, [Pollin, 1964].

3.3 Ideal Collisionless Sheath

Assessing the appropriate length scales, λ_D, r_p, λ_{rs}, for all fourteen micro-probes was required to determine the sheath collisionality. In an ideal situation the attracted particles will travel to the probe unimpeded by collisions in the sheath. For the collisionless case, analysis of the probe V-I characteristic is straightforward. A simple analytical fit to the ion current, e.g. using either the Laframboise analysis (Sec. 3.3.2) or collisionless Child's Law (Sec. 3.3.4) is required at all probe voltages up to ϕ_{pl}, allowing calculation of the electron current, $I_e(V_p) = I_p(V_p) - I_i(V_p)$. With I_e (V_p), a plot of $\ln[I_e(V_p)]$ versus V_p provides I_{esat}, ϕ_{pl} and T_{es}, as discussed below.

In Sec. 3.2 it was shown that for electron collection probes 1-3 have thin, moderately collisional sheaths and probes 4-10′ have thin collisionless sheaths; for ion collection probes 1-2 are collisional, probes 3-6 are transitional and probes 7-10′ are collisionless. In this work the transitional case will be treated as collisionless, since: (1) there are at most 1-2 particle collisions in the sheath for this case; and (2) $|I_i| << |I_e|$, and any correction to I_i has minimal effect on I_e and T_{es}; for example, if $I_i \sim 0$ mA is assumed, then there is ~6% difference in T_{es} if I_i is calculated with an analytical fit.

The approach used here, for both the flush-mounted and cylindrical probe analysis, is presented in the following sections.

3.3.1 Conventional Langmuir Probe Theory

The probe V-I characteristic is the main data, providing the experimental measurements of ϕ_s, j_a, T_{es} and n_{es}.

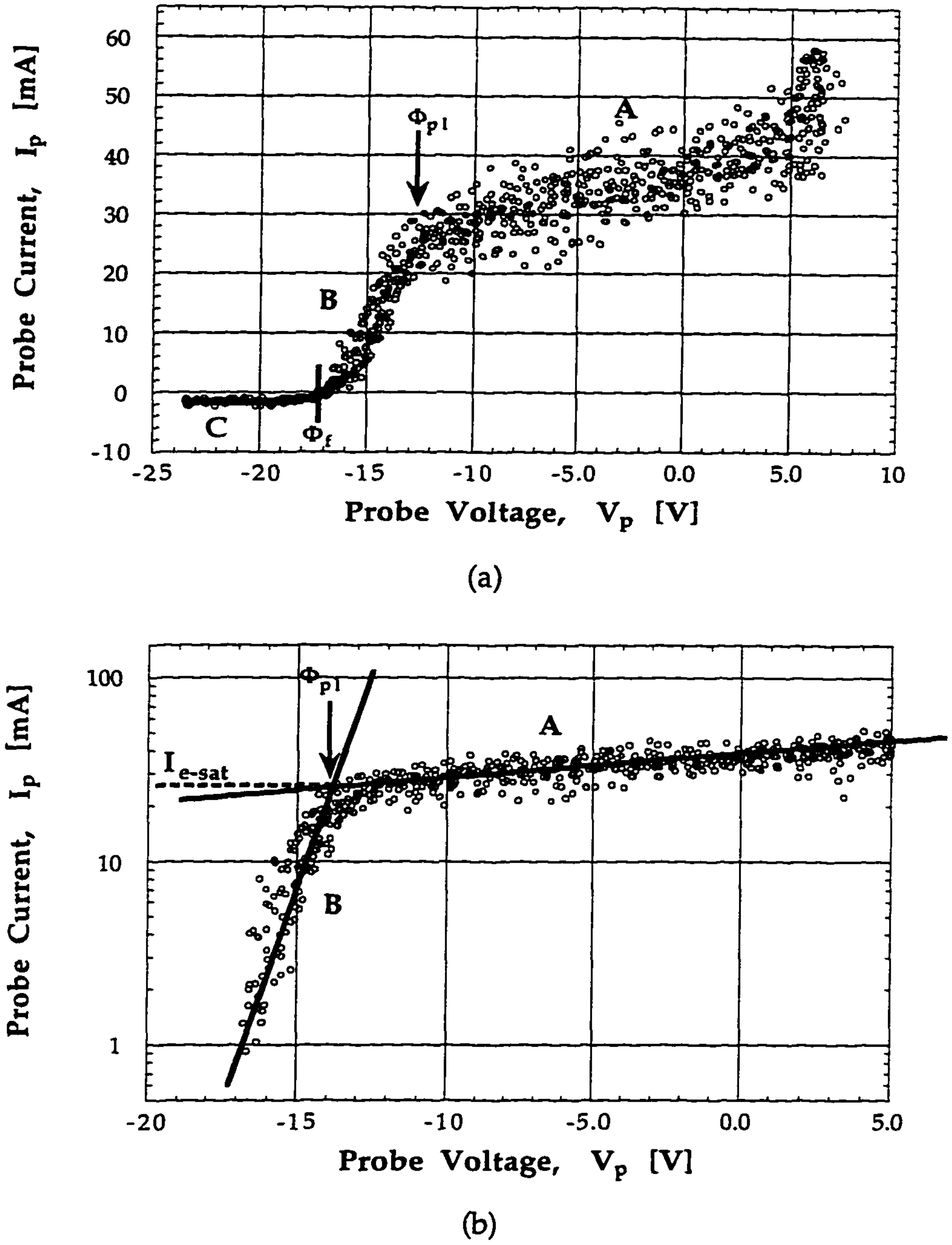

Fig. 3.18 Shown above are the various regions of interest which provide information on plasma properties: 'A' is the electron-saturation region, 'B' is the electron-retarding region and 'C' is the ion saturation region. (a) a typical flush probe characteristic for $\dot{m} = 50$ mg/sec, $I_{arc} = 9.8$ A; and (b) a semilog plot of the data from (a); the electron-retarding region, is linear over two decades, implying an electron Maxwellian energy distribution.

If the Knudsen number is larger than 1 and $\lambda_{rs} >> r_p >> \lambda_D$ or the Knudsen number is less than 1 and $r_p >> \lambda_{rs} >> \lambda_D$, then conventional

Langmuir probe theory is applicable for stationary plasmas, [Chung, *et al.*, 1975]. As stated in Sec. 3.2.1, for both electron and ion collection $Kn \leq O[1]$ for all probes, i.e. continuum electrostatic probes.

The electrostatic probe is a metallic electrode inserted into a plasma, biased at positive and negative voltages V_p with respect to the plasma potential, ϕ_{pl}. The probe current I_p, is measured as a function of V_p, generating a V-I characteristic, Fig. 3.18, which provides information on the plasma properties, [Langmuir, *et al.*, 1926; Schott, 1968]. During data reduction the probe voltage and current data are smoothed using a 2 point moving average routine.

Region A, Fig. 3.18a, is called the electron saturation region, where $V_p > \phi_{pl}$ so that electrons are attracted to the probe and ions are repelled. This region provides the magnitude of the electron saturation current, $I_{e\text{-}sat}$, shown in Fig. 3.18b.

When $V_p = \phi_{pl}$, the probe electric field approaches zero and the probe sheath vanishes so that the charged particles migrate to the probe because of their random thermal velocities. The electron current at ϕ_{pl}, $I_{e\text{-}sat}$ is ~ $(M_i/2\pi m_e)^{1/2}$ times the ion saturation current, $I_{i\text{-}sat}$. In region 'B', the electron-retarding region, low energy electrons are repelled and ions are accelerated to the probe. The electron saturation current $I_{e\text{-}sat}$, is the probe current at ϕ_{pl} and is obtained from the "knee" in the V-I characteristic between regions A and B, Fig. 3.18b. This point provides both ϕ_{pl} and $I_{e\text{-}sat}$. The current in this region is still predominantly due to the electrons. If the electron distribution is Maxwellian, then the slope of region B, after I_i is subtracted from I_p, is linear and from this slope T_{es} is determined as described below, [Chung, *et al.*, 1975] .

The equation governing the probe current collected in the electron-retarding region is derived by calculating the flux of charged particles to the probe, assuming a Maxwellian velocity distribution for the electrons and a collisionless thin sheath. The derivation for the electron current variation in the transition region is found in Swift *et al.*, [1969]:

$$I_e = e n_{es} \bar{R} A_p \sqrt{\left(\frac{kT_{es}}{2\pi m_e}\right)} \exp\left[\frac{-e\left(V_p - \phi_{pl}\right)}{kT_{es}}\right] \tag{3.31}$$

Equation (3.31) is for a thin, collisionless sheath and is independent of probe shape. In this work, $\bar{R}$ varies from 1.05-1.10, Fig. 3.7. The electron temperature is found by taking the natural logarithm of Eq. (3.31) and differentiating with respect to the probe voltage assuming T_{es} is independent of V_p:

$$\frac{d(\ln I_e)}{dV_p} = - \frac{e}{kT_{es}} \tag{3.32}$$

Once T_{es} is obtained from Eq. (3.32), the electron number density is found from $I_{e\text{-sat}}$. The electron number density at the plasma/pre-sheath interface is then found by setting $V_p = \phi_{pl}$ in Eq. (3.31), and solving for n_{es} to get [Swift, *et al.*, 1969]:

$$n_{es} = \left(4.025 \times 10^{15}\right) \frac{I_{e\text{-sat}}}{A_p} \sqrt{\frac{1}{T_{es}}} \qquad [m^{-3}] \tag{3.33}$$

(all units MKS)

In Eq. (3.33), the geometric probe area is used because at $V_p = \phi_{pl}$ a sheath does not exist around the probe, [Swift, *et al.*, 1969], therefore $A_s = 0$ and $A_{eff} = A_p$.

When the probe potential equals the floating potential, labeled ϕ_f in Fig. 3.18a, the flux of electrons equals the flux of ions to the probe so $I_p = 0$. At the floating potential the probe is still biased negative with respect to ϕ_{pl}, collecting the ion-saturation current as well as an electron current, [Chung, *et al.*, 1975]. In region C, $V_p << \phi_{pl}$ so that almost all electrons are repelled, resulting in an ion sheath. The ion saturation current is much less than the electron saturation current because $m_e << M_i$ and $T_{es} >> T_{is}$, with $I_{i\text{-sat}}$ given by the Bohm current, I_B.

As described in Sec. 3.1.1, the Bohm criterion for an ion-attracting probe states requires the ions to enter the collisionless ion sheath with the Bohm velocity, $u_B = (kT_{es}/M_i)^{1/2}$ in order for Poisson's equation to be satisfied. The ions enter the collisionless pre-sheath with their random thermal velocity, $v_{th,i} = (8kT_i/\pi M_i)^{1/2}$. The pre-sheath voltage drop, $\phi_{pre} = -kT_{es}/2e$ serves only to accelerate the ions to the required Bohm velocity. Therefore, for a collisionless ion pre-sheath and sheath, $I_{i\text{-}sat}$ is approximated by the Bohm current:

$$I_B = -en_{e_{p,s}} u_B A_{eff} \tag{3.34}$$

The electron number density at the pre-sheath/sheath interface $n_{e_{p,s}}$ is given by the Boltzmann relation, accounting for the pre-sheath voltage drop:

$$n_{e_{p,s}} = n_{es}\exp\left[\frac{-e}{kT_{es}}\left(\frac{kT_{es}}{2e}\right)\right] \tag{3.35}$$

$$n_{e_{p,s}} = n_{es}\exp\left[-\frac{1}{2}\right] = (0.61)n_{es} \tag{3.36}$$

Combining Eqs. (3.34) and (3.36), the Bohm current in a thin collisionless ion sheath is:

$$I_B = -e(0.61)n_{es}\sqrt{\frac{kT_{es}}{M_i}}\bar{R}A_p \tag{3.37}$$

Equation (3.37) can be used to approximate $I_{i\text{-}sat}$. For cylindrical probes, the collisionless ion current is also given by the Laframboise theory, as described in the following section.

3.3.2 Theory of Laframboise

The electron current to the probe is required for deriving T_{es}, Eq. (3.32). However, to obtain I_e the ion current component of the total probe current must be known for all negative voltages up to ϕ_{pl}, since $I_e(V_p) = I_p(V_p) - I_i(V_p)$. An analytical expression for the ion current is required to evaluate I_i at all negative voltages up to ϕ_{pl}. This ion current is dependent on the sheath collisionality, i.e. the length-scale regime. For example, for a collisionless thin sheath the Bohm current is appropriate for the current entering the ion sheath, as discussed earlier. For collisional ion sheaths the Bohm current requires modification, Sec. 3.4. However, the Bohm current is a function of n_{es} and T_{es} which are not known a priori, and it is desirable to have $I_i = f(V_p)$ only.

Laframboise [1966, 1982] provided a practical theory for describing the ion current in a thin, moderate and thick collisionless sheath surrounding spherical and cylindrical probes, in a stationary plasma [Laframboise, 1966] and a flowing plasma [Godard, *et al.*, 1983].

Laframboise numerically solved Poisson's equation for various ratios of r_p/λ_D, and T_i/T_e for both spherical and cylindrical probes. Both ions and electrons were assumed to have Maxwellian distributions at temperatures T_i and T_e, respectively. This method does not provide an analytic form for the sheath thickness but it does give numerical results. The thin sheath, transition to a thick sheath and the thick sheath regimes can all be treated by the Laframboise method [Ruzic, 1994]. Laframboise obtained a plot of nondimensional ion current j_i^* and nondimensional voltage, $\chi=e(\phi_{pl}-V_p)/kT_{es}$, with an upper limit of $\chi = 25$.

The nondimensional ion current j_i^* is given as the ion current normalized by the Bohm current and is defined by:

$$I_i = \frac{1}{4}en_{es}\sqrt{\frac{8kT_{es}}{\pi M_i}}A_p j_i^* \tag{3.38}$$

The Laframboise method requires some iteration, but converges quickly. However, iteration can be circumvented with an empirical fit to Laframboise's numerical results. For the thick sheath case, i.e. $r_p/\lambda_D < 4$, [Laframboise, 1966; Ruzic, 1994]:

$$j_i^* = 1.127(\chi)^{1/2} \tag{3.39}$$

With this empirical fit, an expression for the theoretical ion current is found independent of T_{es}, [Laframboise, 1966; Ruzic, 1994]:

$$I_i = \frac{1}{4} e n_{es} \sqrt{\frac{8e}{\pi M_i}} A_p (1.127) \sqrt{\phi_{pl} - V_p} \tag{3.40}$$

Use of Eq. (3.40) provides a simple fit to the ion saturation region because it is only a function of probe voltage. The plasma potential ϕ_{pl} in Eq. (3.40) is found from a graphical analysis of the probe characteristic, Fig. 3.18b. To use Eq. (3.40), an estimate of n_{es} is required. This is done by solving Eq. (3.40) for n_{es} and choosing a point (V_p, $I_p = I_i$) in the ion saturation region. This data is substituted back into Eq. (3.40) for an estimate of n_{es}. Using this n_{es} and ϕ_{pl} in Eq. (3.40), a theoretical fit to I_i is found for all $V_p \leq \phi_{pl}$.

Though Eq. (3.40) was derived for $r_p/\lambda_D < 4$, i.e. thick sheaths, it also provides a reasonable fit for experimental data of $15 \leq r_p/\lambda_D \leq 40$, i.e. thin to transitional sheaths, and can be used as an analytical fit to the ion current data.

Experimental verification from the work of Sonin [1966], Dunn, *et al.*, [1970] and Lederman, *et al.*, [1968] have shown that the Laframboise results can also be applied to aligned cylindrical probes in *flowing* as well as stationary plasmas.

3.3.3 Cylindrical Probe Theory

The Laframboise theory can be used for predicting the ion saturation current to a cylindrical probe in a stationary plasma. If a cylindrical probe is aligned with the plasma flow direction and if $\lambda_{rs} >> r_p$, then it can be assumed that the Laframboise approach is applicable. However, this is not the case when the "end-effect" becomes important and additional parameters, e.g. L_{ext}/λ_D and L_{ext}/r_p influence the analysis.

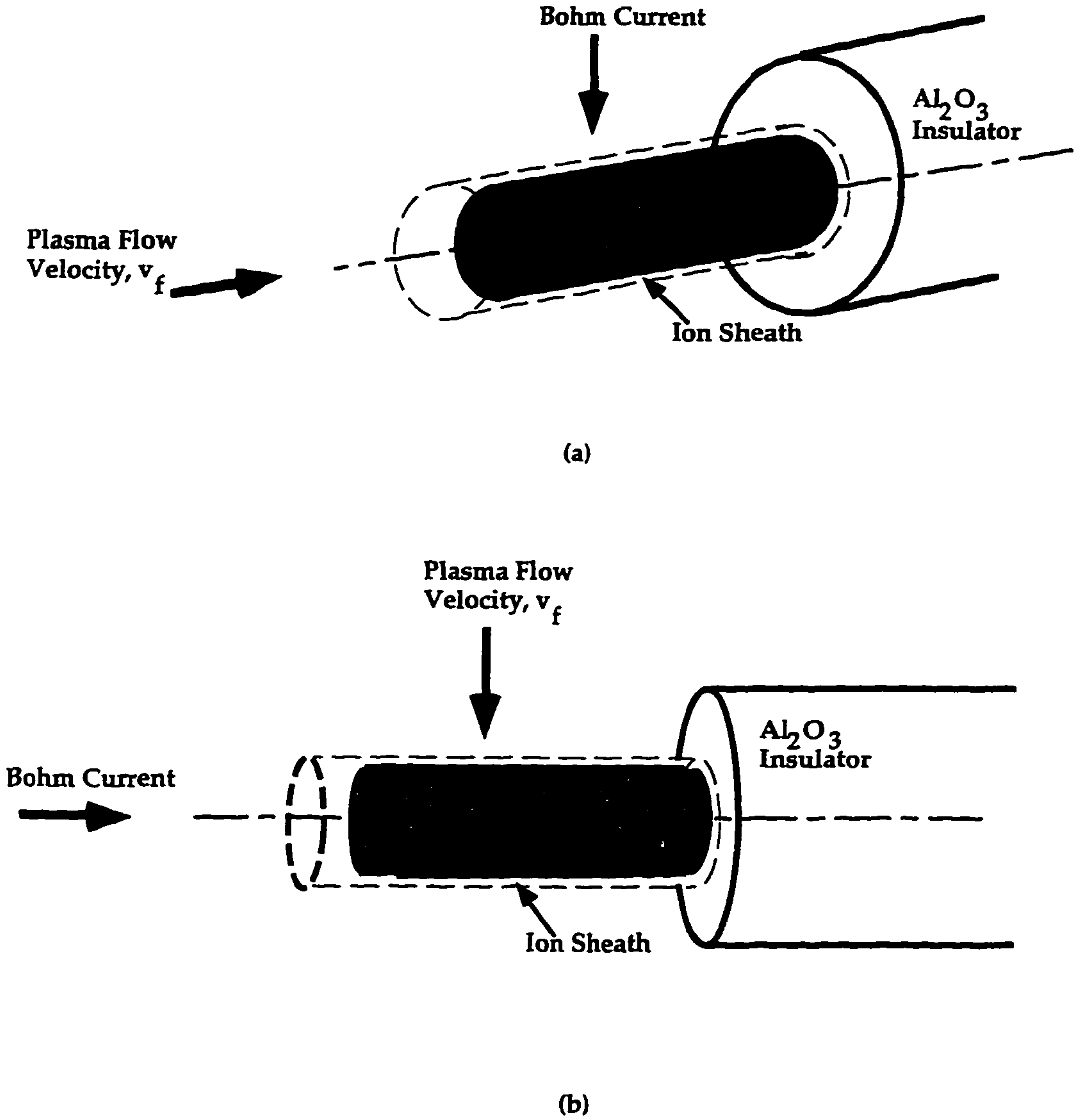

Fig. 3.19 Schematic of the ion sheaths and end effect for a cylindrical probe (a) aligned with the plasma flow velocity and (b) transverse to the flow.

The end effect was first described by Bettinger, *et al.* [1968] concerning measurements made by the satellite Explorer 17. If the ion current to a cylindrical probe is measured at various angles of attack θ, a peak in current is observed at $\theta = 0°$, i.e. when the probe is aligned with the plasma flow. This maximum in collected ion current occurs because the aligned probe can collect particles through the transverse sheath area, as well as through the sheath at the end of the probe, Fig. 3.19, [Chung, *et al.*, 1975]. If the sheath thickness is large enough and if the plasma flow velocity, v_f exceeds the Bohm velocity then an appreciable number of ions can reach the probe through the end of the sheath as well as through the sides. This end effect phenomenon depends on the end effect parameter τ_l, [Chung, *et al.*, 1975], defined as:

$$\tau_l = \frac{L_{ext}}{\lambda_D}\frac{(kT_{es}/M_i)^{1/2}}{v_f} \tag{3.41}$$

where L_{ext} is the extension length of the probe from the anode surface.

The end effect parameter relates the ion current contribution from the probe sides to the current from the probe end. For $\tau_l >> 1$, the end effect is negligible. If the probe is turned at a slight angle to the plasma flow direction, a portion of the streaming ions which enter the end of the sheath will have sufficient angular momentum to escape and will therefore not be collected by the probe, [Chung *et al.*, 1975]. The end effect occurs for $r_p/\lambda_D << 1$. i.e. the sheath thickness is much larger than the probe radius. This is referred to as the OML, 'Orbital Motion Limit, regime, [Chung, *et al.*, 1975]. In this investigation, T_{es} ~O(15,000°K), v_f~O(3000 m/s) at $r = L_{ext}$~0.25-0.30 mm, so that τ_l ~O(10^2) >>1, i.e. the end-effect is negligible. However, when calculating the probe collection area for analyzing the cylindrical probe data (Chapter 5), the probe end was included.

Cylindrical probes were also used to obtain radial profiles of ϕ_f, ϕ_s, j_a, n_{es} and T_{es} at all fourteen probe locations. Probes 2-10' are extended about 0.25-0.3 mm into the plasma flow. Initial experiments also had probes 1, 1' (with a diameter of about 0.006 ") extended ~0.1-0.15 mm into the flow as well; however, this was abandoned due to the severe melting and damage of the probe and the alumina tubing.

Collisional sheath effects for probes aligned with the plasma flow exhibit similar phenomena to those for collisionless conditions, e.g. for small τ_i a peak in ion current at $\theta = 0$ °, [Chung, *et al.*, 1975]. This may be the result of ion-ion collisions [Hester, *et al.*, 1970]; if $\theta \neq 0°$, the flow momentum dominates over ion-ion collision effects and the collected probe current is governed by orbital motion effects, [Chung, *et al.*, 1975].

The ion current to cylindrical probes oriented transverse to the flow direction, with a collisionless sheath, is: [Chung, *et al.*, 1975; Clayden, 1963]:

$$I_i = 2en_{es}v_f r_p L_{ext} \tag{3.42}$$

The behavior of a transverse cylindrical probe in a high speed plasma flow differs from an aligned cylindrical probe in several aspects: (1) the electron temperature cannot generally be determined from a semilog plot of I_e versus V_p; a higher T_{es} is obtained than the true electron temperature, which must be corrected for velocity effects, (2) the plasma potential cannot be readily identified from a change in slope of the probe characteristic, and (3) electron current saturation does not occur under conditions where it would be present for a probe in stationary plasma, [Chung, *et al.*, 1975]. This is because the shielding effect provided by the probe electron sheath is destroyed by the high speed ion flow.

According to Ruzic [1997] the main concern with cylindrical probes transverse to a plasma flow is if the electrons or ions have a directed energy, i.e. a beam, since the neutral gas flow is irrelevant to the probe signal. In arcjet thrusters no particle beams are present, so that cylindrical probe data can be reliably analyzed using similar methods used for the flush probes. Concerns with cylindrical probes transverse to a flowing plasma are addressed in more detail in Chapter 5, along with the presentation of cylindrical probe results obtained in this work.

3.3.4 Flush-Mounted Probe Theory

Obtaining the Ion Current

In this section a method of interpreting the data from a flush-mounted, planar probe surrounded by a thin collisionless sheath is presented. Calculation of T_{es} requires knowing the electron current I_e and the ion current I_i. An analytical fit to the ion saturation current region of a flush probe is found by several methods:

(1) applying the Laframboise analytic fit for I_i Eq. (3.40), calculating $I_e(V_p)$ and then obtaining T_{es} from the inverse slope of the electron-retarding region, Eq. (3.32). Using the Laframboise equation for $I_i(V_p)$ is applicable for cylindrical probes but also provides a reasonable curve fit to the ion current saturation region for flush probes.

(2) the collisionless form of Child's Law is used to calculate $I_i(V_p)$, for $V_p \leq \phi_{pl}$, [Liebermann, 1994]:

$$I_i(V_p) = \frac{4}{9}\varepsilon_0\left(\frac{2e}{M_i}\right)^{1/2}\frac{|V_p|^{3/2}}{\lambda_{s,i}^2(V_p)}\bar{R}\left[\lambda_{s,i}(V_p)\right]A_p \qquad (3.43)$$

where ε_0 is the permitivity of free space, $\lambda_{s,i}$ is the collisionless ion sheath thickness given by Eq. (3.26) and M_i is the reduced ion mass, Sec. 3.1.1.

(3) Graphical analysis of the flush probe V-I characteristic has shown that the ion saturation current region is fairly flat, i.e. $I_i(V_p) \sim$ constant, e.g. Fig. 3.18a. As discussed in Sec. 3.2.3 this means the sheath is thin with respect to the boundary layer so that convective effects can be ignored. Also, since $I_i(V_p < \phi_{pl}) \sim$ constant, a simpler approach than methods (1)-(2) above would be to subtract a constant I_i value from I_p, obtaining I_e. As suggested by Ruzic [1994], the easiest approach is to use the most positive ion current value and use a number a few percent higher than that as the constant ion current to subtract from I_p. Since I_i is constant for $V_p \leq \phi_{pl}$, the value of the ion saturation current

at -20 volts was selected as I_i, so that $I_i(V_p = -20V) = I_{i\text{-sat}} \sim I_i$. The voltage of -20V is well into the ion saturation current region. Using I_i~constant tends to overestimate the contribution from the highest energy electrons in the tail of the Maxwellian distribution and leads to considerable error in plasmas where $|I_i| \approx |I_e|$, [Ruzic, 1994]. However, in this experimental study, this is not the case since $|I_i| << |I_e|$.

Therefore, because of its applicability and its simplicity, method (3) is used to derive I_i and I_e. A semilog plot of I_e versus V_p provides the slope of the electron-retarding region. Once the slope is found T_{es} is calculated from Eq. (3.32). An alternate method for calculating Tes is based on the potential data, outlined in Sec. 4.2.5.

Obtaining the Electron Number Density

Once the electron temperature is obtained, the electron number density at the plasma/pre-sheath edge n_{es}, can be found:

(1) Use Eq. (3.33) to obtain n_{es}. This equation was derived assuming that a thin collisionless electron sheath surrounds the probe. Based on the length scale calculations presented in Sec. 3.2.1, this condition is satisfied at all probe locations.

(2) For a thin collisionless ion sheath the Bohm current equation also provides n_{es}:

$$I_B = I_{i\text{-sat}} = en_{es}(0.61)\sqrt{\frac{kT_{es}}{M_i}}\bar{R}A_p \qquad (3.44)$$

Solving Eq. (3.44) for n_{es}:

$$n_{es} = \frac{I_{isat}}{e(0.61)\sqrt{\frac{kT_{es}}{M_i}}\bar{R}A_p} \qquad (3.45)$$

The main difference between methods (1) and (2) for calculating n_{es} is that method (1) depends on information from the electron collecting portion of the probe V-I characteristic where the probe signal-to-noise ratio (S/N) is relatively high. Method (2) requires information from both the electron current and ion current collecting portions of the probe characteristic, which has a smaller S/N. Therefore, in this work, method (1) is used to evaluate n_{es}.

3.4 Collisional Effects in Sheaths

When the charged particle mean free paths for collisions with neutrals or other charged particles are smaller than the sheath thickness, then the sheath is collisional with the number of collisions given by $\alpha \equiv \lambda_S / \lambda_{rS}$. For $\alpha >> 1$, collisionless theory is not applicable, i.e. T_{es} is not a simple function of the electron-retarding slope. In the collisional case, for continuum probes $Kn < 1$, the motion of the charged carriers may be determined by convection, diffusion, mobility-dominated transport and charge-generation within the sheath, where the continuum equations and Poisson's equation apply, [Chung, *et al.*, 1974; 1975].

The goal of any probe theory is to construct V-I characteristics and obtain analytic and/or empirical expressions for predicting n_{es} and T_{es} in the plasma. The current collection by a continuum probe of a certain geometry depends on many parameters: $I = I[A_p, (\lambda_D/r_p)^2, \chi_p, R_E,$ Damkohler numbers, etc.]. It appears that there is no simple way of deriving an explicit, general expression for the probe current for collisional sheaths. Historically, continuum probe theories have been developed by considering various limiting cases for one-dimensional or quasi-one-dimensional situations, [Chung, *et al.*, 1974; 1975].

Non-dimensional parameters such as electric Reynolds number and Damkohler number are important in selecting and formulating the appropriate theoretical or empirical form of the ion-saturation current, which is required for n_{es} and I_e determination. For a collisional probe, the probe current in the ion saturation region is reduced due to ion-neutral scattering collisions, [Chung, *et al.*, 1975; Ruzic, 1994]. The collisionless equations overestimate the collected current, thus presenting an upper bound to T_{es}. In order to calculate the reduction in collected current, the scattering collisions must be considered in detail, [Ruzic, 1994].

Collisions in the sheath tend to reduce the probe current. If the collisions are energetic enough inelastic processes may also occur. In Sec. 3.2 it was established that the ion sheath is highly collisional for probes 1-2 and moderately collisional for electron collection. Using the collisionless theory for probes 1-2 provides an upper bound to the true magnitude of T_{es}.

The transitional sheath refers to the borderline collisional-collisionless sheath, where the collisional effects are small, but non-negligible. A simple interpolation formula for calculating the ion current for this case is, [Schultz, *et al.*, 1955; Thornton, 1971]:

$$j_i = \frac{j_{i,\infty}}{1 + \dfrac{j_{i,\infty}}{j_{i,o}}} \tag{3.46}$$

where $j_{i,\infty}$ and $j_{i,o}$ are the collisionless and collisional ion current densities respectively. Equation (3.46) shows that the current collection to a probe of any geometry, with a transitional sheath, can be estimated if the collisionless and collisional currents are available.

The effect of collisions, especially electron-neutral collisions, on the analysis of the electron-retarding region, is not well understood, [Chung, *et al.*, 1975]. The current in the electron-retarding region is described as: $I_e = I_{e\text{-}sat}\exp[e(V_p - \phi_{pl})/kT_{es}]$ and is used to infer the electron temperature from its slope. However, there is both theoretical and experimental evidence that the electron Maxwellian characteristic is sufficiently altered by collisions that the classical method of obtaining T_{es} from the slope is not applicable. Peterson [1971] has studied the effect of electron-neutral collisions on the electron saturation current to cylindrical and spherical probes in a stationary plasma.

In the electron-retarding region of the V-I characteristic the effect of electron-neutral collisions on the probe current is less well understood compared with the collisionless case, [Peterson, 1971].

Kirchoff *et al.,* [1971] have evaluated the effect of electron-neutral collisions on the derivation of the electron temperature and concluded that a double cylindrical probe is less sensitive than a single probe to collisional effects. Therefore, double probes may be used to determine T_{es} for situations where single probes may give erroneous results.

Double probes consist of two electrodes that are floating with respect to each other; as such they do not draw the large magnitudes of electron current that single probes do. Implementation of double probes in this work was attempted but found to be impractical because: (1) the probe hole diameter required alumina tubing sized with an O.D. of 0.79 mm and the tungsten wire diameter for each of the double probe wires would be at most .05-.08 m m which proved impractical to fabricate, clean and implement; (2) the double probe could not be used to obtain radial plasma property profiles since it would melt because of the small diameter, Sec. 2.3.1; and (3) large sheath-edge effects would be introduced, Sec. 3.2.2.

Charged-neutral collisions reduce the probe current below the collisionless value. However, the effect of ion-ion collisions, when ion-neutral collisions are negligible, actually increases the current to a cylindrical probe, [Sonin, 1966]. This is not the case in this work, since ion-neutral collisions are not negligible, e.g., for ion collection $\nu_{H^+-H_2} >> \nu_{H^+-H^+}, \nu_{N^+-N^+}$.

3.4.1 Interpretation of Probe Characteristic for Collisional Sheaths

For electron collection the probe sheath is fairly collisionless so that the electron-retarding region of the probe characteristic is used to calculate T_{es}, Eq. (3.32) and n_{es} is calculated using Eq. (3.33). For ion collection the probe sheath varies from highly collisional at x=1 and 2 mm to moderately collisional for x $\geq$ 3 mm.

This section focuses on the interpretation of the probe characteristic for collisional ion sheaths. The approach used in this work for interpreting such characteristics for both flush and cylindrical probes is described in the following sections.

3.4.2 Flush-Mounted and Cylindrical Electrostatic Probe Theory

Obtaining the Ion Current

The ion current to a flush-mounted planar probe surrounded by a thin collisional ion sheath can be calculated with the following methods:

(1) The collisional form of Child's Law, also known as the planar, space-charge limited, mobility-controlled diode equation, [Lieberman, *et al.*, 1994; Cobine, 1941]:

$$I_{i,sat}\left(V_p\right) = \frac{\frac{9}{8}\varepsilon_o \mu_i \left|V_p\right|^2 \bar{R} A_p}{\lambda_{s,i}^3} \tag{3.47}$$

where μ_i is the mobility of the H^+ ion since $\mu_{H^+} >> \mu_{N^+}$; $\lambda_{s,i}$ is an average collisional ion thickness evaluated at the most negative potential used in this work, V_p = -24 V with Eq. (3.27) and with the Sheridan *et al.*, model [1991]; $\bar{R}$ is an average value based on the average $\lambda_{s,i}$, and is equal to ~1.06 (Fig. 3.7). Equation (3.47) also provides a simple analytical fit to the ion current region, -24 V $\leq V_p \leq \phi_{pl}$, as a function of the probe voltage.

(2) As described in Sec. 3.3.4 the ion saturation current for the flush probe data is fairly constant with increasing negative probe voltage so the following equation is used as a fit to the ion saturation region:

$$I_i\left(V_p\right) = I_i(-20\text{ V}) = I_{isat} \tag{3.48}$$

(3) The Laframboise method, Sec. 3.3.2, can also be used for obtaining a theoretical fit to the ion saturation region, $I_i(V_p)$, Eq. (3.40).

A comparison of methods (1)-(3) for evaluating I_i, I_e and T_{es} is shown in Fig. 3.20.

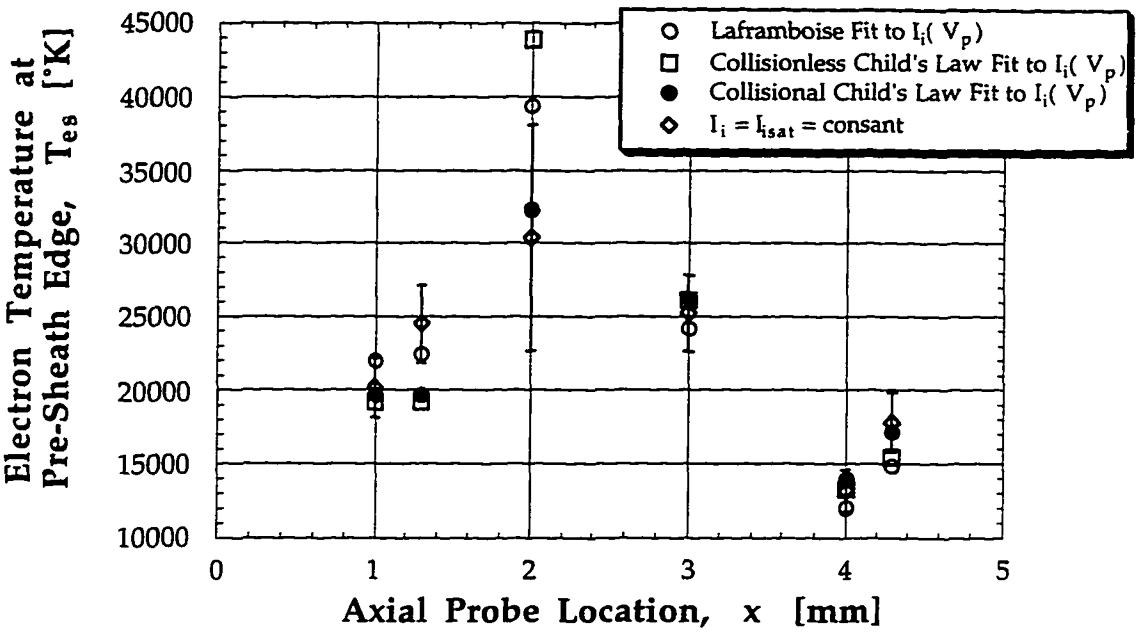

Fig. 3.20 Comparison of methods (1)-(3) for evaluating I_i, used for calculating I_e and T_{es} for the experimental conditions of $\dot{m}$ = 50 mg/sec, I_{arc} = 9.8 A for flush probes 1-3.

As shown in Fig. 3.20, except for probe 2, the difference between using the Laframboise approach, Child's Law or assuming $I_i(V_p)$ = constant = $I_{isat}(-20\ V)$ is minimal. Therefore, method (2), $I_i(V_p)$ = constant = $I_i(-20V)$, is used in this work since: (a) it is the most convenient to use; and (b) it provides a self-consistent approach that is only dependent on the *experimental* data and does not rely on the accuracy of transport property calculations, such as mobility.

If the electron sheath is collisional, the electron-Maxwellian distribution may be sufficiently altered, so that obtaining T_{es} from the electron-retarding slope is not applicable.

However, according to Kozlov [1969] the electron current to a probe in a collisional electron sheath is reduced in comparison with the collisionless electron current, Eq. (3.31), by the factor:

$$\gamma \approx 1 + \alpha \left[\frac{\lambda_{s,e}(V_p)}{\lambda_{e-H_2}}\right]\left[\frac{kT_{es}}{e(V_p - \phi_{pl})}\right] \qquad (3.49)$$

where α is approximately 0.5. For probe 2, γ~1.35, so that collisions in the electron sheath decrease the probe current by 35%. However, according to Fig. 3.11, the number of collisions in the electron sheath is at most 1. Therefore, in this work it is *assumed* that the electron sheath is collisionless, so that T_{es} is correctly obtained from the inverse slope of the electron-retarding region, Eq. (3.32).

Obtaining the Electron Number Density

During the data reduction process it was found that accounting for collisions did not have much influence on the $I_{e\text{-}sat}$, ϕ_{pl}, and I_e data. This is because, for electron collection, the sheath is fairly collisionless. Therefore, n_{es} can be obtained using Eq. (3.33), knowing $I_{e\text{-}sat}$, A_p and T_{es}. Other methods for calculating n_{es} for a collisional sheath include:

(1) The collisional form of the Bohm current is used:

$$I_{i,sat}(V_p) = en_{es}(0.61)u_s\bar{R}A_p \qquad (3.50)$$

where u_s is the ion velocity at the sheath edge, no longer equal to the Bohm velocity u_B, since the pre-sheath is collisional. The velocity u_s is given by the following analytic approximation to the numerical work of Godyak, *et al.* [1990]:

$$\frac{u_S}{u_B} \approx \left[1 + \frac{\pi\lambda_D}{2\lambda_i}\right]^{-1/2} \equiv \alpha_c \qquad (3.51)$$

where $\lambda_i = \lambda_{H^+-H_2}$, $u_B = \sqrt{kT_{es}/M_i}$. Combining Eqs. (3.50) and (3.51) and solving for n_{es}, gives:

$$n_{es} = \frac{I_{i,sat}}{e(0.61)u_B\alpha_c\bar{R}A_p} \qquad (3.52)$$

(2) The collisional form of Child's law, Eq. (3.47), is combined with Eq. (3.50):

$$n_{es} = \frac{\frac{9}{8}\varepsilon_o\mu_i\left|V_p\right|^2}{e(0.61)u_B\alpha_c\lambda^3_{s,i}} \qquad (3.53)$$

where $\left|V_p\right|$ is equal to -20 V, a point in the ion saturation region. For probe 3, Eq. (3.53) predicts n_{es} ~ 20% higher than Eq. (3.50) and ~ 85% higher than Eq. (3.33).

3.5 Probe-Plasma Interactions

The extent of plasma perturbation due to the presence of a probe depends on the following characteristic lengths: (1) probe geometry, i.e. probe radius; (2) the electron Debye length λ_D; and (3) the mean free paths for ionization λ_{ioniz} and charge exchange reactions, λ_{ce}, [Hershkowitz, 1989].

Some sources of probe perturbation include: (1) perturbations associated with the physical size of the probe; (2) probe shadowing effects; (3) desorption of gases on the probe shaft and probe material; and (4) the probe insulator may drain ions that are trapped in potential wells in the plasma, [Hershkowitz, 1989].

It is important to understand the effects the probe may have on the surrounding plasma, so that any information from the probe data can be interpreted as accurately describing the plasma state in the probe's absence. In the following sections a brief attempt is made to discuss the various perturbations the probe may cause and how the experimentalist can minimize them.

3.5.1 Minimizing Probe Perturbation Effects on the Plasma

Probe perturbation effects due to probe size, including sheath-edge effects, probe cooling, etc. As discussed in Secs. 2.3.1 and 3.2 these effects were minimized as much as possible and do not pose a problem in this work.

Probe shadows become important when the probe is situated near a boundary, because there the charged particles are prevented from reaching the back end of the probe. As a result, the plasma there is different than it would be in the absence of the probe. This perturbation is especially serious for probes inserted into a sheath, since ions enter with a directed Bohm velocity which can produce more well defined shadows, [Hershkowitz, 1989]. In our experimental set-up probe shadowing is not a serious concern since the entire physical area of the probe is exposed to the local plasma.

Another perturbation by probes is due to the desorption of gases onto the probe and its insulator, in pulsed plasmas This may result in a relatively large concentration of impurities in the surrounding plasma. The larger the probe is, the more gas desorption to its surface; however, if the probes are made too small they will melt, thereby depositing more impurities into the system. However, this is not critical since once the probe has melted it does not contribute useful data.

When the probe support structure is fabricated out of insulators, they may drain ions trapped in potential wells in the surrounding plasma. This can lead to potential disturbances in the plasma, related to the presence of the probe[Hershkowitz, 1986]. The support structure for the fourteen electrostatic micro-probes i.e., the Al_2O_3 tubing, is embedded in the anode, with minimal exposure to the plasma. Therefore, any such potential disturbances were minimized.

Secondary electron emission associated with ion bombardment of the probe is not believed to be a problem. This is because the incoming energy of the ion and/or electron particles collected by the probe is sufficiently low (at most 20 eV in a collisionless sheath) so that secondary emission due to these particles bombarding the probe surface is negligible.

3.5.2 Effects of Probe Measurements in Sheaths

The objective of this work is to obtain plasma property measurements at various axial and azimuthal locations inside the anode boundary layer, by implementing electrostatic micro-probes. This requires positioning the probes inside the anode sheath. However, problems may arise due to probe perturbation effects in the sheath, [Hershkowitz, 1989]. A probe that is biased positive can "short out" the sheath, consequently collecting electron current far in excess of that actually present if the probe were absent. Coakley, *et al.* [1979], have studied the interaction of probes with sheaths. They conducted an experiment where a 2 cm diameter probe, biased at zero volts, was placed in a sheath, near a plasma boundary that was biased at -50 V. When the equipotential contours were measured with an emissive probe, it appeared as if the probe had "sucked in" or "shorted out" the contours.

In plasmas with high neutral pressures ($\geq$ 100 mTorr) ionization mean free paths can become comparable to the probe dimensions; therefore ionization near the probe may be significant. Enhanced ionization is obtained when the probe is biased at $\phi_{pl} + \varepsilon_i$, where ϕ_{pl} is the plasma potential and ε_i is the ionization potential, [Hershkowitz, 1989]. If the mean free paths are short, compared to the Debye length or sheath thickness, then this disturbance does not extend far beyond the probe. A consequence of this local sheath ionization is an increase in electron current collection and is apparent as an additional glow discharge near the probe.

An example of enhanced sheath ionization effects on a probe V-I characteristic is shown in Fig. 3.21. The second "knee" in the characteristic, at V_I, corresponds to $\phi_{pl} + \varepsilon_I$. This enhanced ionization is due to the probe biasing at $\phi_{pl} + \varepsilon_I$ and is a perturbation to the surrounding plasma. Therefore, it is recommended that the probe not be biased at this potential. As shown in Fig. 3.21 the current at zero volts I_a, is near the region where the probe current increases dramatically beyond the electron saturation current. Also from Fig. 3.21, ϕ_{pl} ~-14 V, V_I ~ 5 V so that ε_i~19 V ± 2 V, which is close to the ionization potential of H_2 (15.4 eV) and N_2 (15.6 eV).

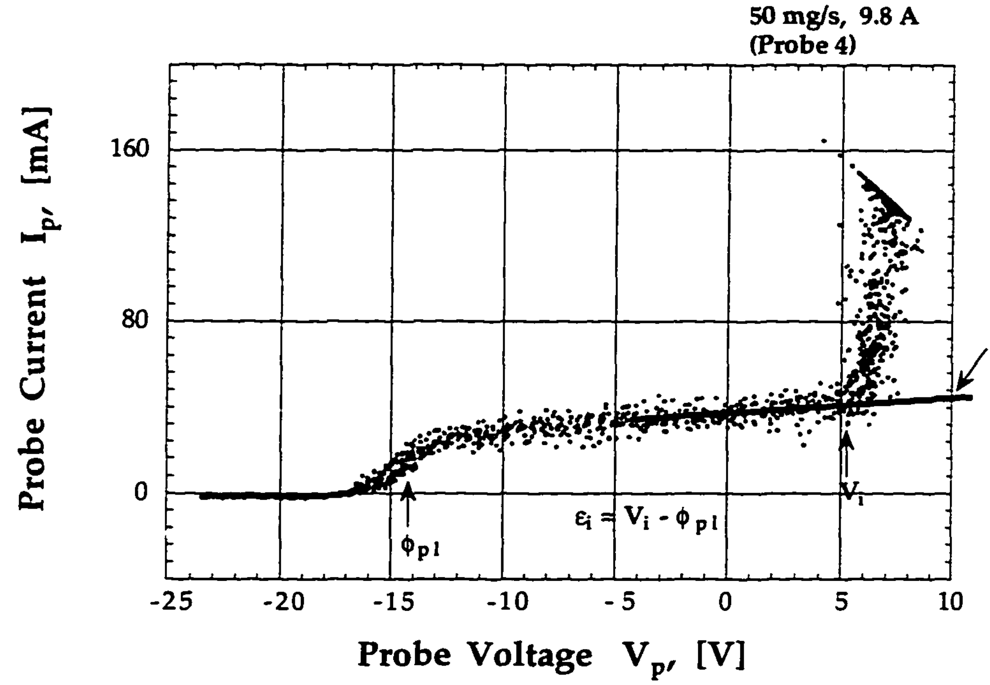

Fig. 3.21 Probe 4 V-I characteristic showing the second knee in the curve due to enhanced ionization effects. This increase in probe current can be a problem when interpreting I_a data from the V-I curve that fall within this second knee. In this case the electron-saturation region is extrapolated and independent measurements from a multimeter are also used to verify the I_a data.

For some V-I characteristics, (particularly probes 2 and 3), depending on the arcjet operating conditions, the I_a data may be located within this second knee. Independent I_a measurements with a multimeter have verified that the I_a data can be extrapolated from the electron saturation region as shown in Fig. 3.21. An example of this problem occurred for the conditions of $\dot{m} = 60$ mg/s, 9.9 A, when the V-I curve for probe 3 had a second knee at 0 V. According to the characteristic I_a varied from ~30 mA to as high as 120 mA. However, independent multimeter readings showed that I_a varied from 40-79 mA, for an average value of 60 mA.

3.6 Data Analysis

The practical implementation of Langmuir probes for internal arcjet boundary layer diagnostics: (1) requires careful consideration of how the probes are cleaned, Sec. 2.4; (2) understanding the regime in which they operate so as is to avoid perturbation of the surrounding plasma thus complicating the analysis, Sec. 3.2.3; and (3) an understanding of collisional affects on the interpretation of the probe V-I characteristics, Sec. 3.4.

However careful interpretation of the data also requires a thorough analysis of the sources of error. In the following sections the error analysis for each of the main experimental data is assessed as well as an overview of the data reduction procedure.

3.6.1 Error Analysis

The main data obtained in this experimental work is the floating potential ϕ_f, the anode sheath potential ϕ_s, the anode current density j_a, the electron temperature T_{es}, the electron number density, n_{es} and the anode heating, q_e. All possible steps were taken to ensure the data was reliable and repeatable, e.g. adequate cleaning of the probes during operation. However, there were uncertainties associated with each of the data, some more difficult to ascertain than others, such as determining the effective probe collection area in calculating the anode current density, j_a. The uncertainties associated with each of the data are now assessed.

A calculated result can be described as: $R = R(x_1, x_2, x_3, ..., x_n)$, where R is the result and the x_n represent the primary measurements, e.g. ϕ_f, ϕ_s, etc. If the uncertainties in the independent variables are all given the same odds, then the uncertainty in the result having these odds is, [Kline, *et al.*, 1953]:

$$u_R = \left[\left(\frac{\partial R}{\partial x_1} u_1\right)^2 + \left(\frac{\partial R}{\partial x_2} u_2\right)^2 + ... + \left(\frac{\partial R}{\partial x_N} u_N\right)^2\right]^{1/2} \tag{3.54}$$

where u_R represents the uncertainty in the result, R, and the u_N represent the uncertainties in the independent variables.

Floating Potential Measurement Uncertainty

The floating potential data is the most straightforward measurement to make; the probe is disconnected from the circuit and the voltage it attains is measured with the 10 MHz SOLTEC oscilloscope. The uncertainty in the ϕ_f data is thus related to the resolution of the oscilloscope given as:

$$u_{SOLTEC} = \text{SOLTEC Resolution} = \frac{\text{Channel Voltage Setting (V)}}{2^8 \text{ bits}} \tag{3.55}$$

The channel setting for the ϕ_f measurements is typically 30 V, so that the oscilloscope resolution is 0.12, i.e. a 12% uncertainty in the floating potential data. This represents a maximum range of ~2 volts, so that the uncertainty in this measurement is ± 1 V. This is consistent with deriving ϕ_f from the V-I characteristic, which was found to be within 1-3 V of the SOLTEC measurement.

Sheath Potential Measurement Uncertainty

Deriving the sheath potential depends on the plasma potential which is obtained by: (1) extrapolating the electron-retarding region and electron saturation regions of the probe characteristic to the "knee" in the V-I curve; or

(2) taking the first derivative of the electron current and finding the voltage at peak current, i.e. voltage at which $\frac{dI_e}{dV_p} = 0$.

Taking the derivative of experimental data introduces noise, so the method of choice for obtaining ϕ_{pl} and thus ϕ_s is by identifying the "knee" in the characteristic. Though this method relies on accurate extrapolation of the electron-retarding and electron-saturation regions of the V-I curve, this procedure was found to be straightforward due to the relative "cleanliness" of the probe characteristic. The uncertainty in measuring the plasma potential and thus ϕ_s was found to be ± 1 V.

Current Density Measurement Uncertainty

The accuracy of the current density data depends on the accuracy of the probe current data I_a and the calculation of the effective probe collection area A_{eff}, as described in Secs. 2.3.3 and 3.2.2.

The accuracy of measuring I_a depends on the data scatter in the probe V-I characteristic. At all probe locations, $\phi_{pl} << 0$, Fig. 3.6 so that I_a is located in the electron saturation region, which normally exhibits the most data scatter due to the electron current noise, a result of the electron's high thermal energy. This data scatter depends on probe location. For example, closest to the constrictor exit (within 1-4 mm) where most of the current density exists, there is more scatter in I_a for probes 1-4, than for data from probes further downstream, probes 5-10'.

To calculate I_a, several points are recorded at 0 V ± 0.1 V and an average value for I_a is obtained. The relative uncertainty in deriving I_a from the characteristic is represented as:

$$u_{I_a} = \frac{\frac{1}{2}\left[(I_a)_{upper} - (I_a)_{lower}\right]}{\frac{1}{n}\sum_n (I_a)_n} \qquad (3.56)$$

where n is the total number of data points obtained for I_a and $(I_a)_{upper}$ and $(I_a)_{lower}$ refer to the maximum and minimum values of I_a obtained from the characteristic, respectively. Equation (3.56) only represents the uncertainty in deriving the current at zero volts from the probe characteristic. The actual measurement of probe current also depends on the accuracy of the shunt resistor value R_s, the measurement of the voltage drop ΔV_{R_s} across R_s, and the oscilloscope resolution. The probe current is given as:

$$Ip = \frac{\Delta V_{R_s}}{R_s} \qquad (3.57)$$

Using Eq. (3.54), the uncertainty in the probe current measurement is:

$$u_{I_p} = \left[\left(\frac{\partial I_p}{\partial\left(\Delta V_{R_s}\right)} u_{\Delta V_{R_s}}\right)^2 + \left(\frac{\partial I_p}{\partial R_s} u_{R_s}\right)^2\right]^{1/2} \qquad (3.58)$$

Evaluating the terms in parenthesis using Eq. (3.57), results in:

$$u_{I_p} = \left[\left(\frac{1}{R_s} u_{\Delta V_{R_s}}\right)^2 + \left(\frac{-\Delta V_{R_s}}{R_s^2} u_{R_s}\right)^2\right]^{1/2} \qquad (3.59)$$

The total uncertainty for the probe current measurement $u_T(I_a)$, must also include the uncertainty in the oscilloscope measurement u_{SOLTEC}, and the uncertainty in the derivation of I_a from the probe V-I characteristic u_{Ia}:

$$u_T(I_a) = \left[\left(\frac{1}{R_s} u_{\Delta V_{R_s}}\right)^2 + \left(\frac{-\Delta V_{R_s}}{R_s^2} u_{R_s}\right)^2 + (u_{SOLTEC})^2 + \left(u_{I_p}\right)^2\right]^{1/2} \qquad (3.60)$$

The value for R_s is 103.7 Ω ± 2% as measured with a multimeter, a typical value for ΔV_{R_s} is ~ 8 V and $u_{\Delta V_{R_s}} = u_{R_s} = 2\%$. Evaluation of the terms in Eq. (3.60) show that the dominant term is u_{I_a} with ~15-25% uncertainty, whereas the first three terms contribute about 10% uncertainty.

The uncertainty in the probe area is mainly due to the geometric area since the sheath area correction is at most 10%, Sec. 3.2.2. As discussed in Sec. 2.3.3, the post test approximation of probe geometric area is:

$$A_{Post-Test} = \frac{\pi D_p^2}{4} + \varepsilon \pi D_p \left(\bar{L}c + L_{ext} \right) \qquad (3.61)$$

The uncertainty in A_p is:

$$u_{A_p} = \left| \frac{\left(A_p\right) - \left(\bar{A}_p\right)}{\left(\bar{A}_p\right)} \right| \qquad (3.62)$$

where $\bar{A}_p$ is the average geometric probe area between the pre-test value and the post test value. The pre-test and post-test quantities are different *only if* damage has occurred to the probes during the experiment.

Based on the above analysis, the total relative uncertainty in the current density data is given as:

$$u_{j_a} = \sqrt{\left[u_T(I_a)\right]^2 + \left[u_{A_p}\right]^2} \qquad (3.63)$$

Electron Temperature Measurement Uncertainty

The electron temperature is calculated from the slope of the transition region, assuming the electrons exhibit a Maxwellian distribution at the sheath edge and the sheath is thin and collisionless:

$$T_{es} = -\frac{e}{k\left(\frac{d(\ln I_e)}{dV_p}\right)} \qquad (3.64)$$

The main uncertainty in the T_{es} calculation is in calculating the slope, $d(\ln I_e)/dV_p$, by evaluating the ion current at all potentials up to ϕ_{pl} and then subtracting this from the total current to obtain I_e. A semilog plot of I_e versus V_p is made and an exponential fit to the transition region provides the slope. The slope is derived twice from different portions of the electron-retarding region so that the uncertainty in the slope is:

$$u_{slope} = \frac{\frac{1}{2}\left[\left(\frac{d(\ln I_e)}{dV_p}\right)_1 - \left(\frac{d(\ln I_e)}{dV_p}\right)_2\right]}{\left(\frac{d(\ln I_e)}{dV_p}\right)_{AVG}} \tag{3.65}$$

where the subscripts (1) and (2) refer to the two separate slope calculations.

The total relative error in the T_{es} measurement also includes the uncertainty in the probe current data, $u_T(I_a)$, given by the first three terms in Eq. (3.60):

$$u_{T_{es}} = \left[\left(u_{slope}\right)^2 + \left(u_T(I_a)\right)^2\right]^{1/2} \tag{3.66}$$

<u>Electron Number Density Measurement Uncertainty</u>

The electron number density is given as:

$$n_{es} = \left(4.02 \times 10^{15}\right)\frac{I_{e-sat}}{A_p}\sqrt{\frac{1}{T_{es}(^\circ K)}} \tag{3.67}$$

The main error in the electron number density measurement is due to the electron-saturation current and probe geometric area measurements. The electron saturation current is calculated twice, based on the variation of the slope and ϕ_{pl}. Therefore, the uncertainty in I_{e-sat} is:

$$u_{I_{e-sat}} = \frac{\frac{1}{2}\left[\left(I_{e-sat}\right)_1 - \left(I_{e-sat}\right)_2\right]}{\left(I_{e-sat}\right)_{AVG}} \tag{3.68}$$

The total uncertainty in n_{es} is:

$$u_{n_{es}} = \left[\left(u_{I_{e\text{-sat}}}\right)^2 + \left(u_{A_p}\right)^2 + \left(u_{\text{slope}}\right)^2\right]^{1/2} \tag{3.69}$$

3.6.2 Overview of Data Reduction Procedure

Figure 3.22 below shows a flowchart diagram summarizing the data reduction procedure used in this work.

The first step is to plot the probe V-I curve and derive the relevant information from the characteristic, as described in Sec. 3.3. A theoretical fit to the ion current is particularly important since this is required to calculate I_e, from which T_{es} is then derived using the slope method, i.e. Eq. (3.32). In this investigation, because the ion sheath was collisional, the ion saturation current was constant so that a theoretical fit to the ion saturation region was not required, as described in Secs. 3.3.4 and 3.4.2.

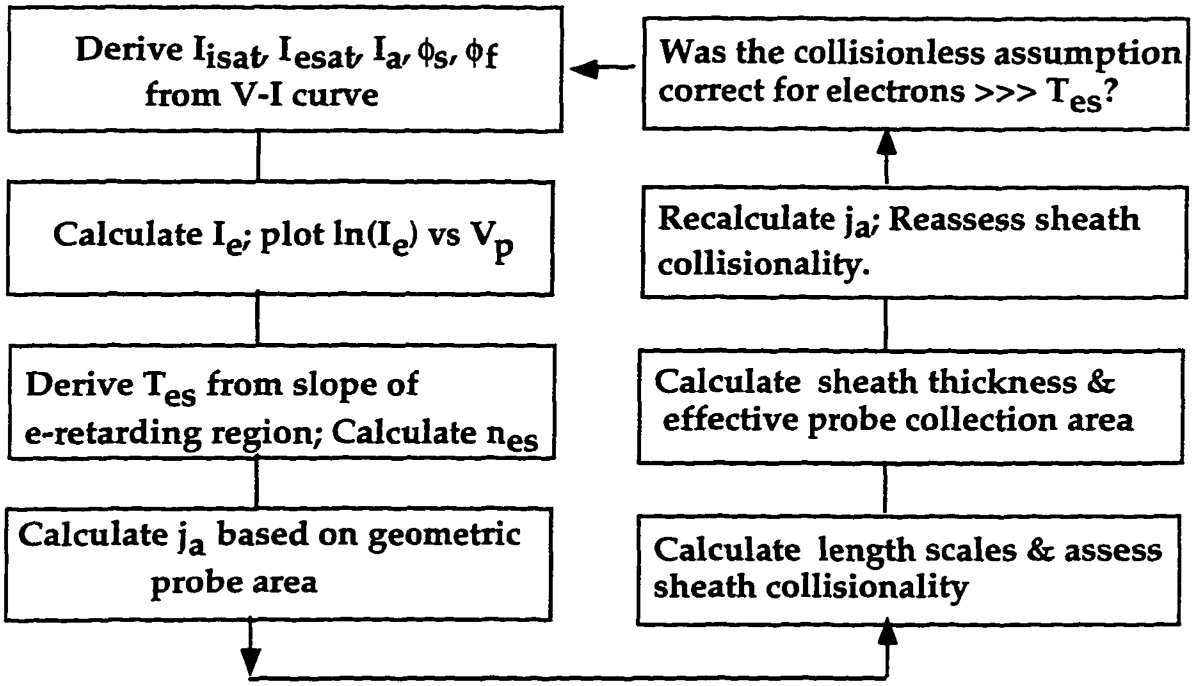

Fig. 3.22 Shown above is a flowchart summarizing the key procedures in obtaining plasma properties from the probe V-I characteristic.

An alternate method for calculating T_{es} based on the ϕ_f and ϕ_s data is later shown in Sec. 4.2.5, with further description in Sec. 7.3.6. It should be noted that initially, the electron sheath is ***assumed*** to be collisionless and T_{es} is found based on this assumption. After the electron number density is calculated (Sec. 3.3) the mean free paths are evaluated at each probe location based on the experimental data for n_{es}, T_{es} and j_a and the MKB model. The electron and ion sheath thickness for both collisional and collisionless cases must also be evaluated, Sec. 3.2.2. The sheath collisionality is reassessed to verify the collisionless sheath assumption. If the sheath is collisional for electron collection, a closed-form analytical expression for T_{es} does not exist. In this case an anode sheath model may have to be formulated; the collisionless approach would provide an upper limit to T_{es}.

The length scales are also required for evaluating sheath collisionality, Sec. 3.2. The sheath thickness is calculated as described in Sec. 3.2.2 and used for assessing the effective probe collection area, required for determining j_a.

The flowchart in Fig. 3.22 summarizes the data analysis, which is initially iterative, but converges quickly once the sheath collisionality is determined.

4. FLUSH-MOUNTED PLANAR PROBE RESULTS

4.1 Experimental Operating Conditions

The purpose of this research effort was to investigate the anode sheath boundary layer of a 1 kW arcjet in order to: (1) obtain a better understanding of arc attachment in low power arcjet thrusters; (2) obtain an understanding of anode heating; (3) verify azimuthal current symmetry; and (4) provide appropriate plasma property data for calibration of the Megli-Krier-Burton (MKB) numerical arcjet model [Megli, *et al.*, 1996], Chapter 7. The plasma property data that were experimentally obtained included: floating potential ϕ_f, anode sheath potential ϕ_s, current density at anode potential j_a, electron temperature at the plasma/pre-sheath edge T_{es}, and electron number density at the plasma/pre-sheath edge, n_{es}. From these, primary plasma properties were also calculated (Section 4.6): scalar electrical conductivity σ, ohmic heating O_h, sheath electric field E_{sh} and the resistive electric field E_{pl}. From the j_a, T_{es} and ϕ_s data the anode heating distribution $q_e(x)$ was calculated for various arcjet operating conditions, Chapter 6.

The above goals were met by probing the anode sheath boundary layer with an array of fourteen electrostatic micro-probes embedded inside the anode at 10 different axial locations and 4 different azimuthal locations. Axial and azimuthal distributions of ϕ_f, ϕ_s, j_a, T_{es}, n_{es} were measured under the following experimental conditions: (1) propellant flow rates of 40, 45, 50 and 60 mg/sec; (2) arc currents of $7.8 \leq I_{arc} \leq 10.6$ A; and (3) various radial positions of the probe, e.g., $L_{ext} = 0$ mm, i.e. flush probes, and L_{ext} approximately 0.1-.15 mm for probes 1,1′ and 0.25-.3 mm for probes 2-10′, i.e. cylindrical probes. Varying the probe extension L_{ext}, allowed plasma properties to be obtained in the near-anode region. The various thruster operating conditions are outlined in Table 4.1. All data is presented for steady state arcjet operating conditions.

In this chapter data is presented for the flush-probe configuration only, with a summary of the cylindrical probe results in Chapter 5.

Table 4.1 Summary of the steady state arcjet thruster operating conditions using the flush probe configuration. The operator specifies I_{arc} and flow rate, while the remaining parameters are either measured or derived.

Operating Condition	$\dot{m}$ (mg/sec)	Avg. I_{arc} (Amps)	Avg. V_{arc} (Volts)	Power (Watts)	$P/\dot{m}$ (MJ/kg)	T_{noz} (°K)
a	40	10.6	104	1102	27.4	945
b	45	9.8	109	1068	23.6	935
c	50	7.8	121	944	18.8	870
d	50	8.9	115	1023	20.6	900
e	50	9.8	112	1098	22.0	910
f	60	9.9	121	1198	20.0	895

4.2 Potential Measurements

The most straightforward measurement is the floating potential ϕ_f, a direct measurement with no detailed data reduction process required. The probes are disconnected from the biasing circuit and ϕ_f is measured with the SOLTEC data acquisition system. The probes are sequentially turned on-off, providing an axial and azimuthal distribution of ϕ_f. A sample "raw" output of ϕ_f is shown in Fig. 4.1, displaying the sequential switching of the probes.

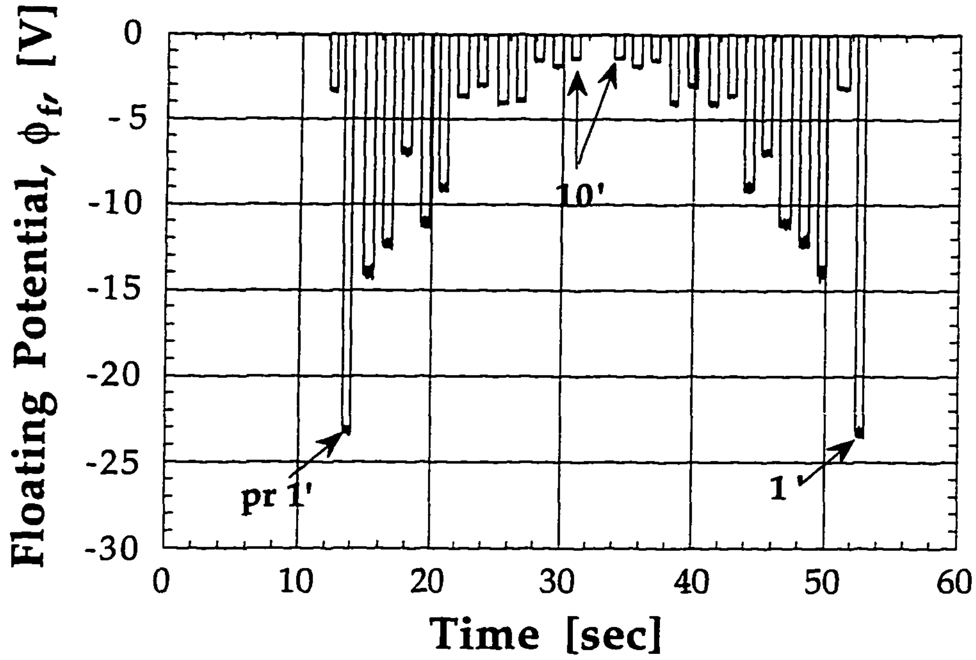

Fig. 4.1 A typical output of floating potential data for each of the fourteen probes. The data acquisition is repeated to check for hysteresis.

Obtaining the anode sheath potential ϕ_s is not a direct measurement, instead requiring analysis of the probe V-I characteristic. As discussed in Sec. 3.1.2, the sheath potential is the negative of the plasma potential ϕ_{pl} where ϕ_{pl} is derived by extrapolating the electron-retarding and the electron saturation regions of the probe V-I characteristic, Fig. 3.18, Chapter 3.

Floating and sheath potential data obtained using the flush-mounted probes are discussed below. Results are presented for various propellant flow rates $\dot{m}$, arcjet operating currents I_{arc}, and specific energies $P/\dot{m}$.

4.2.1 Significance of Floating & Sheath Potential Data

The first step in the experimental procedure was to obtain the floating potential of each probe, since it was readily measurable and because it provided a convenient check as to whether the probes were operating properly, i.e. no "shorts" to ground. The floating potential is expected to be largest in regions of high current density j_a and smallest in regions of low j_a. This is because a large potential is required to maintain $j_a = 0$ for a floating probe, in a region of high electron density and electron temperature. Assuming, for purposes of clarity, that the plasma potential ~ 0, then the floating potential is given as [Chen, 1965]:

$$\phi_f = \frac{kT_{es}}{e}\left\{\ln(0.61) + \ln\left[\sqrt{\frac{2\pi m_e}{M_i}}\right]\right\} \tag{4.1}$$

where M_i is the reduced ion mass defined in Sec. 3.1.1; recall that the term ln(0.61) was discussed in Sec. 3.1.2. Equation (4.1) shows that the floating potential is directly proportional to the electron temperature at the sheath edge, T_{es}. The ϕ_f measurement can therefore provide an approximate estimate of the electron temperature (Sec. 4.2.5), and the distribution of ϕ_f in the nozzle qualitatively denotes the regions of high j_a and n_{es}.

At locations 1, 4, 7, and 10 mm downstream of the constrictor exit a pair of probes exist, separated by 180°. The floating potential data from each pair may infer the existence of azimuthal current symmetry in the nozzle. The final statement on this condition is determined directly from the j_a data, but the ϕ_f data provides a convenient consistency check on this result.

Figures 4.2-4.3 present a typical floating potential distribution along the anode wall and in the anode sheath layer, approximately 0.25-0.3 mm away from the anode. Notice the ϕ_f symmetry for the 0° and 180° probes; these results imply azimuthal current symmetry; though the results for the cylindrical probes at x = 1 mm are somewhat asymmetric for the experimental conditions of Fig. 4.3. It was observed that regardless of the arcjet operating conditions, the floating potential data for the 120° and 240° probes lie on the same curve as the 0° and 180° probes, Figs. 4.2-4.3.

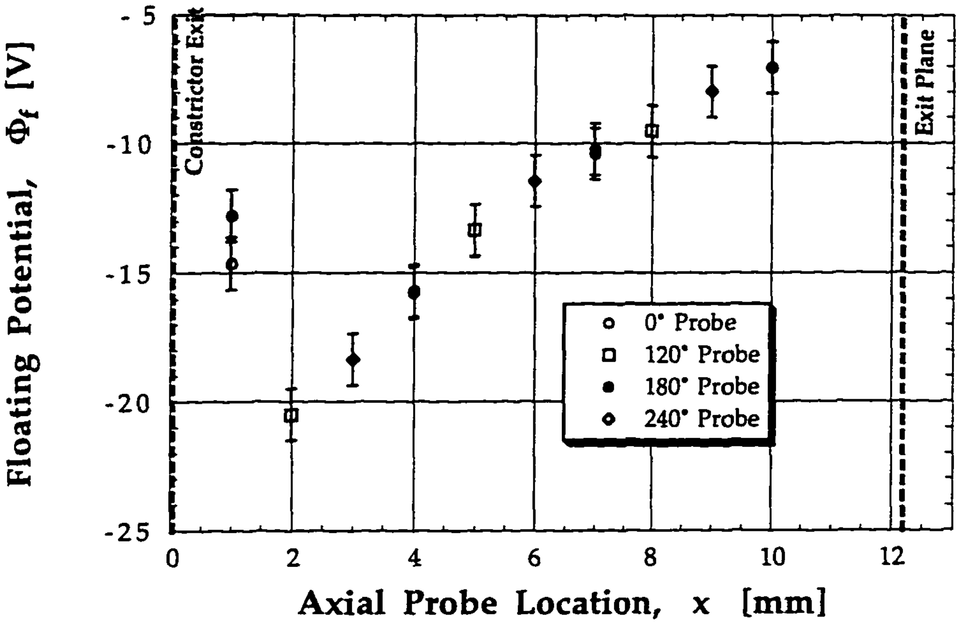

Fig. 4.2 Floating potential data for $\dot{m}$= 50 mg/sec 9.8 A and 112 V are presented at all probe locations for the flush-probe configuration.

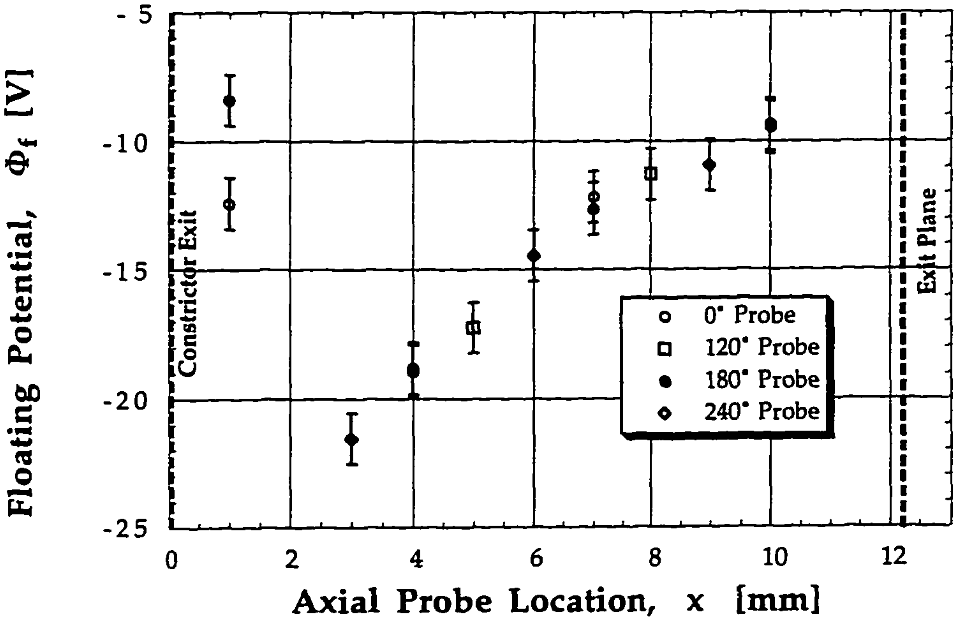

Fig. 4.3 Floating potential data for $\dot{m}$= 50 mg/sec 9.9 A and 114 V are presented at all probe locations for the cylindrical probe configuration.

The sheath potential measurement, when combined with the floating potential data provides an estimate of the electron temperature as follows, [Chen, 1965]:

$$\phi_s = -\phi_f + \frac{kT_{es}}{e}\left\{\ln(0.61) + \ln\left[\sqrt{\frac{2\pi m_e}{M_i}}\right]\right\} \tag{4.2}$$

Equation (4.2) is similar to Eq. (4.1) for a nonzero plasma potential; Eq. (4.2) is derived based on the assumption of a collisionless pre-sheath. For a collisional pre-sheath the current at the sheath edge u_s is decreased by the factor α_c, compared with the Bohm velocity u_B, [Godyak, *et al.*, 1990]:

$$\alpha_c \equiv \left[1 + \frac{\pi\lambda_D}{2\lambda_i}\right]^{-1/2} \approx \frac{u_s}{u_B} \tag{4.3}$$

where λ_i is the ion mean free path, $\lambda_{H^+-H_2}$. Equation (4.2) then becomes:

$$\phi_s = -\phi_f + \frac{kT_{es}}{|e|}\left\{\ln(\alpha_c) + \ln\left[(0.61)\sqrt{\frac{2\pi m_e}{M_i}}\right]\right\} \tag{4.4}$$

With the anode sheath potential distribution known the electrical characteristics of the anode boundary layer, e.g. electron attracting versus electron repelling sheaths, are identified. This sheath potential is also added to the cathode sheath potential and the voltage drop across the bulk plasma, providing the total arcjet voltage drop in the MKB model, V_{arc} (See discussion in Chapter 7). The sheath characteristics are also related to the location of high j_a and therefore high anode heating. For example, it is shown below that because $\phi_s > 0$, the anode-sheath boundary layer is electron-attracting in character, contributing to higher anode heat loads. This has significant ramifications with regards to the anode heating, Chapter 6.

One of the main contributions to anode heating is the electron power deposition in the anode sheath, which depends on ϕ_s [Oberth, 1970; Tiliakos, *et al.*, 1996]. Knowledge of ϕ_s is also important for understanding arc attachment, since an electron-repelling sheath $\phi_s < 0$, or electron-attracting sheath $\phi_s > 0$, relate to the so called "low intensity" or "high intensity" modes of arc attachment at the anode, [Capelli, *et al.*, 1994]. For $\phi_s > 0$, the applied current is larger than the random thermal electron current. In order to satisfy global current conservation, electrons are allowed to escape the bulk plasma and proceed more readily the anode. To achieve this condition the anode sheath characteristics adjust to attract electrons. In this investigation for $\phi_s > 0$, $j_a > j_{th,e}$ at all probe locations, where $j_{th,e}$ is the electron random thermal current density. Further away from the constrictor, in regions of low current density, it is possible that $j_a < j_{th,e}$ and ϕ_s adjusts to repel electrons, i.e. $\phi_s < 0$, confining electrons predominantly in the bulk plasma. Previous experiments [Tiliakos, *et al.*, 1996] with a tungsten alloy nozzle, HD-18, [Mi-Tech Metals, Inc.] have shown that both an electron-attracting and electron-repelling anode sheath can exist in a low power arcjet.

For a collisionless, electron-attracting thin sheath, the anode heating due to electrons is given by [Oberth, 1970]:

$$q_e = j_a\left(\frac{5kT_{es}}{2e} + \phi_s + W\right) \tag{4.5}$$

where ablation, thermionic emission, Joule heating of the anode, convection, and radiation from the plasma are neglected. In Eq. (4.5) W is the work function of the 2% thoriated tungsten anode. The work function varies from 2.8 eV for 2% thoriated tungsten and 4.5 eV for pure tungsten [Goodfellow *et al.*, 1995], so that an average value of 3.7 eV is selected for partially depleted thorium. Therefore, knowing the electron temperature and sheath potential distributions along the anode, Eq. (4.5) provides anode heating distribution. This equation and the results derived from it based on the experimental data are discussed further in Chapter 6.

Also, like the floating potential measurements, the sheath potential data provides a convenient consistency check on the current density distribution. For example, in regions of high anode current density, one expects to find a relatively high positive anode sheath potential.

4.2.2 Effect of Flow Rate on Floating & Sheath Potential

In order to study the effect of the propellant flow rate on the floating and sheath potential distributions, experiments were conducted using flush-mounted planar probes and cylindrical probes. In most cases during this parameter study the arcjet operating current was fixed at approximately 10 A.

For the flush probe configuration the propellant flow rate was varied from 40 mg/sec to 60 mg/s (see Table 4.1). Figures 4.4-4.6 display typical ϕ_f data for various $N_2 + 2H_2$ flow rates, at a fixed arc current of 9.8 A and 10.6 A. In Fig. 4.4, only probes 1, 1′ show an asymmetry in ϕ_f. The results for probes 1, 1′ should be interpreted with care, because of their proximity to the sonic point and high heat load region in the nozzle.

For the nominal arcjet operating conditions of 50 mg/s, 9.8 A (Fig. 4.5) excellent agreement exists for ϕ_f between the 0° and 180° probes, implying azimuthal symmetry. Notice that for $\dot{m}$ = 40 mg/s there is some asymmetry at x = 1 mm only; this flow rate is the *lower* limit of operation for this arcjet design, [Curran, *et al.*, 1992]. Results for the above conditions are shown simultaneously in Fig. 4.6. As the propellant flow rate increases, i.e. $P/\dot{m}$ decreases for fixed I_{arc}, the floating potential becomes more negative. The ϕ_f results imply azimuthal symmetry at all conditions except at $\dot{m}$ = 40 and 45 mg/s at probes 1,1′ only. Also, regardless of flow rate, the ϕ_f distribution exhibits the same trends, and the ϕ_f data for the 120° and 240° probes lie on the same curve as the ϕ_f data for the 0° and 180° probes.

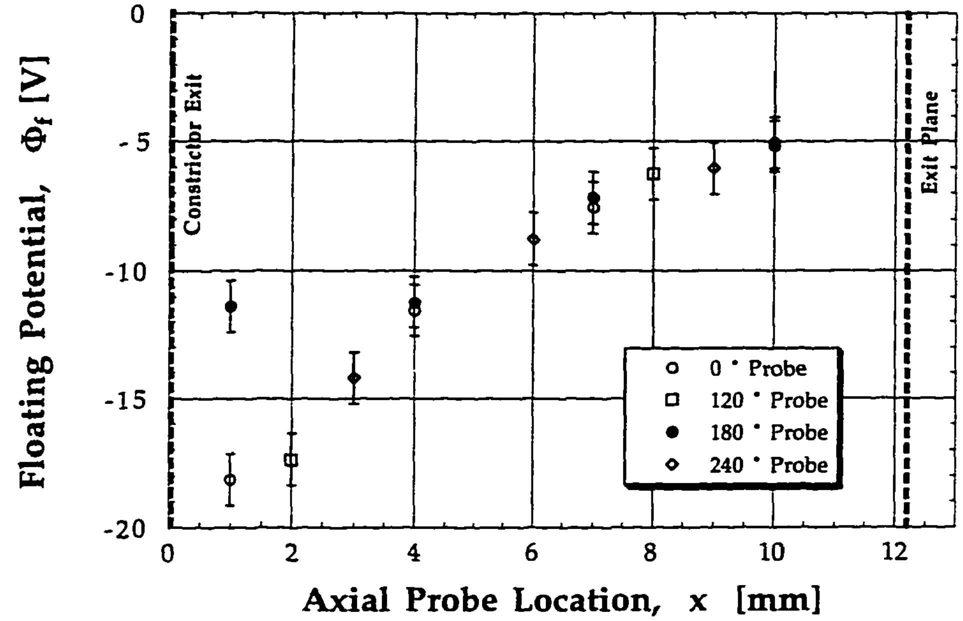

Fig. 4.4 Floating potential data for $\dot{m}$ = 40 mg/sec (lower limit), I_{arc} = 10.6 A (upper limit) and V_{arc} = 104 V.

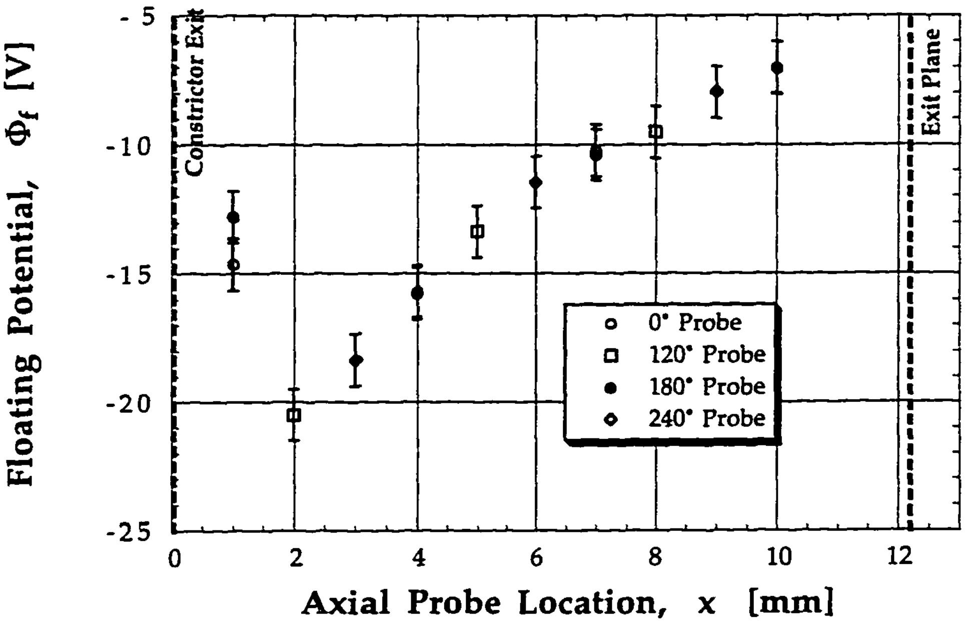

Fig. 4.5 Floating potential data for the nominal conditions of $\dot{m}$ = 50 mg/sec, I_{arc} = 9.8 A and V_{arc} = 112 V.

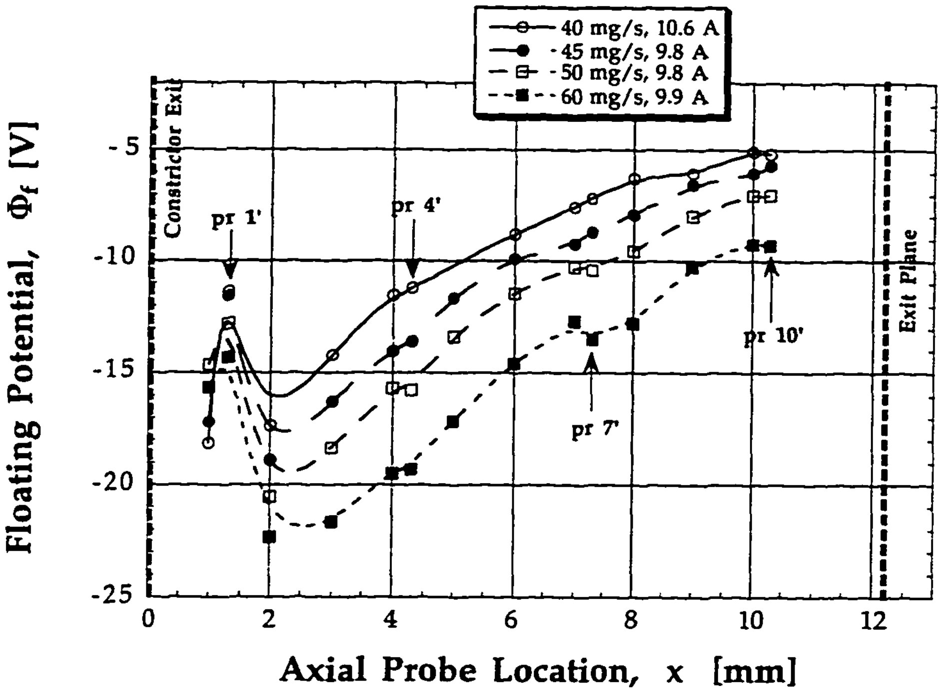

Fig. 4.6 Floating potential data at all probe locations for $\dot{m}$ = 45, 50 and 60 mg/sec and I_{arc} = 9.9 A, and $\dot{m}$ = 40 mg/sec, I_{arc}=10.6 A, V_{arc}=104 V. Note that the error on the floating potential is ± 1 V; the error bars were omitted for clarity.

At all flow rates studied there is an absolute maximum in floating potential at x = 2 mm; for x > 2 mm, ϕ_f becomes monotonically less negative. This result follows from the fact that closest to the constrictor exit, in a region of high current density, the electron temperature is higher so that a larger potential is required to maintain $j_p = 0$ for a floating probe. Likewise, as the plasma flow expands through the nozzle, the electron temperature decreases, so that a smaller ϕ_f is required to maintain $j_p = 0$ for a floating probe.

The results for the sheath potential distribution are shown in Fig. 4.7. As the propellant flow rate is increased, the sheath potential increases at all probe locations. As the $N_2 + 2H_2$ flow rate increases from 40 mg/sec to 60 mg/sec, the maximum in the ϕ_s axial profile distribution $(\phi_s)_{max}$, shifts from probe 2 to probe 3. It is later shown that this shift in ϕ_s corresponds to a similar shift in the maximum current density $(j_a)_{max}$ and maximum anode heating, $(q_e)_{max}$.

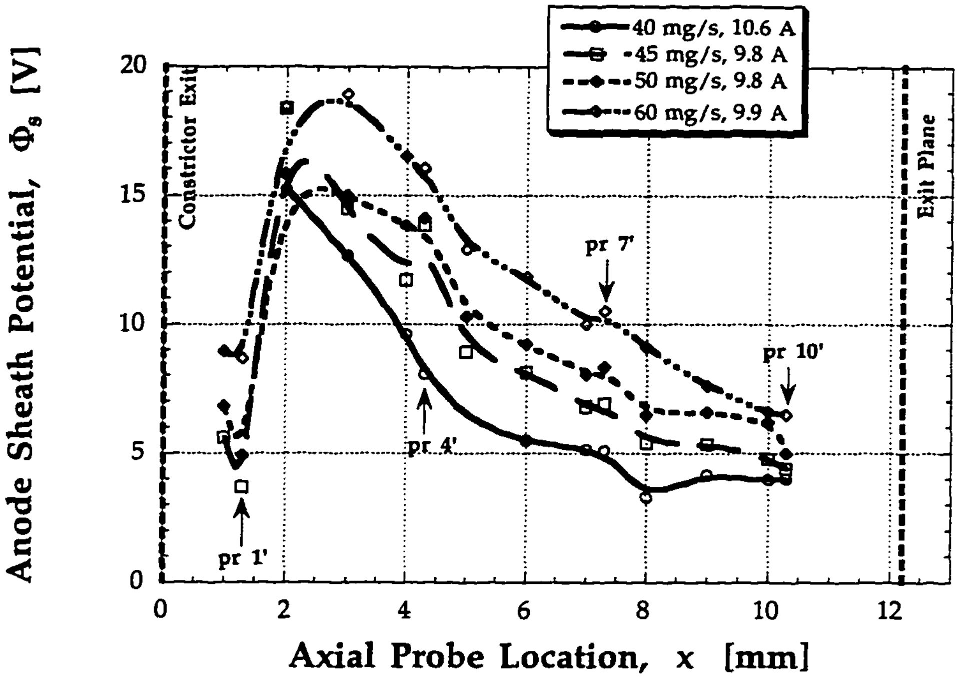

Fig. 4.7 Sheath potential data for $\dot{m}$ = 45, 50 and 60 mg/sec and I_{arc}=9.9 A, and $\dot{m}$ = 40 mg/sec , I_{arc}= 10.6 A. In all cases the sheath is electron attracting since $\phi_s > 0$. Note that the error on the sheath potential is ± 1 V; the error bars were omitted for clarity. Data for probes 1,1' (40 mg/s, 10.6 A) were not available.

For flow rates of $40 \leq \dot{m} \leq 50$ mg/sec an absolute maximum exists in the sheath potential data, occuring at about x = 2 mm, similar to the ϕ_f data. In all cases, the sheath potential decreases monotonically for $x \geq 2$ mm, similar to the ϕ_f data. Throughout the anode boundary layer $\phi_s > 0$, so that the anode sheath is electron-attracting. It is later shown (Sec. 4.3.3) that in regions of high current density ϕ_s is largest, decreasing in magnitude in regions of low current density.

4.2.3 Effect of Arcjet Current on Floating & Sheath Potential

In addition to the $N_2 + 2H_2$ propellant flow rate the arcjet operating current I_{arc}, is the remaining independent variable. As discussed in Sec. 2.1.1, the arcjet operating voltage V_{arc}, is determined by $\dot{m}$ and I_{arc} and is not an independent control variable. The effect of variable I_{arc} on the floating and anode sheath potential was studied for the nominal propellant flow rate of 50 mg/sec.

The ϕ_f and ϕ_s results for the flush probes are shown in Figs. 4.8 - 4.9.

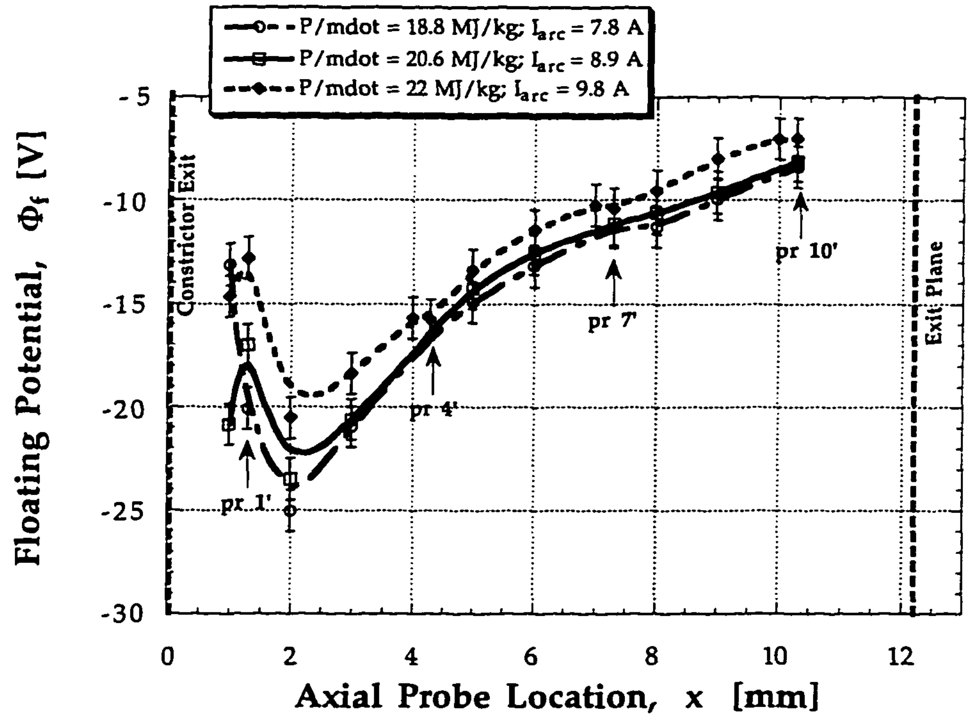

Fig. 4.8 Floating potential measurements for $\dot{m}$=50 mg/s with $7.8 \le I_{arc} \le$ 9.8A.

Figure 4.8 shows the ϕ_f distribution for $\dot{m}$= 50 mg/sec and I_{arc} of 7.8, 8.9 and 9.8 A, i.e. for increasing specific energy, P/$\dot{m}$. For all probes, except probe 1, ϕ_f becomes slightly less negative as the arcjet operating current increases and P/$\dot{m}$ increases. At the location of maximum $|\phi_f|$, x = 2 mm, a 21%

increase in specific energy corresponds to a decrease in $|\phi_f|$ from 24 V to 19 V. Varying the arc current has the largest effect on the ϕ_f distribution within 3 mm of the constrictor. However, the variation of ϕ_f with I_{arc} is within the experimental error of ± 1 V and is therefore considered negligible, except at x = 2 mm, where the variation is ± 2.5 V.

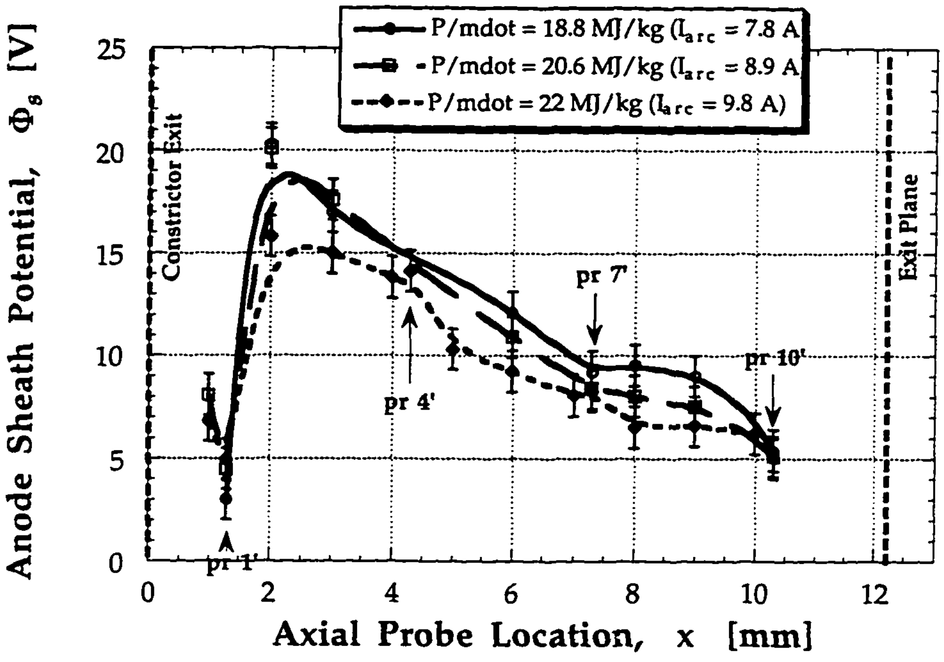

Fig. 4.9 Sheath potential measurements for $\dot{m}$ = 50 mg/s with $7.8 \leq I_{arc} \leq 9.8$A.

Figure 4.9 displays the anode sheath potential distribution for $\dot{m}$ = 50 mg/sec and I_{arc} = 7.8, 8.9, and 9.8 A. For all arc currents tested, ϕ_s has a maximum at x = 2 mm, like ϕ_f and for x > 2 mm ϕ_s decreases as the flow expands through the nozzle. As I_{arc} increases, P/$\dot{m}$ increases and ϕ_s decreases at all probe locations, with a more pronounced affect at x = 2 and 3 mm. A 21% increase in P/$\dot{m}$ results in a decrease in anode sheath potential from 18 V to 15 V. Notice that for all conditions ϕ_s never reverses sign and is always positive, i.e., electron-attracting everywhere.

4.2.4 Effect of Specific Energy on Floating & Sheath Potential

As mentioned in Chapter 1, low power arcjets are playing a major role in satellite stationkeeping. However, the present on orbit duties of low power arcjets may expand to include orbit maneuvering and some repositioning activities. This will require higher I_{sp}, consequently increasing arcjet operation to higher specific energies $P/\dot{m}$, while maintaining or improving thrust efficiency, [Butler, *et al.*, 1996]. Unfortunately, the present technology is limited by the inability of the anode to handle the high heat loads associated with operations at high $P/\dot{m}$, e.g. either higher power input and/or lower mass flow rates, [Butler, *et al.*, 1996].

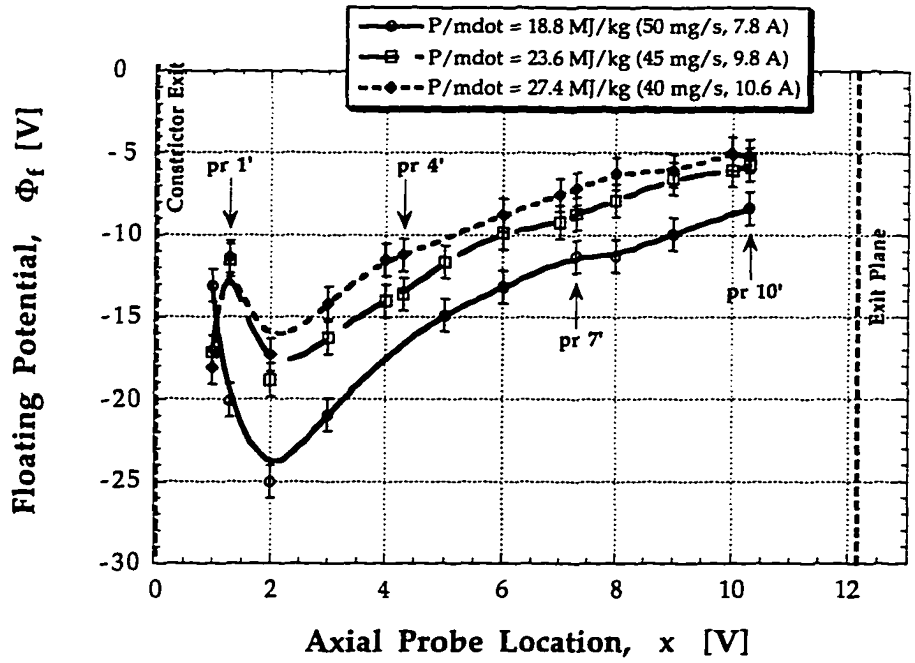

Fig. 4.10 Axial distribution of ϕ_f for various specific energies, 18.8 MJ/kg $\leq P/\dot{m} \leq$ 27.4 MJ/kg.

Since $P/\dot{m}$ is important in assessing arcjet efficiency, this parameter was studied for its effect on the plasma properties and anode heating. Several conditions were tested (Table 4.1, Sec. 4.1) with specific energies in the range of $18.8\ \mathrm{MJ/kg} \le P/\dot{m} \le 27.4\ \mathrm{MJ/kg}$. Results for the flush probes are presented in Figs. 4.10-4.13.

Figure 4.10 shows the effect of $P/\dot{m}$ on the ϕ_f distribution at all probe locations and Fig. 4.11 shows $(\phi_f)_{max}$ as a function of $P/\dot{m}$.

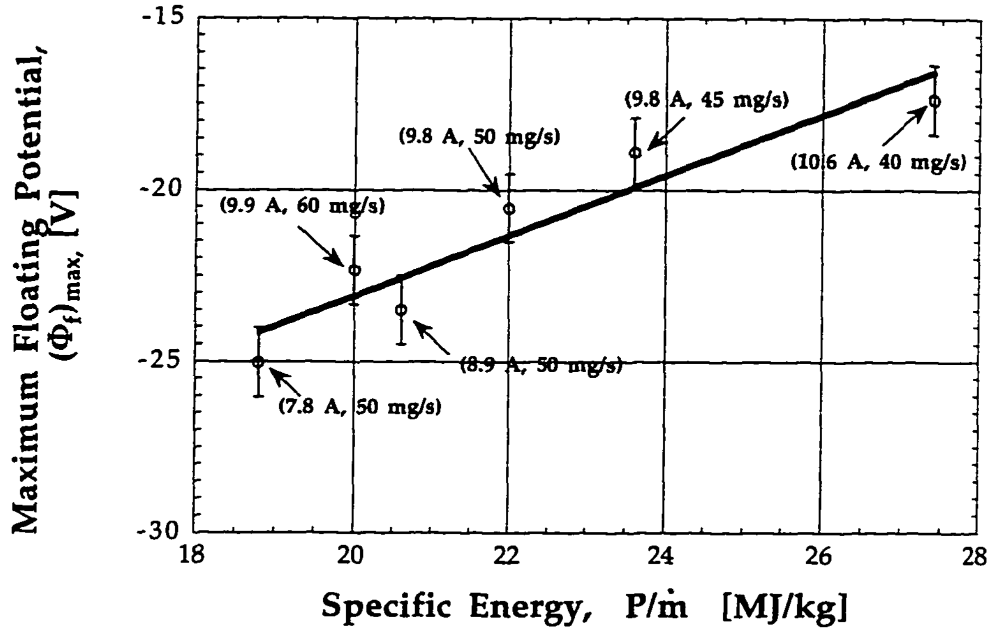

Fig. 4.11 Effect of varying $P/\dot{m}$ on $(\phi_f)_{max}$. The specific energy is varied by either increasing/decreasing the flow rate, arc current or both simultaneously.

For the data in Fig. 4.10, $P/\dot{m}$ was increased by varying both the flow rate and arc current simultaneously. As shown, as $P/\dot{m}$ increases $|\phi_f|$ decreases. The same result was earlier observed when the flow rate was fixed and I_{arc} was increased, Fig. 4.8. However, varying the flow rate has a larger overall effect on the ϕ_f distribution, not just at x = 2 mm where $\phi_f = (\phi_f)_{max}$. The flow rate scales directly with ϕ_f regardless of I_{arc} and increasing $P/\dot{m}$, Fig. 4.11.

In Fig. 4.11, cases (a)-(f) in Table 4.1 are presented. This graph displays three distinct arcjet operational envelopes used to vary P/ṁ: (1) the flow rate was fixed at the nominal value of 50 mg/s and I_{arc} was varied, cases (c)-(e); (2) the arcjet operating current was fixed at the nominal value of 9.8 A and flow rate was varied, cases (b), (e), (f); and (3) I_{arc} was increased to 10.6 A, the maximum current the NASA PPU can supply and the flow rate was simultaneously decreased to 40 mg/s, case (a), the minimum condition for stable arcjet operation, [Curran, *et al.*, 1992].

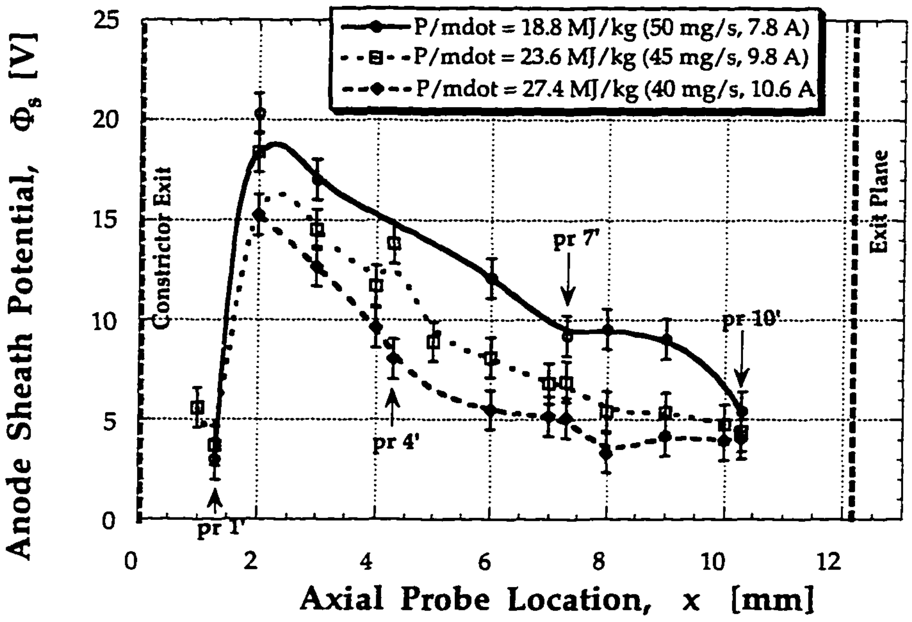

Fig. 4.12 Axial distribution of ϕ_s for various specific energies, 18.8 MJ/kg ≤ P/ṁ ≤ 27.4 MJ/kg.

The results of sheath potential as a function of P/ṁ are shown in Fig. 4.12 and $(\phi_s)_{max}$ as a function of P/ṁ is shown in Fig. 4.13. As P/ṁ increases, ϕ_s decreases; at x = 2 mm, where ϕ_s is maximum, a 31% increase in P/ṁ results in a 25% decrease in ϕ_s. The reason for this trend is similar to that observed for ϕ_f; the overriding variable is propellant flow rate and since ϕ_s

scales directly with $\dot{m}$, ϕ_s decreases as P/ $\dot{m}$ increases. This has ramifications with regards to anode heating, as discussed in Chapter 6. The curvature in ϕ_s for $x > 7$ mm changes character as P/ $\dot{m}$ increases, i.e. as P/ $\dot{m}$ increases the shape of the curve changes from concave (P/ $\dot{m}$ = 18.8 MJ/kg) to convex (27.4 MJ/kg).

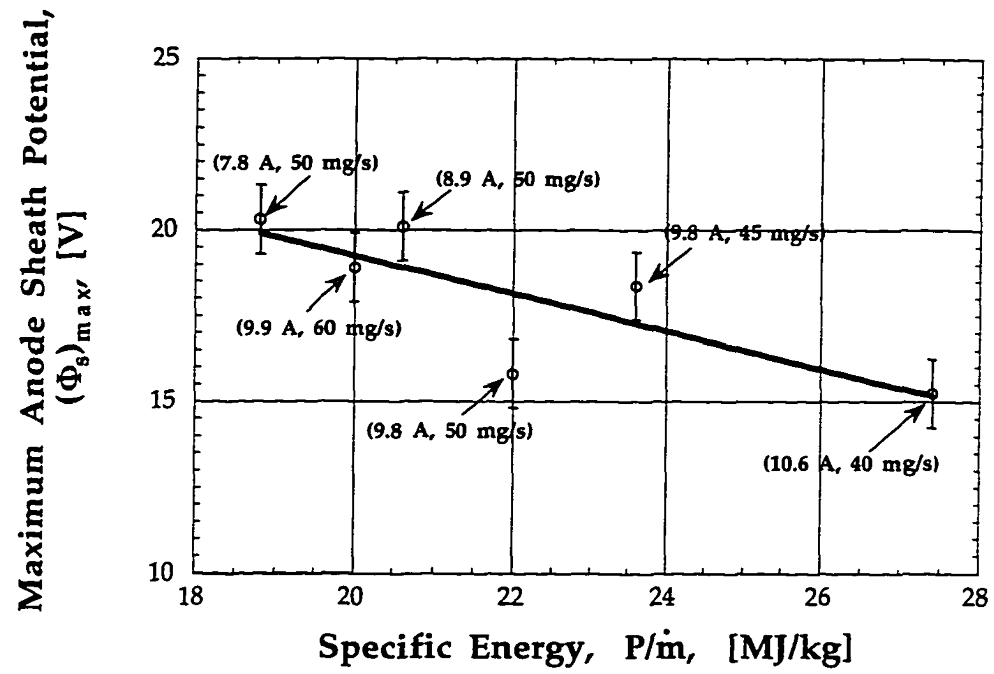

Fig. 4.13 Effect of varying P/ $\dot{m}$ on $(\phi_s)_{max}$. The specific energy is varied by changing only the flow rate, only the arc current or both simultaneously.

Both ϕ_f and ϕ_s behave similarly to variations in P/ $\dot{m}$; for example, at x = 2 mm, a 21% increase in specific energy results in a 24% decrease in ϕ_f and a 22% decrease in ϕ_s.

Figure 4.13 displays the three operational envelopes discussed earlier, for $(\phi_s)_{max}$. Figure 4.13 shows the maximum anode sheath potential $(\phi_s)_{max}$, as a function of specific energy. The flow rate scales directly with ϕ_s therefore as $\dot{m}$

decreases, $P/\dot{m}$ increases and $(\phi_s)_{max}$ decreases regardless of I_{arc}, Fig. 4.13, similar to $(\phi_f)_{max}$, Fig. 4.11.

For both the floating and anode sheath potential results, the hydrazine flow rate has a larger effect on their overall distribution than the arcjet operating current, I_{arc}. However, with respect to $(\phi_f)_{max}$ and $(\phi_s)_{max}$ varying $P/\dot{m}$ produces similar trends; varying $\dot{m}$ has a larger affect on the *location* of $(\phi_s)_{max}$.

4.2.5 Use of Potential Data to Deduce Electron Temperatures

In this experimental work, the plasma potential measurements coupled with the j_a, n_{es} and T_{es} data provide an estimate of the anode heating, q_e. The floating potential can be combined with the anode sheath potential data to provide estimates of the electron temperature at the pre-sheath/plasma edge, T_{es}. Since the floating and sheath potential are readily obtainable data, a relation between ϕ_f and ϕ_s is of interest.

The current density to a probe at potential V_p is:

$$j_p = j_e + j_i \tag{4.6}$$

where j_e is the electron current to the probe given as [Swift, *et al.*, 1969]:

$$j_e = en_{es}\sqrt{\frac{kT_{es}}{2\pi m_e}}\exp\left[\frac{e\left(V_p - \phi_{pl}\right)}{kT_{es}}\right] \tag{4.7}$$

and j_i is given by the Bohm current density for a collisionless pre-sheath [Bohm, *et al.*, 1949]:

$$j_i = j_B = en_{e_{p,s}}u_B \tag{4.8}$$

If a thin collisionless pre-sheath and sheath is assumed, then the pre-sheath potential drop is $-kT_{es}/2e$, [Bohm, *et al.*, 1949], Sec. 3.1.1. Combining this with the Boltzmann relation for electrons, n_{e_B} becomes:

$$n_{e_{p,s}} = n_{es}\exp\left[\frac{e}{kT_{es}}\left(\frac{-kT_{es}}{2e}\right)\right] = (0.61)n_{es} \tag{4.9}$$

Substituting Eq. (4.9) into (4.8) and noting that $u_B = (kT_{es}/M_i)^{1/2}$, j_i becomes [Allen *et al.*, 1957]:

$$j_i = j_B = en_{es}(0.61)\sqrt{\frac{kT_{es}}{M_i}} \tag{4.10}$$

Note that the ion current density depends primarily on the electron temperature when $T_e >> T_i$ and $\lambda_D << 2r_p$. Equating j_e and j_i, since for a floating probe $j_p = 0$, and noting that $\phi_s = -\phi_{pl}$ for a grounded anode and $V_p = \phi_f$, an equation relating ϕ_f, ϕ_s and T_{es} follows:

$$\phi_s = -\phi_f + \frac{kT_{es}}{e}\left\{\ln(0.61) + \ln\left[\sqrt{\frac{2\pi m_e}{M_i}}\right]\right\} \tag{4.11}$$

Equation (4.11) is similar to Eq. (1) of [Oberth, *et al.*, 1972], Eq. (202) in [Chen, 1965] and Eq. (32) of Hershkowitz [1989]. It immediately follows from Eq. (4.11) that given ϕ_f and ϕ_s, T_{es} is calculated as:

$$T_{es} = \frac{|e|(\phi_f + \phi_s)}{k\left\{\ln\left[(0.61)\sqrt{\frac{2\pi m_e}{M_i}}\right]\right\}} \tag{4.12}$$

In Eq. (4.12) M_i is the reduced ion mass, $M_i = \frac{M_{H^+}M_{N^+}}{M_{H^+} + M_{N^+}}$. For singly charged H^+ and N^+ ions, $M_i \sim 1.5 \times 10^{-27}$ kg.

For a *collisional* pre-sheath the velocity at the sheath edge u_s, is $u_s = u_B\alpha_c$ where α_c is given by[Godyak, *et al.*, 1990]:

$$\alpha_c \equiv \left[1 + \frac{\pi\lambda_D}{2\lambda_i}\right]^{-1/2} \tag{4.13}$$

where λ_i is the H^+-H_2 mean free path. Equation (4.12) becomes:

$$T_{es} = \frac{|e|(\phi_f + \phi_s)}{k\left\{\ln(\alpha_c) + \ln\left[(0.61)\sqrt{\frac{2\pi m_e}{M_i}}\right]\right\}} \qquad (4.14)$$

For the nominal conditions of 50 mg/s and 9.8 A, Fig. 4.14 shows a comparison of flush probe T_{es} results obtained two ways: (1) from the electron-retarding region of the V-I characteristic, Eq. (3.32); and (2) using Eq. (4.14), with experimental data for ϕ_f and ϕ_s.

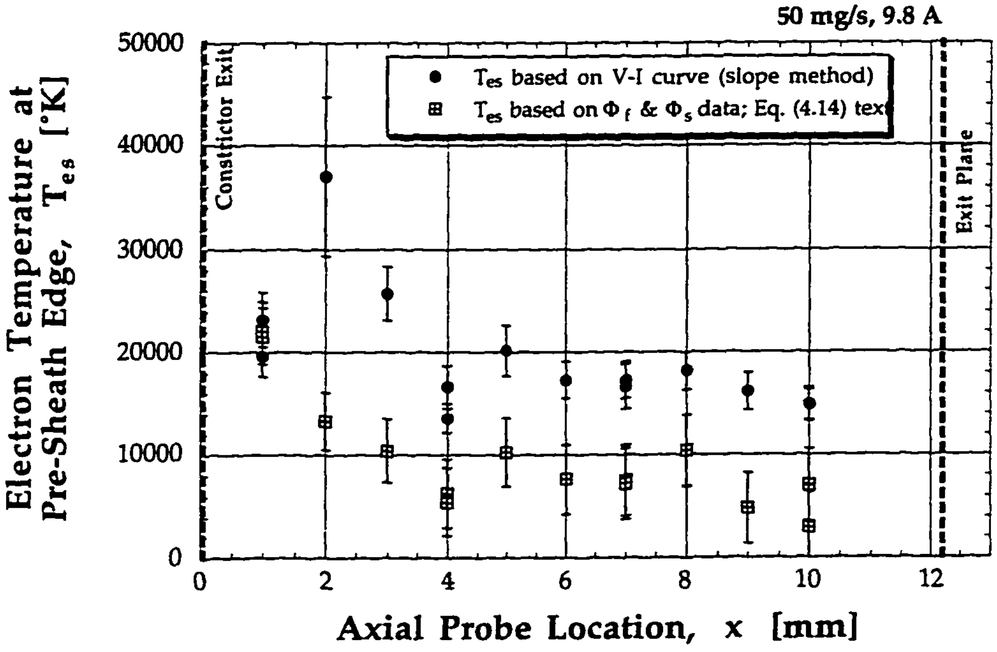

Fig. 4.14 A comparison of two methods for calculating the electron temperature distribution. The ϕ_f and ϕ_s data are used to approximate T_{es}, Eq. (4.14) in the text and T_{es} is also obtained from the slope of the electron-retarding region of the V-I curve. The data are for $\dot{m}$ 50 mg/s and I_{arc} = 9.8 A, using flush probes.

For x > 1 mm, the T_{es} calculations based on probe potential are lower than T_{es} derived from the probe V-I characteristic slope. The drawback of using Eq. (4.12) or Eq. (4.14) to approximate T_{es} is that it is very sensitive to the accuracy of the potential data; e.g., a ± 1 V error in ϕ_f or ϕ_s can result in a ± 3500 - 5000 °K error in electron temperature; in this investigation the error in the potential data is ± 1 V.

4.2.6 Calculation of a Weighted Anode Sheath Potential

The total arcjet operating voltage is comprised of: (a) the cathode sheath potential drop ϕ_c, (b) the potential drop in the arc column, i.e. in the bulk plasma, ϕ_{bulk} and (c) the anode sheath potential, ϕ_s. Numerical arcjet models can calculate ϕ_{bulk}, but to evaluate ϕ_{ca} and ϕ_s the sheath regions must also be included in the model. To do this accurately and self-consistently, Poisson's equation, coupled with the ion and electron species conservation equations must be solved in the sheath, obtaining an "inner" solution, with boundary conditions from the solution to the Navier Stokes and Maxwell's equations in the quasineutral plasma region. This "inner" solution is then matched with the "outer" solution, i.e. the quasineutral plasma region where Poisson's equation reduces to Laplace's equation, at the sheath edge. This is a very difficult scheme to implement and most likely will increase computational time, since the sheath thickness is only 5-10 λ_D, requiring a fine computational grid for enhanced spatial resolution.

In Secs. 4.2.2-4.2.4 the anode sheath potential distribution was presented for various arcjet operating conditions. The anode sheath potential measurements are important because: (1) they will provide a required boundary condition at the anode for numerical models; and (2) the anode sheath potential is required to calculate the anode heating distribution, Chapter 6.

A weighted anode sheath potential is calculated as:

$$\bar{\phi}_S = \frac{\int_1^{10} \left[j_a(x) \phi_S(x) dA(x) \right]}{I_{arc}} \qquad (4.15)$$

where x is in mm, $j_a(x)$ is the current density distribution presented in Sec. 4.3 and $\phi_s(x)$ is the anode sheath potential distribution. For the $j_a(x)$ and $\phi_s(x)$ distributions the values for the 0° and 180° are averaged to obtain a single data point in Eq. (4.15). The differential anode element, dA(x), is given as $dA(x) = 2\pi r(x)(\cos 20)^{-1}$, where cos 20° accounts for the nozzle divergence angle and $r(x) = r_c + x\tan 20°$, where r_c is the constrictor radius = 0.3175 mm.

Equation (4.15) was used to calculate a weighted anode sheath potential for all the operating conditions studied, cases (a)-(f), Table (4.1), with the results shown in Table (4.2) and Figs. 4.15-4.16. Because ϕ_s is approximately constant within 0.25-0.3 mm of the anode (Chapter 5), the $\bar{\phi}_S(x)$ data from the flush probes only is presented.

Table 4.2 Summary of the weighted anode sheath potential, equivalent voltage and fraction of electron energy deposited into the anode for each arcjet operating condition.

$\dot{m}$ (mg/s)	I_{arc}(A)	V_{arc}(V)	Arc Power, P (W)	P / $\dot{m}$ (MJ/kg)	$\bar{\phi}_s$ (V)	$f_{\bar{\phi}_s}$	$\bar{\phi}_{eq}$ (V)	f_{Q_a}
50	7.80	120.8	942	18.8	14.5 ± 3.1	0.12	26.4 ± 6.1	0.22
60	9.90	121.0	1198	19.9	17.0 ± 5.1	0.14	28.8 ± 8.2	0.24
50	8.94	115.3	1026	20.6	15.2 ± 3.5	0.13	25.6 ± 5.5	0.22
50	9.81	112.2	1101	22.0	11.3 ± 2.4	0.10	20.1 ± 4.3	0.18
45	9.80	108.5	1063	23.6	11.4 ± 2.3	0.10	20.5 ± 5.1	0.19
40	10.6	104.0	1102	27.6	8.1 ± 1.6	0.08	21.2 ± 5.3	0.20

$f_{Q_a} \equiv \frac{Q_a}{P}$: ratio of anode heat transfer to arc power.

$f_{\bar{\phi}_s} \equiv \frac{\bar{\phi}_s}{V_{arc}}$: ratio of weighted anode sheath potential to arc voltage.

$\bar{\phi}_s$: weighted anode sheath potential.

$\bar{\phi}_{eq} \equiv \frac{Q_a}{I_{arc}}$: equivalent anode potential; ratio of anode heat transfer to arc current.

It is interesting to note that the largest value for $\bar{\phi}_S$ is for the highest propellant flow rate, 60 mg/s and $P/\dot{m}$ of 19.9 MJ/kg, where $\bar{\phi}_S = 17$ V ± 5.1 V. Similarly, for the lowest propellant flow rate (40 mg/s) and highest specific energy obtained (27.6 MJ/kg), $\bar{\phi}_S$ is the lowest value at 8.1 V ± 1.6 V. This is because ϕ_s scales directly with $\dot{m}$ as discussed earlier. The results agree with Curran *et al.*, [1990] who found that the anode fall voltage is O(10-20V).

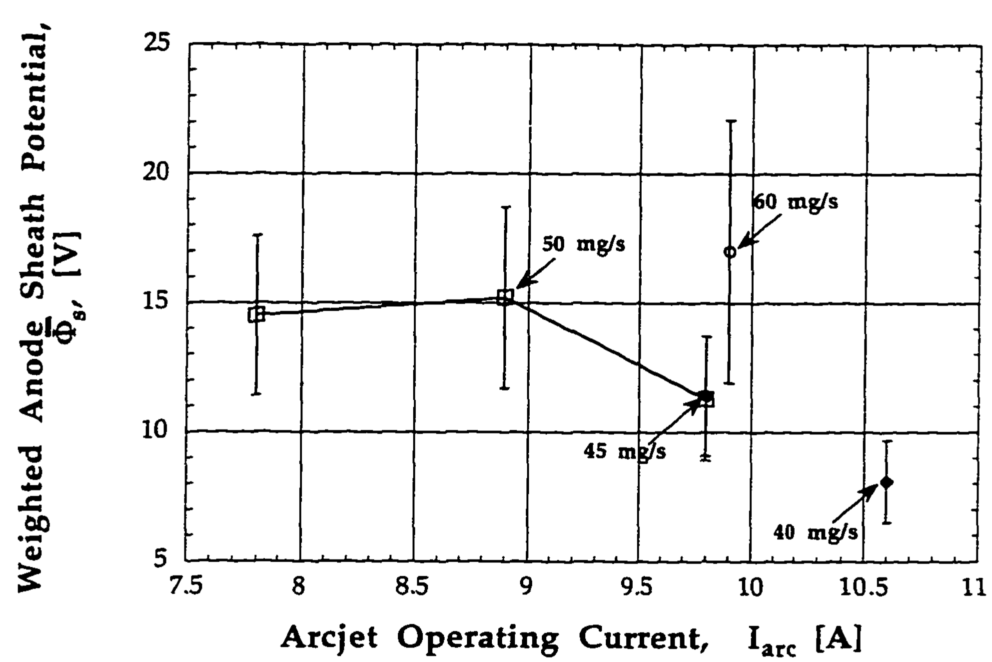

Fig. 4.15 The weighted anode sheath potential as a function of the various arcjet operating currents and propellant flow rates tested in this work.

Figure 4.16 clearly shows that $\bar{\phi}_S$ is affected by both varying I_{arc} or $\dot{m}$, with a minimum value of $\bar{\phi}_S$ at 50 mg/s and 9.8 A. However, the propellant flow rate has a relatively larger effect on $\bar{\phi}_S$ (and ϕ_s) than I_{arc}. It is later shown that this has ramifications with regards to anode heating.

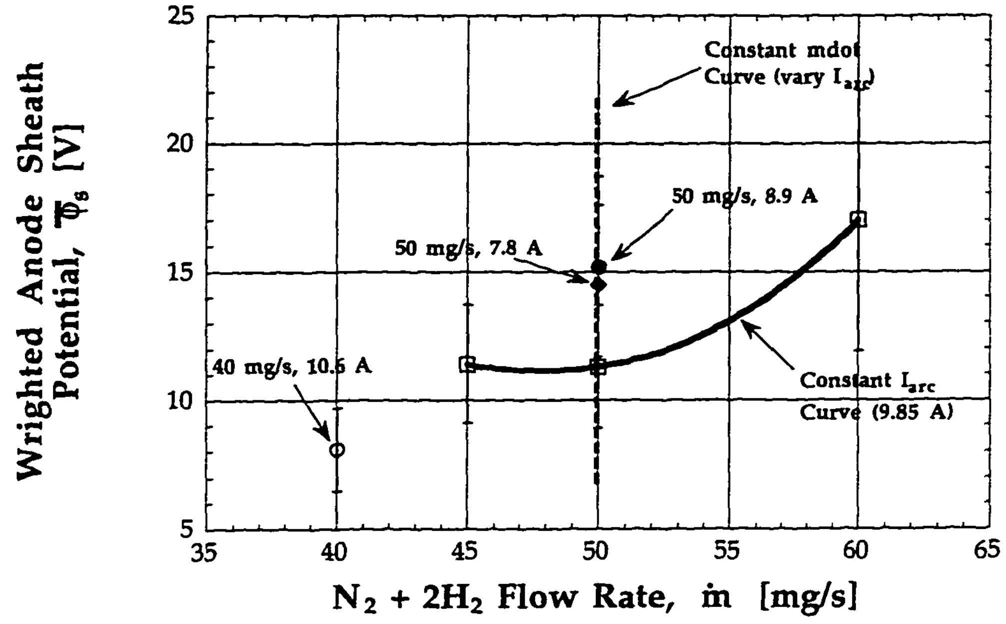

Fig. 4.16 The weighted anode sheath potential as a function of the propellant flow rates tested in this research.

Table (4.2) shows values for the weighted anode sheath potential and an anode sheath equivalent potential defined as:

$$\bar{\phi}_{eq} \equiv \frac{Q_a}{I_{arc}} \tag{4.16}$$

where Q_a is the total electron energy power deposition to the anode, given as:

$$Q_a = \int_1^{10} \bar{q}_e(x) dA(x) = \int_1^{10} j_a \left[\frac{5kT_{es}}{2e} + \phi_s + W \right] dA(x) \tag{4.17}$$

Calculations for Q_a are also presented in Table (4.2) as a fraction of the total arcjet input power, $f_{Q_a} \equiv \frac{Q_a}{P}$.

The electron energy deposition in the anode, as a fraction of total arcjet power input, ranges from f_{Q_a}=18-24% over a range of specific energies of 18.8

MJ/kg $\leq P/\dot{m} \leq$ 27.4 MJ/kg. These fractional energy values agree well with the results of Curran [1985] who found that in experiments with a water-cooled arcjet simulator, the percentage of the total power lost to the anode is between 20-25 % of the total input power.

4.3 Current Density Measurements

Achieving a high specific impulse, above 600 sec for a hydrazine arcjet, requires a power-to-mass flow rate of $P/\dot{m}$ of ~ 40-80 MJ/kg, resulting in anode heating rates that can cause electrode failure. Anode heating, a critical life-limiting factor for high performance arcjets [Lichon, *et al.*, 1996], is determined by the physics of arc attachment [Meeks, *et al.*, 1993]. Since most of the current to the anode is carried by the more mobile electrons, anode heating is governed by the electron energy deposition into the anode, Chapter 6. To evaluate this energy loss, the current density j_a, electron temperature T_{es} and anode sheath potential ϕ_s must be known.

Electrothermal arcjets are operated in a 'high' voltage mode, so that the arc attaches in the supersonic region. If the flow rate is too low so that the gasdynamic forces are insufficient to force the arc through the constrictor channel, subsonic arc attachment can occur resulting in unstable electrode erosion and a 'low' mode operation. Though stable and efficient arcjet operation requires arc attachment in the supersonic region, it has not been known where in the diverging portion of the nozzle the arc attaches and what affects the attachment location.

4.3.1 Significance of Current Density Data

In this section current density j_a, data are presented for various propellant flow rates, arc currents and specific energies $P/\dot{m}$. Once this data is obtained, the subject of azimuthal current symmetry and anode heating can be addressed.

It was shown earlier that the floating and sheath potential data can be used, with caution, to approximate T_{es} and to infer azimuthal current symmetry. However, in order to verify azimuthal symmetry, j_a must be determined at all fourteen probe locations. The current density at anode potential is calculated by averaging multiple samples of the probe current at zero volts, I_a. The probes are biased with a sinusoidal signal, an average of 5-10 cycles and I_a is obtained through graphical analysis of the V-I curve. Due to the resolution of the oscilloscope, values at exactly $V_p = 0$ V are not always obtainable. Therefore, probe current data points within a ± 0.1 V range of $V_p = 0$ V are used to calculate I_a. The effective probe collection area at zero volts is also required to calculate j_a, Sec. 3.2.2.

Obtaining the j_a distribution is important because: (1) azimuthal current symmetry can be verified; (2) the location of arc attachment is readily determined; (3) effects of propellant flow rate and arcjet operating current on the j_a distribution are evaluated; and (4) j_a is required to calculate the anode heating, q_e. The verification of azimuthal current symmetry is also of significance to numerical arcjet models, which *assume* current symmetry, eliminating the need for solving the governing equations in three dimensions. Obtaining the j_a distribution and knowing where the arc attaches in the nozzle will also enhance our understanding of arcjet plasma physics in the near-electrode regions as well as the dynamics of arc attachment [Butler, *et al.*, 1996].

4.3.2 Effect of Flow Rate on Current Density

The current density j_a is evaluated using the following equation:

$$j_a = \frac{(1/N)\sum_{n=1}^{N} I_a}{A_{eff}} \tag{4.18}$$

where I_a is the probe current at 0V ± 0.1 V and N is the total number of I_a samples obtained from graphical analysis of the probe V-I characteristic. The effective probe collection area A_{eff} for a planar probe includes corrections for the sheath area A_{sh}, which is at most a 10% correction, Sec. 3.2.2. In evaluating A_{eff}, it was assumed that the probe collects current across its entire surface, i.e. there are no preferential arc spots on the probe's smooth surface.

Figures 4.17-4.21 show the current density at all probe locations for $\dot{m}$ = 60, 50, 45, and 40 mg/sec, respectively. For $\dot{m}$ = 45, 50, 60 mg/sec, $(I_{arc})_{avg}$ = 9.8 A, and for $\dot{m}$ = 40 mg/sec, I_{arc} = 10.6 A. From these figures it is shown that:

(1) the current density j_a decreases montonically with increasing distance from the constrictor, except for the case of $\dot{m}$ = 60 mg/s, 9.9 A where j_a peaks at x = 3 mm, and decreases for x > 3 mm. The current density is much lower near the exit plane than near the constrictor exit. For example, for $\dot{m}$ = 60 mg/s and 9.9 A, ja decreases from $(j_a)_{max}$ = 37.9 A/cm^2 ± 11.5 A/cm^2 at x = 3 m m to j_a ~3.0 A/cm^2 ± 0.6 A/cm^2 at x = 10 mm.

(2) as the propellant flow rate is increased from 40 mg/to 60 mg/sec, the location of peak current density $(j_a)_{max}$ shifts to x = 3 mm, with smaller peaks at x = 1, 5 and 8 mm, Fig. 4.17. This is because as the propellant flow rate increases the gasdynamic forces increase, pushing the arc further downstream and increasing V_{arc} as well. Note that the magnitude of j_a at x = 3 mm has a large uncertainty associated with its value because I_a at that location is in the enhanced ionization region of the probe V-I characteristic, Sec. 3.5.2. However, independent multimeter measurements of I_a, for a grounded probe: (1) also show a shift in $(j_a)_{max}$ to x = 3 mm as $\dot{m}$ is increased from 45 to 60 mg/s; and (2) provide I_a values that fall within the experimental error for j_a at x = 3 mm.

(3) for $\dot{m}$ = 40, 45, 50 mg/sec the current density is maximum at x = 1 mm, with indications of a second, smaller peak at x = 4 mm, Figs. 4.18-4.20.

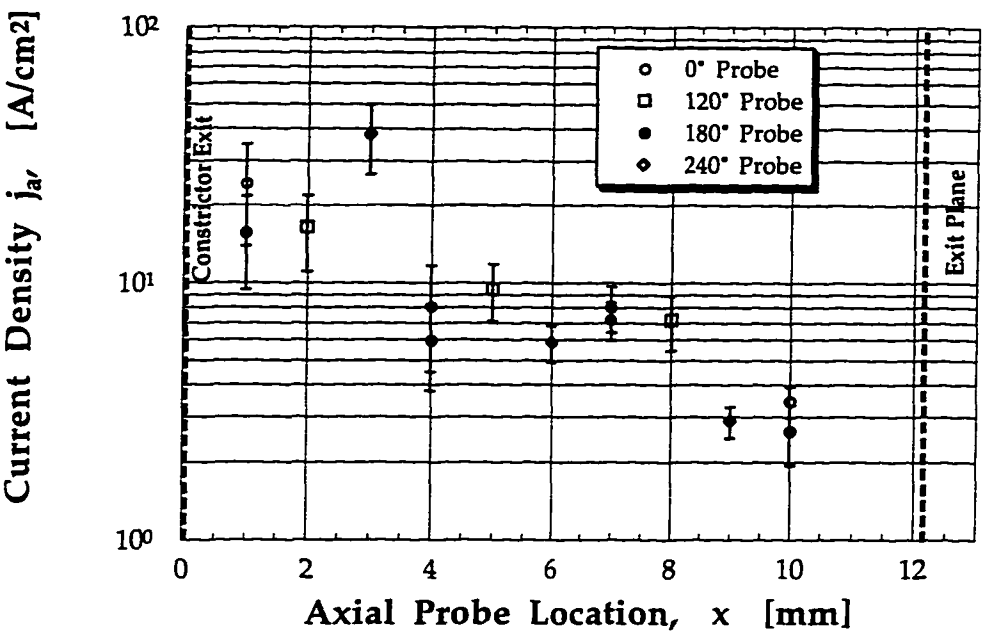

Fig. 4.17 Current density distribution along the anode for ṁ = 60 mg/s, 9.9 A and 121 V.

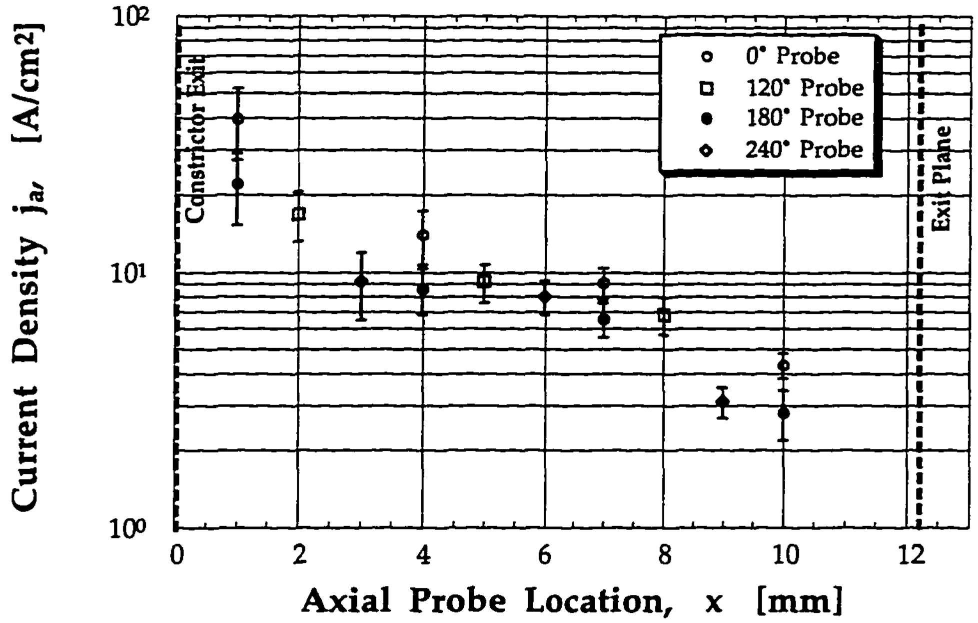

Fig. 4.18 Current density distribution along the anode for ṁ = 50 mg/s ,9.8 A and 112 V.

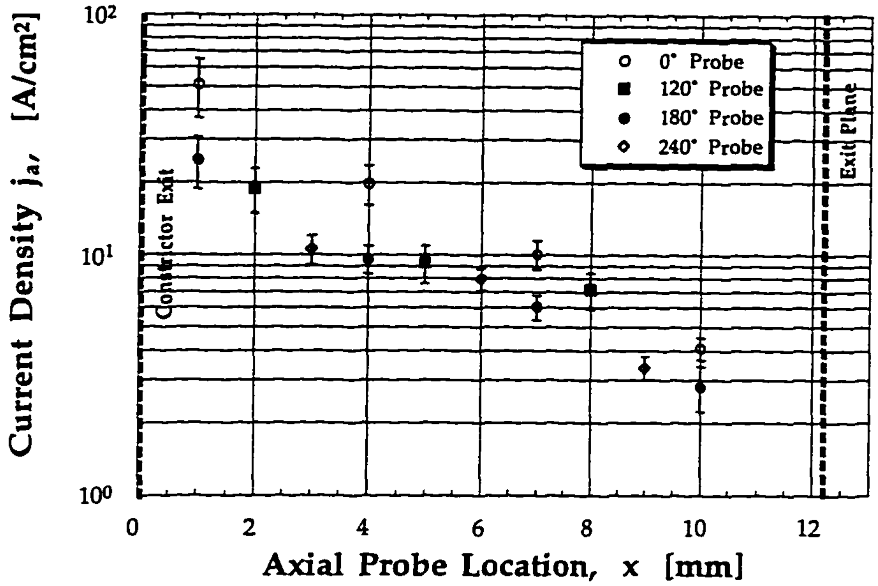

Fig. 4.19 Current density distribution along the anode for $\dot{m}$ = 45 mg/s, 9.8 A and 109 V.

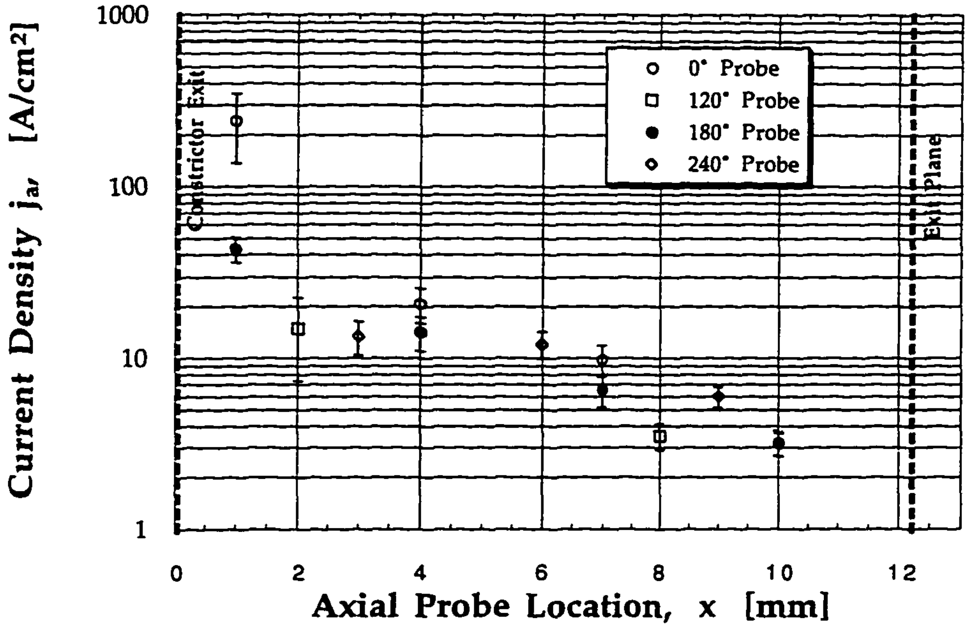

Fig. 4.20 Current density distribution along the anode for $\dot{m}$=40 mg/s , 10.6 A and 104 V.

(4) for most of the experimental conditions studied, azimuthal current symmetry is inferred from the j_a data obtained from the 0° and 180° probes, within experimental error. However, there is a large discrepancy between probes 1 and 1′ for the lower flow rates of $\dot{m} = 40$ and 45 mg/sec. Though this may not be the reason for the asymmetry in the low flow rate $j_a(x)$ data, it has been observed in earlier tests with a HD-18 tungsten alloy nozzle that a cathode misalignment (~10-20% of the constrictor diameter) results in unsteady plume behavior and may lead to current asymmetry.

As the propellant flow rate is increased to 60 mg/sec, this large asymmetry in j_a for probes 1 and 1′ decreases. The average percent difference for j_a between the 0° and 180° probes decreases from 42% for $\dot{m}$=45 mg/sec ($P/\dot{m}$ = 23.6 MJ/kg), 36% for $\dot{m}$ = 50 mg/sec (22 MJ/kg), to 24% for $\dot{m}$ = 60 mg/sec (19.9 MJ/kg). It is interesting to note that the asymmetry decreases with decreasing $P/\dot{m}$, i.e. lower anode thermal loading. Higher anode thermal loading leads to increased thermal stresses on the alumina tubing surrounding the probes. The uncertainty in the j_a asymmetry, especially for the probes at x = 1 mm, is believed to be largely due to the uncertainty in the probe collection area, since these probes experience the largest thermal stresses due to their location in the arc attachment zone.

As a result of the large heat intensity within 2-3 mm of the constrictor exit, it was found that the Al_2O_3 tubing for probes 1,1′ and 2 occasionally experienced cracking. Thus, it is imperative that accurate photomicrographs before and after testing are made, as well as visual observations of the probe surface condition. This was done in this investigation, with a sample shown in Fig. 2.18, Chapter 2.

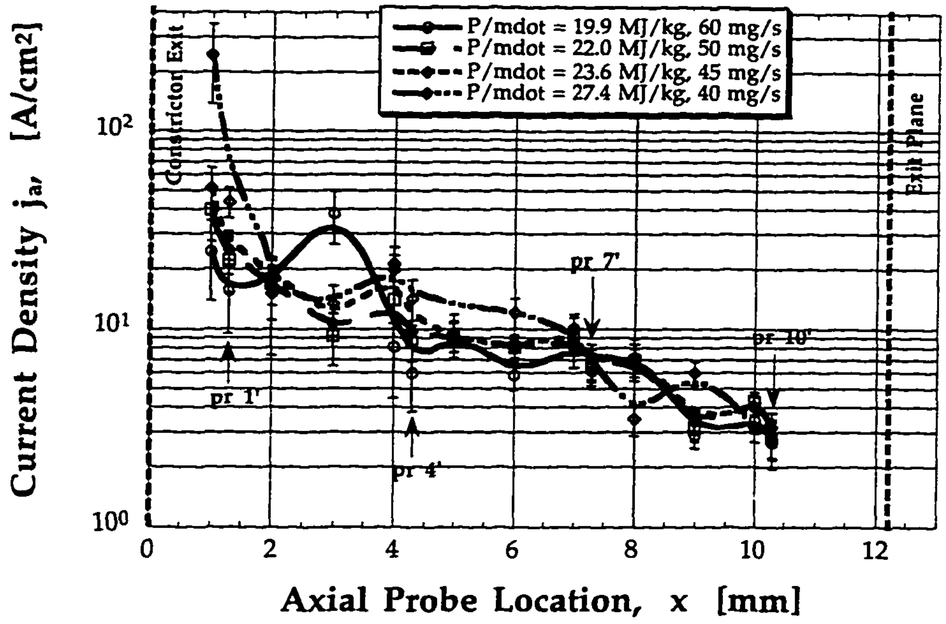

Fig. 4.21 Current density distribution along the anode for $\dot{m}$= 45, 50 and 60 mg/s, $(I_{arc})_{avg}$= 9.8 A and for $\dot{m}$ = 40 mg/s, I_{arc} = 10.6 A.

(5) Figure 4.21 shows that as $P/\dot{m}$ increases, j_a increases at x =1 mm, 4 mm and 9 mm. The most significant changes in the current density distribution occurred for $\dot{m}$ = 60 mg/s, I_{arc} = 9.9 A. In this case the current density peak shifted downstream, from x = 1 mm to x = 3 mm. Also for the highest specific energy tested, $P/\dot{m}$ = 27.4 MJ/kg, $(j_a)_{max}$ increased over 300% compared to its value obtained for the other test conditions. As the propellant flow rate decreased from 60 mg/s to 40 mg/s, $(j_a)_{max}$ was fixed at x = 1 mm.

This arc attachment behavior may explain why arcjet operation becomes unstable at low flow rates. As $\dot{m}$ decreases the point of maximum arc attachment shifts upstream towards the constrictor and for unacceptably low flow rates it could attach inside the constrictor, leading to large erosion and 'low' mode operation. At low flow rates the gas dynamic forces are not strong enough to force arc attachment into the supersonic region. For arcjets to run at very low flow rates [~O(1-10 mg/s)] the constrictor diameter must be decreased accordingly, thus increasing the gas dynamic pressure forces. However, high thermal loads in the constrictor resulting from the smaller diameter can lead to constrictor closure, a phenomenon due to thermal creep and hoop stresses in the constrictor wall [Lichon, *et al.*, 1996]. This shows why arcjet design is highly complicated, with competing design issues.

The azimuthal current symmetry for probes 4,4′ and 7, 7′ and 10, 10′ is within experimental error for all flow rates studied, except for $\dot{m} = 45$ mg/sec, Fig. 4.19. Observation of the post-test probe surface condition for this case revealed that probe 4′ was lightly discolored, perhaps contributing to some contamination which lead to a lower j_a signal, as compared to probe 4 which had no discoloration of its surface.

The region of arc attachment L_{arc}, is important to identify since most of the anode heating occurs here, Chapter 6. In this work L_{arc} is defined as the region where j_a is within 1/e of $(j_a)_{max}$. For $\dot{m} = 45$, 50 and 60 mg/sec, $(I_{arc})_{avg} =$ 9.9 A, L_{arc} is 3-4 mm wide; for $\dot{m} = 40$ mg/sec, $I_{arc} = 10.6$ A, which has the highest $P/\dot{m}$ studied (27.4 MJ/kg), most of the arc attachment, i.e., ~60-70% of $(j_a)_{max}$, is within 1 mm of the constrictor. This suggests that the region of arc attachment is most influenced by the propellant mass flow rate and not the arc current, as shown later. Similar flow rate effects were also observed earlier for the ϕ_f and ϕ_s results.

In order to check for self-consistency in the experimental data, the current per unit length dI/dx, was calculated for all experimental conditions, at all probe locations. The values were then integrated over all the probes to obtain a comparison to I_{arc} from the PPU. The current per unit axial length is given as:

$$\frac{dI}{dx} = \frac{2\pi r(x) j_a(x)}{100\cos(20°)} \qquad (4.19)$$

where r(x) is the nozzle radius in mm at each probe location, $j_a(x)$ is the current density distribution in A/cm^2, and dI/dx is in units of A/mm. Figure 4.22 shows a typical dI/dx result for the nominal experimental conditions of $\dot{m} = 50$ mg/sec and $I_{arc} = 9.8$ A. It is interesting to note that $j_a(x)$ varies from about 40 A/cm^2 at x = 1 mm to ~3 A/cm^2 at x = 10 mm (Fig. 4.18), a change of a factor of 13. However, the current density per unit length, dI/dx only varies by a factor of two. This is because dI/dx at x = 1 mm is limited by the available area at x = 1 mm, compared with the larger nozzle area downstream which effectively equalizes the contribution to dI/dx, Eq. (4.19).

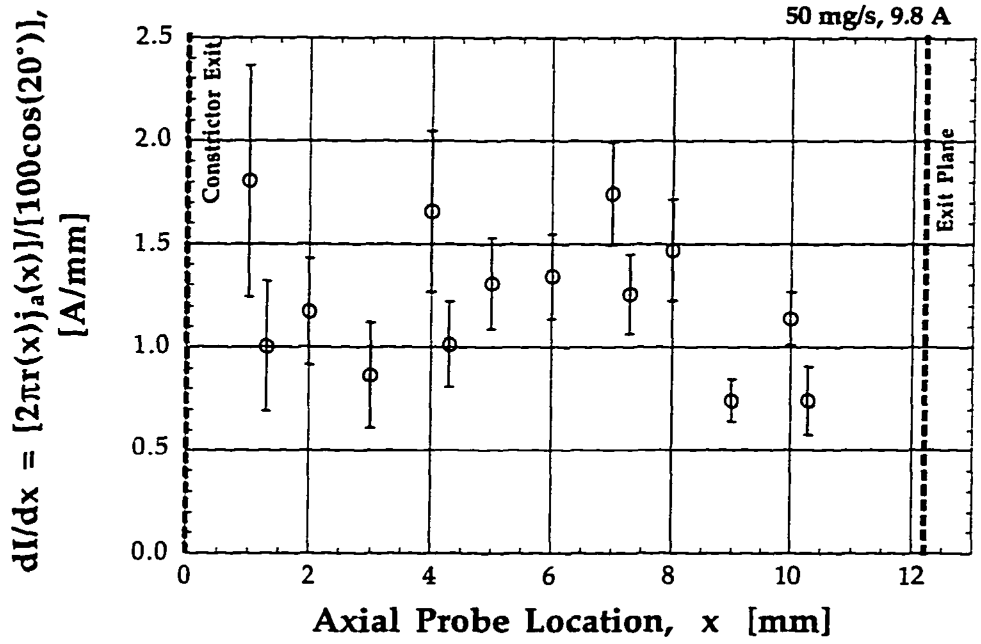

Fig. 4.22 Current per unit length dI/dx, with the N_2+$2H_2$ flow rate fixed at 50 mg/sec and $I_{arc} = 9.8$ A. The integral of dI/dx provides a total arcjet current of 10.9 A ± 2.1 A.

An estimate of the arcjet operating current based on the j_a data is given as:

$$I_{arc} = \int_{1}^{12} \left(\frac{dI}{dx}\right) dx = \int_{1}^{12} \frac{2\pi r(x) j_a(x)}{100\cos(20^\circ)} dx \qquad (4.20)$$

The integration limits are taken from x = 1 mm to x = 12 mm, the exit plane, where j_a= 0 A/cm^2 is assumed. The integral is evaluated using Simpson's rule, with the results presented in Table 4.3 for various cases studied.

Table 4.3 Comparison of applied I_{arc} and derived I_{arc} data based on experimental results. Note that the error in the applied I_{arc} is due to the arcjet current PPU ripple, [Bufton, 1996].

$\dot{m}$ (mg/s)	Applied I_{arc} (A)	I_{arc} Derived From j_a Data, (A)	% Error
40	10.6 ± .8 A	13.8 ± 3.5 A	+30
45	9.8 ± .8 A	12.5 ± 2.0 A	+27
50	9.8 ± .8 A	11.6 ± 2.2 A	+18
60	9.9 ± .8 A	12.0 ± 3.2 A	+21

The major contribution to the source of error in the j_a data and the derived I_{arc} is calculation of the probe collection area. An accurate assessment of the probe collection area was difficult to achieve, mainly because: (1) estimation of the sheath area was made using a semi-empirical approach, combining the experimental data of n_{es}, T_{es} and j_a with numerical data for the H^+ ion mobility and various plasma composition number densities; and (2) on several occasions, the alumina tubing surrounding the probe would partially crack, exposing an unknown amount of collection area difficult to measure, Fig. 2.15. If cracking of the alumina tubing occurred it was almost exclusively to probes 1, 1′ and 2.

4.3.3 Effect of Arcjet Current on Current Density

The range of arcjet operating currents used in this research was limited to 7.8 A $\leq I_{arc} \leq$ 10.6 A due to the operational limitations of the NASA-Lewis PPU, Sec. 2.2. The effect of varying the arcjet operating current on the current density distribution was shown in Figs. 4.18 for $\dot{m}$ = 50 mg/sec, I_{arc}=9.8 A, Fig. 4.20 for $\dot{m}$ = 40 mg/s, I_{arc}=10.6 A, and Figs. 4.23-4.25 for $\dot{m}$ = 50 mg/s and I_{arc} = 7.8, 8.9 and 9.8 A. Some data points are not shown in the figures due to probe surface contamination.

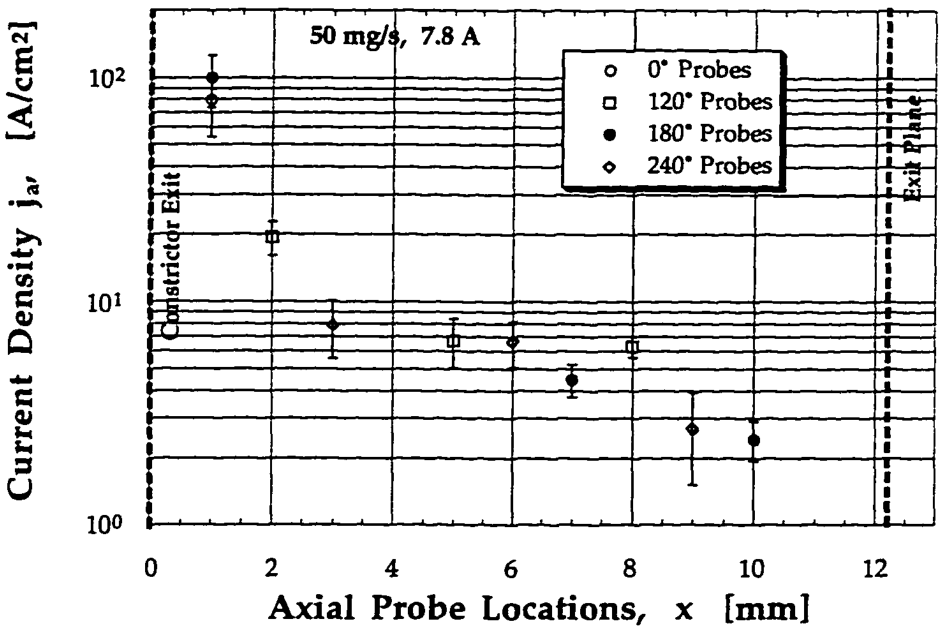

Fig. 4.23 Current density distribution for $\dot{m}$ = 50 mg/, I_{arc}= 7.8 A, V_{arc}= 121 V. Note that probes 4, 4′ and 7, 7′ and 10 were contaminated, hence data from these probes are not shown.

At all arc currents studied, except 10.6 A, azimuthal current symmetry is observed. For I_{arc} = 10.6 A and $\dot{m}$ = 40 mg/s, azimuthal current symmetry is observed for probes 4, 4′ and 7, 7′ and 10, 10′. Only probes 1, 1′ show any asymmetry for I_{arc} = 10.6 A and m = 40 mg/s. This asymmetry may be largely due to: (1) the uncertainty in collection area for probes 1, 1′ cited earlier; and (2) the low flow rate rather than the high current since it has been observed that the propellant flow rate has a larger effect on the measured plasma properties than I_{arc}. It should be noted that $\dot{m}$ = 40 mg/s is the lowest flow rate the 1 kW arcjet, with a 225 area ratio, can tolerate, [Curran, *et al.*, 1992].

As with the flow rate parameter study discussed earlier, the j_a distribution is maximum at x = 1 mm for all arc currents tested (except for 60 mg/s and 9.9 A) and decreases monotonically towards the nozzle exit. Azimuthal current symmetry is observed for probes 1 and 1′ under most arcjet operating conditions.

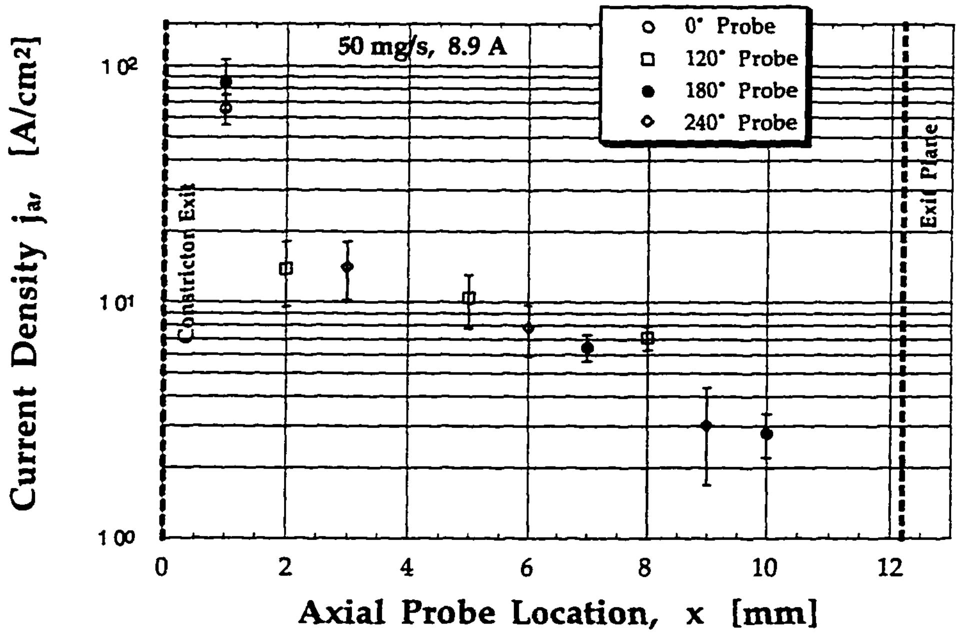

Fig. 4.24 Current density distribution for $\dot{m}$ = 50 mg/, I_{arc}= 8.9 A, V_{arc}= 115 V. Note that probes 4,4′ and 7,7′ and 10 were contaminated, hence data from these probes are not shown.

Figure 4.25 shows the cumulative results for I_{arc}= 7.8, 8.9, 9.8 A and 50 mg/s together with data for the high P/$\dot{m}$ case of $\dot{m}$ = 40 mg/s and I_{arc}= 10.6

A. For the nominal flow rate of 50 mg/s, increasing the arcjet operating current has a relatively negligible effect on the current density distribution, except at x = 1 mm, the location of $(j_a)_{max}$. A 26% increase in I_{arc}, from 7.8 to 9.8 A, leads to an approximately 64% decrease in $(j_a)_{max}$ at x = 1 mm. The axial gradient in j_a, within 3 mm of the constrictor, increases as I_{arc} decreases: e.g., for 9.8 A, dj_a/dx = (7.2 A/cm²)/mm; for 8.9 A, dj_a/dx = (20.4 A/cm²)/mm; and for 7.8 A, dj_a/dx = (27 A/cm²)/mm. For the largest specific energy tested, $P/\dot{m}$ = 27.4 MJ/kg, dj_a/dx = (43 A/cm²)/mm, within 3 mm of the constrictor exit.

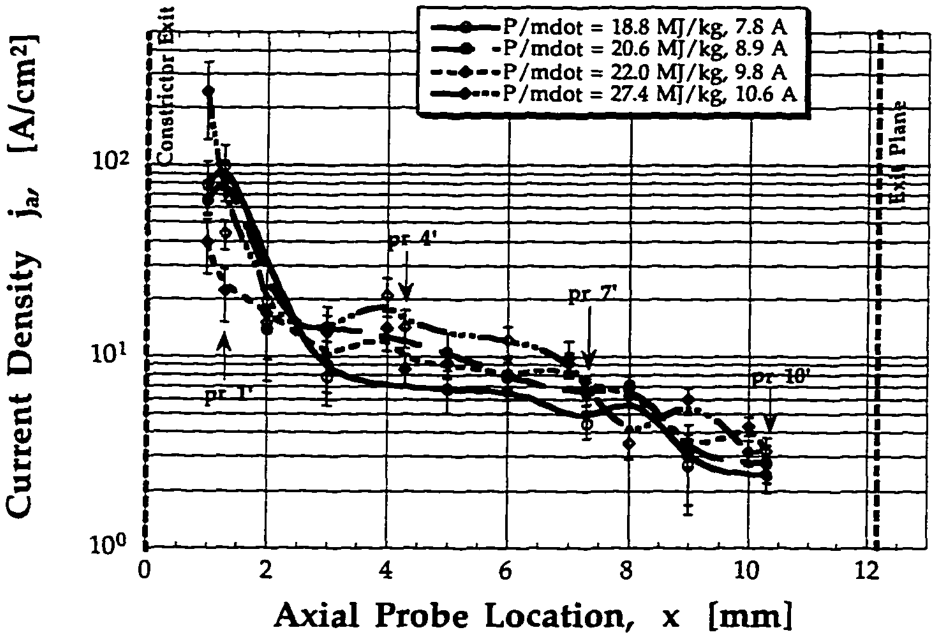

Fig. 4.25 Current density distribution along the anode for various arcjet operating currents. For I_{arc}= 7.8, 8.9 and 9.8 A, $\dot{m}$= 50 mg/s and for $\dot{m}$ = 40 mg/s, I_{arc}=10.6 A.

As the arcjet operating current increases, Fig. 4.25, $P/\dot{m}$ increases (for a fixed flow rate) and the j_a profile becomes more "flat" in the axial direction, coupled with larger j_a gradients near the constrictor. This was also observed for the n_{es} and T_{es} profiles, shown later in Secs. 4.4 and 4.5.

For all arcjet currents tested azimuthal current symmetry prevails at x = 1 mm for P/ $\dot{m}$ = 18.8 and 20.6 MJ/kg, and at x = 1, 4, 7, 10 mm for 22 MJ/kg and at x = 4, 7, 10 mm for 27.4 MJ/kg. For P/ $\dot{m}$=27.4 MJ/kg, there is a large discrepancy in j_a between the 0° and 180° probes at x = 1 mm. As stated earlier, this is believed to be mostly due to the large uncertainty in the effective probe collection area for probes 1, 1'.

Based on the $\dot{m}$ and I_{arc} parameter studies it appears that $\dot{m}$ affects the current density distribution more than I_{arc} with regards to the location of $(j_a)_{max}$. Due to the PPU limitations the arc current could only be varied 25%. Perhaps a larger variation in I_{arc} would show a more pronounced effect on the plasma properties studied.

Figure 4.26 shows $j_a/j_{th,e}$ and ϕ_s versus x. The anode sheath potential is largest in regions of high ja; also note how $j_a/j_{th,e}$ and ϕ_s exhibit similar trends.

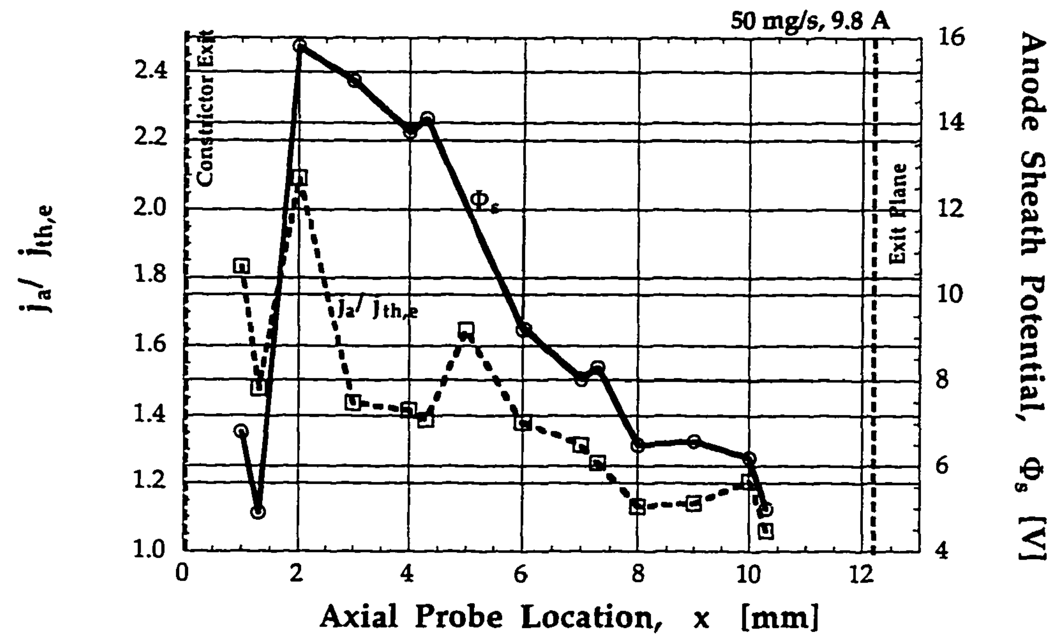

Fig. 4.26 Shown above is the current density normalized by the electron random thermal current density and the anode sheath potential along the anode for $\dot{m}$ = 50 mg/s, I_{arc}= 9.8 A.

4.3.4 Effect of Specific Energy on Current Density

In this section the effect of specific energy $P/\dot{m}$, on j_a and $(j_a)_{max}$ is studied. The specific energy is varied by changing $\dot{m}$ or I_{arc} individually or both simultaneously. In Fig. 4.27, $P/\dot{m}$ is increased by decreasing $\dot{m}$ and increasing I_{arc} simultaneously. This leads to an increase in $(j_a)_{max}$ to ~ 140 A/cm^2 at $x = 1$ mm as well as a larger $j_a(x)$ distribution along the anode.

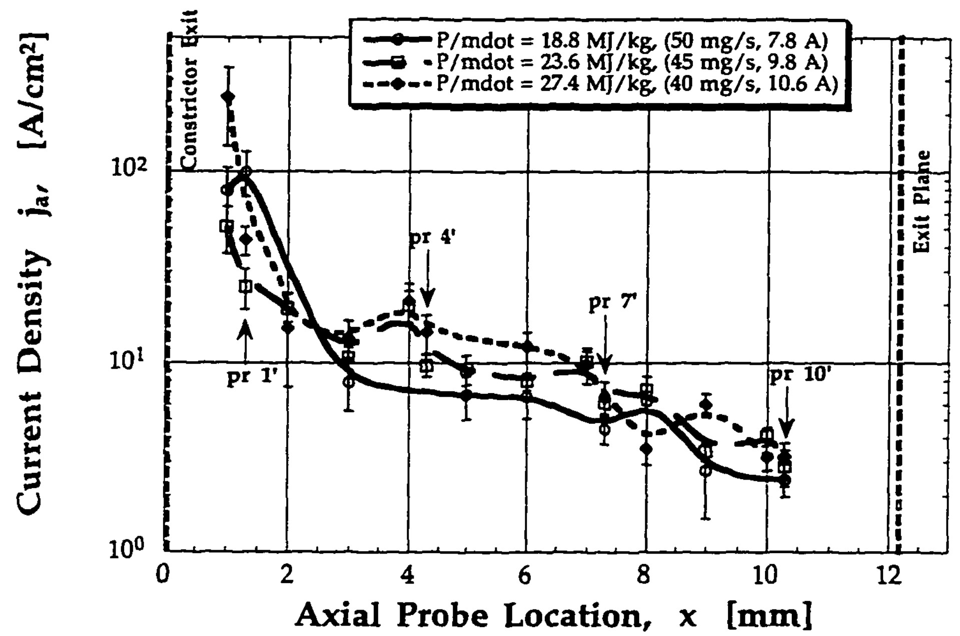

Fig. 4.27 Current density distribution for various specific energies, $P/\dot{m}$. Both arc current and propellant flow rate are varied simultaneously.

Figure 4.28 shows $(j_a)_{max}$ as a function of $P/\dot{m}$. There appears to be a relative minimum in $(j_a)_{max}$ for $P/\dot{m}$ = 22 MJ/kg; this corresponds to the minimum observed in $\bar{\phi}_S$, Fig. 4.16. For $P/\dot{m} > 22$ MJ/kg, $(j_a)_{max}$ increases as $P/\dot{m}$ increases. The minimum in $(j_a)_{max}$ at $P/\dot{m}$ = 22 MJ/kg corresponds to the minimum in f_{Q_a} of 18%, Table (4.2). The largest affect on $(j_a)_{max}$ is for $P/\dot{m}$ = 27.4 MJ/kg, the upper limit tested in this investigation.

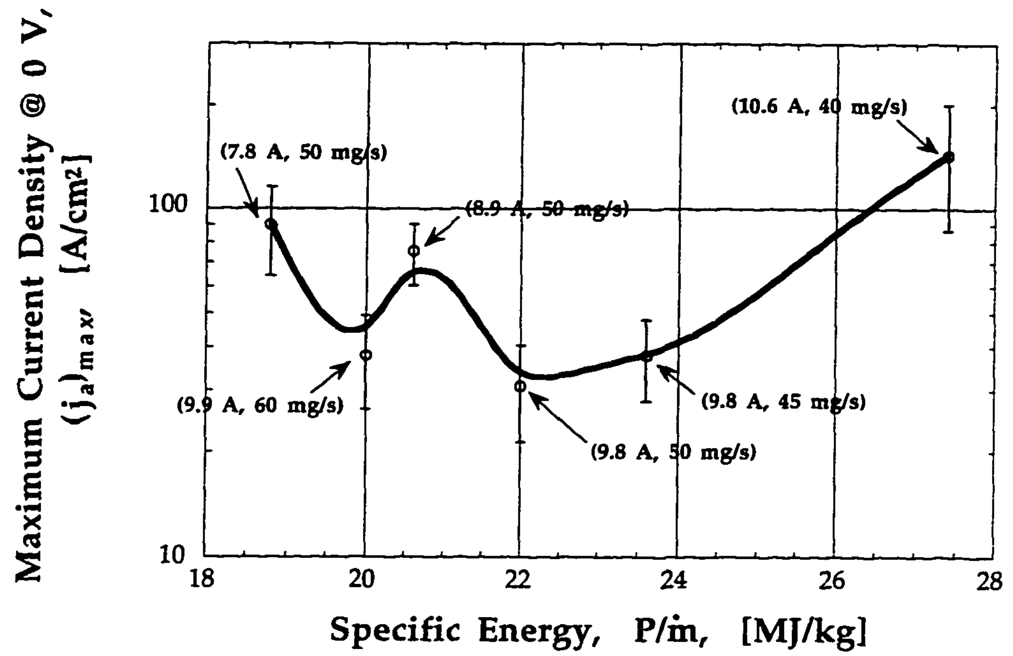

Fig. 4.28 The effect of varying the specific energy $P/\dot{m}$ on $(j_a)_{max}$ is shown.

4.4 Electron Number Density Measurements

In this section the electron number density distribution along the anode is presented for various flow rates, arc currents and specific energies. The affect of each operating condition on the electron number density distribution $n_{es}(x)$ is studied.

4.4.1 Significance of Electron Number Density Data

Of equal importance to the current density data is evaluation of the electron number density n_{es} and electron temperature T_{es} (Sec. 4.5) at the anode pre-sheath/plasma edge. This data, coupled with the ϕ_s and j_a results, will provide estimates of the anode heating q_e, Chapter 6. In addition, n_{es} and T_{es} allow calculations of scalar electrical conductivity σ, thermal conductivity κ and ohmic heating Ω, in the anode boundary layer. The ultimate goal of this work is to provide experimental data to assist in validation of numerical arcjet models, in particular the MKB model.

4.4.2 Effect of Flow Rate on Electron Number Density

Figures 4.29 - 4.33 present the electron number density data for $\dot{m} = 60$, 50 and 45 mg/sec, and $I_{arc} = 9.8$ A and $\dot{m} = 40$ mg/s and $I_{arc} = 10.6$ A. For all flow rates studied, the electron number density at the plasma/pre-sheath edge n_{es}, is largest at x = 1 mm with a secondary peak at x = 4 mm and decreases as the gas flow expands through the nozzle.

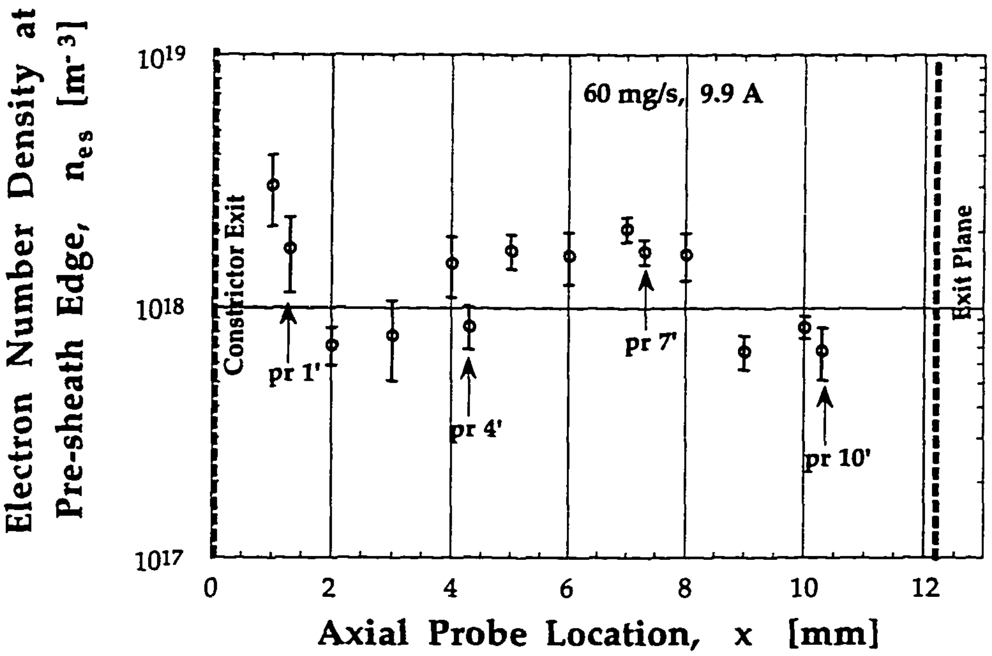

Fig. 4.29 The n_{es} distribution along the anode for $\dot{m}$=60 mg/s and 9.9 A.

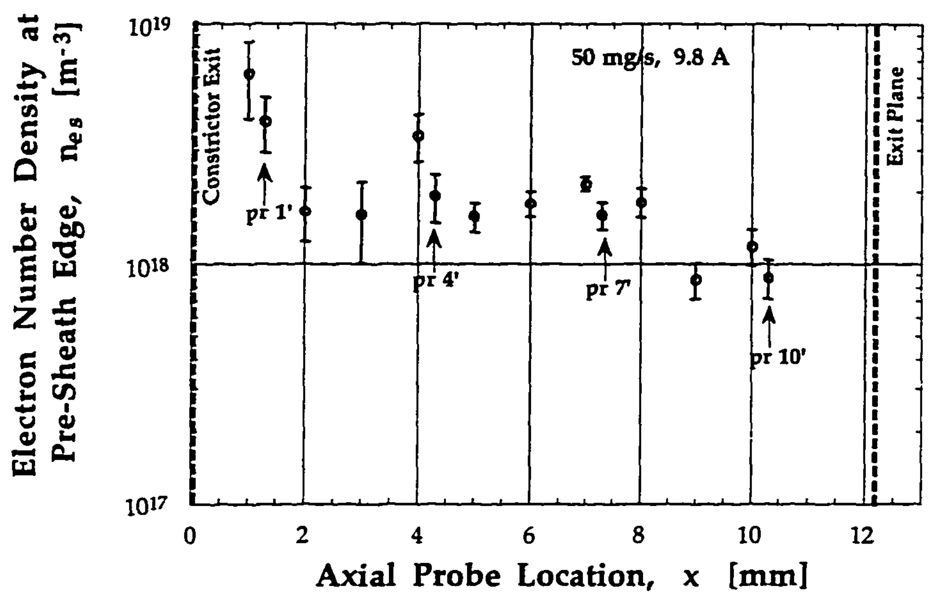

Fig. 4.30 The n_{es} distribution along the anode for $\dot{m}$ = 50 mg/s and 9.8 A.

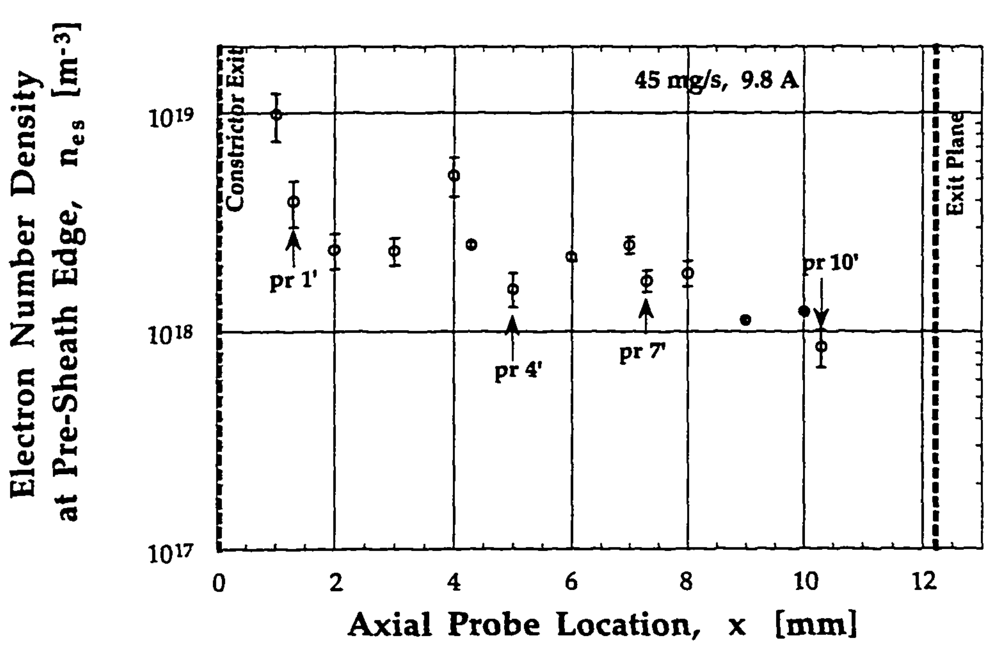

Fig. 4.31 The n_{es} distribution along the anode for $\dot{m}$ = 45 mg/s and 9.8 A.

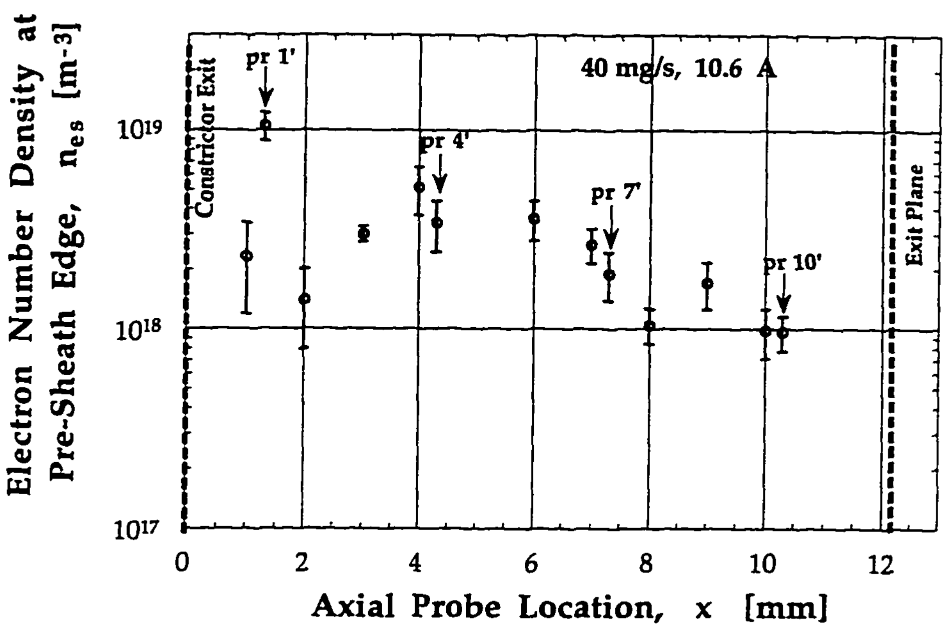

Fig. 4.32 The n_{es} distribution along the anode for $\dot{m}$ = 40 mg/s and 10.6 A.

For all cases studied, the axial variation of n_{es} is gradual, varying from n_{es} = 3.5-10 x 10^{18} m^{-3} at x = 1 mm, to n_{es} = 7-10 x 10^{17} m^{-3} at x = 10 mm. This is approximately a 87% decline in n_{es}. For the higher flow rates of 50 and 60 mg/s, n_{es} reaches a plateau for $4 \leq x \leq 8$ mm, with steep gradients at x = 1-2 mm and 8-10 mm downstream of the constrictor exit. For the lower flow rates, 40 and 45 mg/s, the region where n_{es} plateaus increases in width to $4 \leq x \leq 10$ mm, with steep gradients now only at 1-2 mm downstream of the constrictor.

Symmetry in the n_{es} data is reasonable for all flow rates except $\dot{m}$ = 45 mg/sec, where the largest n_{es} difference between the 0° and 180° probes is 60%, for probes 1 and 1' only. This corresponds to the asymmetry observed earlier for the j_a data for the same conditions; the T_{es} distribution exhibits the same asymmetry as discussed later in Sec. 4.5.

In the region of attachment $1 \le x \le 4$ mm, n_{es} increases with increasing $P/\dot{m}$, with fixed I_{arc}, Fig. 4.33. For $2 \le x \le 4$ mm, as $P/\dot{m}$ increases 38% n_{es} increases by 74%; for $x > 5$ mm increasing $P/\dot{m}$ does not have as large an effect on the n_{es} distribution. For all flow rates studied the maximum electron density is at $x = 1$ mm, corresponding to $(j_a)_{max}$, except for $\dot{m} = 60$ mg/s, where $(j_a)_{max}$ shifts to $x = 3$ mm. For this case (60 mg/s, Fig. 4.33) n_{es} decreases within the first 2 mm of the constrictor and then at $x = 3$ mm n_{es} starts to increase again to a second peak at $x = 4$ mm, where it then levels off until $x = 8$ mm.

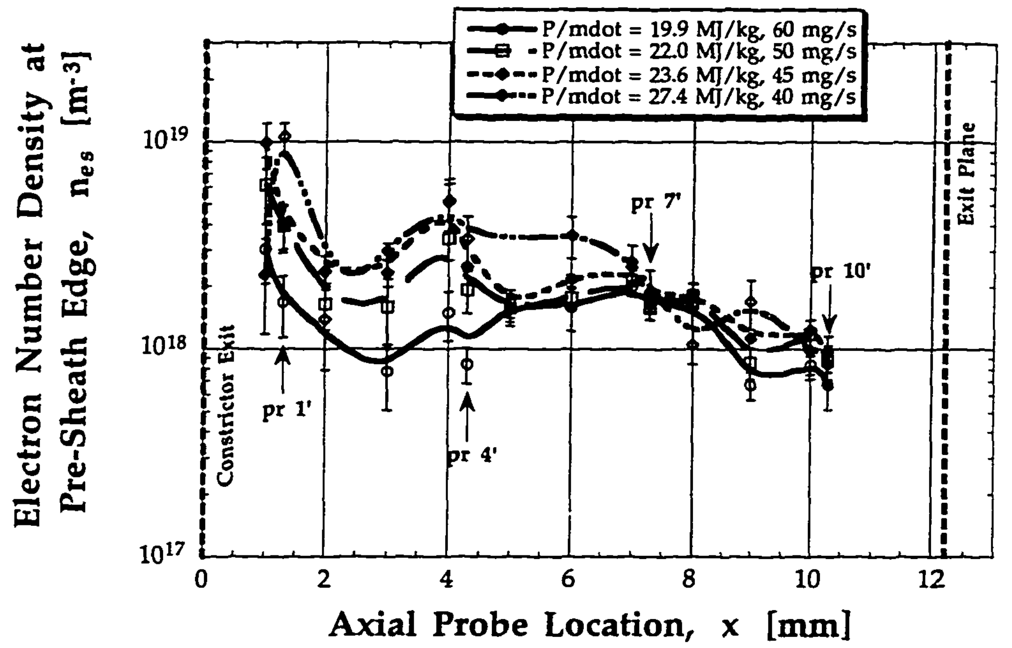

Fig. 4.33 Electron number density distribution along the anode for various propellant flow rates. For $\dot{m}$ = 45, 50 and 60 mg/s I_{arc}= 9.8 A and for $\dot{m}$ = 40 mg/s, I_{arc}=10.6 A.

For all flow rates studied $(n_{es})_{max}$ occurs at $x = 1$ mm with a secondary peak at $x = 4$ mm.

4.4.3 Effect of Arcjet Current on Electron Number Density

The electron number density distribution is important to know since it is the electrons which are the predominant carriers of electrical energy to the anode. Thus, n_{es} should be largest in regions of high current density. This is exactly what has been experimentally observed, as shown in Figs. 4.34-4.35.

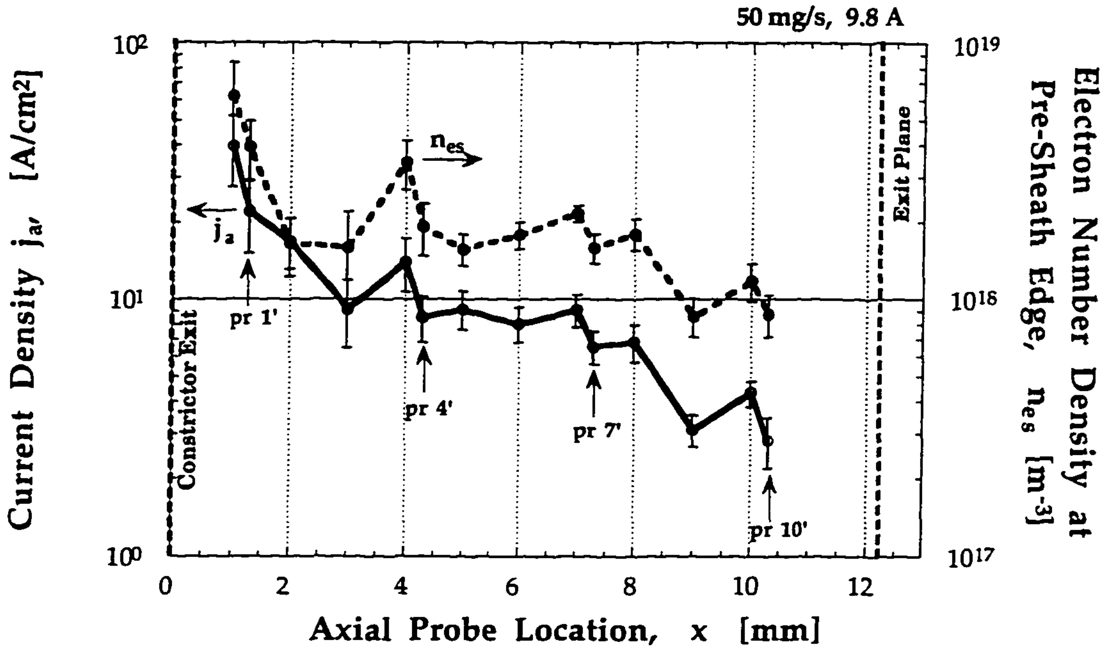

Fig. 4.34 Current density and electron number density distributions for the nominal conditions of 50 mg/s, 9.8 A. The n_{es} profile follows the j_a profile very closely.

The arc ohmically heats the propellant, leading to ionization and the creation of secondary electrons, which carry the current to the anode. These energetic electrons are elevated to a temperature T_{es} much higher than the gas temperature near the anode, due to ohmic heating j_a^2/σ, where σ is the electrical conductivity, Sec. 4.6.1. This elevated T_{es} leads to ionization reactions and an increase in the n_{es} population, resulting in a large electrical conductivity near the wall. Due to the finite electrical conductivity a conduction path is provided for the anodic current attachment. The elevation of T_{es}, coupled with radial diffusion of electrons from the arc core, generates the enhanced electron population near the anode. If T_{es} were equal to T_{gas}, then the electrical conductivity near the anode would be insufficiently low and arc attachment would be difficult. This is why numerical models that assume thermal equilibrium near the anode cannot accurately describe the arc attachment physics and artificially impose limitations on σ. Figure 4.35 presents the electron number density as linearly increasing with j_a. This shows that the arc attachment is dependent on the mechanisms of n_{es} production near the wall through j_a, Fig. 4.34-4.35.

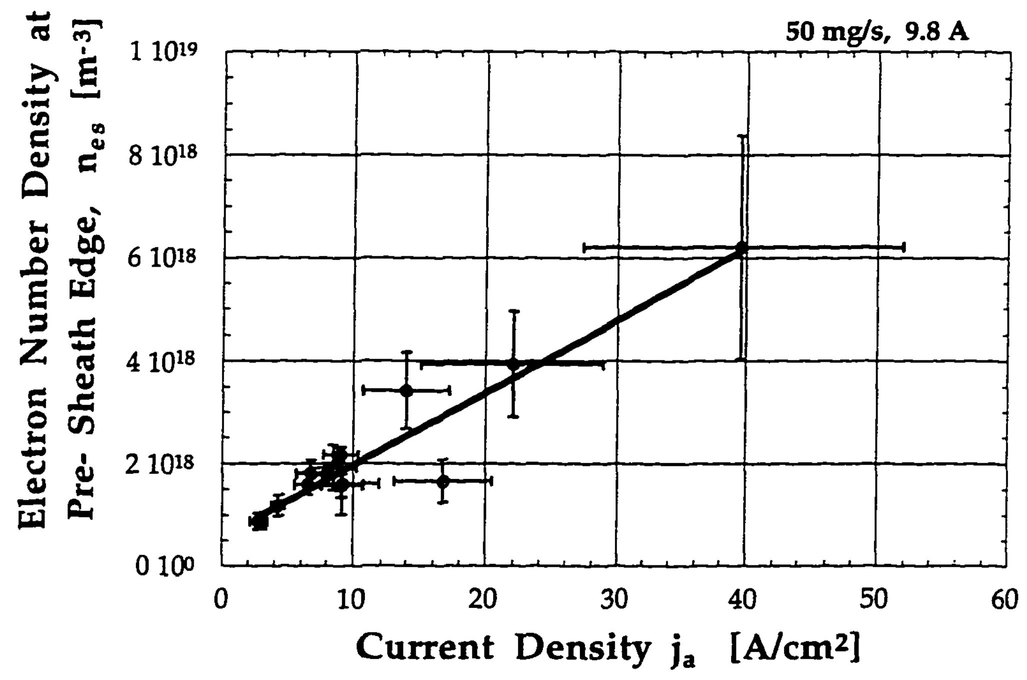

Fig. 4.35 The electron number density is shown as a function of j_a for the nominal conditions of 50 mg/s, 9.8 A.

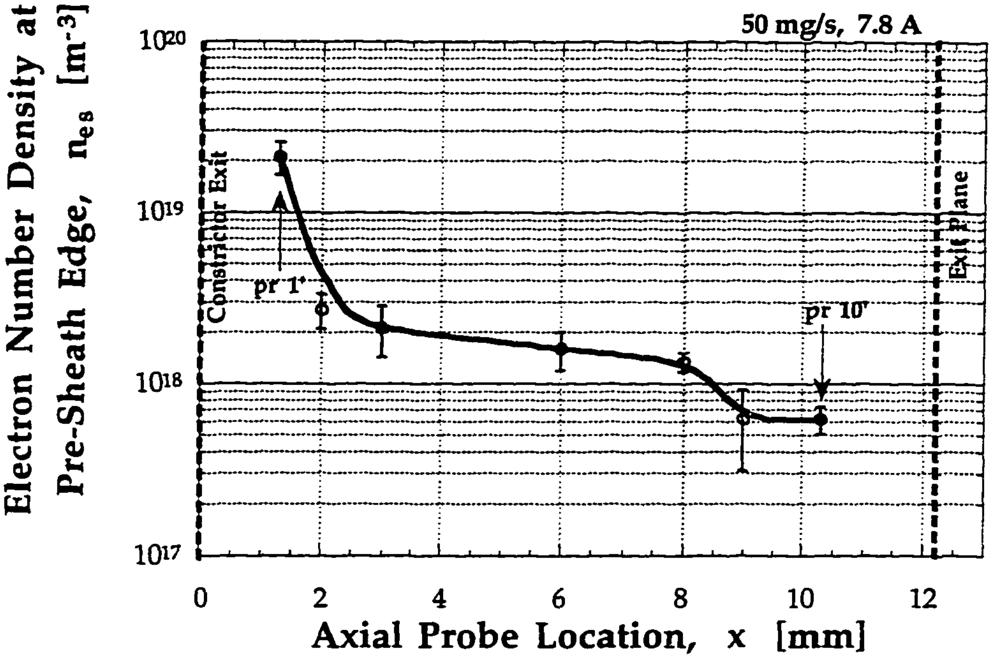

Fig. 4.36 The electron number density distribution is shown for ṁ =50 mg/s, 7.8 A. Data for probes 4,4',5,7 and 10 are not shown due to probe contamination effects.

The effect of varying the arc current on the near-anode electron population was also studied. The results for ṁ = 50 mg/s, I_{arc} = 7.8, 8.9 and 9.8 A are shown in Figs. 4.36, 4.37 and 4.30 respectively. The high P/ ṁ case of 27.4 MJ/kg was presented in Fig. 4.32. For all cases studied, n_{es} decreases as the flow expands toward the nozzle exit. Reasonable azimuthal symmetry in the n_{es} data for the 0° and 180° probes is observed for all arcjet operating conditions.

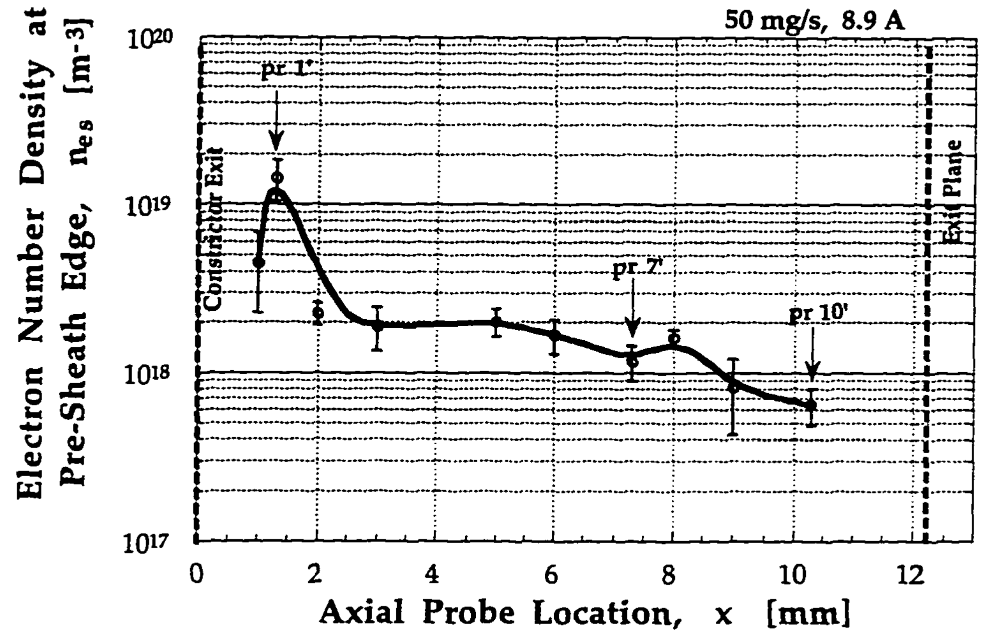

Fig. 4.37 The electron number density distribution is shown for $\dot{m}$=50 mg/s, 8.9 A. Data for probes 4, 4', 7 and 10 are not shown due to probe contamination effects.

Figure 4.38 shows various cases studied of I_{arc} effects on n_{es}. In the region of maximum current density, $1 \leq x \leq 4$ mm, as I_{arc} increases ($P/\dot{m}$ increases), n_{es} increases. For example, for probe 3, as I_{arc} is increased 27%, n_{es} increases by ~ 74%. For the relatively low arc currents of 7.8 and 8.9 A, the axial gradient in electron number density dn_{es}/dx, within 3 mm of the constrictor exit decreases about 87%. As the arcjet operating current decreases $(dn_{es}/dx)_{x=1\text{-}3mm}$ becomes steeper. With increasing arc current, the n_{es} axial profile develops a second plateau in the region $4 \leq x \leq 8$ mm with a concurrent decrease in dn_{es}/dx near the constrictor. Varying I_{arc} does not affect the location of $(n_{es})_{max}$, but it does affect the magnitude of $(n_{es})_{max}$ at x = 1 mm and x = 4 mm, Fig. 4.38.

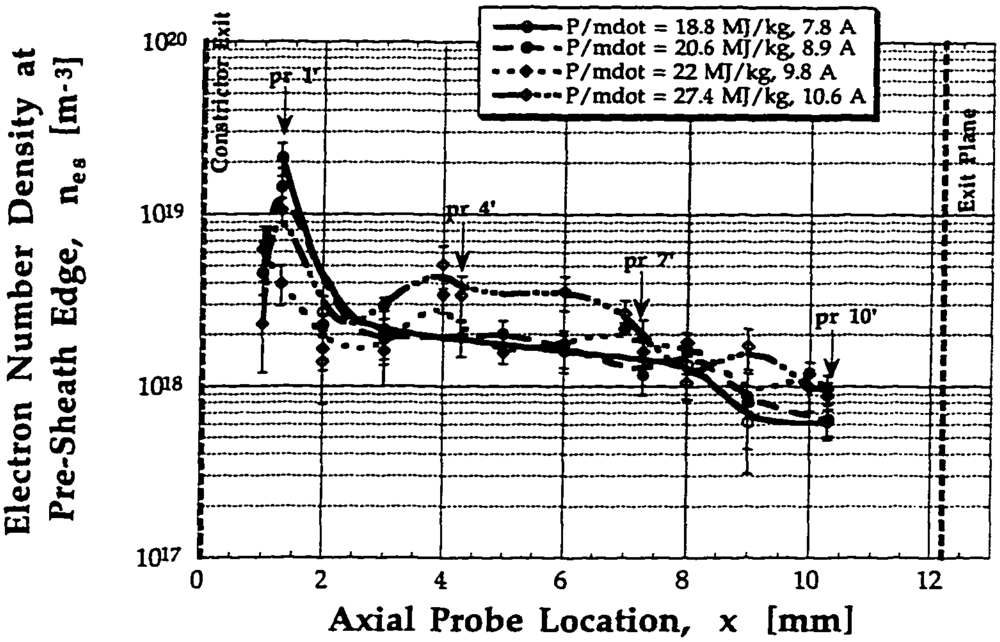

Fig. 4.38 Electron number density distribution along the anode obtained for various arcjet operating currents. For I_{arc}= 7.8, 8.9 and 9.8 A, $\dot{m}$ = 50 mg/s, and for $\dot{m}$ = 40 mg/s, I_{arc}=10.6 A.

With higher arc current and P/$\dot{m}$, the electron population near the anode is redistributed further downstream of the constrictor exit. This coincides with the earlier observation of the I_{arc} and P/$\dot{m}$ effect on the j_a distribution. As I_{arc} increased the j_a profile also developed a plateau region, after initially large axial gradients in j_a within 3 mm of the constrictor, similar to the n_{es} results.

Figure 4.39 shows how n_{es}, T_{es} and j_a are coupled through the electron pressure. As the electron pressure $p_e = n_{es}kT_{es}$, decreases, the current density j_a also decreases; notice the coinciding peaks in p_e and j_a. The electron pressure is part of the total plasma pressure given by Dalton's Law for partial pressures [Megli, 1995]:

$$p = n_e k T_e + \left(n_{N_2} + n_{H_2} + n_N + n_H + n_e\right) k T_{gas} \qquad (4.21)$$

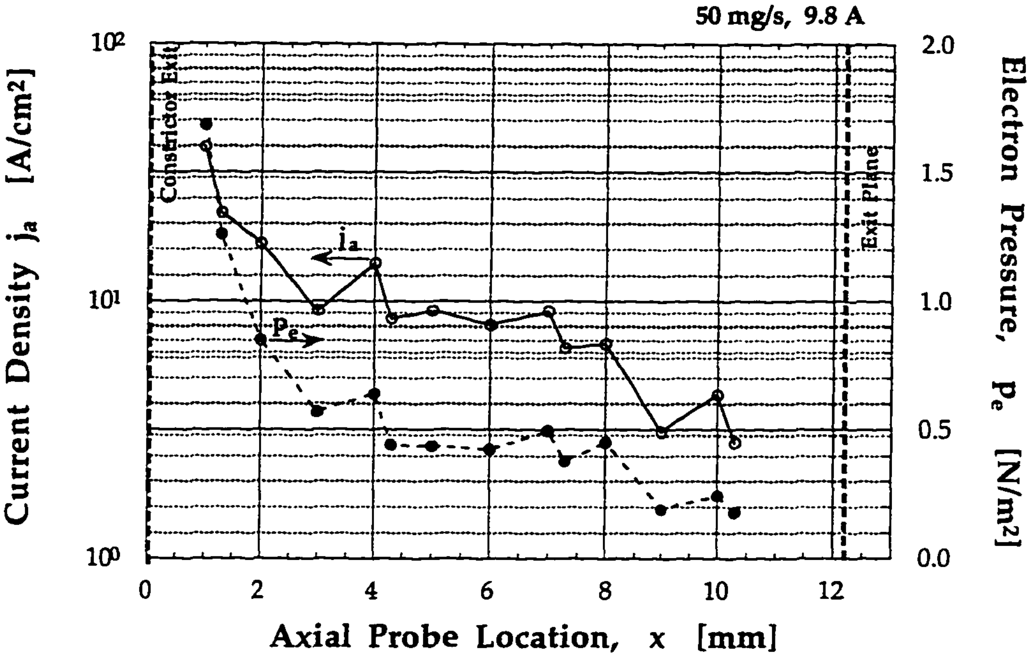

Fig. 4.39 The electron pressure and current density distributions are shown for $\dot{m}$=50 mg/s, 9.8 A.

4.4.4 Effect of Specific Energy on Number Density

The effect of P/ $\dot{m}$ is shown in Fig. 4.40 for the range $18.8 \leq P/\dot{m} \leq 27.4$ MJ/kg. All P/ $\dot{m}$ cases exhibit the same trends: n_{es} is maximum at x = 1 mm with a secondary peak at x = 4 mm. This is similar to the $j_a(x)$ distribution. At x = 1 mm, $(n_{es})_{max}$ occurs for 18.8 MJ/kg and at x = 4 mm n_{es} is largest for 23.6 and 27.4 MJ/kg.

Figure 4.41 shows the effect of P/ $\dot{m}$ on $(n_{es})_{max}$ which approximately follows $(j_a)_{max}$ as a function of P/ $\dot{m}$, Fig. 4.28. For $P/\dot{m} \geq 20.6$ MJ/kg $(n_{es})_{max}$ appears to be relatively independent of increasing specific energy.

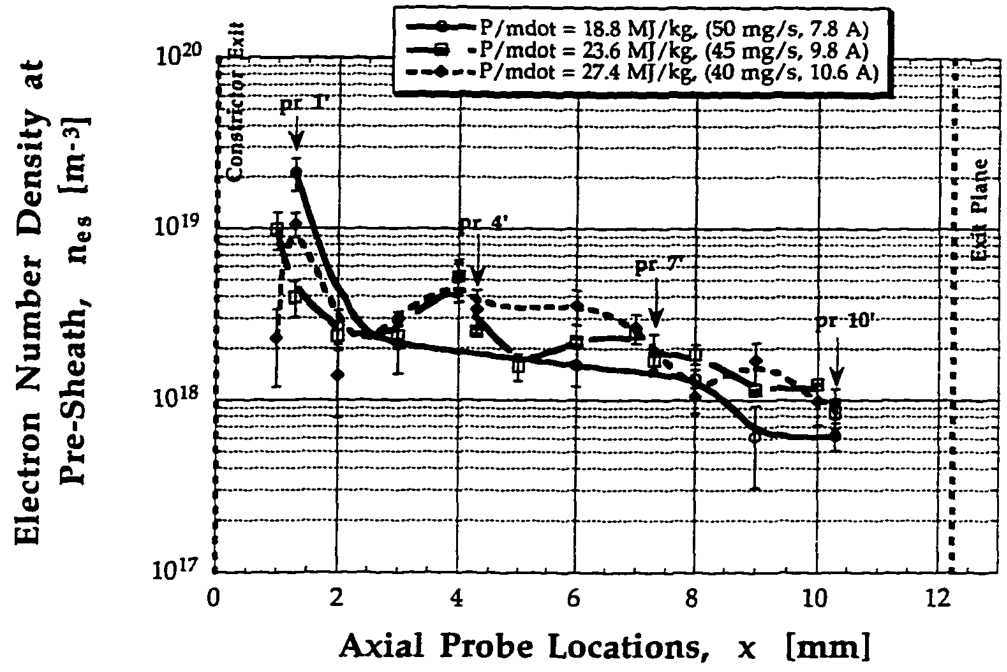

Fig. 4.40 Effect of specific energy on electron number density distribution.

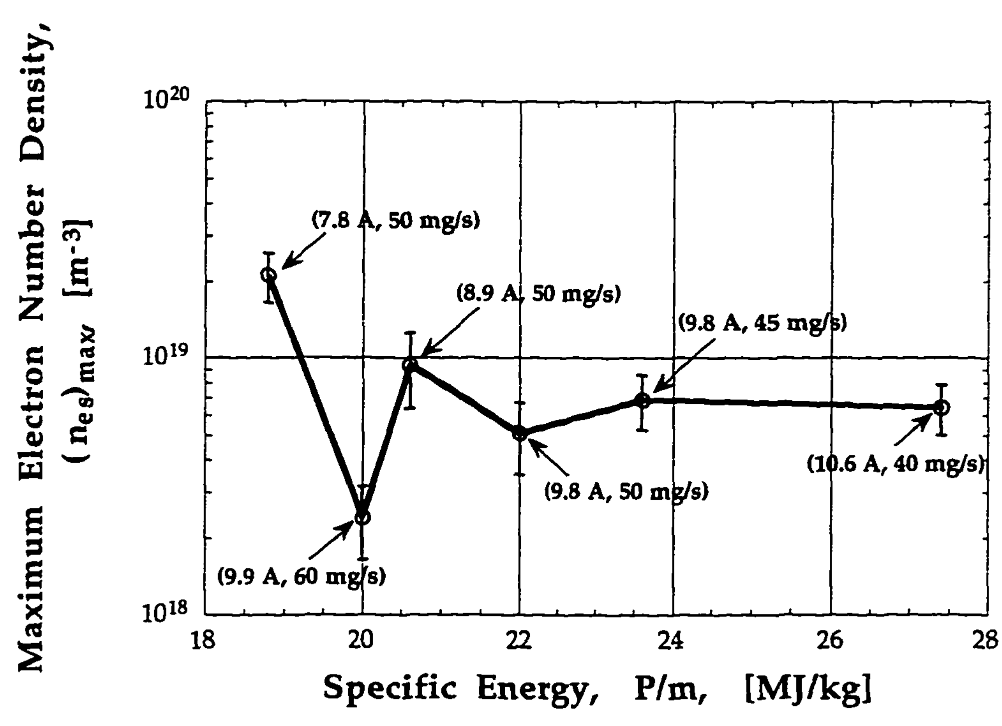

Fig. 4.41 Effect of specific energy on $(n_{es})_{max}$ for various arcjet operating conditions.

4.4.5 Degree of Ionization

The degree of ionization a for a multi-species plasma is defined as:

$$\alpha_{ioniz} \equiv \frac{n_e}{n_{H_2} + n_{N_2} + n_H + n_N} \approx \frac{n_e}{n_{H_2} + n_{N_2}} \tag{4.22}$$

For the nominal arcjet operating conditions of $\dot{m}$ = 50 mg/s, 9.8 A, based on the experimental flush probe data for n_e and the n_{H2} and n_{N2} data from the MKB model, α_{ioniz} varies from $6.6\text{x}10^{-6}$ at x = 1 mm, to $2.7\text{x}10^{-5}$ at x = 5 mm to $7.7\text{x}10^{-5}$ at x = 10 mm.

4.5 Electron Temperature Measurements

In this section the electron temperature distribution along the anode is presented for various flow rates, arc currents and specific energies. The affect of each operating condition on T_{es} is individually studied.

4.5.1 Significance of Electron Temperature

Of equal importance to the current density data is evaluation of the electron temperature T_{es} at the anode pre-sheath/plasma edge. This data, coupled with the ϕ_s and j_a results, will provide estimates of the anode heating q_e. In addition, T_{es} allow calculations of scalar electrical conductivity σ, thermal conductivity κ and ohmic heating O_h, in the anode boundary layer.

4.5.2 Effect of Flow Rate on Electron Temperature

The electron temperature data for $\dot{m}$= 60, 50, 45 mg/sec and I_{arc} = 9.8 A and $\dot{m}$ = 40 mg/s, I_{arc} = 10.6 A, are shown in Figs. 4.42-4.45, respectively. The T_{es} distribution is calculated from the inverse slope of the electron-retarding region, discussed in Sec. 3.3.1. Only for $\dot{m}$= 50, 60 mg/s does the electron temperature at the plasma/pre-sheath edge decrease with increasing distance from the constrictor, for x ≥ 2 mm. Also, for $\dot{m} = 50$ and 60 mg/sec there is an obvious maximum in the T_{es} data, at x = 2 mm. This maximum may be due to artificially large T_{es} values for probe 2, which was found to be slightly contaminated, since post-test observations of probe 2 showed a light discoloration of the probe tip. However, a continuity check on the probe showed good conduction and inspection of its V-I curve displayed minimal hysteresis in the electron-retarding region used to derive T_{es}; therefore this data point was included in the analysis.

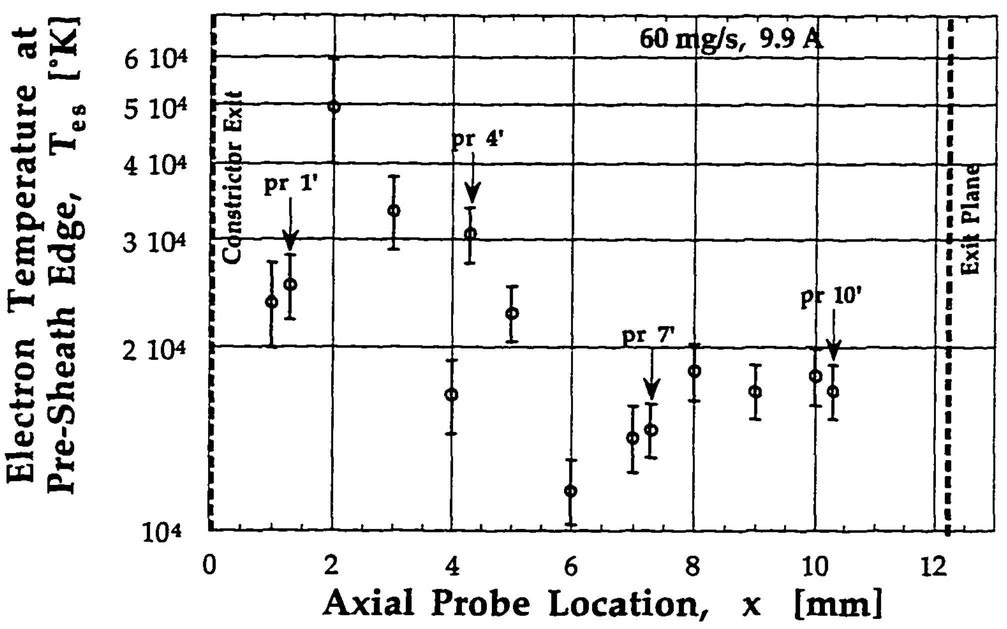

Fig. 4.42 Electron temperature distribution along the anode for $\dot{m} = 60$ mg/s and 9.9 A.

For 40 and 45 mg/sec flow rate, Figs. 4.44-4.45, the axial electron temperature gradient in the arc attachment region 1 ≤ x ≤ 4 mm, is small, with a relatively flat T_{es} distribution along the anode. Similarly, as the flow rate is increased to 50 and 60 mg/sec, dT_{es}/dx in the arc attachment region increases, "compressing" the electron temperature profiles in the low current density region, for x ≥ 4 mm. As the flow rate decreases, for $\dot{m}$ = 45-60 mg/sec, P/ $\dot{m}$ increases for a fixed I_{arc}. This leads to a flatter T_{es} distribution throughout the anode sheath layer. The increased heat transfer in the anode sheath at higher P/ $\dot{m}$ is convected along the anode at all probe locations, perhaps contributing to the relatively flat axial T_{es} distribution for the higher P/ $\dot{m}$ situations, i.e. lower flow rates.

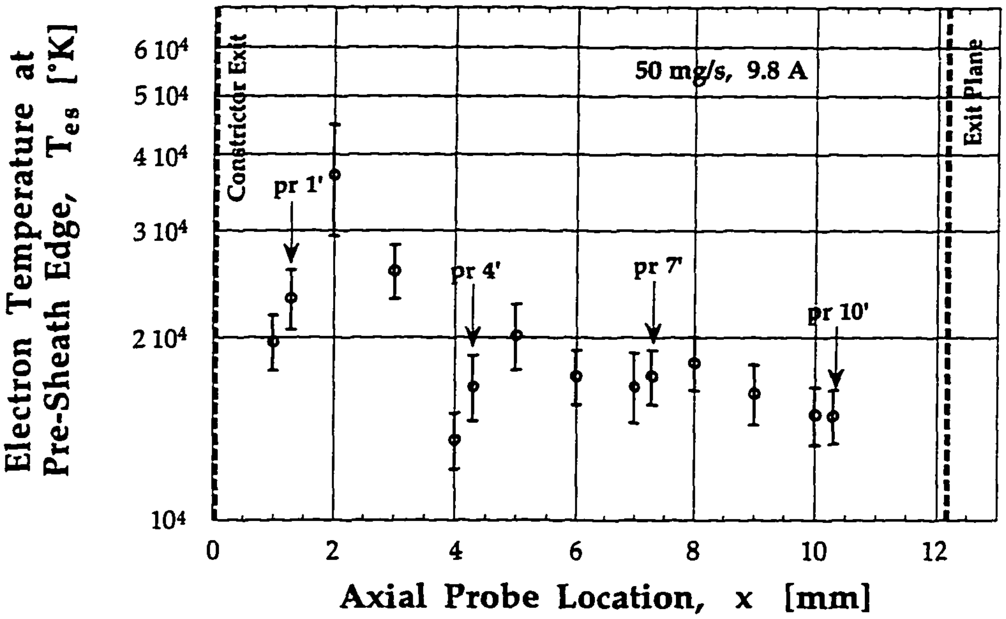

Fig. 4.43 Electron temperature distribution along the anode for $\dot{m}$ = 50 mg/s and 9.8 A.

The symmetry in the T_{es} data for the 0° and 180° probes is reasonably good, except for the high P/ $\dot{m}$ case (27.4 MJ/kg) for $\dot{m}$ = 40 mg/sec and I_{arc} = 10.6 A, where the average T_{es} data for probes 1 and 1′ differ by about 35%. For $\dot{m}$ = 45 mg/sec the average T_{es} data for probes 1, 1′ and probes 7, 7′ differ by about 32%.

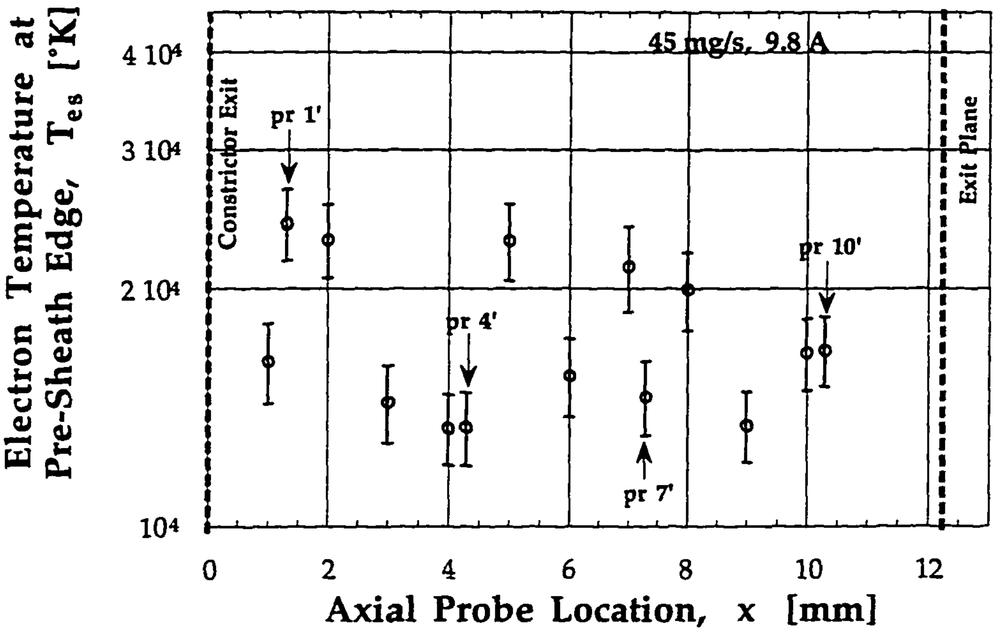

Fig. 4.44 Electron temperature distribution along the anode for $\dot{m}$ = 45 mg/s and 9.8 A.

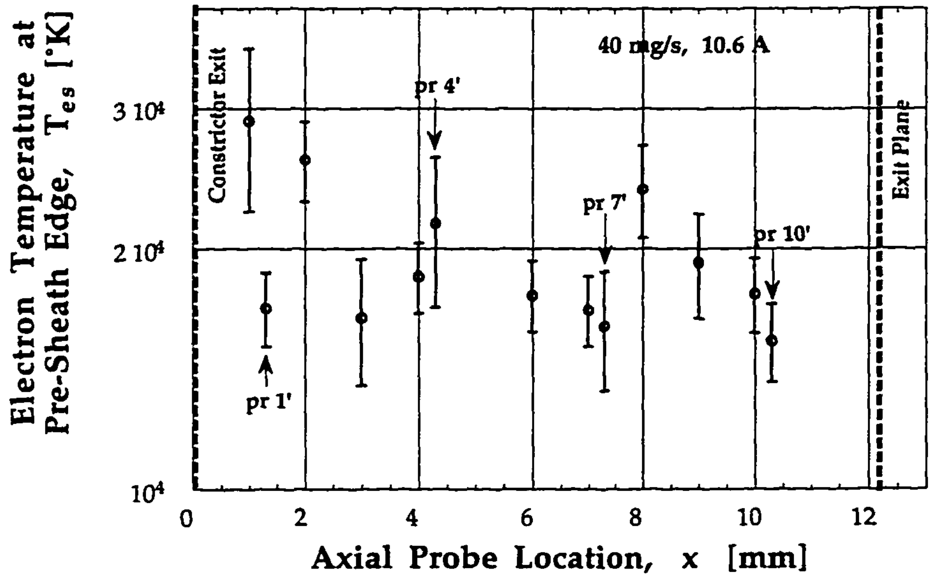

Fig. 4.45 Electron temperature distribution along the anode for $\dot{m}$= 40 mg/s and 10.6 A.

For all propellant flow rates tested, the ratio $T_{es}/T_g >> 1$ in the near-anode region, at all probe locations. If an average gas temperature at the anode wall of 1400 °K is assumed then $T_{es}/T_g \sim O(10\text{-}20)$. This value for the gas temperature is reasonable since nozzle surface temperature measurements yield $T_{noz} \sim 950$ °K and the MKB model predicts $T_{gas} \sim 1200$ ° K along the interior anode surface. The fact that $T_{es}/T_g >> 1$ clearly demonstrates that a nonequilibrium plasma, with dual temperatures, exists in the near anode region of an electrothermal arcjet thruster. The MKB model, discussed in Chapter 7, accounts for this nonequilibrium plasma condition throughout the arcjet nozzle.

4.5.3 Effect of Arcjet Current on Electron Temperature

The effect of varying the arcjet operating current on the electron temperature distribution is shown in Fig. 4.46 for a fixed $\dot{m}$ of 50 mg/s and I_{arc} = 7.8, 8.9 and 9.9 A.

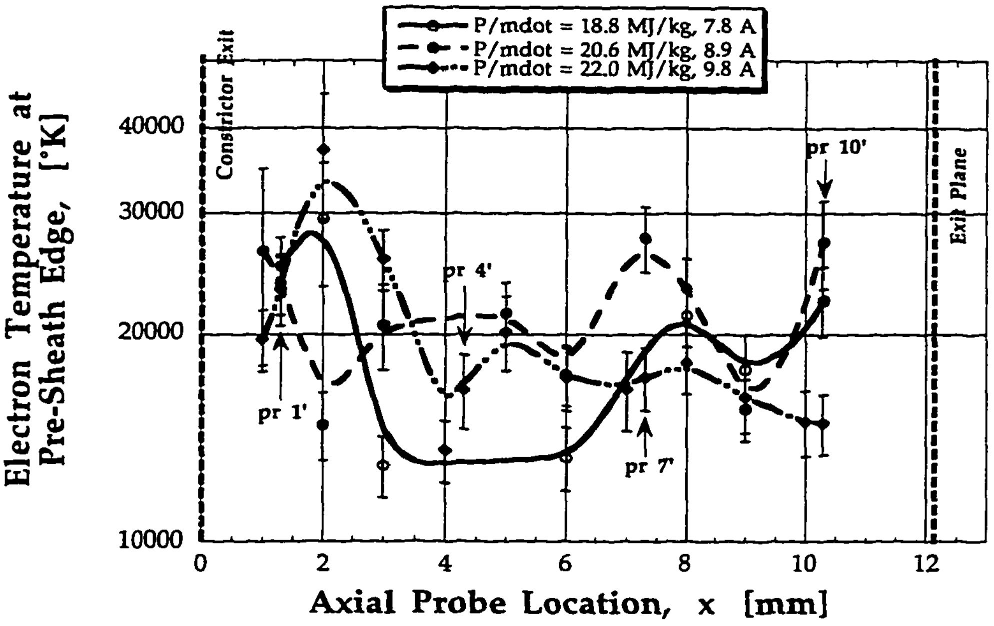

Fig. 4.46 The effect of I_{arc} on the T_{es} distribution for fixed $\dot{m}$ = 50 mg/s.

The T_{es} profiles for each of the above conditions are shown in Figs. 4.43, 4.45 and Figs. 4.47-4.48. There appears to be no obvious trend in the T_{es} profiles with increasing arc current.

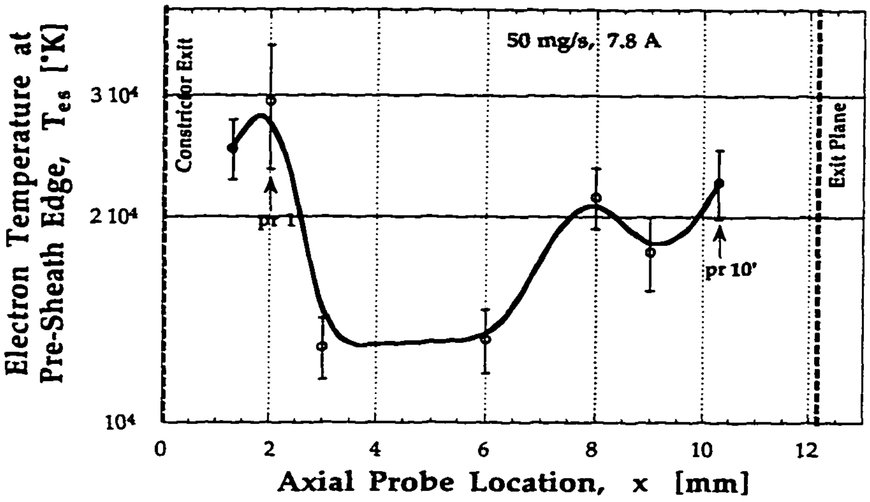

Fig. 4.47 The T_{es} distribution for $\dot{m}$ = 50 mg/s, I_{arc}= 7.8 A and V_{arc}= 121 V.

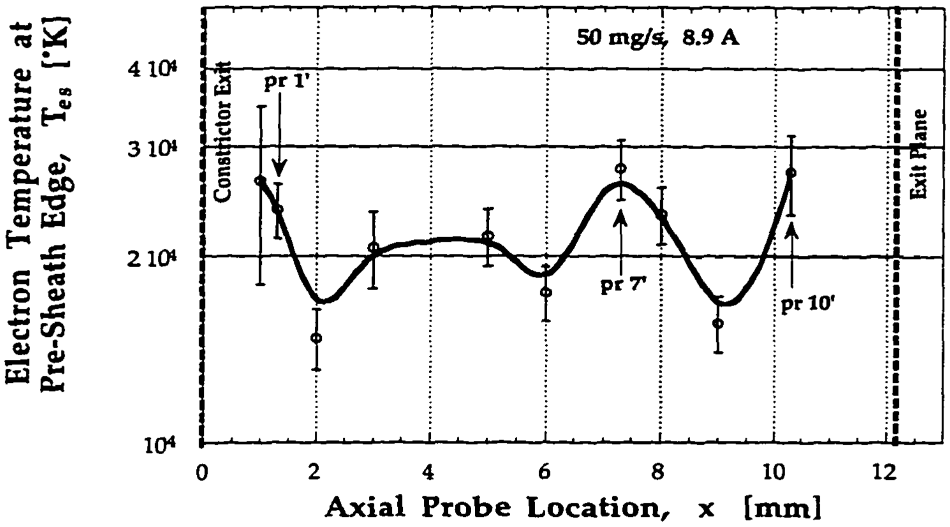

Fig. 4.48 The T_{es} distribution for $\dot{m}$ = 50 mg/s and I_{arc}= 8.9 A, V_{arc}=115 V.

4.5.4 Effect of Specific Energy on Electron Temperature

Figure 4.49 shows the effect of $P/\dot{m}$ on the electron temperature distribution T_{es}, for three different flow rates and arc currents. At x = 1 mm and x = 4 mm as the specific energy increases, T_{es} increases as well.

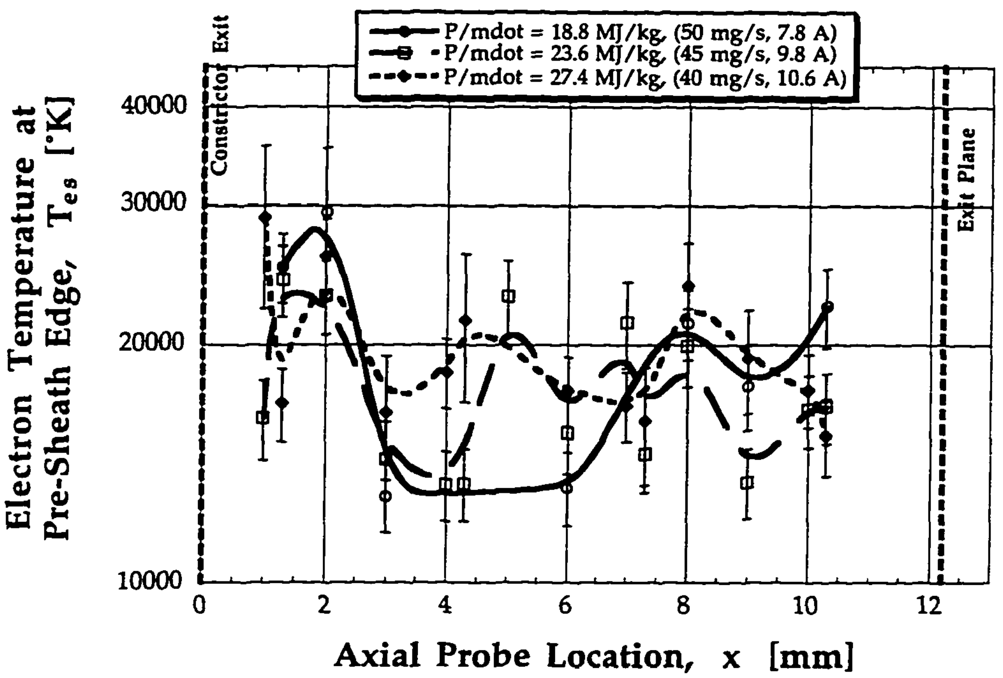

Fig. 4.49 The electron temperature distribution at all probe locations for various specific energies studied.

Figure 4.50 shows $(T_{es})_{max}$ as a function of $P/\dot{m}$. The largest effect on $(T_{es})_{max}$ is for the lower $P/\dot{m}$ values, $20 \leq P/\dot{m} \leq 22$ MJ/kg.

Figure 4.51 displays the maximum electron temperature for each operating condition tested as a function of $N_2 + 2H_2$ flow rate. From Fig. 4.51 it is shown that: (1) for constant I_{arc}, as the flow rate increases $(T_{es})_{max}$ increases; (2) the largest $(T_{es})_{max}$ is for $\dot{m}$ = 60 mg/s and P_{max} = 1200 W, which also corresponds to $(\phi_s)_{max}$ and the largest $\bar{\phi}_S$ value, Fig. 4.16; and (3) for constant m = 50 mg/s, $(T_{es})_{max}$ is largest for I_{arc} = 9.9 A.

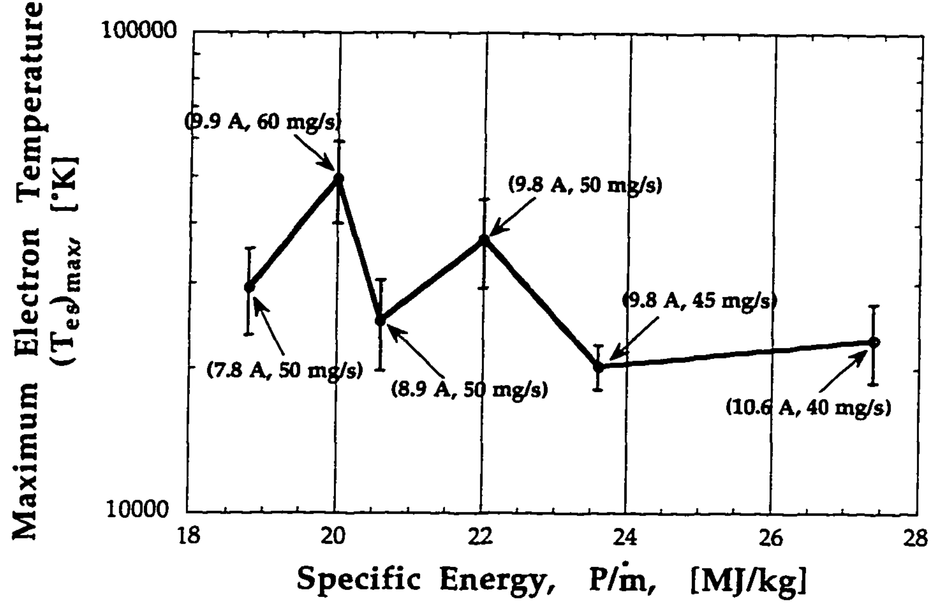

Fig. 4.50 The effect of varying the specific energy P/ ṁ on $(T_{es})_{max}$.

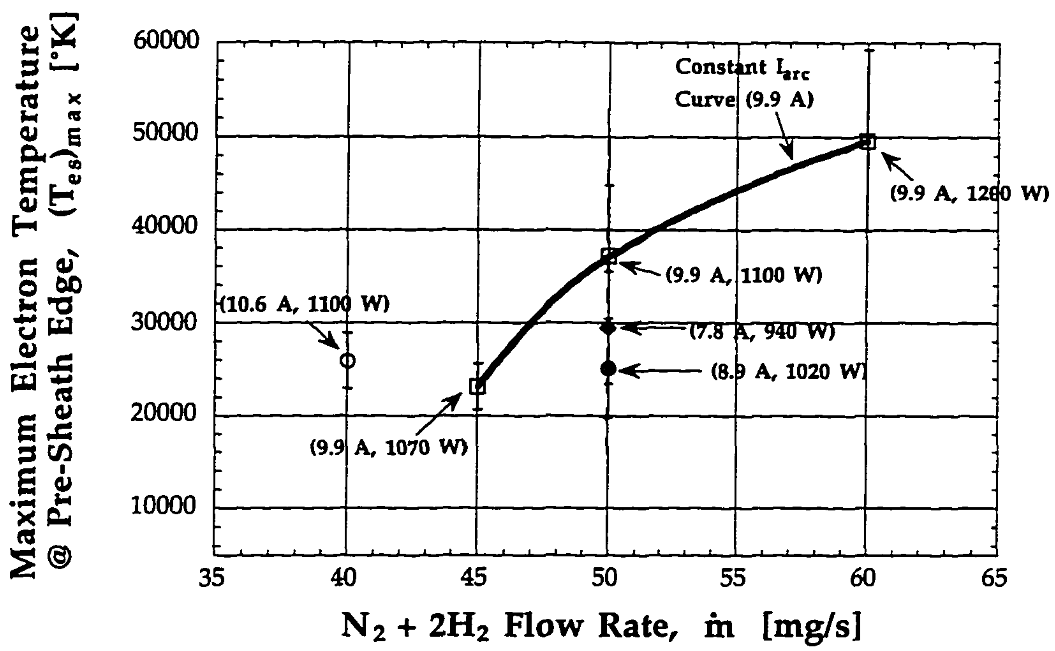

Fig. 4.51 The maximum electron temperature obtained for each operating condition tested as a function of propellant flow rate.

4.6 Measurement of Plasma Properties

The numerical simulation of the arcjet is complicated by the fact that the inherent gas dynamic and plasmadynamic phenomena are highly coupled. Simulation of arcjet behavior and performance requires an accurate prediction of the voltage and current distributions, which affect the heat addition, which controls the pressure and temperature, in turn feeding back to the mass and energy transport mechanisms. For example, mass, thermal energy diffusion and species diffusion both influence the electron population distribution, especially near the anode, thus coupling with the electrical and thermal conductivities. Therefore, knowledge of the transport properties is vital to predicting current attachment and therefore anode heating. This is especially important for evaluating thruster performance at high specific energies. An accurate assessment of the plasma properties in the flowfield, especially near the anode, is also required to realistically model and predict arc attachment and thruster performance.

In this section, calculations of the scalar electrical conductivity σ, the resistive electric field E_{pl} in the bulk plasma at the pre-sheath/plasma edge, and the anode sheath electric field E_{sh}, are presented for the nominal experimental conditions of 50 mg/s and 9.8 A. It is the author's intention to provide the numerical arcjet modeling community with some experimental data and references to calculate these properties for other arcjet operating conditions.

4.6.1 Calculation of Scalar Electrical Conductivity

The main function of any rocket nozzle is to efficiently extract kinetic energy from the generation of thermal and chemical energy in the plenum chamber. In electrothermal arcjets the thermal energy is created by the interaction of the arc with the propellant gas flow. The electrons are ohmically heated by the electric field, exchanging energy with the ions and neutrals via collisions. The ohmic heating is given by j^2/σ, where σ is the scalar electrical conductivity of the plasma, [Mitchner *et al.*, 1973]:

$$\sigma = \frac{n_{es}e^2}{m_e \sum\limits_{i \neq e} n_i c_e \overline{\Omega}^{(1,1)}_{e-i}} \tag{4.23}$$

where $\overline{\Omega}^{(1,1)}_{e-i}$ is the energy-averaged collision integral for heavy particle collisions, [Spencer *et al.*, 1976]. Equation (4.23) is for a partially ionized plasma, which exists near the anode since the ionization fraction is ~ 10^{-6}-10^{-5}, Sec. 4.4.5. The concept of electrical conductivity, as well as other transport properties derived based on the Chapman-Enskog theory, is meaningless inside a sheath. This is because large sheath electric fields lead to deviations from a Maxwellian distribution violating a critical assumption of the Chapman-Enskog theory [Mitchner, *et al.*, 1973] which is that only small deviations from the Maxwellian distribution are allowed. Also, plasma property measurements are obtained at the sheath edge, so that σ can only be evaluated at the sheath edge, i.e. in the quasineutral plasma, and not inside the sheath.

For a fully ionized plasma, or a partially ionized plasma if $\nu_{ei} \gg \nu_{en}$, Eq. (4.23) is replaced with the Spitzer conductivity, [Mitchner, *et al.*, 1973]. Based on the mean free path calculations presented earlier the electron-H_2 collision frequency is dominate over ion-H_2 collisions and $\nu_{ei} \ll \nu_{en}$ so that:

$$\nu_c \equiv \sum_{i \neq e} n_i c_e \overline{\Omega}^{(1,1)}_{e-i} = \nu_{e\text{-}H_2} + \nu_{e\text{-}N_2} \tag{4.24}$$

The electrical conductivity controls the current distribution, which as shown later (Chapter 6), controls the anode heating, q_e. Many of the earlier single fluid ($T_e=T_i=T_{gas}$) numerical models [Rhodes *et al.*, 1990; Butler, *et al.*, 1994] have the shortcoming of predicting unrealistically low n_{es} and σ in the near anode region, so that no mechanism exists for the current to reach the anode. These single fluid models remedy this situation by introducing a conductivity floor σ_a, ~O(10-100[Ω-m]$^{-1}$). This number is selected to provide a good prediction of total arcjet voltage. However, once the constant conductivity floor is implemented, the model loses the ability to predict the current distribution along the anode, [Martinez-Sanchez, *et al.*, 1996].

In this work, the electrical conductivity along the anode is calculated knowing n_{es} and T_{es} from the experimental data and using Eqs. (4.23) and (4.24) with constant collision cross sections for $Q_{e\text{-}H_2}$ and $Q_{e\text{-}N_2}$, [Spencer, *et al.*, 1976; Megli, 1995]. Figure 4.52 shows σ and j_a along the anode wall for the nominal conditions of $\dot{m} = 50$ mg/s and 9.8 A; σ varies between 1.2 $[\Omega\text{-m}]^{-1}$ at $(j_a)_{max}$ (x = 1 mm) to 17 $[\Omega\text{-m}]^{-1}$ (x = 10 mm). It is interesting that σ increases with increasing distance from the constrictor. This is primarily due to the rapid expansion of the propellant gas, resulting in a faster decrease in the electron-heavy particle collision frequency than n_{es}, leading to the observed increase in electrical conductivity, since $\sigma \sim 1/\nu_c$. At x = 1 mm, where $(j_a)_{max}$ occurs, σ is at its minimum because the e-H_2 collision frequency is relatively large, ~ 10^{11} sec^{-1}, decreasing to ~10^{9} sec^{-1} at x = 10 mm.

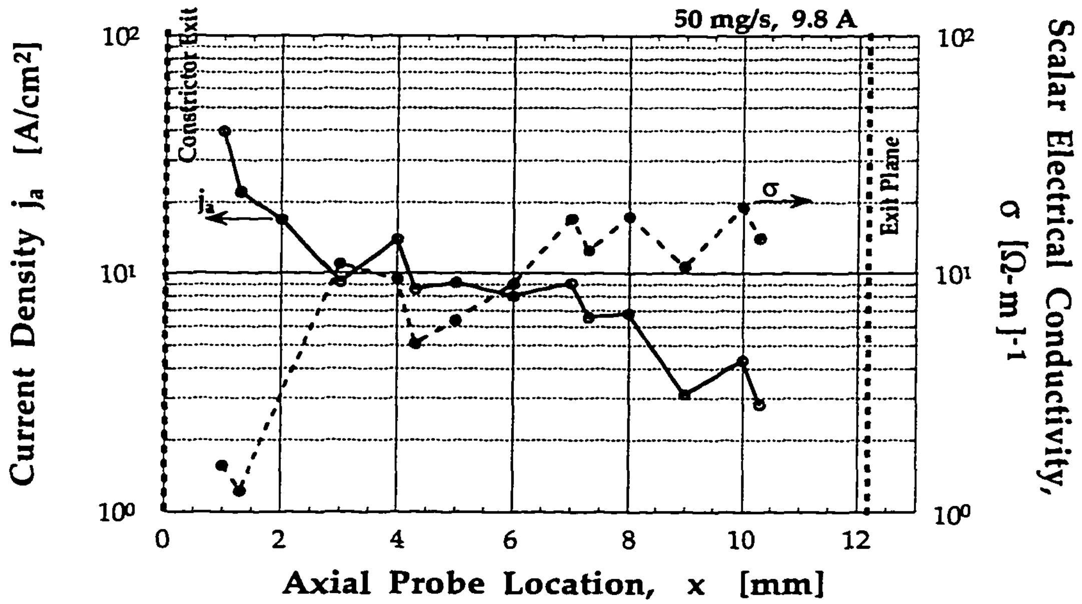

Fig. 4.52 The electrical conductivity and current density distributions for $\dot{m} =$ 50 mg/s and $I_{arc} = 9.8$ A.

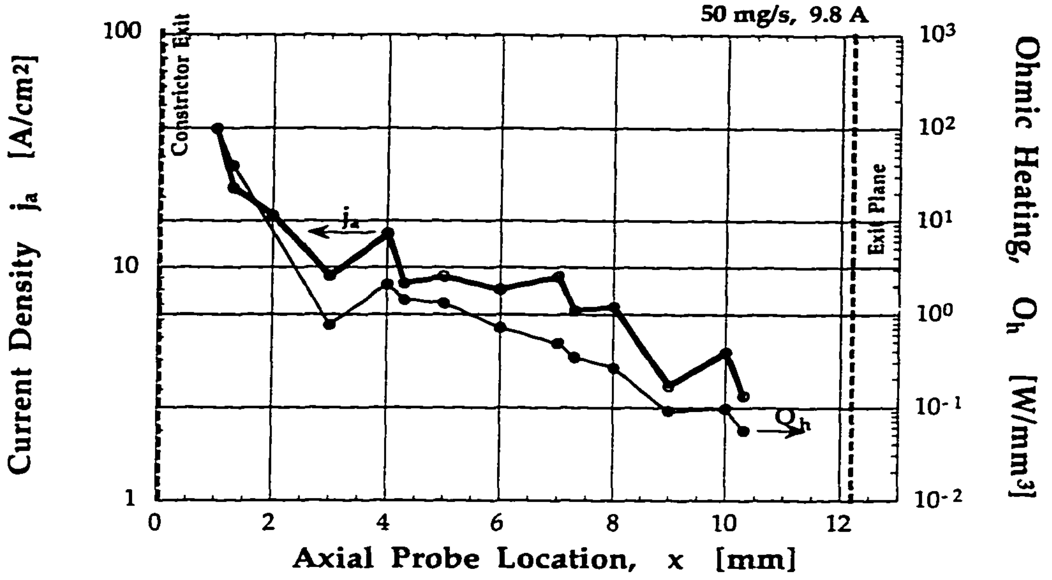

Fig. 4.53 The O_h and j_a distributions for $\dot{m} = 50$ mg/s and $I_{arc} = 9.8$ A.

Once σ is known, the ohmic heating distribution $O_h = j_a(x)^2/\sigma(x)$ is calculated and was found to vary from 100 W/mm^3 at x = 1 mm to 0.1 W/mm^3 at x = 10 mm; since $O_h(x) \sim j_a(x)^2$, the ohmic heating profile is similar to the $j_a(x)$ distribution and is presented in Fig. 4.53.

4.6.2 Calculation of Ambipolar Electric Field

An electric field is created by the presence of the arc and serves to ohmically heat the electrons as it accelerates them towards the anode.

In a quasineutral plasma the electron and ion number densities are approximately equal. If there were a charge imbalance then the flux of electrons and ions would not be equal and the rates of species diffusion would have to adjust themselves to correct the imbalance. This is accomplished by an ambipolar electric field. Because the electrons are the lighter species with a higher thermal velocity they would diffuse from the bulk plasma at a faster rate than the more heavy ions. An electric field is then set up to oppose the electron motion and aid the ion motion thus producing the necessary species flux balance, [Chen, 1983].

The electric field near the anode is given by [Sutton, *et al.*, 1965]:

$$E \cong \frac{j_a}{\sigma} - \frac{kT_{es}}{e}\frac{\nabla n_{es}}{n_{es}} \tag{4.25}$$

where the first term on the RHS of Eq. (4.25) is the resistive electric field in the bulk plasma at the sheath edge E_{pl} and the second term is the ambipolar electric field at the sheath edge. The resistive electric field is not definable in the sheath since the electrical conductivity is meaningless in the sheath, for reasons discussed earlier in Sec. 4.6.1. The sheath electric field $E_{sh}=\phi_s(x)/\lambda_{s,e}(x)$ where ϕ_s is the anode sheath potential and $\lambda_{s,e}(x)$ is the collisionless electron sheath thickness at $V_p= 0$ V, given by Eq. (3.17).

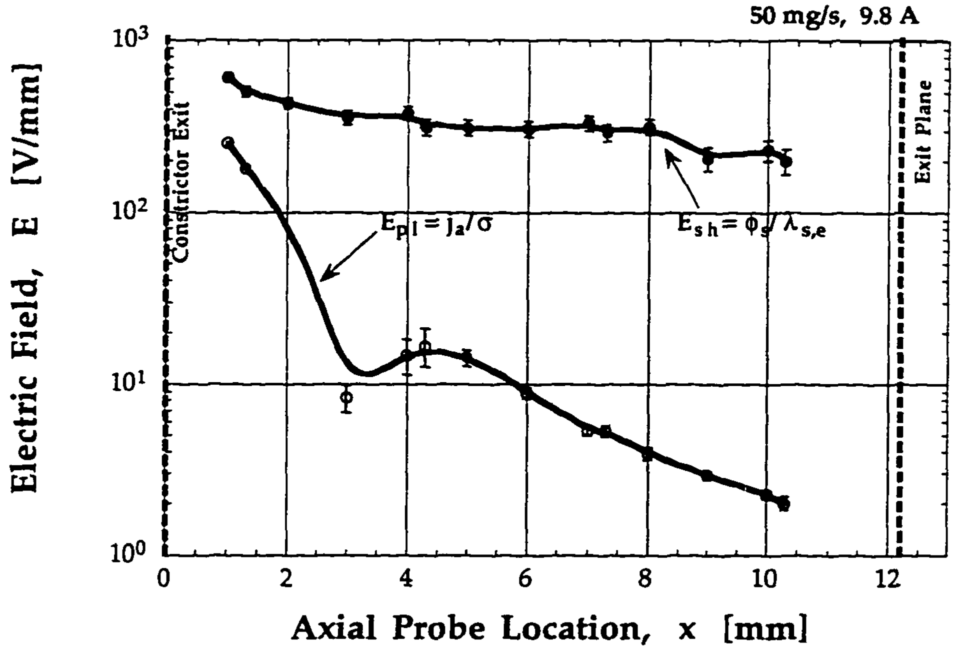

Fig. 4.54 The resistive (j_a/σ) and sheath electric field ($\phi_s/\lambda_{s,e}$) distributions are shown for the nominal experimental conditions of $\dot{m}= 50$ mg/s and $I_{arc} = 9.8$ A; the data is from the flush probe configuration. The sheath electric fields are much larger than the resistive electric fields since the sheath is a region of non-neutrality.

Figure 4.54 shows both the sheath and resistive electric field distributions for the nominal experimental conditions. As expected, the sheath electric field is much larger than the resistive field, since the sheath is a region of non-neutrality and large electric field strength. The resistive electric field varies from ~250 V/mm at x = 1 mm to ~2 V/mm at x = 10 mm. The sheath electric field varies from ~600 V/mm at x = 1 mm to ~200 V/mm at x = 10 mm; thus, the ratio of E_{sh}/E_{pl} varies from ~ 3:1 at x = 1 mm to ~20:1 at x = 10 mm.

5. CYLINDRICAL PROBE RESULTS

5.1 Experimental Operating Conditions

An interesting and useful feature that electrostatic probes have over several spectroscopic methods is their ability to provide relatively high spatial resolution. In this work, in addition to flush-mounting the probes, they were also extended approximately 0.25-.3 mm for probes 2-10′ and ~0.1-0.15 mm for probes 1,1′, into the plasma flow. This is referred to as the cylindrical probe configuration. Though the boundary layer was not probed extensively, information about ϕ_f, ϕ_s, j_a, n_{es} and T_{es} was obtained. Cylindrical probe data is presented for the nominal arcjet conditions of 50 mg/s, 9.9 A and 112 V.

In this chapter cylindrical probe results are presented for various flow rates and comparisons are made between the flush probe and cylindrical probe data for ϕ_f, ϕ_s, j_a, n_{es}, and T_{es} distributions.

5.2 Utility of Cylindrical Probes for Arcjet Diagnostics

When the electrostatic probes are flush-mounted along the anode wall no physical disturbance to the plasma flow is induced. In an attempt to probe the anode sheath boundary layer, cylindrical probes were fabricated and positioned transverse to the flow, with the alumina tubing flush with the anode wall. The possible flow disturbance due to the physical presence of the cylindrical probe is a concern. To address this situation, radial flow Mach number profiles are calculated using the MKB model, Chapter 7, at each probe location for L_{ext} ~ 0.25 mm and 60 mg/s, as shown in Fig. 5.1.

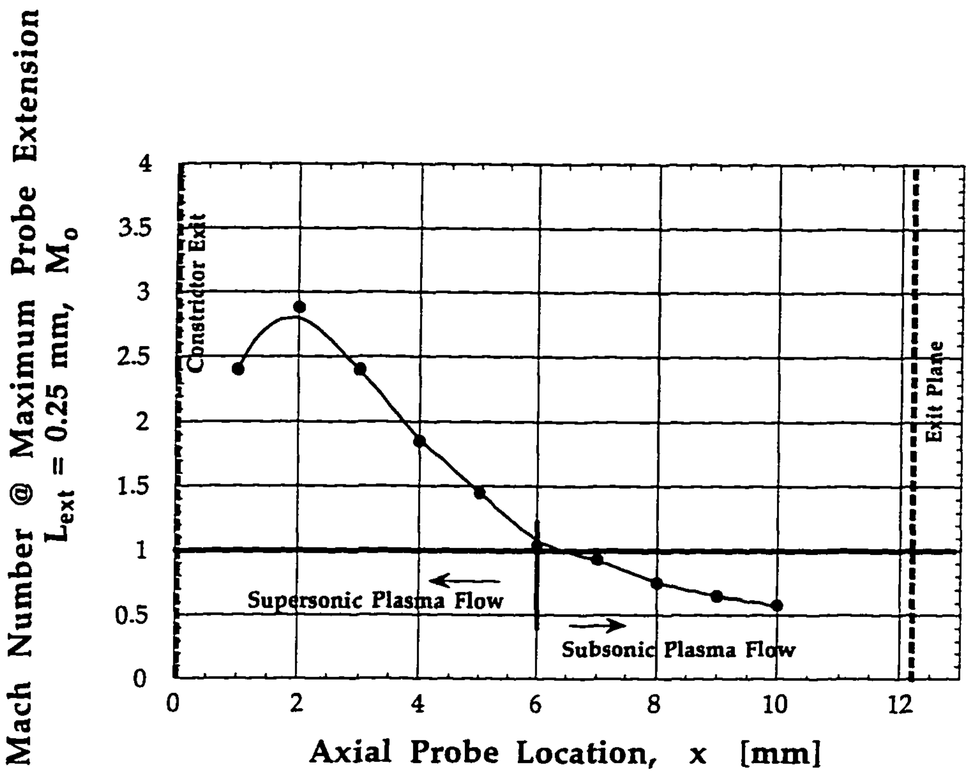

Fig. 5.1 Flow Mach numbers at each probe location are calculated using the MKB model for the cylindrical probe configuration and $\dot{m}$ = 60 mg/sec and I_{arc} = 10 A.

Figure 5.1 shows that the plasma flow Mach number M_0 is supersonic within 6 mm of the constrictor exit. Because the cylindrical probe, a blunt body, is positioned in a supersonic plasma flowstream, weak Mach waves or Prandtl-Meyer expansion fans may form near the probe surface, based on the MKB model calculations. However, in the region between the probe leading edge, facing the oncoming flow and the anode, strong oblique shocks may also form. Since large density and temperature gradients exist across a shock wave, such a condition may complicate the data analysis for calculating the electron number density and electron temperature at the sheath edge.

In order to establish whether cylindrical probe-induced shocks affect the probe response, the cylindrical and flush probe V-I characteristics for probe 4 are compared. Approximations were made for the probe collection area so that the probe current could be normalized with respect to this area to obtain the probe current density j_p versus V_p. Figures 5.2-5.3 show j_p-V_p characteristics for probe 4. The j_p-V_p characteristic for probe 1 was also analyzed and similar trends are observed between the flush and cylindrical probes. Differences between the two probe configurations are attributed to uncertainties in the probe collection area; for example, for probe 1 the alumina tubing was partly cracked exposing an unknown amount of probe area. Excellent agreement between the two probe configurations for the region of interest, $V_p \leq 0$ V (Fig. 5.2), shows that the cylindrical probe is not disturbing the flow, thus eliminating the concern of induced shock formation on its surface.

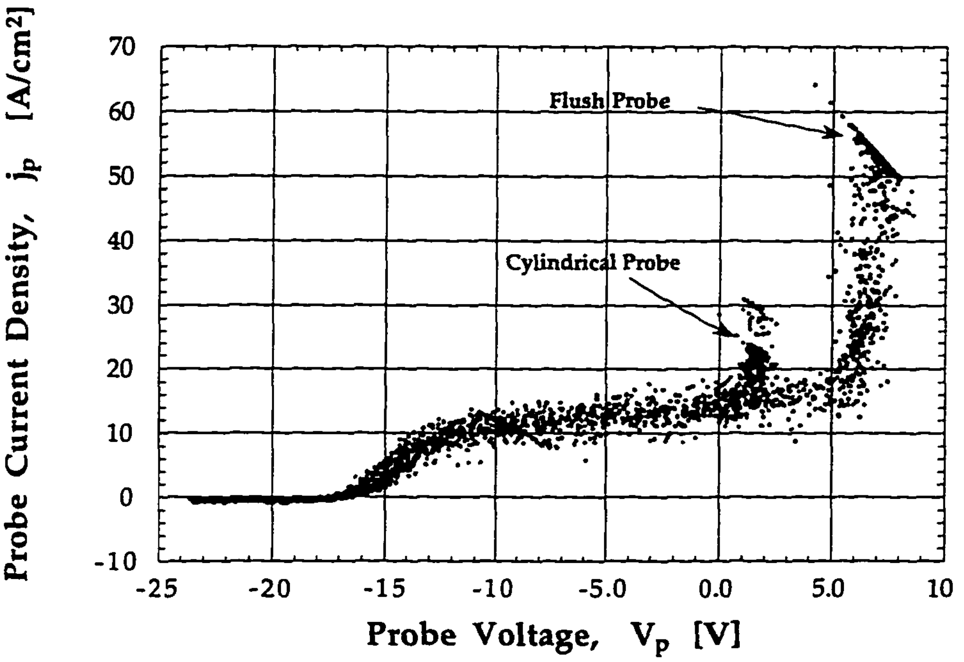

Fig. 5.2 Normalized probe current density versus probe voltage for probe 4. Both j_p-V_p characteristics obtained with the flush probes and cylindrical probes are compared. Conditions are for $\dot{m} = 50$mg/s, $I_{arc} = 9.9$ A and $V_{arc}=112$ V.

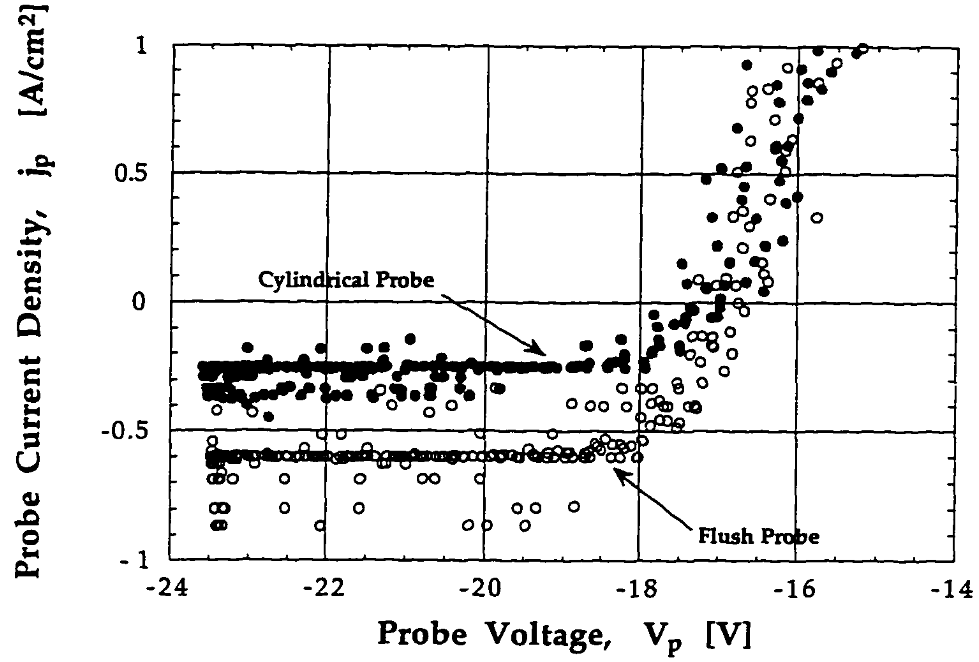

Fig. 5.3 Shown above is a close-up of the ion saturation region for probe 4 from the j_p-V_p plot shown in Fig. 5.2.

According to Clayden [1976] an ion shock may form about the probe if: (a) the ion-ion mean free path is less than the probe size; and (b) if the plasma flow velocity v_f is greater than the Bohm velocity u_B for $T_e >> T_i$. For this case the probe will be in supersonic continuum flow with respect to the ions.

Calculations of the ion-ion mean free path for probes 1-5 show that the interaction of H^+ and H^+ ions is most probable, with $\lambda_{H^+-H^+} \sim O(10^4\text{-}10^5\ \mu m)$, $r_p \sim 210\ \mu m$ giving an average value for $\lambda_{H^+-H^+}/r_p \sim O(20\text{-}500)$. Also, calculations of the Bohm velocity show that $u_B \sim O(10^3\text{-}10^4)$ m/s, compared with the MKB results for plasma flow velocity $v_f \sim O(10^3)$ m/s, calculated at L_{ext} = .15 mm for probes 1,1′ and L_{ext}= 0.25 mm for probes 2-5. Since $\lambda_{H^+-H^+} >> r_p$ and $u_B > v_f$, an ion shock is not likely to form on probes 1-5.

If an ion shock did form on the cylindrical probes then the ion current density would increase as the probe was biased with a positive voltage. To maintain charge neutrality the electron density will closely follow the ion density, so that the electron collection by the probe will also be enhanced, [Clayden, 1976]. Figures 5.2-5.3 do not show any enhancement of the electron or ion current density for the cylindrical probes, compared with the flush probe results. The ion current density for the cylindrical probes exhibit the same invariance with increasing negative V_p as the flush probes.

According to Ruzic [1997] a concern for cylindrical probes transverse to the plasma flow is if the electrons or ions have a directed energy component, i.e. a beam source. The neutral gas flow around the cylindrical probe, for the most part, is irrelevant to the probe signal. Because there are no electron or ion beam sources in an arcjet, positioning of cylindrical probes transverse to the plasma flow should not pose a problem with respect to the probe signal.

Based on the above information it is concluded that extension of cylindrical probes a maximum of ~ 0.25-.3 mm away from the anode, transverse to the plasma flow will: (a) not induce any shock formation on the probe surface; (b) will not pose any significant flow disturbance; and (c) the probe signal can be interpreted in a similar fashion as the flush probe signal. Because of these reasons, it is believed that useful data can be obtained from the cylindrical probes. The only problem with cylindrical probes transverse to the plasma flow has been occasional melting of the tip for probes 1, 1' and 2. Data for the cylindrical probe configuration is presented and compared with the flush probe results.

5.3 Plasma Property Measurements

In this section, cylindrical probe data are presented only for $\dot{m}$ = 45, 50 and 60 mg/s and 9.9 A for j_a, T_{es} and n_{es}. Only the affects of $\dot{m}$ on the plasma properties are presented since the flow rate has a larger effect on the plasma properties than I_{arc}, as shown earlier with the flush probe results. Note that the data at x = 1 mm was obtained for L_{ext}~0.1-.15 mm for probes 1,1′ and $(L_{ext})_{avg}$ ~ 0.25-0.3 mm for probes 2-10′.

Figures 5.4-5.6 display j_a, T_{es} and n_{es} data respectively, for $(I_{arc})_{avg}$~ 9.9 A and $\dot{m}$= 45, 50 and 60 mg/s. The current density distribution, Fig. 5.4, is similar for all flow rates tested for x ≥ 6 mm, in contrast with the flush probe results where there is some difference in j_a for all flow rates, Fig. 4.21.

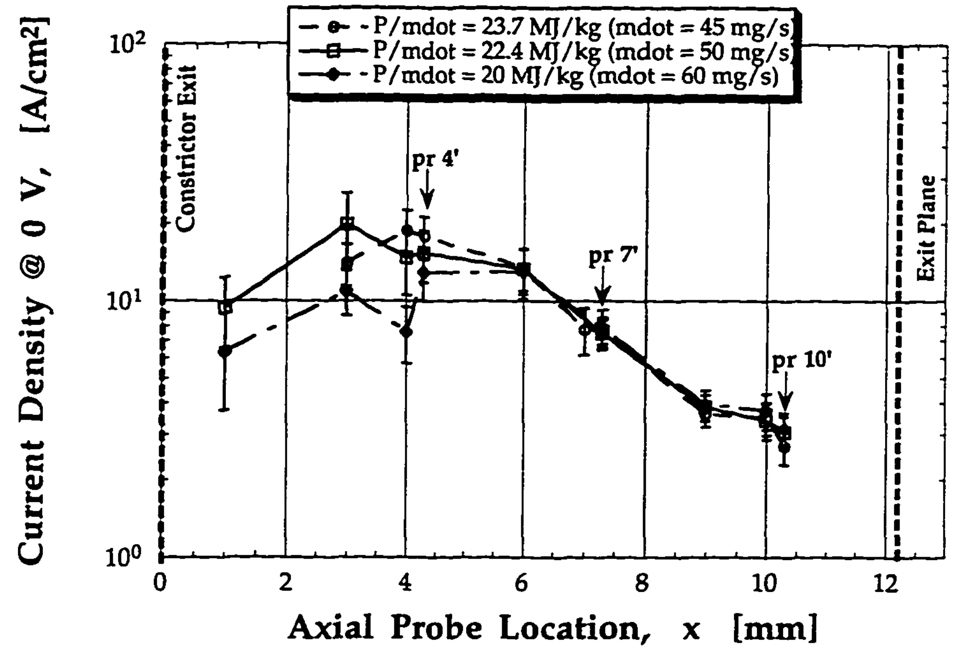

Fig. 5.4 Current density distribution obtained from the cylindrical probe configuration for $(I_{arc})_{avg}$= 9.9A and $(V_{arc})_{avg}$=112 V.

In the arc attachment region, 1 ≤ x ≤ 6 mm, as the flow rate decreases and P/$\dot{m}$ increases, j_a increases, e.g. at probe 4 as P/$\dot{m}$ increases by 16%, j_a increases 250%. For $\dot{m}$ = 45 mg/s, $(j_a)_{max}$ occurs at x = 4 mm for L_{ext} ~ 0.25-.3 mm and at x = 1 mm along the anode wall, L_{ext} ~ 0 mm, Fig. 4.21. In contrast to the cylindrical probe data, the flush probe results show a maximum at x = 1 mm (40, 45, 50 mg/s, 9.8 A) or x = 3 mm (60 mg/s, 9.9 A) and a secondary peak in j_a at x = 4 mm for $\dot{m}$ = 40, 45 and 50 mg/s. The cylindrical probe data show that for $\dot{m}$ = 50 mg/s, $(j_a)_{max}$ occurs at x = 3 mm and between x = 4-6 mm as $\dot{m}$ is increased to 60 mg/s.

The cylindrical probe results, similar to the data at the anode wall, are also sensitive to the propellant flow rate. These differences in j_a peaks, within ~ .25-0.3 mm of the anode, suggest a complex arc structure that changes abruptly near the attachment location on the anode. The distinctive shift in $(j_a)_{max}$ along the anode wall due to increasing flow rate from 45 to 60 mg/s is not observed for the cylindrical probe results. This result perhaps suggests that the flow rate affects the arc attachment location only *along* the anode for the flow rates studied in this work.

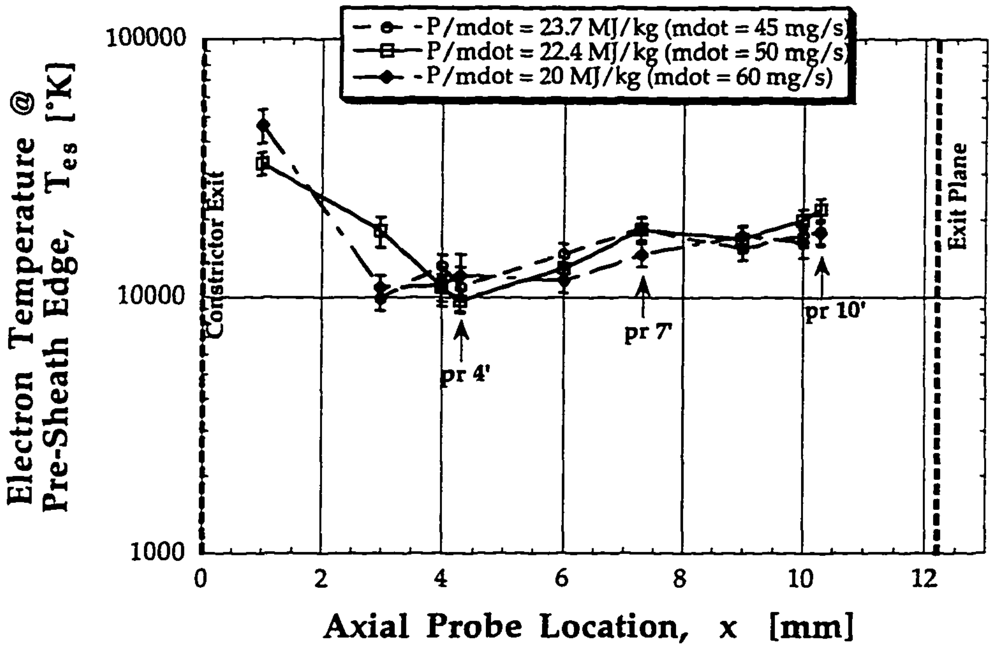

Fig. 5.5 Electron temperature distribution obtained from the cylindrical probe configuration for $(I_{arc})_{avg}$ = 9.9A and $(V_{arc})_{avg}$ = 112V.

Figure 5.5 shows cylindrical probe results for T_{es} at various axial locations. These T_{es} profiles show a distinct maximum at $x = 1$ mm, monotonically decreasing to a minima at $x = 4$ mm and then slightly increasing for $4 \leq x \leq 10$ mm. This is in contrast to the T_{es} profiles along the anode wall, where $(T_{es})_{max}$ occurs at $x = 2$ mm for $\dot{m} = 50$ and 60 mg/s, Figs. 4.42-4.43, and at $x = 1$-2 mm for $\dot{m} = 45$ mg/s, Fig. 4.44.

Along the anode, the electron temperature distribution becomes more flat as the specific energy is increased. However, at a radial distance of ~0.25 mm from the anode, as $P/\dot{m}$ increases, the T_{es} profile remains fairly invariant, except that $(dT_{es}/dx)_{prs1-4}$, becomes more shallow and the T_{es} distribution is not as flat as the flush probe results, (compare Figs. 4.42-4.44 with Fig. 5.5).

As shown in Fig. 5.6, the electron number density profile has a distinct maximum at $x = 4$ mm at all flow rates studied. The flow rate does not affect the location of $(n_{es})_{max}$ along the anode, as well as at a radial distance of ~.25-.3 mm from the anode. For the n_{es} distribution along the anode wall, $(n_{es})_{max}$ occurred at $x = 1$ mm, with a secondary peak at $x = 4$ mm. The cylindrical probe n_{es} data for $x \geq 6$ mm at all flow rates are very similar and do not vary much. However, for $1 < x < 6$ mm as the flow rate decreased, $P/\dot{m}$ increased, resulting in an increase in the electron number density. This corresponds well with the j_a profiles, Fig. 5.4 implying that the current density distribution is closely coupled with the electron number density, a result found earlier for the flush probe data.

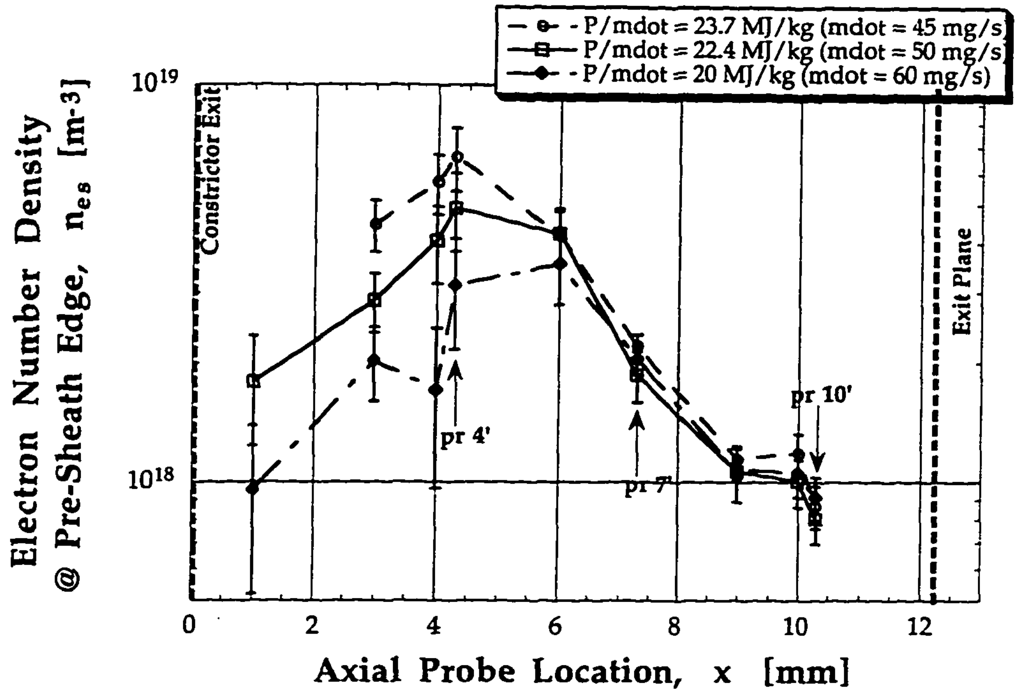

Fig. 5.6 Electron number density distribution obtained from the cylindrical probe configuration for $(I_{arc})_{avg}$=9.9A and $(V_{arc})_{avg}$=112V.

The floating potential data, from the cylindrical probes, for $\dot{m}$ = 50 mg/sec and $(I_{arc})_{avg}$ varying from 9.7 to $(I_{arc})_{avg}$ = 8.9 A are shown in Figs. 5.7-5.8 respectively. The propellant flow rate for the cylindrical probes was varied between 45, 50 and 60 mg/s. The ϕ_f radial distribution at all probe locations is shown in Fig. 5.9 for $\dot{m}$ = 60 mg/s, $(I_{arc})_{avg}$= 9.9 A and Fig. 5.10 for $\dot{m}$ = 45 mg/s, $(I_{arc})_{avg}$= 9.9 A. Some data points are not shown at certain probe locations because the respective probes' post-test surface condition appeared contaminated. Some probes were observed to have slight surface discoloration but showed no signs of hysteresis in the probe V-I characteristic; this data was included in the analysis and probes that were severely dirty were excluded.

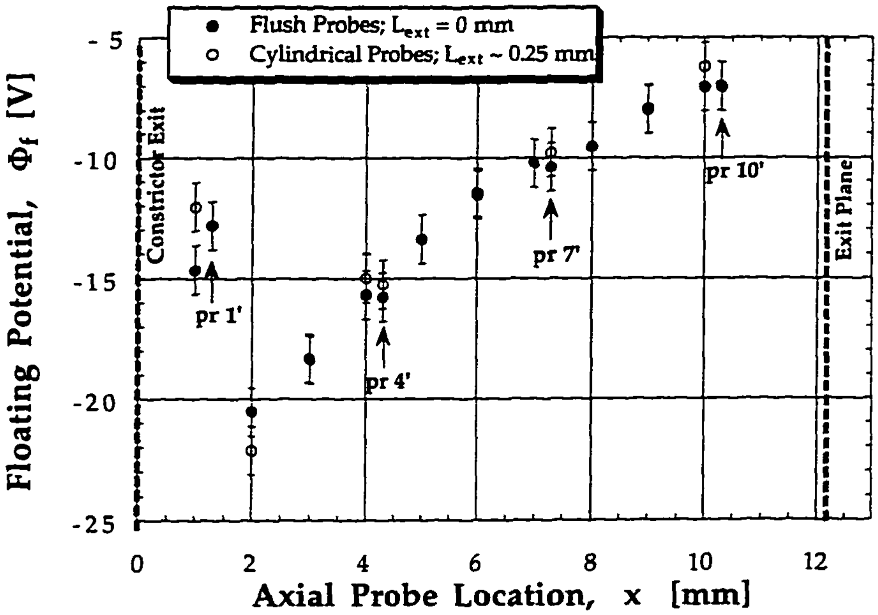

Fig. 5.7 Floating potential data from both flush and cylindrical probes are presented for $\dot{m}$ = 50 mg/s, $(I_{arc})_{avg}$= 9.7 A, and $(V_{arc})_{avg}$= 112.5 V.

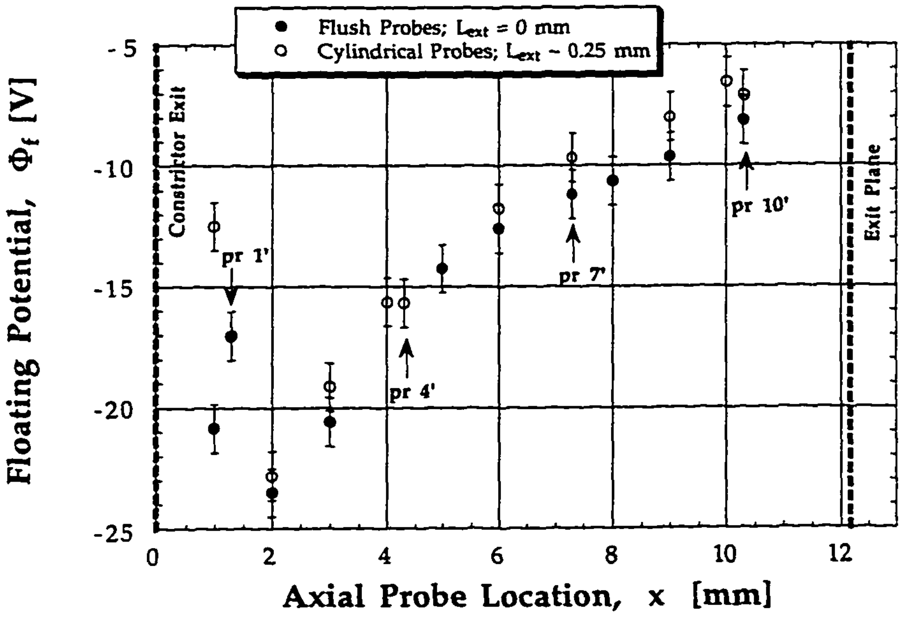

Fig. 5.8 Floating potential data from both flush and cylindrical probes are presented for $\dot{m}$ = 50 mg/sec, $(I_{arc})_{avg}$= 8.9 A, and $(V_{arc})_{avg}$= 116 V.

Figures 5.7-5.10 show that within ~ 0.25 mm of the anode wall ϕ_f is approximately constant, except at probes 1,1′ where ϕ_f becomes less negative further away from the anode. Both the cylindrical and flush probe data exhibit the same trends in the ϕ_f distribution, with a peak at x = 2 mm. Obtaining cylindrical probe data at x = 1 mm was very difficult because: (1) at x = 1 mm the nozzle diameter is only 1.4 mm, making exact positioning of the probe critical; and (2) due to the intense heating near the constrictor, the cylindrical probes sometimes partially melted and did not provide reliable data at that location.

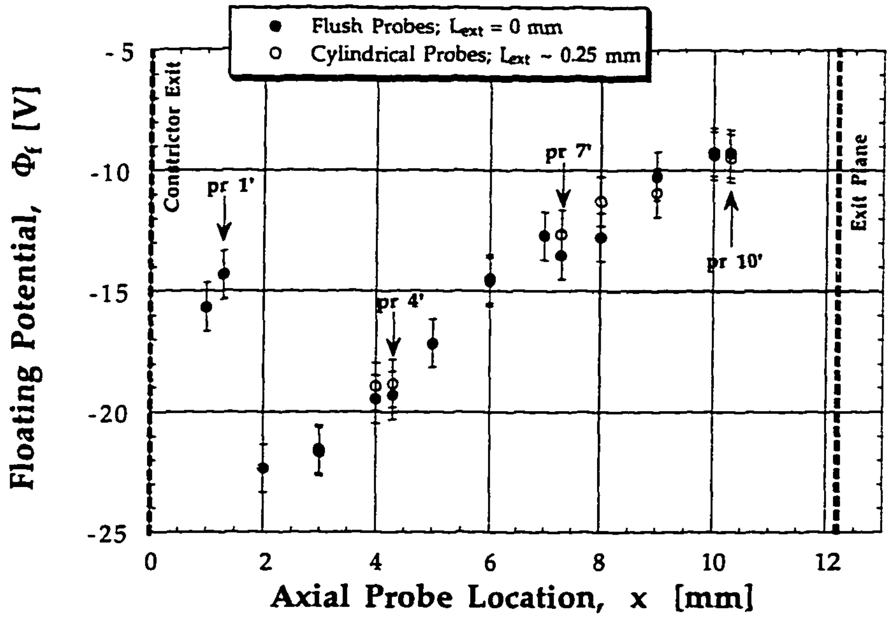

Fig. 5.9 Floating potential data from both flush and cylindrical probes are presented for $\dot{m}$ = 60 mg/sec, $(I_{arc})_{avg}$ = 9.9 A, and $(V_{arc})_{avg}$ = 121 V.

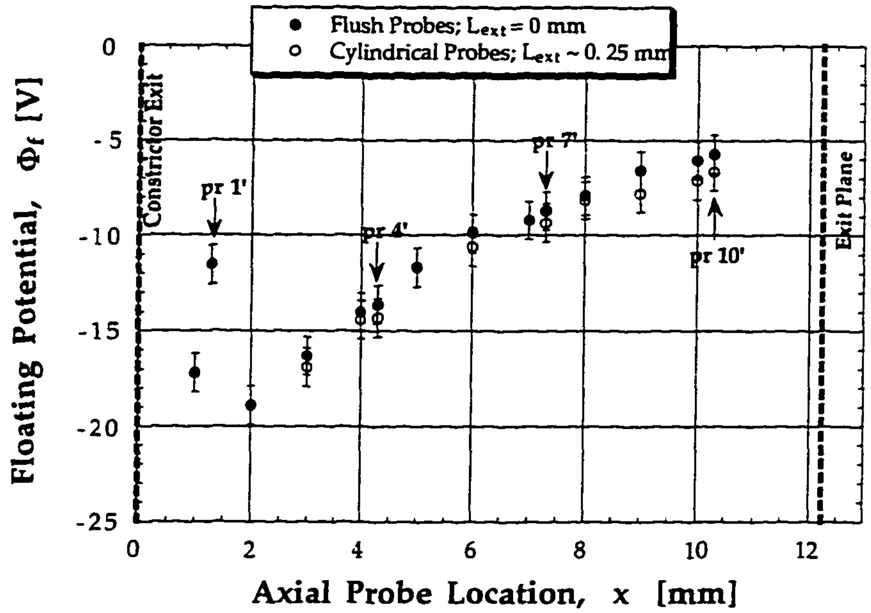

Fig. 5.10 Floating potential data from both flush and cylindrical probes are presented for $\dot{m}$ = 45 mg/sec, $(I_{arc})_{avg}$= 9 .9 A, and $(V_{arc})_{avg}$= 108 V.

Figures 5.11-5.13 below show the radial profiles of anode sheath potential ϕ_s at various axial and azimuthal locations. Both probe configurations exhibit similar trends, with a maximum in ϕ_s at x = 2 mm. The anode sheath potential, like ϕ_f, is approximately constant within ~ 0.25 mm of the anode, within experimental error, regardless of flow rate. This serves to further verify that the extension of the cylindrical probes transverse to the flow does not perturb the plasma or induce any shocks, since, according to Smetana [1963], for a cylindrical probe in a flowing plasma, the floating potential is a function of the plasma flow velocity, v_f:

$$\phi_f = \frac{kT_{es}}{e}\ln\left(\frac{1}{v_f}\sqrt{\frac{\pi k T_{es}}{2m_e}}\right) \qquad (5.1)$$

Since the floating potential distribution derived from the cylindrical probes is similar to the flush probe results, within experimental error, it is concluded that the plasma flow velocity does not affect the cylindrical probe results with regards to obtaining information on the plasma properties. Therefore, positioning of probes transverse to the arcjet plasma flow does yield useful data.

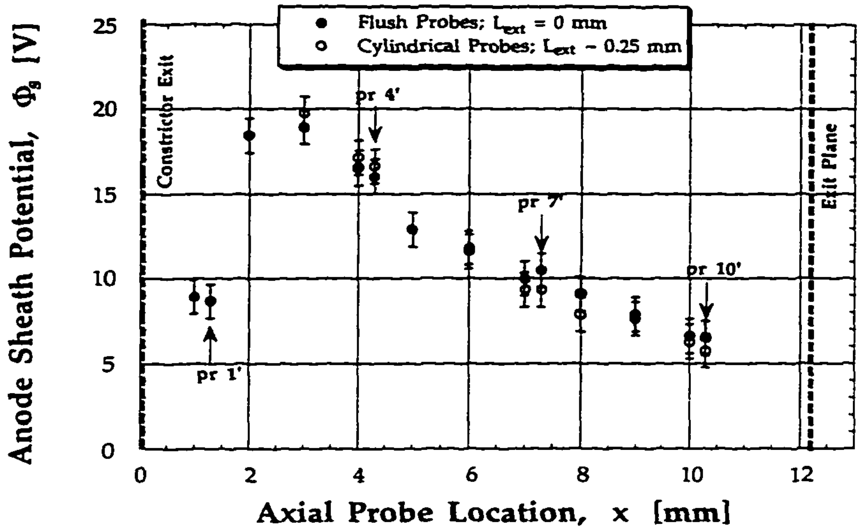

Fig. 5.11 ϕ_s data from flush and cylindrical probes for $\dot{m}$=60 mg/sec, $(I_{arc})_{avg}$=9.9 A, and $(V_{arc})_{avg}$ = 121 V.

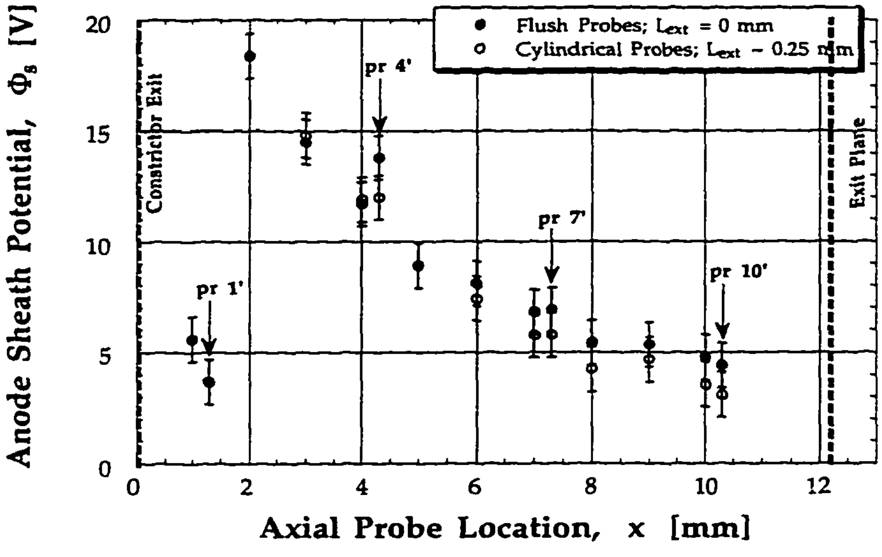

Fig. 5.12 ϕ_s data from both flush and cylindrical probes for $\dot{m}$= 45 mg/sec, $(I_{arc})_{avg}$= 9.9A and $(V_{arc})_{avg}$ = 108 V.

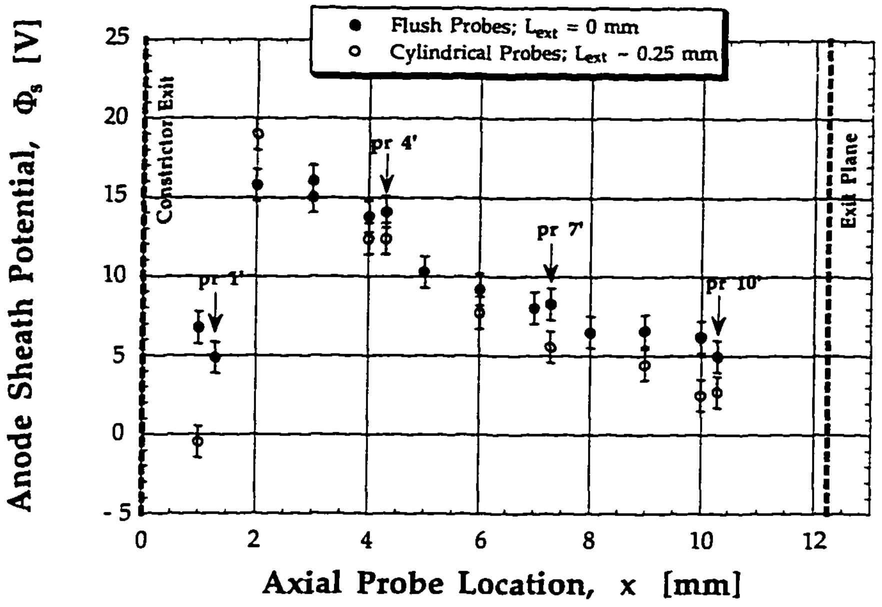

Fig. 5.13 Anode sheath potential data from flush and cylindrical probes are presented for $\dot{m}$ = 50 mg/sec, $(I_{arc})_{avg}$= 9.7 A, and $(V_{arc})_{avg}$ = 112 V.

Figure 5.14 shows j_a at all probe locations for both the flush and cylindrical probe configurations. For $x \geq 7$ mm, j_a does not change appreciably with radial distance from the anode. There is a major difference at x = 1 m m between $(j_a)_{flush}$ and $(j_a)_{cyl}$; as radial distance from the anode increases, j_a decreases corresponding to a large radial gradient $dj_a/dr > 0$. In the region $2 < x \leq 6$ mm, the current density decreases towards the anode so that $dj_a/dr < 0$, perhaps suggesting that the arc structure attaches diffusely to the wall.

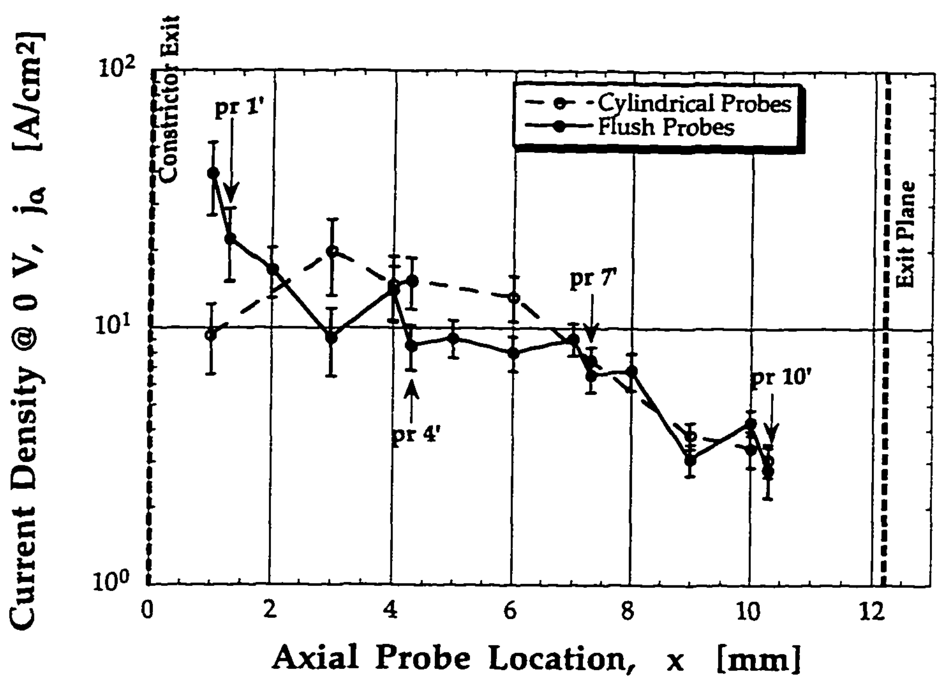

Fig. 5.14 Current density data at various axial locations for the nominal experimental conditions of m = 50 mg/s, $(I_{arc})_{avg}$= 9.9A and $(V_{arc})_{avg}$ = 112 V, from the flush and cylindrical probe configurations.

Similar to the flush probe j_a data, azimuthal current symmetry exists away from the anode as well.

These differences in j_a profiles from the flush and cylindrical probes may suggest a shift in arc attachment behavior. For example, at x = 1 mm $(j_a)_{cyl} < (j_a)_{flush}$ perhaps suggesting a large and diffuse arc root at the anode and a more narrow arc stem away from the wall. Conversely, in the region $2 \leq x \leq 6$ mm $(j_a)_{cyl} > (j_a)_{flush}$ corresponding to a relatively narrower arc root and a wider, more diffuse arc stem. The radial profile data for j_a is consistent with the earlier observation (for $\dot{m}$ = 50 mg/s, 9.9 A) that the arc attachment region is predominantly within 2-4 mm of the constrictor exit. It is interesting that $(j_a)_{max}$ along the anode occurs at x = 1 mm, while $(j_a)_{max}$ occurs at x = 3 mm at a radial distance of ~0.25-0.3 mm from the wall.

Figure 5.15 shows the electron temperature distribution at various axial locations for both the flush and cylindrical probe configurations. For positions at the anode wall $(T_{es})_{max}$ is at x = 2 mm, while at r ~ 0.25 -0.3 mm into the plasma $(T_{es})_{max}$ occurs at x = 1 mm. For $x \geq 7$ mm $dT_{es}/dr \sim 0$. In the region $2 \leq x \leq 6$ mm, $dT_{es}/dr < 0$ within 0.25 mm of the anode, in qualitative agreement with the MKB model and the numerical model of [Miller, *et al.*, 1996]. In the region of maximum arc attachment ($1 \leq x \leq 4$ mm) the electron temperature decreases with increasing distance from the anode because the electron-H_2 molecule collision frequency (which dominates over other collisional reactions) increases as well. Therefore, the electrons more readily thermalize with the H_2 molecules via collisions, consequently decreasing their temperature further away from the anode. It is possible that this may only be true within 0.25 mm of the anode, because in the arc core $T_e \sim T_{gas} \sim$ 10,000-20,000 °K; thus, there may be a local maximum in the radial T_{es} profile.

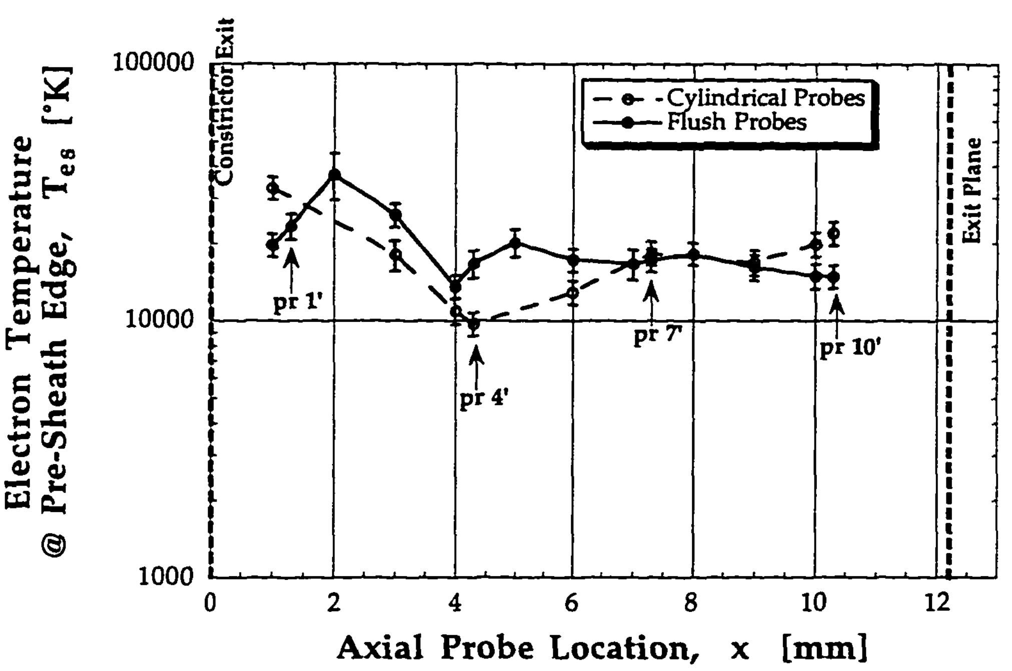

Fig. 5.15 Electron temperature data at various axial locations for the nominal experimental conditions of $\dot{m}$ = 50 mg/s, $(I_{arc})_{avg}$ = 9.9A and $(V_{arc})_{avg}$ = 112 V, from both the flush and cylindrical probe configurations.

Figure 5.16 presents the electron number density distribution at various axial locations for both the flush and cylindrical probe configurations. As with the j_a and T_{es} data, n_{es} (r) ~ constant for $x \geq 7$ mm. In the region $1 \leq x \leq 6$ mm large differences exist between $(n_{es})_{flush}$ and $(n_{es})_{cyl}$; this is seen in the j_a and T_{es} data as well. As radial distance from the anode increases, n_{es} increases following closely with the j_a data, suggesting that the n_{es} and j_a distributions are coupled; this was also observed for the flush probe results, Chapter 4. An increasing n_{es} with distance from the anode is also consistent with the fact that in the arc core there exists a very high degree of ionization, 10-20% [Megli, 1995] and large n_e, ensuring strong collisional coupling with the heavy particles [Martinez-Sanchez, *et al.*, 1996]. Outside the arc core, n_e falls rapidly as the arc approaches the anode, but is still high enough, ~$O(10^{18}\text{-}10^{19}\ m^{-3})$ to provide the sufficient electrical conductivity for arc attachment.

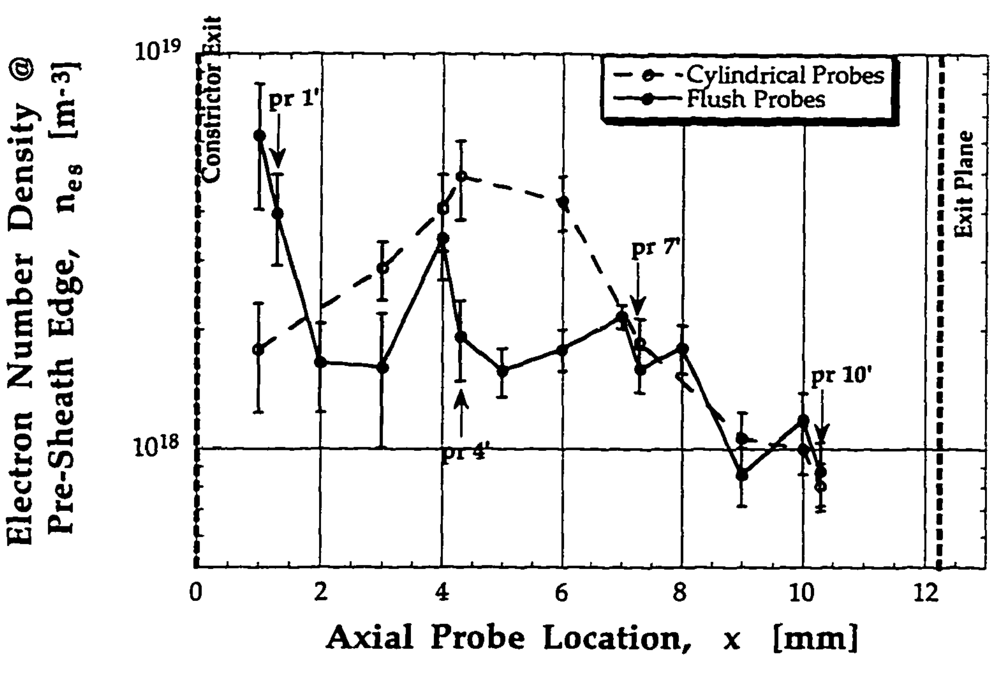

Fig. 5.16 Electron number density data at various axial locations for the nominal experimental conditions of $\dot{m}$ = 50 mg/s, $(I_{arc})_{avg}$ = 9.9A and $(V_{arc})_{avg}$ = 112 V, from both the flush and cylindrical probe configurations.

5.4 Assessment of Flush versus Cylindrical Probes

In this investigation both flush and cylindrical probes were utilized to probe the anode boundary layer of a 1 kW electrothermal arcjet. Most of the results presented were for the flush-mounted probe configuration, though a fair amount of cylindrical probe data was also obtained and analyzed, with a brief description in the previous sections.

The utility of the flush and cylindrical probes can now be assessed. The main requirements for successful application of the electrostatic micro-probe were: (1) minimal flow disturbances, i.e. minimize intrusiveness of the probe; (2) maintenance of probe integrity; and (3) ease of operation and application. Based on these criterion, which are very much dependent on the type of experiments conducted, the flush-mounted probe is preferred over the cylindrical probe. The main reason is that the cylindrical probe increases the chances of the probe melting, since it is exposed further into the flow. The signal from the cylindrical probe has a larger probability of being effected by thermionic emission and wake effects which are also difficult to assess. In contrast, the flush probe is relatively unintrusive, minimizing the chances for melting, thermionic emission and/or wake effects.

This work has shown that useful data can be obtained from cylindrical probes positioned *transverse* to the plasma flow; however, due to the small volume of low power arcjets (~ 0.6 cm^3) the experimentalist is encouraged to use flush probes over cylindrical probes, especially if $P/\dot{m} > 30$ MJ/kg are encountered.

6. ANODE HEATING

The anode energy deposition q_e, is mainly due to the electron energy transferred from the arc to the anode, via the current attachment. This is because the electrons are the dominant carriers of current, being more mobile than the ions. The anode heating was studied as a function of propellant flow rate $\dot{m}$, arcjet operating current I_{arc} and specific energy $P/\dot{m}$.

In the following sections, only flush probe results are presented for the anode heating distribution q_e, for $\dot{m}$ = 40, 45, 50 and 60 mg/s and I_{arc} = 7.8, 8.9, 9.8 and 10.6 A.

6.1 Significance of Anode Heating

Electrothermal arcjets have demonstrated higher specific impulse than conventional chemical propulsion thrusters, requiring less propellant for satellites. The achievement of high specific impulse, above 600 seconds for a hydrazine arcjet, requires a specific energy $P/\dot{m}$ of 40-80 MJ/kg, resulting in anode heating rates which can cause electrode failure. Anode heating, a critical life-limiting factor for high performance arcjets [Lichon, *et al.*, 1996], is determined by the physics of arc attachment [Meeks, *et al.*, 1993].

As discussed in Sec. 3.1.2, the energy deposition into the anode for an electron-attracting sheath is:

$$q_e = j_a \left[5kT_{es}/2e + \phi_s + W\right] \tag{6.1}$$

where the first term represents the thermal energy of the electrons, the second term is the electron energy expended in traversing the sheath and the last term is the energy gained when the electron recombines with the anode surface, of work function W. The plasma properties j_a, n_{es}, and T_{es} vary with propellant flow rate, arcjet operating current and specific energy, so that understanding how each of these effects their distribution will help to understand the dependence of anode heating.

Because the role of arcjets as a primary satellite propulsion system is expected to grow in the future [Butler, *et al.*, 1996], their operation at high $P/\dot{m}$ is required. However, arcjet operation at the high specific energies required for orbit maneuvering and satellite repositioning increases the anode thermal loading, thus reducing thruster lifetime. Therefore, understanding how the anode heating q_e is affected by $\dot{m}$, I_{arc} and $P/\dot{m}$ is vital to understanding how arcjet design can be improved for these ambitious future space mission scenarios.

In the following sections, results of the effects of $\dot{m}$, I_{arc} and $P/\dot{m}$ on q_e are presented and discussed. The data for q_e were derived from the j_a, T_{es} and ϕ_s results obtained with the flush-probe configuration, presented earlier in Chapter 4.

6.2 Effect of Flow Rate on Anode Heating

It was earlier shown (Chapter 4) that the location of $(j_a)_{max}$ was more sensitive to the $N_2 + 2H_2$ flow rate, than to the arcjet operating current. The effects of propellant flow rate on the anode heating are shown in Figs. 6.1-6.4 for I_{arc} = 9.8A, $\dot{m}$ = 45, 50 and 60 mg/s and Fig. 6.5 for $\dot{m}$ = 40 mg/s and I_{arc} = 10.6 A.

There is minimal difference in the q_e distribution for $\dot{m}$ = 45 mg/s and 50 mg/s, Figs. 6.1-6.2. Results for both these flow rates show a peak in q_e at x = 1 mm, coinciding with the location of $(j_a)_{max}$, with a secondary peak at x = 4 mm. For $\dot{m}$ = 45 mg/s the anode heating varies from an average of 480 W/cm^2 at x= 1 mm to an average of 41 W/cm^2 at x = 10 mm. Similarly, for $\dot{m}$ = 50 mg/s, $(q_e)_{avg}$ = 440 W/cm^2 ± 140 W/cm^2 at x = 1 mm to $(q_e)_{avg}$ = 45 W/cm^2 ± 8 W/cm^2 at x = 10 mm.

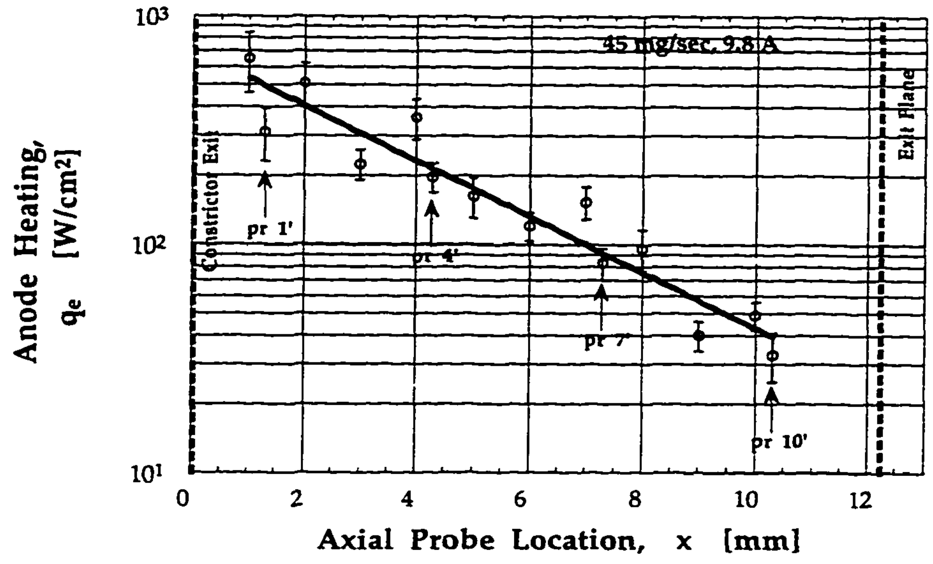

Fig. 6.1 The anode heating distribution q_e for $\dot{m}$ = 45 mg/s and I_{arc} = 9.8A; q_e varies from an average of 480 W/cm^2 ± 140 W/cm^2 at x = 1 mm to an average of 41 W/cm^2 ± 8 W/cm^2 at x = 10 mm.

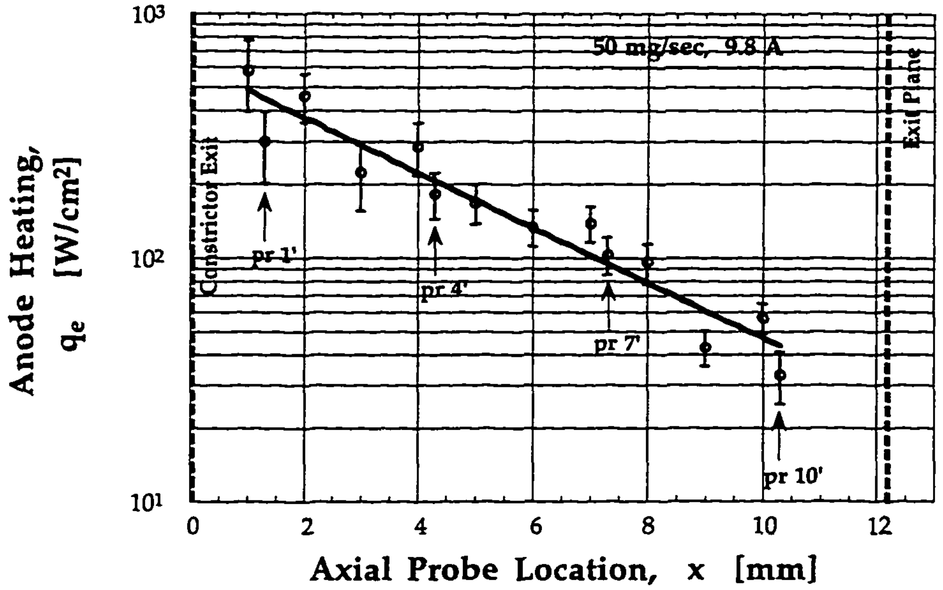

Fig. 6.2 The anode heating distribution q_e for $\dot{m}$ = 50 mg/s and I_{arc} = 9.8A; q_e varies from an average of 440 W/cm^2 ± 140 W/cm^2 at x = 1 mm to an average of 45 W/cm^2 ± 8 W/cm^2 at x = 10 mm.

Varying the propellant flow rate from 45 to 50 mg/s has negligible effect on the location of $(q_e)_{max}$ and the q_e distribution. However, as with the j_a results, when $\dot{m}$ is increased to 60 mg/s, $(q_e)_{max}$ is displaced downstream to x = 3 mm, again coinciding with the shift in $(j_a)_{max}$. Thus, the peak in anode heating $(q_e)_{max}$, is coupled with the current density and both are dependent more on the propellant flow rate Fig. 6.3-6.4, than I_{arc}, as shown later in Sec. 6.3.

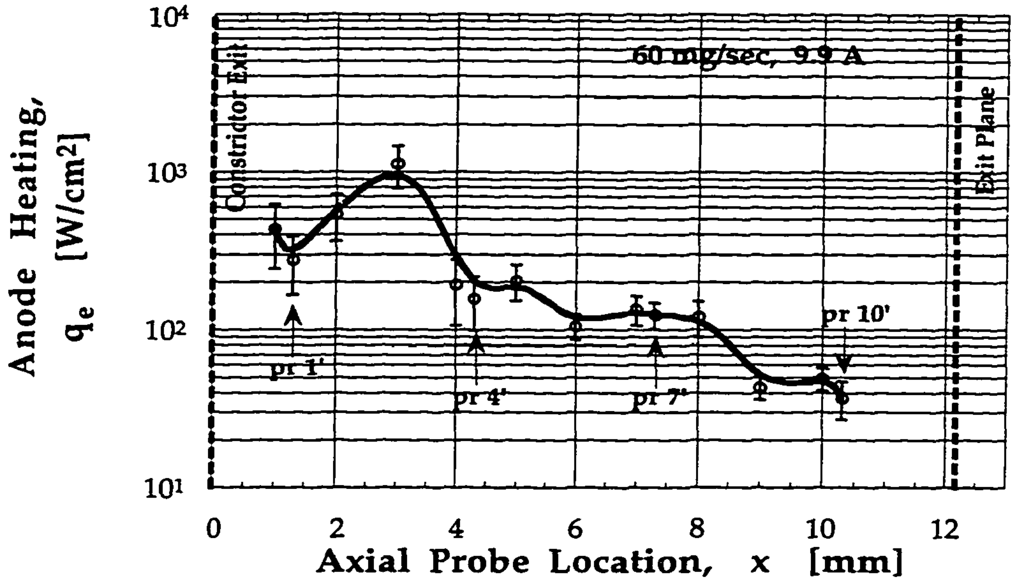

Fig. 6.3 The anode heating distribution q_e, is shown for $\dot{m}$= 60 mg/s and I_{arc}= 9.9 A; q_e varies from an average of 355 W/cm^2 ± 150 W/cm^2 at x = 1 m m to an average of 43 W/cm^2 ± 9 W/cm^2 at x = 10 mm.

Figures 6.1-6.3 show that as the propellant flow rate is increased for a fixed I_{arc} (P/$\dot{m}$ decreases) $(q_e)_{max}$ decreases: (1) for $\dot{m}$ = 45 mg/s, $(q_e)_{max}$ = 480 W/cm^2 ± 140 W/cm^2; (2) for $\dot{m}$ = 50 mg/s, $(q_e)_{max}$ = 440 W/cm^2 ± 140 W/cm^2; and (3) for $\dot{m}$ = 60 mg/s, $(q_e)_{max}$ = 355 W/cm^2 ± 150 W/cm^2. Therefore, as P/$\dot{m}$ decreases, $(q_e)_{max}$ decreases.

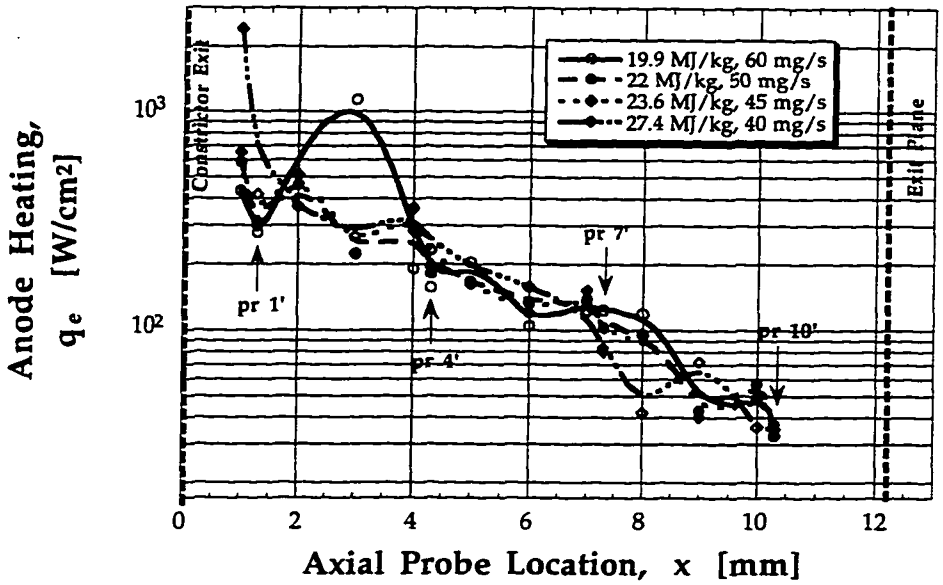

Fig. 6.4 The anode heating distribution q_e, is shown for fixed I_{arc}= 9.8 A and $\dot{m}$ = 45, 50 and 60 mg/s and I_{arc} = 10.6 A for $\dot{m}$ = 40 mg/s.

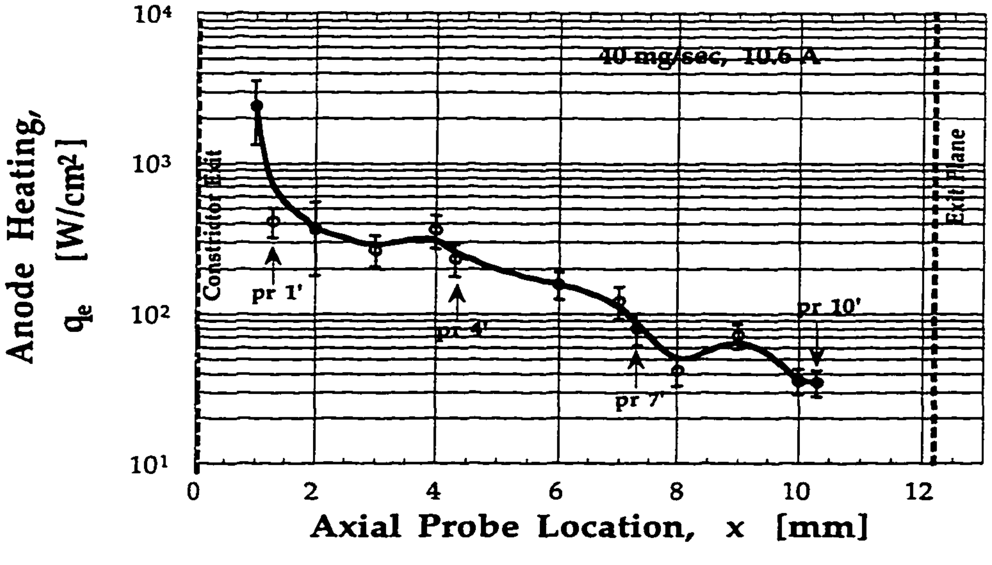

Fig. 6.5 The anode heating distribution q_e for $\dot{m}$ = 40 mg/s and I_{arc} = 10.6 A; q_e from an average of 1420 W/cm^2 ± 600 W/cm^2 at x = 1 mm to an average of 35 W/cm^2 ± 7 W/cm^2 at x = 10 mm.

The q_e distribution for the highest specific energy tested, 27.4 MJ/kg (40 mg/s, 10.6 A), is shown in Fig. 6.5. For this case, an average heat flux of 1420 W/cm^2 ± 600 W/cm^2 at x = 1 mm is the largest value obtained for all flow rates tested; this also coincides with the largest current density obtained, 140 A/cm^2 ± 57 A/cm^2 at x = 1 mm, for the same operating conditions.

For fixed I_{arc}, as the flow rate is increased from 45 to 60 mg/s, the axial gradient in q_e within 1 mm of the constrictor exit, increases slightly. The largest increase in dq_e/dx occurs for the maximum $P/\dot{m}$ of 27.4 MJ/kg. For all propellant flow rates studied, $q_e(x)$ monotonically decreases after $(q_e)_{max}$, a trend also observed in the current density distribution, $j_a(x)$.

6.3 Effect of Arcjet Current on Anode Heating

The effect of varying the arcjet operating current for fixed $\dot{m}$ = 50 mg/s, I_{arc} = 7.8, 8.9 and 9.8 A is shown in Figs. 6.6, 6.7 and 6.2, respectively.

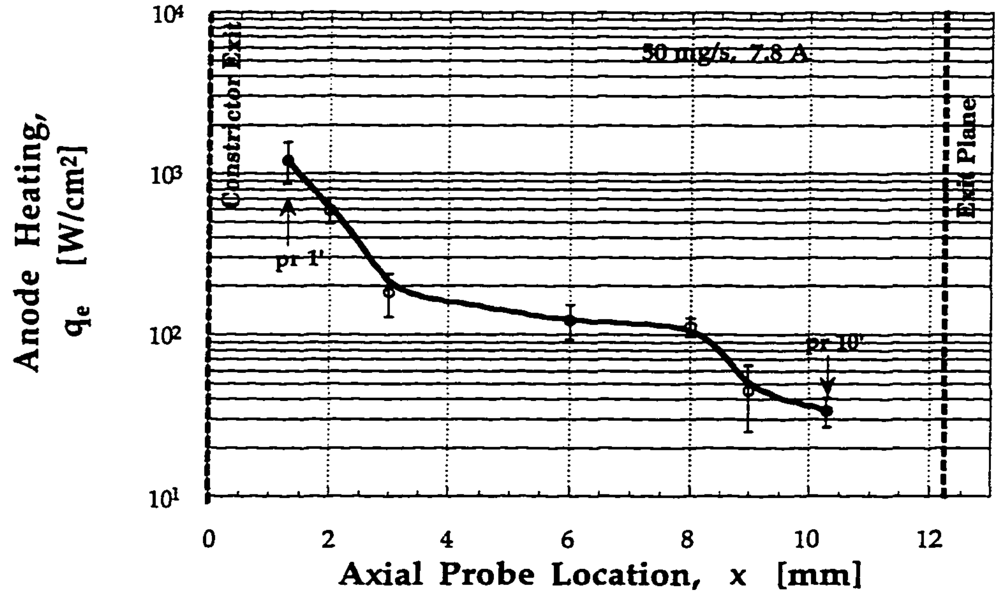

Fig. 6.6 Shown above is the q_e distribution along the anode for $\dot{m}$ = 50 mg/s and I_{arc} = 7.8 A.

For 7.8 ≤ I_{arc} ≤ 9.8 A, $(q_e)_{max}$ is always at x = 1 mm and q_e decreases with increasing distance from the constrictor, i.e. in regions of low j_a; similar to the $\dot{m}$ parameter study. For I_{arc} = 7.8 A, Fig. 6.6, a small plateau in q_e exists in the region 4 ≤ x ≤ 8 mm; the width of this region decreases to 2 ≤ x ≤ 4 mm when I_{arc} is increased to 8.9 A, Fig. 6.7, and for I_{arc} = 9.8 A no distinct plateau for q_e exists, Fig. 6.2.

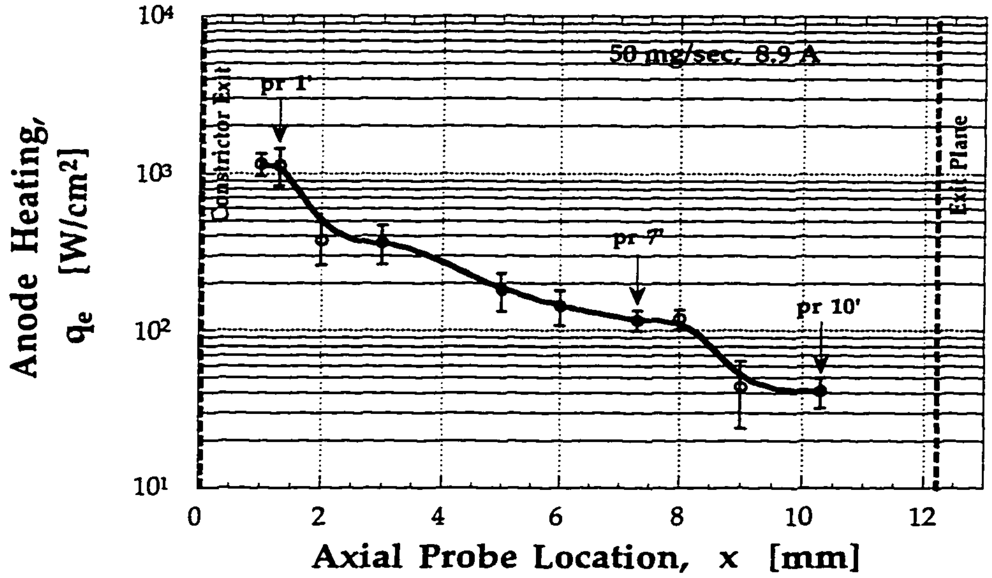

Fig. 6.7 Shown above is the q_e distribution along the anode for $\dot{m}$ = 50 mg/s and I_{arc} = 8.9 A.

The arc current parameter study shows that for the arc currents tested as I_{arc} increases (P/$\dot{m}$ increases), $(q_e)_{max}$ decreases. For $\dot{m}$ = 50 mg/s, I_{arc} = 7.8 A, Fig. 6.6 shows that the q_e distribution varies from a maximum of 1200 W/cm^2 ± 350 W/cm^2 at x = 1 mm to 34 W/cm^2 ± 7 W/cm^2 at x = 10 mm. As the arc current is increased to 8.9 A ($\dot{m}$ = 50 mg/s, Fig. 6.7), $(q_e)_{max}$ = 1135 W/cm^2 ± 240 W/cm^2 at x = 1 mm, decreasing to 42 W/cm^2 ± 9 W/cm^2 at x = 10 mm. For I_{arc} = 9.8 A ($\dot{m}$ = 50 mg/s), $(q_e)_{max}$ = 440 W/cm^2 ± 140 W/cm^2 at x = 1 mm to an average of 45 W/cm^2 ± 8 W/cm^2 at x = 10 mm. Notice that with increasing

I_{arc}, $(q_e)_{max}$ at x = 1 mm decreases, but q_e at x= 10 mm increases, resulting in a slightly more flat q_e distribution. Therefore, increasing $P/\dot{m}$ results in a more flat q_e axial distribution profile; a similar effect of $P/\dot{m}$ on the T_{es} distribution was also observed, Sec. 4.5.4.

When the arcjet operating current is increased to 10.6 A for $\dot{m}$= 40 mg/s, the only noticeable effect on the q_e distribution is that $(q_e)_{max}$ at x = 1 m m increases to 1420 W/cm^2 ± 600 W/cm^2, larger than the $(q_e)_{max}$ values for the lower arc current levels. For x > 1 mm the q_e profile is similar to the cases of $7.8 \le I_{arc} \le 9.8$ A, as shown in Fig. 6.8.

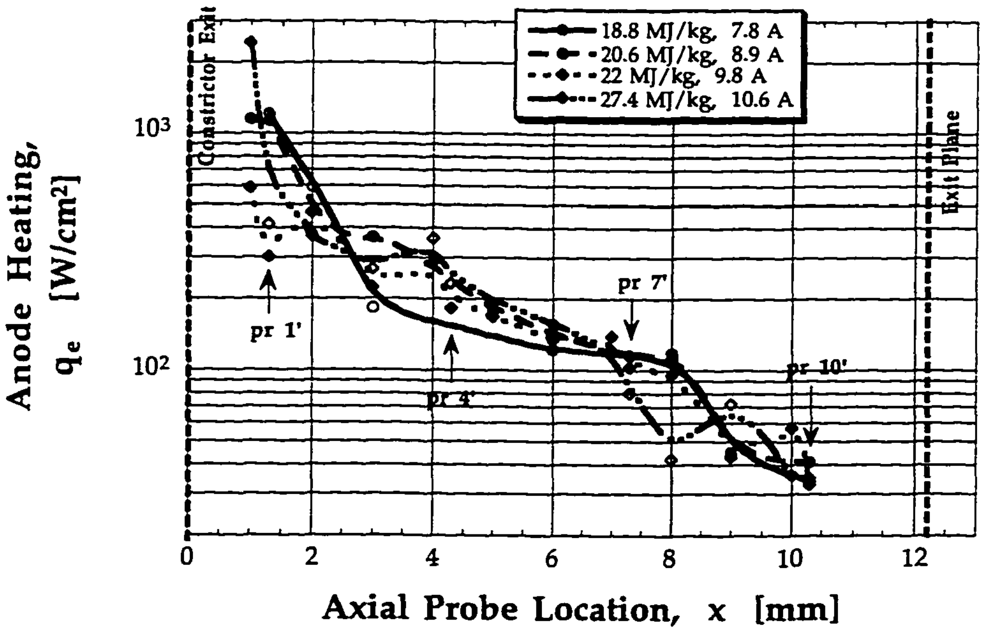

Fig. 6.8 Shown above is the q_e distribution along the anode for $\dot{m}$= 50 mg/s and I_{arc}= 7.8, 8.9, 9.8A and $\dot{m}$= 40 mg/s and I_{arc}= 10.6 A.

The anode heating is coupled with the current density, and the *location* of $(j_a)_{max}$ and $(q_e)_{max}$ is influenced more by the propellant flow rate than the arcjet operating current, Fig. 6.4 versus Fig. 6.8. The relationship between q_e

and j_a is displayed in Fig. 6.9, for the nominal experimental conditions of 50 mg/s and 9.8 A.

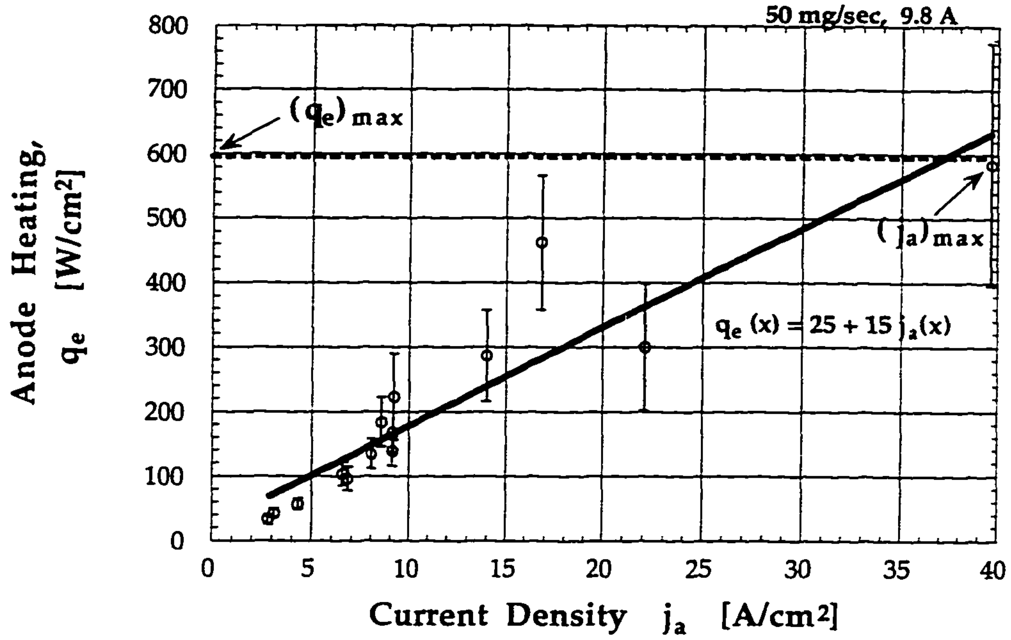

Fig. 6.9 Shown above is the q_e distribution along the anode as a function of current density j_a, for $\dot{m}$ = 50 mg/s and I_{arc} = 9.8A. Note that $(q_{e})_{max}$ corresponds to $(j_a)_{max}$.

Figure 6.9 shows that the anode increases linearly with current density, with $(q_{e})_{max}$ coinciding with $(j_a)_{max}$.

The total power deposited into the anode due to electron energy transfer Q_a, can now be calculated from the $q_e(x)$ data:

$$Q_a = \int_{1}^{10} q_e(x) dA(x) \tag{6.2}$$

where q_e (x) is given by Eq. (6.1) for an electron-attracting sheath and $dA(x) = 2\pi r(x)(\cos 20^\circ)^{-1}dx$. For the 0° and 180° probes an average value is used for

$q_e(x)$ at x = 1, 4, 7 and 10 mm. The functional dependence of Q_a on I_{arc} is shown in Fig. 6.10.

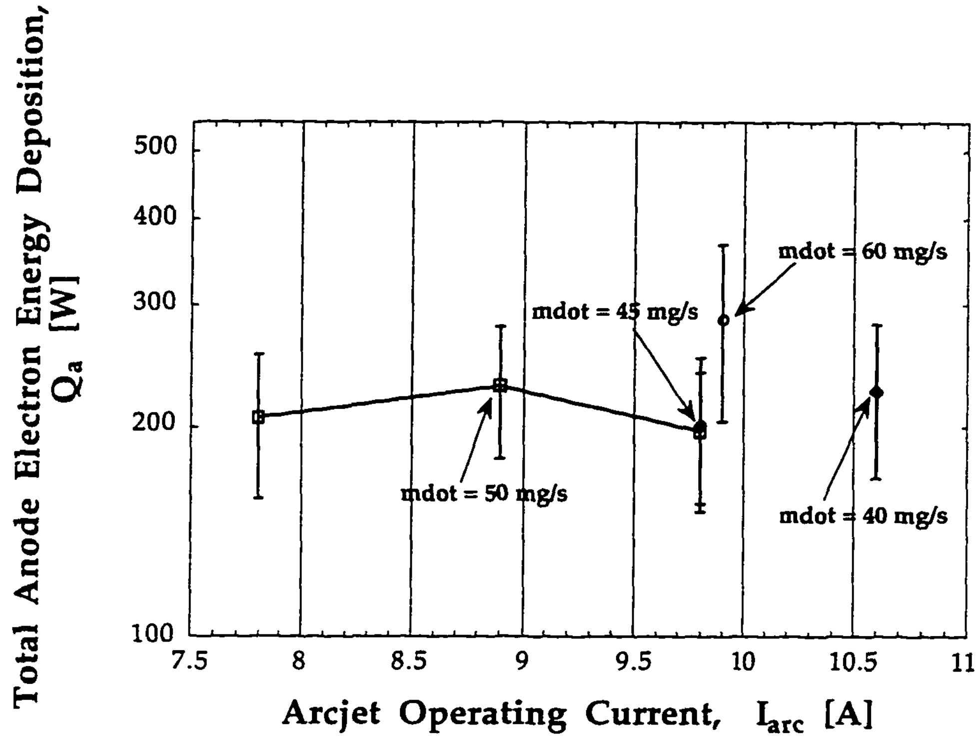

Fig. 6.10 The total anode heating Q_a is shown as a function of arcjet operating current and various $N_2 + 2H_2$ flow rates tested.

Figure 6.10 shows that for a fixed flow rate of 50 mg/s, increasing I_{arc} increases Q_a to a maximum of 229 W ± 49 W (22% of input arc power) at I_{arc} = 8.9 A; then Q_a decreases to 197 W ± 42 W (18% of arc power) as I_{arc} is increased to 9.8 A. The total electron energy deposition in the anode sheath varies from 18% of the total input power for $\dot{m}$ = 50 mg/s, I_{arc} = 9.8 A to 24% of the total input power for $\dot{m}$ = 60 mg/s, I_{arc} = 9.9 A. It is interesting that the maximum anode heating $(Q_a)_{max}$ = 287 W ± 60 W (24% of arc power) does not occur for the high P/$\dot{m}$ case, 27.4 MJ/kg, but for the high propellant flow rate of 60 mg/s (P/$\dot{m}$ = 19.9 MJ/kg). These results agree very well with the work of Curran [1985] who found that 20-25% of the arcjet input power is transferred to the anode. The present results suggest that when operating the arcjet at low P/ṁ, a larger fraction of the input power is absorbed into the anode. Also, arcjet operation for P/ṁ ≥ 22 MJ/kg results in slightly less fractional anode power losses, Table 4.2.

Figure 6.11 shows the maximum anode heating for each arcjet operating condition tested (using the flush probes) as a function of propellant flow rate. Notice that $(q_e)_{max}$ exhibits a minimum at 50 mg/s, beyond which point $(q_e)_{max}$ increases as ṁ increases, for constant I_{arc}. This is exactly the same effect observed for $\bar{\phi}_s$ versus propellant flow rate, Fig. 4.16. This shows that the anode sheath potential (which is most influenced by ṁ) plays a major role in the anode heating; in Chapter 4 it was shown that as ṁ increases, ϕ_s increases.

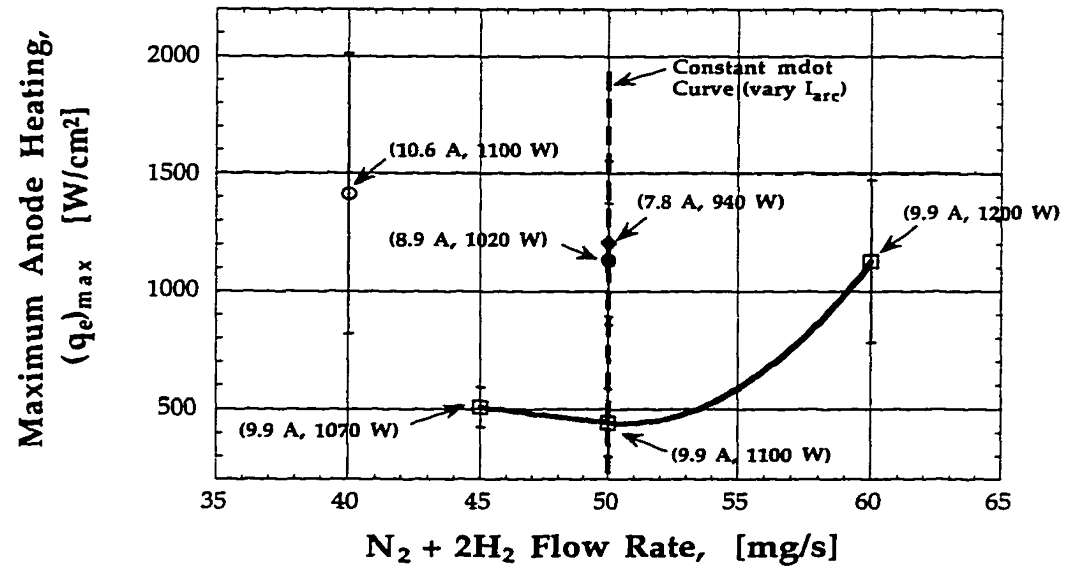

Fig. 6.11 The maximum anode heating $(q_e)_{max}$ is shown as a function of N_2 + $2H_2$ flow rate.

For constant ṁ, as I_{arc} increases, $(q_e)_{max}$ decreases, Fig. 6.11. This is consistent with the results in Chapter 4 which showed that ϕ_s decreases with increasing I_{arc}, and since ϕ_s influences q_e, the same trend in q_e with I_{arc} is observed.

6.4 Effect of Specific Energy on Anode Heating

Sections 6.2 and 6.3 described the effects of varying $\dot{m}$ and I_{arc} on q_e. It was shown that the most noticeable effect on q_e occurred when $\dot{m}$ was increased, i.e. decreasing $P/\dot{m}$ for fixed I_{arc} resulting in a shift of $(q_e)_{max}$ downstream, corresponding to a similar result for $(j_a)_{max}$.

The global effect on the q_e distribution for various specific energies is shown in Figs. 6.12 and 6.13. As $P/\dot{m}$ increases $(q_e)_{max}$ at $x = 1$ mm increases and a second peak in q_e occurs at $x = 4$ mm, coinciding for both $P/\dot{m}$ = 23.6 MJ/kg and 27.4 MJ/kg.

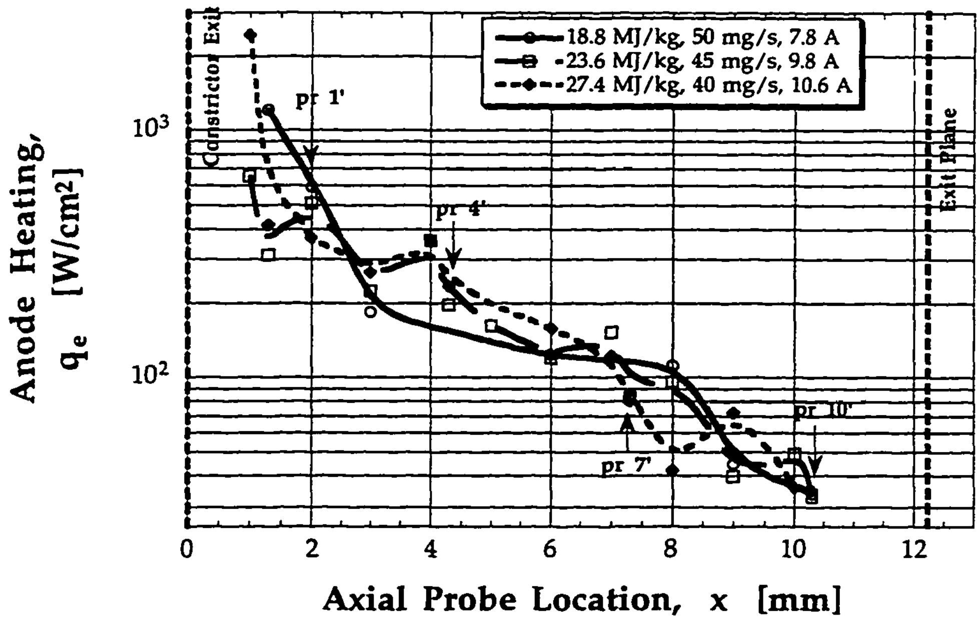

Fig. 6.12 Distribution of anode sheath electron energy deposition for various specific energies.

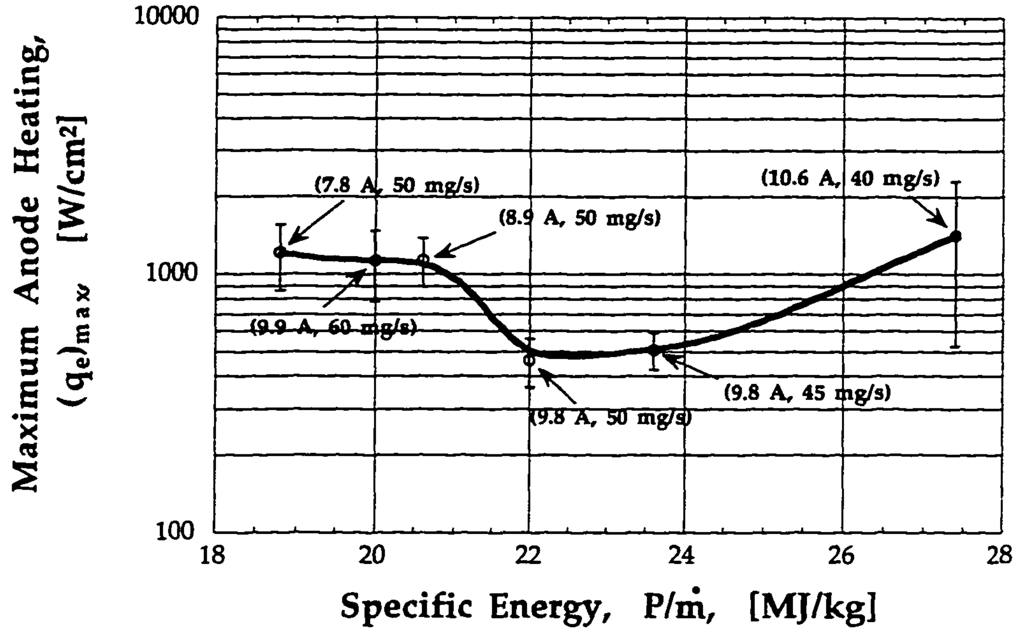

Fig. 6.13 The effect of varying $P/\dot{m}$ on $(q_e)_{max}$ is shown. The specific energy is varied by changing $\dot{m}$, I_{arc} or both simultaneously.

Figure 6.13 shows the effect of varying $P/\dot{m}$ on $(q_e)_{max}$. For $P/\dot{m} \leq 20.6$ MJ/kg, $(q_e)_{max}$ is relatively constant, independent of I_{arc} and $\dot{m}$; however, for $P/\dot{m} > 20.6$ MJ/kg as the specific energy increases $(q_e)_{max}$ decreases to a minimum at 22 MJ/kg. Beyond this minimum, as $P/\dot{m}$ increases, $(q_e)_{max}$ increases.

7. COMPARISON OF DATA WITH PREVIOUS EXPERIMENTS and MKB MODEL

7.1 Comparison of Performance With NASA-Lewis 1 kW Arcjet

As mentioned in Chapter 2, the UIUC arcjet thruster design was based on the standard NASA-Lewis 1 kW arcjet. Both engines have the same constrictor length and nozzle area ratio. However, the main differences are: (1) the UIUC arcjet incorporates a monolithic anode design, eliminating the need for an anode insert and sealing gaskets, simplifying anode heat transfer modeling; and (2) the monolithic anode design facilitates the placement of an array of fourteen electrostatic micro-probes.

Due to the geometric similarities between the thruster used in this work and the NASA 1 kW arcjet, the NASA-Lewis thruster is referenced as a baseline when comparing operating performance conditions, as shown in Fig. 7.1.

The NASA-Lewis data [Curran *et al.*, 1992] presented in Fig. 7.1 was taken after 144 cycles (288 hours) of run time; the UIUC data was taken after approximately 30-36 hours of run time. Curran *et al.* [1992] found that as the amount of cycles of thruster operation increased, the thruster operating voltage increased. Perhaps this was related to the erosion of the cathode tip, since cathode recession increases with run time, the arc length increases for a given flow rate and I_{arc}, thus increasing V_{arc}. Appendix I shows some micro-photographs of the UIUC cathode taken after approximately 15 - 20 hours of run time. Shown are the front and side views of the cathode tip and arc attachment area.

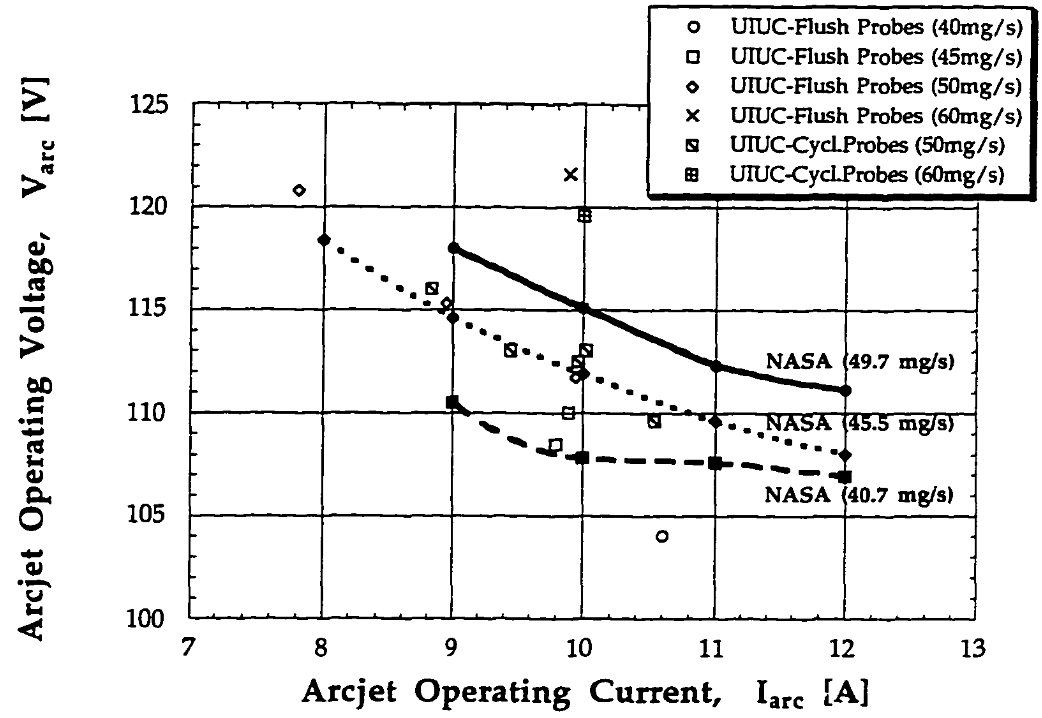

Fig. 7.1 A comparison of the V-I curves for the UIUC arcjet and the NASA-Lewis baseline 1 kW arcjet thruster. The data for the UIUC arcjet shows performance measurements taken during both flush-mounted and cylindrical probe experiments for various N_2 + $2H_2$ flow rates and arcjet operating currents.

Comparisons between the UIUC arcjet thruster performance and the NASA-Lewis 1 kW arcjet, Fig. 7.1, shows reasonably good agreement for similar flow rates tested, e.g. $\dot{m}$ = 50 mg/sec. Therefore, the presence of fourteen probe holes and electrostatic micro-probes inserted into the anode body does not have a significant effect on the global performance of the UIUC thruster, when compared with the NASA 1 kW engine. For $\dot{m}$ = 40 mg/sec, the NASA thruster operates at approximately 4 V higher than the UIUC thruster, probably due to the increased cycle time on the NASA engine, mentioned earlier.

7.2 Comparison with Experimental Results

The main objective of this research was to obtain plasma property data in the anode boundary layer of a low power arcjet for various thruster operating conditions. It was also important to add to the published data for the interior arcjet nozzle region and to provide the electric propulsion modeling community with experimental data for model validation.

As discussed in Chapter 1 there has been some excellent interior nozzle diagnostics research conducted in recent years on low power arcjets by [Zube, *et al.*, 1992] and [Hargus, *et al.*, 1994]. These researchers utilized emission spectroscopy to obtain excited species number densities and temperatures at various locations in the nozzle. However, as a result of the Abel inversion technique required in de-convoluting spectroscopy data and the low spatial resolution of spectroscopic methods, results were not obtainable in the anode sheath region.

The only published work of current density measurements in a low power hydrazine arcjet is that of Curran *et al.*, [1990]. In that work the standard NASA-Lewis 1 kW arcjet anode was segmented in the axial direction, comprised of five conducting segments isolated from each other by 0.25 mm thick boron nitride spacers. The current collected by each segment and the potential difference between the cathode and each segment were monitored under various arcjet operating conditions. The main findings of Curran *et al.*, [1990] were: (1) the total current had minimal effect on the measured current distribution; (2) the propellant flow rate had a great effect on the current distribution; (3) the anode fall was found to be between 10-20V; and (4) for $\dot{m}$ = 49.7 mg/sec of $N_2 + 2H_2$ propellant and I_{arc} = 10 A, approximately half of the total operating arcjet current was collected on the segment closest to the nozzle exit, within 5 mm of the exit plane. The results of this work generally agree with the Curran findings (1)-(3); however, there is some disagreement with (4), since, in this work, most of the arc is found to attach within 4 mm of the constrictor, Sec. 4.3.

Some aspects of Curran's work [Curran, *et al.*, 1990] require attention. For example, the operating voltage of the segmented thruster is ~25 - 30 V higher than the non-segmented version of the same arcjet. Also, the segmented thruster operated about 200 - 300 °K hotter than a baseline device, implying that the presence of the boron nitride spacers alters the anode heat conduction process. Despite these drawbacks, results were obtained and can be compared with the current density measurements made in this research.

7.2.1 Current Density Data

Curran *et al.*, [1990] measured the current to five individually isolated segments in a 1 kW arcjet, for a range of hydrazine propellant flow rates and arc currents. Current density data for all five segments was obtained for $\dot{m}$ = 37.3 mg/sec and 49.7 mg/sec for I_{arc} = 10 A. Figure 7.2 shows a comparison between the experimental flush probe data for 50 mg/sec, I_{arc} = 9.8 A, V_{arc} = 112 V and the data of Curran *et al.*, [1990] for $\dot{m}$ = 49.7 mg/sec, I_{arc} = 10 A and V_{arc} = 134 V.

It is interesting that the experimental data in Fig. 7.2 compare reasonably well with Curran *et al.* [1990], even with a 16% difference in arcjet operating voltage and a 18% difference in $P/\dot{m}$. The largest difference between the two different experimental approaches is at x = 1 mm and the anode region $5 \leq x \leq 8$ mm. At x = 1 mm, Curran's data lies between the results of probes 1 and 1′, though much closer to probe 1′. For $5 \leq x \leq 8$ mm the difference between the data is ~65-70%, with Curran's current density measurements of lower magnitude. Both sets of data display a maximum current density at x = 1 mm, with a secondary peak at x = 4 mm.

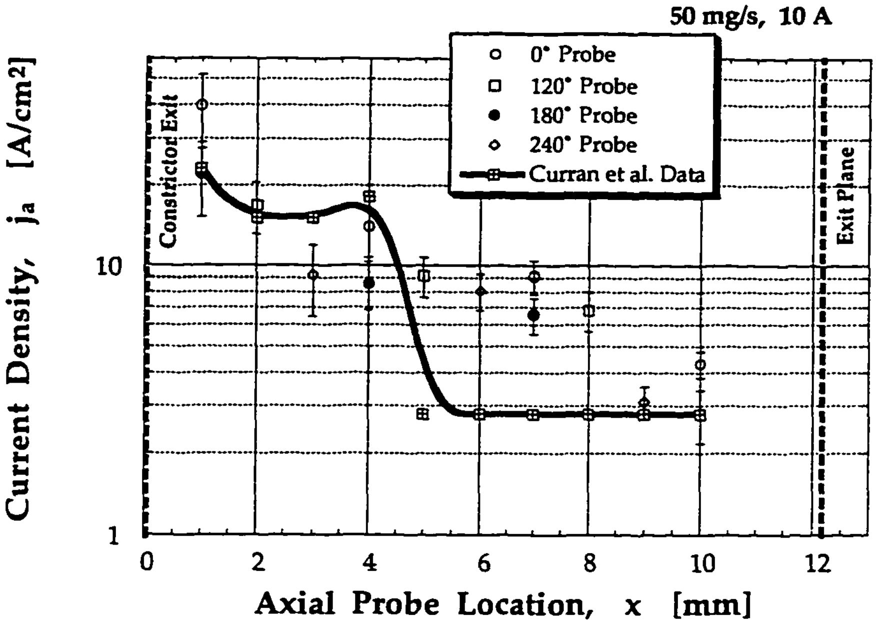

Fig. 7.2 Comparison between the j_a data for $\dot{m}$ = 50 mg/sec, I_{arc} = 9.8 A, V_{arc} =112V and the data of Curran *et al.* [1990] for $\dot{m}$=49.7 mg/sec, 10A and 134 V.

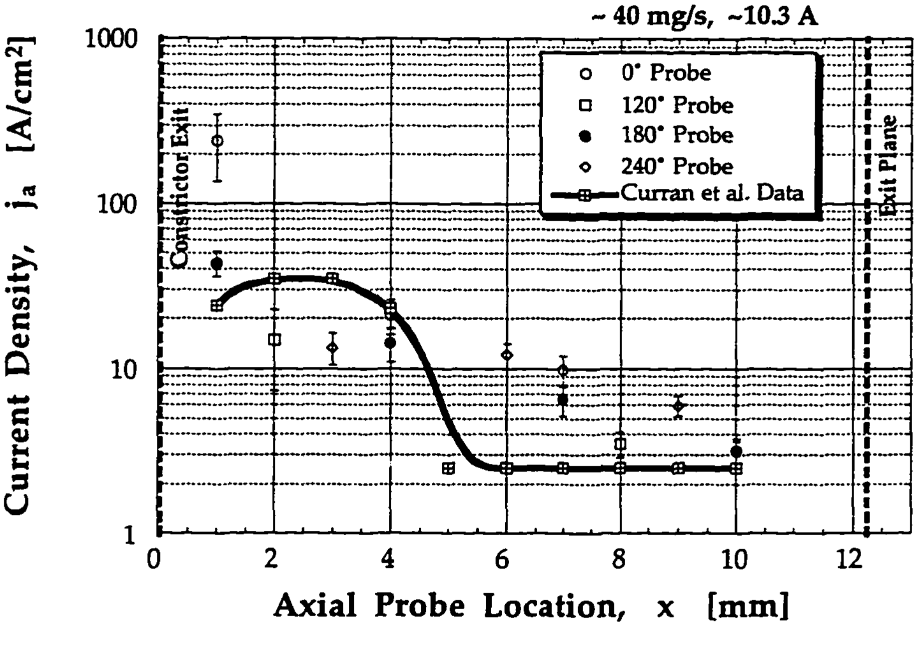

Fig. 7.3 Comparison between the j_a data for $\dot{m}$ = 40 mg/sec, I_{arc} = 10.6 A, V_{arc} = 104 V and the data of Curran *et al.* [1990] for $\dot{m}$= 37.3 mg/sec, I_{arc} = 10 A.

Figure 7.3 shows a comparison between the experimental flush probe data for $\dot{m} = 40$ mg/sec, $I_{arc} = 10.6$ A, $V_{arc} = 104$ V and the data of Curran *et al.*, [1990] for $\dot{m} = 37.3$ mg/sec and $I_{arc} = 10$ A. The data presented in Fig. 7.3 show the same differences as in Fig. 7.2, with the exception of the location of maximum current density. The results of this work for $\dot{m} = 40$ mg/sec and 10.6 A show a maximum current density at x = 1 mm, whereas Curran *et al.* show a smaller peak shifting slightly further downstream with decreasing propellant flow rate. This is opposite from our results, which show that the peak current density shifts downstream with *increasing* propellant flow rate, Sec. 4.3.2. Our results are consistent with the fact that V_{arc} increases with increasing flow rate and fixed I_{arc}. Larger propellant flow rates are associated with larger gasdynamic forces, thus pushing the arc further downstream, increasing the arc length, i.e. arc resistance, and therefore increasing V_{arc} for a constant current power supply.

The main reason some differences exist in the current density measurements of this work and that of Curran *et al.*, [1990] are due to the modification of their anode, discussed earlier. In this work, the presence of the flush-mounted planar micro-probes embedded at fourteen locations in the thruster anode poses minimal disturbance both to nominal arcjet operation and anode heat transfer. In fact, the modified NASA 1 kW thruster used in this work for internal nozzle diagnostics experiments produces similar thruster performance as the standard NASA-Lewis 1 kW rocket engine, as discussed in Sec. 7.1.

7.3 Comparison with MKB Model Predictions

The advances made in the field of numerical arcjet modeling in recent years has been very encouraging, especially since the ultimate goal of the numerical model is to allow a complete design of an arcjet thruster for various power levels. From the early works of Rhodes *et al.*, [1990], Butler *et al.*, [1993, 1994], Miller *et al.*, [1993], to the more recent work of Aithal *et al.*,

[1996], Miller *et al.*, [1996], and Megli *et al.*, [1995, 1996], much progress has been made in understanding arcjet thermophysics through the efforts in numerical arcjet modeling.

One of the important advances in arcjet modeling has been the simulation of arcjet physics with a multifluid nonequilibrium model as was done by Miller *et al.*, [1993, 1996] and Megli *et al.*, [1995, 1996]. However, these models, with the exception of Megli et al., [1995, 1996], do not provide a self-consistent approach to solving Ohm's Law and the energy equation, which is coupled with the nonequilibrium chemical kinetics, the Navier-Stokes equations and Maxwell's equations. Consequently, as discussed in Chapter 1, these models sometimes have to apply an artificial electrical conductivity "floor" in order to maintain arc attachment in the supersonic region, thus assuring stable arcjet operation.

The MKB model self-consistently solves Ohm's Law, coupled with two energy equations and the complete set of Navier-Stokes and Maxwell's equations, with appropriate boundary conditions. However, as is the case with all numerical simulations of complex thermophysics, experimental verification is required to provide acceptance and confidence in a model.

The results of the MKB model for $\dot{m} = 50, 60$ mg/sec, 10 A and various energy loss factors, δ are presented and compared with experimental results for similar conditions, Secs. 7.3.2-7.3.3. Because the model is continually being improved, it is believed that such comparisons will require re-evaluation in the future, but for now the main purpose is to provide initial guidance.

Table 7.1 Comparison of the experimental arcjet operating conditions and the MKB numerical arcjet model for both variable and constant δ factor.

	Experiment (Flush-Probes)				MKB Model Results			
Case	I_{arc} (A)	$\dot{m}$ (mg/s)	V_{arc}(V)	$P/\dot{m}$ (MJ/g)	$\dot{m}$ (mg/s)	V_{arc}(V)	$P/\dot{m}$ (MJ/g)	δ
1	9.8	50	112	22.0	50	105.5	21.1	varies
2	9.8	50	112	22.0	50	106.1	21.2	1200
3	9.8	50	112	22.0	50	113.0	22.6	3000
4	9.9	60	121	19.9	60	114.6	19.1	varies
5	9.9	60	121	19.9	60	116	19.3	1200

In the following sections the MKB model is briefly described and a comparison of experimental and numerical results are made for the conditions shown in Table 7.1. The numerical model data was obtained assuming the pure tungsten cathode is operating at a temperature of T_c= 3680°K, the tungsten melting temperature and the arc attachment area on the cathode tip is assumed to be 2 x 10^{-8} m^2, [Curran *et al.*, 1992]. The energy loss factor δ is discussed in Sec. 7.3.2.

7.3.1 Brief Description of MKB Model

The MKB arcjet model is a steady-state, laminar, two-temperature, chemical non-equilibrium model, that includes injection flow swirl and anode heat transfer in a converging-diverging nozzle geometry with variable cathode arc gap, [Megli, *et al.*, 1996]. The model also allows a variable nozzle geometry and a variable mixture of nitrogen and hydrogen, $x_{mol}N_2 + 2H_2$ and accounts for the chemical kinetics of seven species: H_2, N_2, H, N, H^+, N^+ and e^-.

The MKB model has the capability of predicting thrust, specific impulse I_{sp}, pressure, density and electron and heavy particle temperature distributions, using separate electron and heavy species energy equations, coupled with the Navier-Stokes and Maxwell's equations. In addition, the current density distribution, induced magnetic field, voltage and velocity components are calculated.

The momentum and species continuity equations are solved using a compressible form of the PISO (Pressure Implicit Split Operator) algorithm, [Megli, 1995]. The MKB model also solves for the anode heat transfer and couples the plasma electrical conductivity with the plasma properties, allowing a self-consistent solution for the current distribution. A complete presentation of this model, with assumptions, theory and results is found in the Ph. D. thesis of Megli, [1995].

Earlier versions of the MKB model [Megli, 1995], incorporated a constant inelastic energy loss factor δ, independent of electron energy. This δ factor accounts for inelastic losses to the internal rotational, vibrational, and excitational energy modes, [Sutton, *et al.*, 1965; Martinez-Sanchez, *et al.*, 1996] and is discussed further in Sec. 7.3.2.

Megli *et al.*, [1996] observed that various sources in the literature have stated differing values of δ as a function of electron temperature for H_2 and N_2 molecules, [Sutton, *et al.*, 1965; Martinez-Sanchez, *et al.*, 1996; Morgan, 1994]. Recent improvements to the MKB model have allowed for a variable δ factor. The variable delta factor is derived by solving the time dependent Boltzmann equation in terms of the electron number density [Morgan, *et al.*, 1990], using the software package MacELENDIF [Morgan, *et al.*, 1994] to estimate the δ factor for both N_2 and H_2.

In the following sections, comparisons are made between experimental data from this work and numerical model predictions using both a constant δ of 1200 and 3000 and a variable δ factor.

7.3.2 Calculations of Inelastic Energy Loss Factor

As discussed in Chapter 4, the experimental results for all flow rates and arcjet currents tested show that $T_{es} >> T_g$ near the anode, i.e. a state of thermal non-equilibrium exists. Consequently, a separate electron energy equation is required as follows, [Megli, *et al.*, 1995]:

$$\bar{\nabla}\cdot\left[C_{pe}T_e\left(n_e\bar{v} - \frac{\bar{j}}{e}\right)\right] = \bar{\nabla}\cdot\left[\lambda_e\bar{\nabla}T_e\right] + \bar{\nabla}\cdot\left[\frac{1}{m_e}\rho C_{pe}T_eD_e\nabla y_e\right]$$

$$+ \frac{\bar{j}\cdot\bar{j}}{\sigma} - \text{elst} - \text{radiation} \qquad (7.1)$$

In Eq. (7.1) the electrical current density, $j = \sigma E$, is assumed to be primarily due to the motion of electrons, so that the electron convection due to the mean flow velocity **v** is decreased by the electron drift flux, j/e, [Megli, *et al.*, 1996]. Equation (7.1) shows that the electron energy convection is balanced by thermal conduction, energy transport due to diffusion and ohmic heating, [Megli, *et al.*, 1996]. The term labeled 'elst' above represents the energy that electrons lose due to elastic transfer collisions and is given as, [Megli, *et al.*, 1996]:

$$\text{elst} = 3k\left[T_e - T_{gas}\right]n_em_e\sum_{i\neq e}\frac{\bar{\nu}_{ei}}{m_i} \qquad (7.2)$$

where the average collision frequencies $\bar{\nu}_{ei}$, between electrons and heavy particles are calculated as follows, [Jahn, 1968]:

$$\bar{\nu}_{ei} = \sqrt{\frac{8kT_{es}}{\pi m_e}}n_iQ_{ei} \qquad (7.3)$$

with the Coulombic cross section Q_{ei} given by, [Jahn, 1968]:

$$Q_{ei} = \frac{\pi e^4}{(4\pi\varepsilon_o)^2E^2}\ln\left(\frac{8\pi\varepsilon_o r_o E}{e^2}\right) \qquad (7.4)$$

In Eq. (7.4), E is the relative kinetic energy of the particles before collision. Since r_o is approximately equal to the Debye length, Eq. (7.4) can be written in a simpler form as:

$$Q_{ei} = \frac{\left(5.4 \times 10^{-9}\right)}{T_e^2(^\circ K)} \qquad [m^2] \qquad (7.5)$$

In Eq. (7.4) the logarithmic term was taken as ~10 which is an adequate approximation for ionized gases in the propulsion regime, [Jahn, 1968].

In Eq. (7.2), in order to account for inelastic losses to internal energy modes, e.g. rotational, vibrational and excitational, the electron-molecule collision frequencies are multiplied by an energy loss factor, δ, [Sutton, *et al.*, 1965; Martinez-Sanchez, *et al.*, 1996]. The δ factor varies for different molecules and is a function of the relative percentages of inelastic and elastic energy losses using the relation, [Megli, *et al.*, 1996]:

$$\delta = \frac{100}{\%\text{ of elastic energy transfer}} \qquad (7.6)$$

The δ factor is strongly dependent on the collision partner and T_e and weakly on T_{gas} [Megli, *et al.*, 1996].

Megli *et al.*, [1996] have shown that there are large uncertainties in the literature for δ of various molecules. The selection of a proper energy loss factor greatly affects the arc attachment location, the electron temperature and density populations near the anode wall, [Megli, *et al.*, 1996] as shown in Secs. 7.3.3-7.3.5. Based on the fact that the electron temperature measurements in this work range from 10,000°K-35,000 °K, an energy loss factor for N_2 of δ = 1200 was selected, as shown in Fig. 7.4; note that $\delta_{N_2} >> \delta_{H_2}$.

It is later shown that the experimental flush probe data lie between the MKB model with variable δ and the constant δ = 1200 approach, with better agreement using δ = 1200 in the model. The constant δ = 1200 approach follows the experimental data more closely within 2 mm of the constrictor exit compared with variable δ and agrees reasonably well for part of the region downstream of maximum current density.

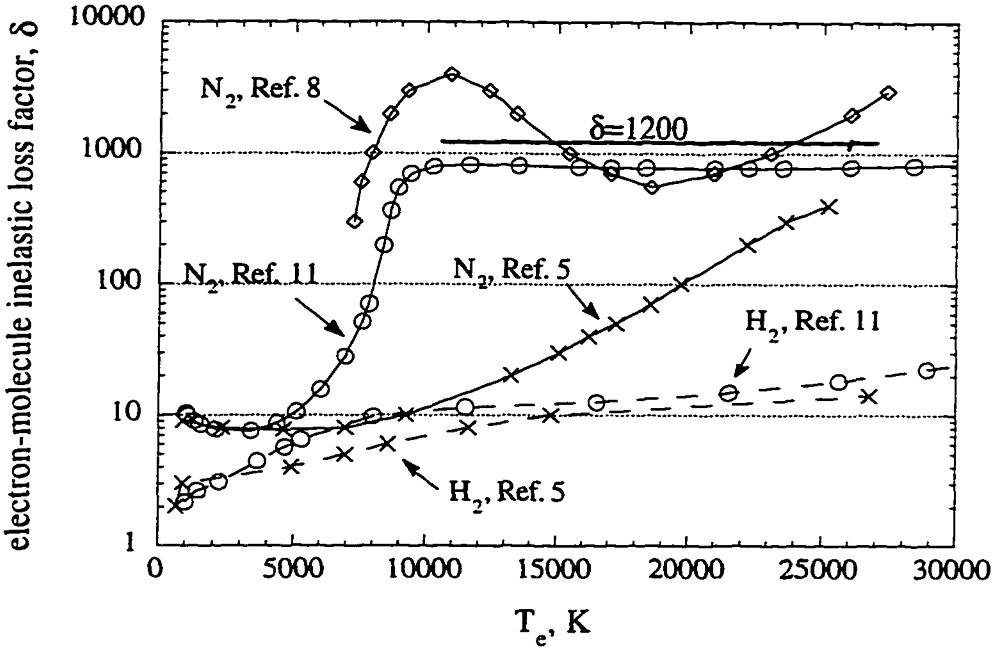

Fig. 7.4 Comparison of the electron-molecule energy loss factor δ from various sources. This plot was obtained from [Megli, *et al.*, 1996; Megli, 1995].

Now that an estimate of the energy loss factor was obtained, results of the MKB model using this δ factor are presented in the following sections.

7.3.3 Comparison of Experiment and Model Current Density

A major difficulty in developing a numerical arcjet model is realistically simulating the current attachment at the anode, in a self-consistent manner, [Miller, *et al.*, 1993]. Therefore, an important test for any arcjet model is to accurately describe the current attachment, which is coupled to the plasmadynamics and anode heating, Chapter 6.

In this section, the MKB model is compared with experimental flush probe data for $\dot{m} = 50$ and 60 mg/sec and $(I_{arc})_{avg} = 9.8$ A, i.e. cases (1)-(5), Table 7.1. For the nominal experimental conditions of $\dot{m} = 50$ mg/sec, $I_{arc} = 9.8$ A, numerical results for both a variable δ, $\delta = 1200$ and $\delta = 3000$ are compared with experimental data in Fig. 7.5. The value of $\delta = 1200$ was based on the data in Fig. 7.4.

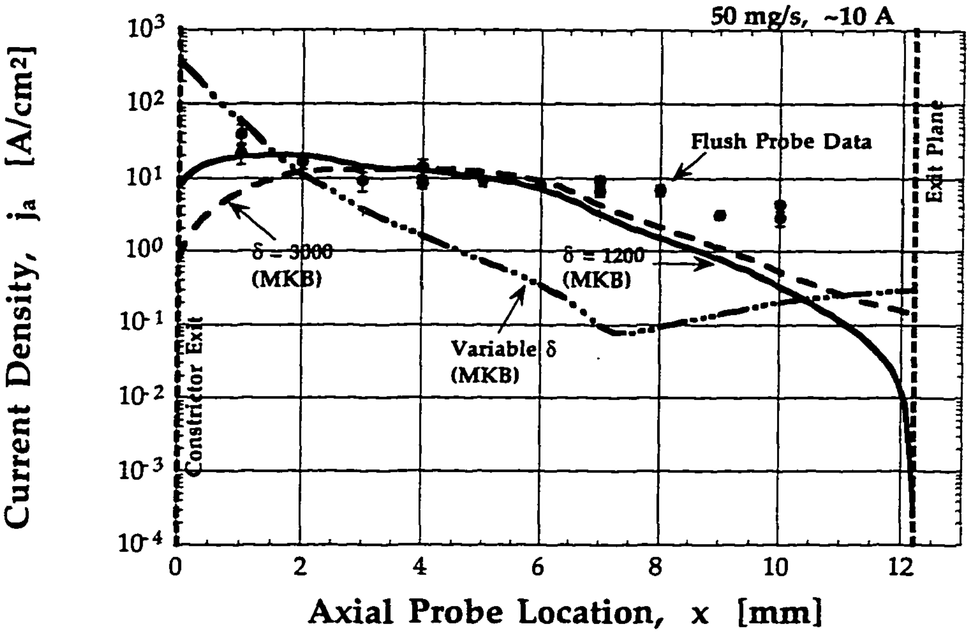

Fig. 7.5 Comparison of experimental and numerical results for current density j_a data at all probe locations. The MKB model was used with both variable δ and constant $\delta = 1200$ and 3000; numerical results were taken at r = 0 mm, i.e. at the wall. The experimental conditions were for the flush probe configuration and $\dot{m} = 50$ mg/sec, $I_{arc} = 9.8$ A.

As shown in Fig. 7.5, there is a significant difference between the variable δ and constant δ calculations. There is also reasonably close agreement between experiment and the $\delta = 1200$ and 3000 cases. The $\delta = 1200$ provides better agreement than $\delta = 3000$ within 2 mm of the constrictor exit, where the axial current density gradient is largest. Both the experimental data and the constant δ show a more gradual current density distribution than the variable δ case, suggesting a more diffuse current density distribution along the anode than the variable δ results show.

The δ = 1200 case matches the experimental j_a data well for $1 \le x \le 7$ mm, especially in the region of arc attachment, $1 \le x \le 4$ mm. For $x > 7$ mm δ = 1200 diverges from the experimental data.

Figure 7.6 below shows experimental flush probe data for $\dot{m} = 60$ mg/sec, $I_{arc} = 9.9$ A compared to the MKB model results.

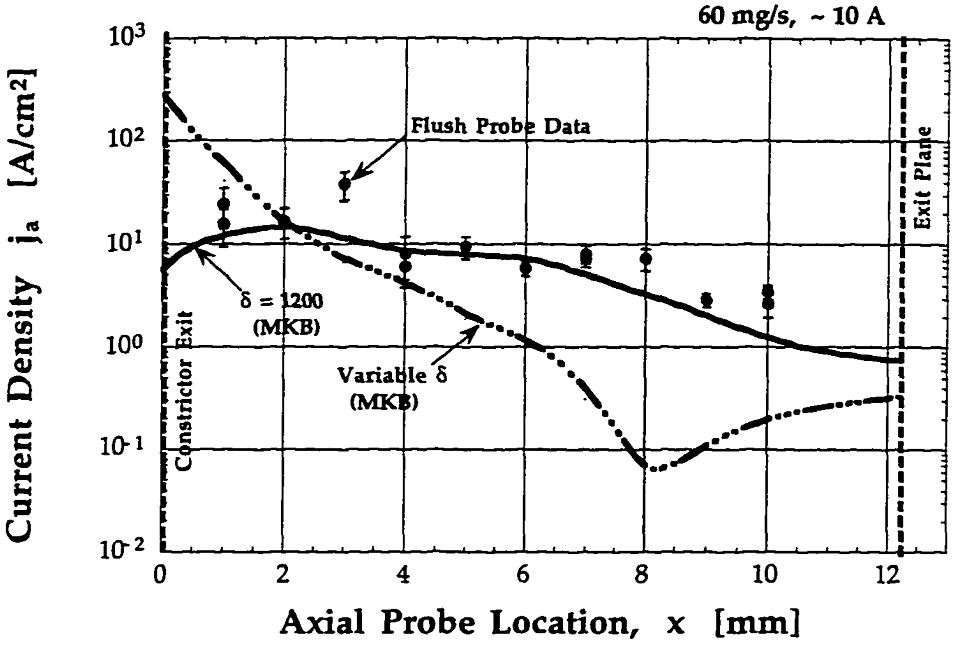

Fig. 7.6 Comparison of experimental and numerical results for current density j_a data at all probe locations. The MKB model was used with variable δ and δ = 1200; numerical results were taken at r = 0 mm, i.e. at the wall. The experimental conditions were for the flush probe configuration and $\dot{m} = 60$ mg/sec, $I_{arc} = 9.9$ A.

Comparing Figs. 7.5 and 7.6 shows that for the variable δ case the model does not predict the shift of the peak current density j_a with increasing propellant flow rate, a result observed in the experimental data, Sec. 4.3.2.

The model predicts maximum current density at the constrictor exit, compared with the experimental result of maximum j_a at 3 mm downstream of the constrictor exit. However, the MKB model results using $\delta = 1200$ does predict a shift in $(j_a)_{max}$ to about $x = 2$ mm. As with the experimental results for $\dot{m} = 50$ mg/sec, the model underpredicts the current density in the region $x > 6$ mm. Also, the variable δ case causes the anode current attachment to shift upstream compared with $\delta = 1200$, thus decreasing the arc length and arcjet voltage, [Megli, *et al.*, 1996].

These results imply that the anode arc attachment and therefore the arcjet operating voltage, are dependent on the δ factor so that an accurate accounting of inelastic energy losses in the anode sheath layer is critical for realistic simulation of current attachment. The best agreement (especially in the arc attachment zone) between the experimental current density data (using flush probes) and the MKB model is obtained if $\delta = 1200$ is used; also a better fit to the experimental data is obtained near the constrictor exit using $\delta = 1200$. Obtaining good agreement between the MKB model and the experimental j_a data in the arc attachment zone is important because this is the region of interest since most of the anode heating occurs here, Chapter 6.

7.3.4 Comparison of Electron Number Density Data

As with the current density distribution results, the electron number density distribution $n_{es}(x)$ in the anode sheath layer, as predicted by the MKB model, is dependent on the δ factor. Figure 7.7 shows n_{es} at all probe locations for the experimental conditions of 50 mg/sec and 9.8 A, compared with the MKB model with variable and constant $\delta = 1200$ and $\delta = 3000$.

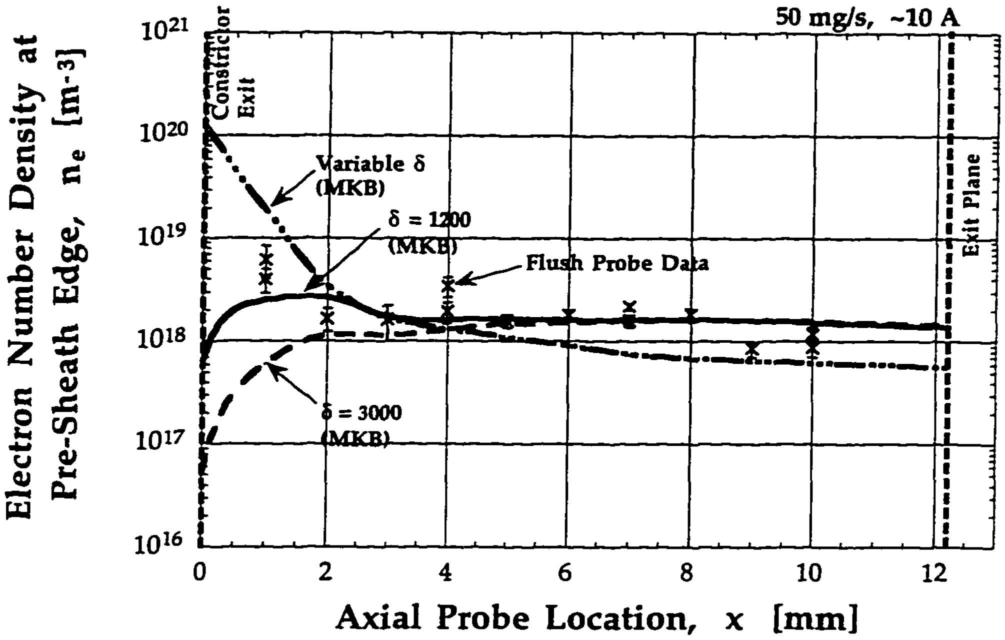

Fig. 7.7 Comparison of experimental and numerical results for electron number density data at all probe locations. The MKB model was used with both variable δ and constant δ = 1200 and 3000; numerical results were taken at r = 0 mm, i.e. at the wall. The experimental conditions were for the flush probe configuration and $\dot{m}$ = 50 mg/sec, I_{arc} = 9.8 A.

As with the current density predictions, reasonable agreement between experiment and δ = 3000 results exists for the region 2 ≤ x ≤ 10 mm, though δ = 1200 provides a better fit to the experiment over a wider range, 1 ≤ x ≤ 10 mm, especially in the region of arc attachment, 1 ≤ x ≤ 4 mm.

Electron number density results are presented in Fig. 7.8 for $\dot{m}$ = 60 mg/sec and 9.9 A, with only the variable δ and δ = 1200 cases shown. The model (using δ =1200) and experiment match reasonably well at x = 1 mm and in the region 3 ≤ x ≤ 5 mm. Within 3 mm of the constrictor, the MKB model results using δ = 1200 provides better agreement with the experiment than the variable δ results.

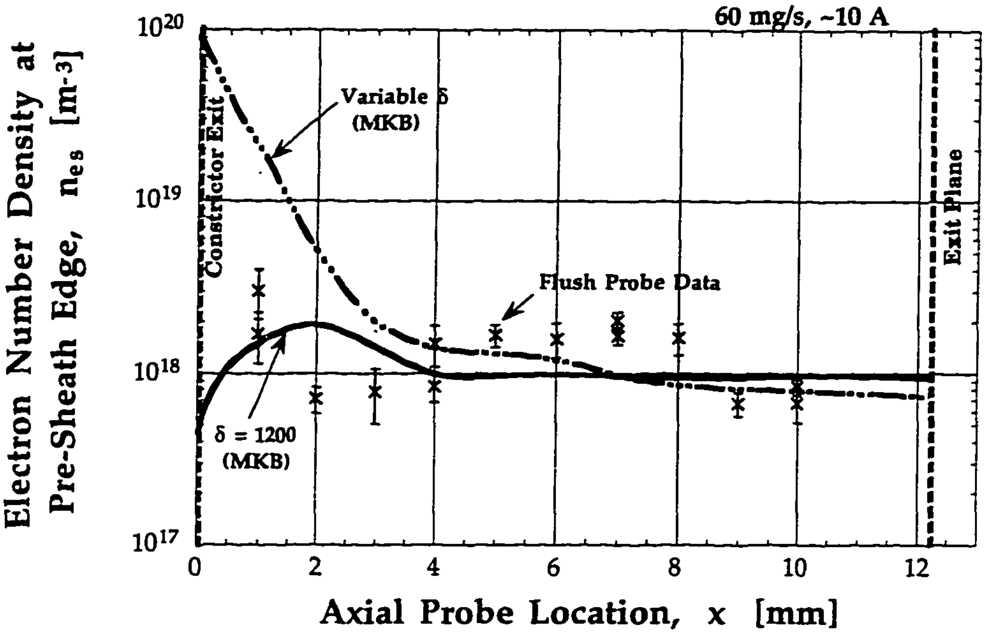

Fig. 7.8 Comparison of experimental and numerical results for electron number density data at all probe locations. The MKB model was used with variable δ and constant δ = 1200; numerical results were taken at r = 0 mm, i.e. at the wall. The experimental conditions were for the flush probe configuration and $\dot{m} = 60$ mg/sec, $I_{arc} = 9.9$ A.

7.3.5 Comparison of Electron Temperature Data

An interesting result of this work is that the experiments have shown, under a variety of arcjet operating conditions, that $T_{es} >> T_g$ near the anode wall so that a high degree of thermal non-equilibrium exists in the anode sheath boundary layer. This condition is responsible for increased ionization rates, resulting in an elevated population of charged species, [Megli, *et al.*, 1996], permitting the conduction of electrical current through the relatively cold gas layer adjacent to the anode. This result implies that a separate energy equation for the electrons and heavy particles is required to capture the arc attachment physics, [Megli, *et al.*, 1996].

The thermal non-equilibrium condition near the wall also controls the near anode electron density, which in turn determines the electrical conductivity of the plasma, Sec. 4.6.1. In addition to n_{es} production near the anode due to the large T_{es}, radial diffusion of the electrons from the much hotter arc core, which is in a state of thermal equilibrium, also increases the electron population in the anode boundary layer. These processes contribute to produce a non-zero, finite value for the electrical conductivity σ near the anode, [Megli, *et al.*, 1996], Fig. 4.52.

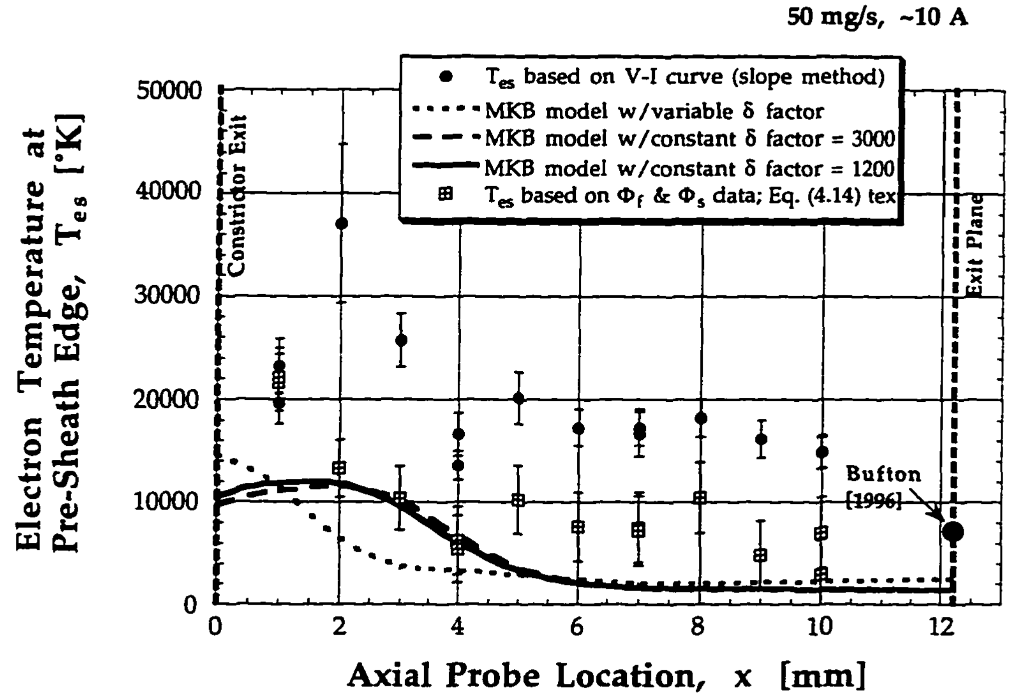

Fig. 7.9 Comparison of experimental and numerical results for electron temperature data at all probe locations. The MKB model was used with variable and δ =1200 and 3000; numerical results were taken at r = 0 mm, i.e. at the wall. The experimental conditions were for the flush probe configuration and $\dot{m}$ = 50 mg/sec and I_{arc} = 9.8 A. The T_{es} data point at the exit plane was obtained from the exit-plane measurements of Bufton [1996]. Note that the uncertainty in the T_{es} data from Bufton [1996] is ± 15%.

Figure 7.9 shows the experimental T_{es} data for $\dot{m}$ = 50 mg/sec and 9.8 A, compared with: (1) the MKB model results with variable and constant δ factors; and (2) T_{es} derived from the slope method, Eq. (3.32) and the potential data, Sec. 4.2.5. For all three δ factors used in the arcjet simulation, the model T_{es} values are much lower than the experimental results, at all probe locations. The $\delta = 3000$ and 1200 cases predict a maximum electron temperature at $x = 2$ mm, in agreement with experiment. The MKB model and experiment both show that the electron temperature decreases after a maximum T_{es} is attained, and both results show that $T_{es} >> T_{gas}$, where $T_{gas} \sim 1400$ °K, based on nozzle surface temperature measurements. The difference between the experimental T_{es} data obtained using the slope method (Eq. 3.32) and the potential data (Sec. 4.2.5) is discussed in detail in Sec. 7.3.6.

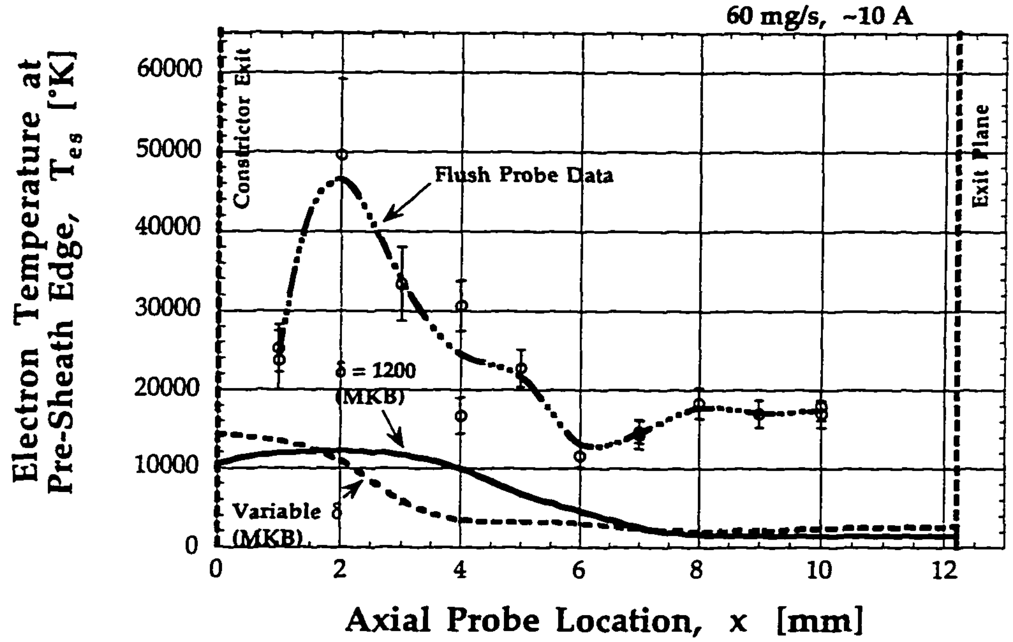

Fig. 7.10 Comparison of experimental and numerical results for electron temperature data at all probe locations. The MKB model was used with variable and constant $\delta = 1200$; numerical results were taken at $r = 0$ mm, i.e. at the wall. The experimental conditions were for the flush probe configuration and $\dot{m} = 60$ mg/sec and $I_{arc} = 9.9$ A.

Figure 7.10 shows comparisons between experimental T_{es} data for $\dot{m} = 60$ mg/sec and $I_{arc} = 9.9$ A and MKB model results with variable δ and $\delta = 1200$. Comparing Figs. 7.9 and 7.10, the MKB model results (especially with variable

δ) show that the axial T_{es} gradient becomes less steep, within 2 mm of the constrictor as the flow rate is increased, while the experimental data does not show much change in dT_{es}/dx with flow rate. As with the nominal conditions, $(T_{es})_{max}$ occurs at $x = 2\text{-}3$ mm for $\delta = 1200$, in agreement with experiment; the variable δ case shows $(T_{es})_{max}$ at $x = 1$ mm.

In summary, there appears to be reasonable agreement between experiment and the MKB model for the current density and electron number density distributions using $\delta = 1200$. These results are encouraging because presently, the major source of problems in numerical arcjet models has been their inability to accurately and self-consistently simulate the current and voltage distributions. The MKB model appears to satisfy both of these important criterion of realistic simulation of arcjet performance.

7.3.6 Interpretation of Electron Temperature Results

In this work, the electron temperature was evaluated two different ways. The first method involved evaluating T_{es} using Eq. (3.32) and the slope of the electron-retarding region. The second method was evaluation of T_{es} based on the potential data, ϕ_f and ϕ_s, Eq. (4.14), Sec. 4.2.5. A comparison between the two methods was shown in Fig. 4.14; also, comparisons with the T_{es} results from the MKB model were made in Sec. 7.3.5, Fig. 7.9. At all probe locations T_{es} based on the potential data is lower than T_{es} based on the slope method.

Both methods assume that the electron sheath is thin and collisionless with the electrons exhibiting a Maxwellian distribution. The electron temperature based on the slope appears to be more sensitive to possible probe contamination effects because: (1) this method relies on a range of data points in the electron-retarding region; and (2) it has been observed that even when a probe is clean, hysteresis is sometimes present in the probe V-I characteristic. However, T_{es} based on the potential data is sensitive to the accuracy of the ϕ_s and ϕ_f results; an error of ± 1 V in ϕ_s and ϕ_f can result in a ±3500-5000 °K error in T_{es}, Sec. 4.2.5.

Using the electron temperature based on the slope method leads to calculations of $j_{th,e}$ which, when integrated over the internal anode surface area, result in numbers reasonably close to the I_{arc} value of 10 A. Using T_{es} based on the potential data results in $I_{arc} < 10$ A. However, better agreement between the MKB model T_{es} results and T_{es} based on the potential data is shown in Fig. 7.9, when compared with the electron temperature derived from the slope method.

Regardless of how T_{es} is evaluated, the experimental measurements show that the plasma in the near-anode region is in a state of high non-equilibrium, with $T_{es} >> T_{gas}$. Due to the T_{es} differences between the two methods outlined above, an uncertainty is created in the anode heating distribution, since $q_e=q_e(j_a, T_{es}, \phi_s)$, as well as in the n_{es} calculations, which are based on the T_{es} data. The n_{es} and q_e calculations were made based on the derivation of T_{es} from the slope of the electron-retarding region; every effort was made to verify that only data from clean probes was included in the analysis.

In summary, it is difficult to state which method of evaluating T_{es} is better or preferable because: (1) there is evidence from the probe V-I curves that the electrons have a Maxwellian distribution since a Maxwellian fit to the electron-retarding region using T_{es} derived from the slope provides better agreement with the data than T_{es} based on the potential data, as shown in Fig. 7.11 below; and (2) T_{es} based on the potential data shows good agreement with the MKB model, Fig. 7.9. However, the MKB model results for T_{es} seem to *underestimate* the electron temperature, especially in the region within 7 mm of the exit plane. The experimental data are more consistent with the Bufton [1996] measurement in the arcjet exit plane, Fig. 7.9.

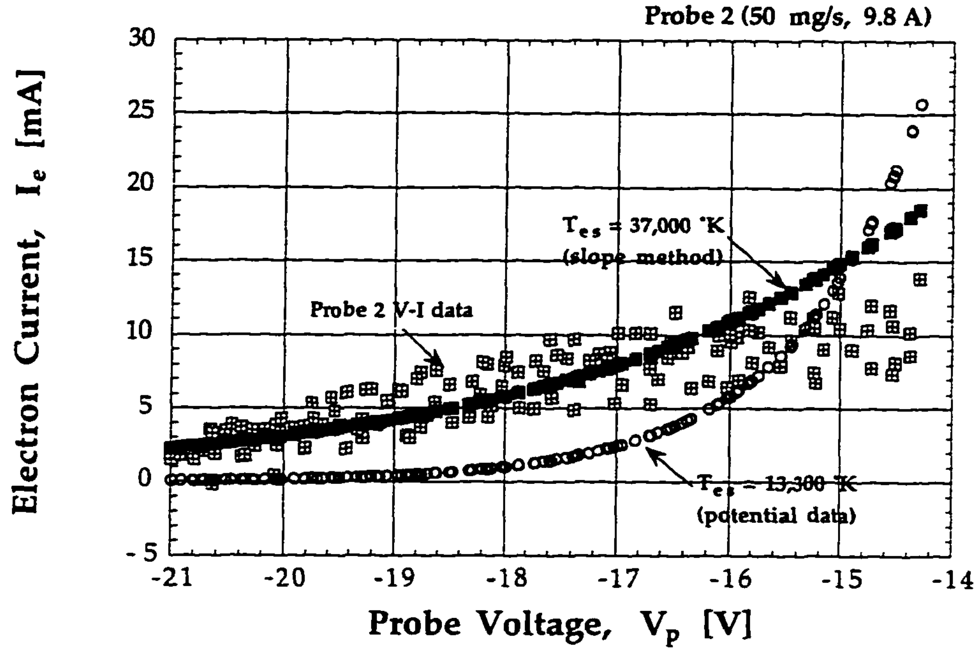

Fig. 7.11 A Maxwellian curve fit to the electron-retarding region of flush probe 2 shows that using T_{es} based on the slope method provides a better fit than using T_{es} based on the potential data. The probe 2 V-I characteristic was obtained for the arcjet conditions of $\dot{m}$ = 50 mg/sec and I_{arc} = 9.8 A.

8. SUMMARY and CONCLUSIONS

8.1 Summary

An experimental investigation of the anode boundary layer of a low power 1 kW electrothermal arcjet thruster was performed by using electrostatic micro-probes. The standard 1 kW NASA-Lewis arcjet design was modified to accommodate fourteen micro-probes in the anode body and to facilitate the heat transfer analysis in the Megli-Krier-Burton (MKB) model. Several parameter studies were conducted, including varying the arcjet operating current (7.8 - 10.6 A), the N_2 + $2H_2$ propellant flow rate (40 - 60 mg/s) and the position of the micro-probes, i.e. flush probe or cylindrical probe.

The main objectives of this experimental investigation were to: (1) understand what controls arc attachment in a modified low power 1 kW arcjet; (2) investigate the anode boundary layer region and obtain data for the plasma properties, ϕ_f, ϕ_s, j_a, T_{es} and n_{es} for different arcjet operating conditions; (3) verify azimuthal current symmetry; (4) understand what affects anode heating; and (5) provide experimental data that will assist arcjet modelers in predicting and calculating more accurately the current and voltage distributions in an arcjet. These objectives were met through the design, fabrication and implementation of an array of fourteen electrostatic micro-probes positioned at various axial and azimuthal locations in the anode.

The only practical probe configuration available was the single probe, used in a flush-mounted configuration allowing plasma property data to be obtained along the anode. It was demonstrated that for all the cases studied in this work and with the use of appropriate probe theory, plasma property conditions at the anode wall as well as electron anode heating can be obtained with the electrostatic flush probe.

Another probe configuration used was the cylindrical probe, which was extended into the flowing plasma stream. Based on numerical calculations with the MKB model and experimental data the cylindrical probe does provide useful information without disturbing the plasma flow. Because of similar V-I characteristics for the flush and cylindrical probes, e.g. a flat ion saturation region, the interpretation of the V-I curves was similar. The volume constraints and intense heating within 1 mm of the constrictor prevented the cylindrical probe from being extended beyond ~ 0.15 mm into the flow for probes 1,1'; for probes 2-10' the maximum probe extension used was 0.25-0.3 mm. Probing the anode boundary at distances larger than 0.3 mm, i.e. near the arc core, may lead to induced flow disturbances and probe melting.

Implementing the electrostatic probe introduced several complications: (1) selecting the appropriate probe size was determined by constraints on melting, sheath-edge effects, probe-capacitance effects and the available internal nozzle volume; (2) assessing the probe collection area and estimating sheath size effects; (3) operating the probe in the appropriate regime to minimize any plasma perturbations, e.g. if biased too high the probe sheath fields may perturb the surrounding plasma; and (4) achieving and maintaining contamination-free probes throughout the experiment.

Though the electrostatic probe is a relatively inexpensive and simple diagnostic its implementation and data interpretation can be involved. Using the MKB model and experimental data for j_a, n_{es} and T_{es}, estimates were made of each probe sheath size and mean free path calculations were performed for 31 separate elastic and inelastic reactions in the anode boundary layer at all probe locations. It was concluded that for electron collection the sheath is thin and collisionless. For ion collection the sheath is thin and varies from highly collisional near the constrictor to moderately collisional near the exit. The data analysis was iterative, i.e. T_{es} was determined from the V-I curve assuming a thin collisionless electron sheath and the mean free path calculations and sheath size estimates were made. The collisionless electron sheath assumption was then verified so that the initial T_{es} and n_{es} data were used.

The fact that the electron sheath was thin and collisionless allowed T_{es} to be determined from the slope of the electron-retarding region, i.e., the slope method. Due to the collisional nature of the ion sheath, the ion saturation current was constant so that a non-linear theoretical curve fit to this region was not required. A constant value of the ion current was used based on the ion saturation current at -20 V and subtracted from the total probe current to obtain the electron current, required for obtaining T_{es}. This procedure was simple, straightforward and self-consistent since it did not rely on uncertain mobility and collision cross-sectional data.

Another method for evaluating T_{es} was based on the potential data. This method provided T_{es} values lower than T_{es} based on the slope method (Eq. 3.32), but higher than the MKB model predictions. Regardless of which method was used to obtain T_{es}, the experimental data show that $T_{es}/T_{gas} >> 1$ near the anode.

Once data was obtained for j_a, ϕ_s and T_{es}, the anode heating due to electrons, q_e, could be calculated for the various arcjet operating conditions tested. In addition, a weighted anode sheath potential $\bar{\phi}_s$ was estimated based on the ϕ_s and j_a distributions, providing the anode sheath boundary condition for the MKB model. Similarly, an energy loss factor δ was determined and implemented in the MKB code providing improved correlation with the experimental data. Estimates of scalar electrical conductivity and electric fields along the anode were also derived based on the experimental data.

In addition to comparisons of the experimental results with the MKB model for certain arcjet conditions, comparisons were also made with the experimental work of others.

8.2 Conclusions

Obtaining useful plasma property data in the anode boundary layer of a low power arcjet by implementing electrostatic probes at several axial and azimuthal locations was demonstrated under various thruster operating conditions. The experimental accuracies of the techniques used in this study were within acceptable limits. Results with high uncertainties were mainly due to large uncertainties in the probe collection area.

The main goal of this work was to provide experimental plasma property data in the anode boundary layer region for arcjet numerical model verification and for use in arcjet thruster design. Based on the results of this research, the following conclusions are made:

(1) Electrostatic micro-probes can be used to obtain valuable plasma property information in the anode boundary layer of a 1 kW arcjet.

(2) The electron temperature was determined using two methods: (1) the slope of the electron-retarding region, Eq. (3.32); and (2) the ϕ_s and ϕ_f potential data. Regardless of which method was used, for all propellant flow rates tested, $T_{es}/T_{gas} >> 1$ (T_{es}/T_{gas} ~10-20) in the anode boundary layer at all probe locations. This demonstrates that a highly non-equilibrium plasma, with dual temperatures, exists in the near-anode region of an electrothermal arcjet.

(3) The flush and cylindrical probe configurations produced similar results and trends, within the experimental error. Flush probes are recommended to study the near-anode region because the likelihood of probe contamination and probe melting is reduced, compared with the cylindrical probe configuration.

(4) Experimental data was obtained to verify and calibrate arcjet numerical models. Based on the experimental data for T_{es} an energy loss factor of $\delta = 1200$ was found to be appropriate for use in the energy equation, resulting in improved correlation between the experimental data and the numerical

model. Also, the correct arcjet operating voltage, consistent with the experimental results, is obtained with $\delta = 1200$. This value of δ improves the agreement between the MKB model and the experimental data for j_a and n_{es} near the constrictor and in the region of maximum arc attachment. Large differences still exist between $(T_{es})_{MKB}$ and $(T_{es})_{expt}$, however the MKB code does accurately predict the location of $(T_{es})_{max}$ using $\delta = 1200$.

(5) For most of the experimental conditions tested, azimuthal current symmetry is inferred from the j_a data. The largest discrepancy is between probes 1,1′ for the lower flow rates, higher $P/\dot{m}$, of 40 and 45 mg/s. This is believed to be predominantly due to the relatively large uncertainty in the probe collection area.

(6) The current density j_a is maximum at $x = 1$ mm for all arc currents tested and for $\dot{m} = 40, 45, 50$ mg/s, with a secondary peak at $x = 4$ mm and decreases monotonically with increasing distance from the constrictor. Increasing I_{arc} has a relatively negligible effect on the current density distribution, except at $x = 1$ mm and $x = 4$ mm. However, increasing the flow rate has a larger overall effect on the current density, shifting $(j_a)_{max}$ downstream to $x = 3$ mm, for $m = 60$ mg/s.

(7) The width of the arc attachment region and location of maximum current attachment is more influenced by the flow rate, than the arcjet current. The arc attachment is dependent on the mechanisms of n_{es} production near the anode, through the current density j_a.

(8) For all flow rates studied the electron number density is largest near the constrictor exit with a secondary peak at $x = 4$ mm, similar to the j_a distribution, suggesting that j_a and n_{es} are strongly coupled.

(9) Increasing the $N_2 + 2H_2$ propellant flow rate from $\dot{m} = 40$ mg/s to 60 mg/s has a relatively larger effect on the ϕ_f, ϕ_s, j_a, n_{es}, T_{es} and q_e distributions than varying the arcjet operating current, in agreement with [Curran *et al.*,

1990]. Also, the maxima in ϕ_s, j_a and q_e moves downstream as $\dot{m}$ is increased to 60 mg/s. No clear trend is observed in the T_{es} distribution for varying propellant flow rate and arcjet operating current.

(10) The sheath potential is electron-attracting $\phi_s > 0$, throughout the anode boundary layer implying that $j_a > j_{th,e}$. The anode sheath potential is largest in regions of high current density and lowest in regions of low current density, except at x = 1 mm. This has direct consequences with regards to anode heating, since $q_e = j_a[5kT_{es}/2e + \phi_s + W]$.

(11) A weighted anode sheath potential $\bar{\phi}_S$ was calculated and found to vary from $8.1 \text{ V} \leq \bar{\phi}_S \leq 17 \text{ V}$ for the arcjet operating conditions tested, in agreement with the results of [Curran *et al.*, 1990]. The weighted anode sheath potential is fairly constant with increasing flow rate and is maximum ($\bar{\phi}_S = 17 \text{ V} \pm 5.1 \text{ V}$) for $\dot{m}$ = 60 mg/s, the largest flow rate studied.

(12) The maximum anode heating is 285 W ± 82 W (24% of arc power) for the conditions of I_{arc}= 9.9 A, V_{arc}= 121 V and $\dot{m}$= 60 mg/s, with $P/\dot{m}$= 19.9 MJ/kg. Operating the arcjet at low $P/\dot{m}$ results in a larger fractional anode power loss, while arcjet operation at $P/\dot{m} \geq 22$ MJ/kg results in slightly less fractional anode power losses.

(13) The anode heating as a fraction of total arcjet power input ranges from 18-24 % over a range of specific energies of $18.8 \text{ MJ/kg} \leq P/\dot{m} \leq 27.4 \text{ MJ/kg}$. These results agree with the segmented anode results of [Curran *et al.*, 1990]. Over half of the anode heating is due to the energy gained by the electrons traversing the anode sheath, $j_a\phi_s$ (a result also obtained by Soulas *et al.*, [1993] in a free burning arc) and ~ one-third of the anode heating is due to the electron thermal energy, $5kT_{es}/2e$. The anode heating distribution closely follows the j_a profiles, so that $(q_e)_{max}$ coincides with $(j_a)_{max}$. After $(q_e)_{max}$ is attained, the anode heating decreases as distance from the constrictor (and the arc attachment region) increases.

(14) Within 0.25-0.3 mm of the anode T_{es} decreases as the radial distance from the anode increases; this is in qualitative agreement with the MKB model and the results of [Miller *et al.*, 1996]. Similar to the flush probe, the cylindrical probe results show that the electron number density follows the j_a profiles for $L_{ext} \neq 0$, with large n_{es} radial gradients in the region $2 \leq x \leq 6$ mm.

(15) Based on the experimental data obtained in this work a scalar electrical conductivity was calculated to range from 1.2 $[\Omega\text{-m}]^{-1}$ at x = 1 mm, (corresponding to $(j_a)_{max}$) to 17 $[\Omega\text{-m}]^{-1}$ at x = 10 mm. These values are generally lower than the artificially imposed conductivity floors used by some numerical models, [Butler *et al.*, 1992], e.g. 10-100$[\Omega\text{-m}]^{-1}$.

8.3 Recommendations for Future Work

This investigation demonstrated that the implementation of a simple and inexpensive diagnostic tool, the electrostatic micro-probe, can provide detailed information on plasma properties in the anode boundary layer of a 1 kW arcjet. During the course of this work, several questions were raised and may warrant future investigation. Based on the knowledge obtained through this work, the following recommendations for future research are made:

(1) The operating range of propellant flow rates and arcjet operating currents used in this investigation were limited either by the thruster design or the operating envelope of the power supply, so that $P/\dot{m}$ was only varied by ~ 30%. For future space mission scenarios the stationkeeping roles of low power arcjets will expand, requiring operation at higher $P/\dot{m}$. Therefore, it would be of interest to the electric propulsion community if a thruster is designed, perhaps using the MKB model, to operate at the higher $P/\dot{m}$ levels of 40-80 MJ/kg. . This would simulate a more realistic, space-qualified thruster. The techniques described in this work, with some modifications, can then be used to investigate the anode boundary layer for these higher specific energies.

(2) Due to its low molecular weight, H_2 is a desirable propellant to use from the standpoint of increased performance, i.e. I_{sp}. This would necessitate a redesign of the arcjet thruster geometry in order to operate at the lower propellant flow rates required. Unfortunately, the low density of H_2 requires large storage capabilities, posing tankage problems on satellites. However, from an academic approach, it would be of interest to perform the same experiments in this work with a hydrogen arcjet. The chemistry in the MKB model could then be greatly simplified and using H_2 would allow another set of data to calibrate the model.

(3) As shown in this work, the current density distribution decreases as the flow expands through the nozzle. However, within 2 mm of the exit plane, the current density is still of non-negligible magnitude, ~O(1-3 A/cm^2), in contrast to the MKB model results. Another probe may be located about 0.5-1.0 mm downstream from the exit plane, of smaller diameter than probes 2-10'. Also, a second probe, of equal diameter may be placed at the nozzle lip, flush with the exit plane. These additional probes would provide information regarding the variation of n_e near the exit plane, discussed previously, [Bufton, 1996].

(4) From his quadrupole probe measurements, Bufton [1996] was able to infer a current density in the exit plane, at r = 2 mm, of ~ 1 A/cm^2. The current density in the nozzle exit plane can be measured using a flat probe cemented to the nozzle exit plane surface. This probe would be biased using a function generator and j_a would be obtained in the same fashion as in this work.

(5) A set-up of a cylindrical probe transverse to the flow and aligned to the flow can be made to provide the plasma flow velocity, v_f. The ratio of the ion saturation currents from each probe respectively is proportional to v_f^2, [Johnson *et al.*, 1969; Poissant *et al.*, 1984; Tan, 1973].

(6) Although the nozzle flow is relatively viscous and therefore damped, the velocity field in the nozzle is probably steady. However, this has not been verified in this work and could be investigated by employing Langmuir probes at much higher sampling rates, e.g., 50 kHz, than were employed here.

APPENDIX I: Cathode Erosion

Cathode erosion is a major problem for long duration (i.e. thousands of hours) arcjet thruster operation.

Figure A.1 shows a front and side view of the 2% thoriated tungsten cathode used in this work. The photomicrograph was taken after about 17.5 ± 2.5 hours of run-time on the cathode, which was used in the HD-18 tungsten alloy nozzle. The same cathode was later used in the 2% thoriated tungsten nozzle for a total run-time of about 35 ± 5 hours.

Initially, when a new cathode is used, its tip is sharp. However, upon start-up, a 4 kV is used to initiate arc breakdown, thus melting the tip to a round shape. As shown in Fig. A.1(a) the cathode tip is a molten shiny convex "bump" (with a diameter of ~ 0.35 mm) in the middle of a crater with an outer diameter of about 0.52 mm. The total surface area of the bump is approximately 0.11 mm^2. If 10 A are applied to the arcjet, and if the current flows uniformly to the bump then the current density emitted from the cathode is ~ 9000 A/cm^2. However, if the current flows uniformly to the entire cathode tip, including the crater surrounding the bump, the current density is ~4100 A/cm^2.

Figure A.1(b), a side view of the cathode, clearly shows the erosion of the tip. As the cathode tip erodes, its recession distance, from an initial cathode gap of ~ 0.6 mm, increases with run-time. Consequently the arc length increases for a given flow rate and I_{arc}, and therefore V_{arc} increases as well. This is also observed in the work of Curran *et al.*, [1992] for the NASA-Lewis 1 kW thruster.

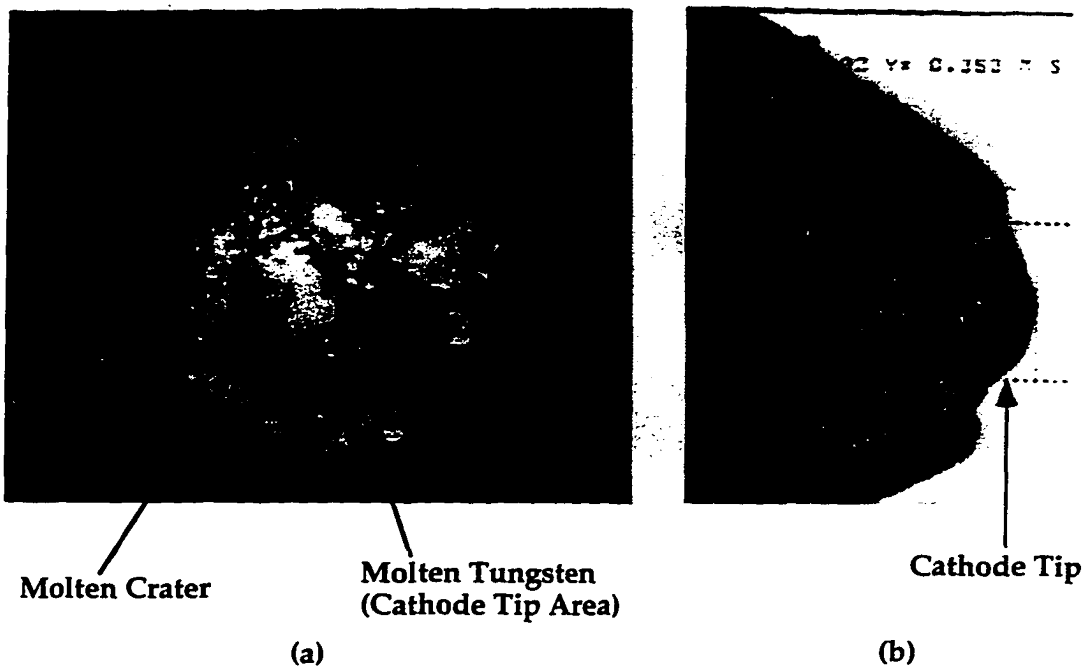

(a) (b)

Fig. A.1 Photomicrograph of the 2% thoriated tungsten cathode used in the UIUC 1 kW arcjet thruster, taken after about 17.5 ± 2.5 hours of run-time. The front view is shown in (a), with the molten cathode tip visible, and the side view is shown in (b). This cathode was used in both the HD-18 tungsten alloy nozzle and the 2% thoriated tungsten nozzle.

References

Aithal, S. M., Subramaniam, V. V., and Babu, V., "Numerical Simulation of Plasma and Reacting Flows," AIAA Paper 96-2024, June, 1996.

Allen, J. E., Boyd, R. L. F., and Reynolds, P., *Proc. Roy. Soc.*, Vol. B70, 1957, pp. 297.

Babu, V., Aithal, S. M., and Subramaniam, V. V., "Numerical Simulation of a Hydrogen Arcjet," *Journal of Propulsion and Power*, Vol. 12, No. 6, Nov.-Dec. 1996, pp. 1114-1122.

Bell, B. C., Glocker, D. A., *J. Vac. Sci. Techn.*, Vol. A6, 1988, pp. 2047.

Bettinger, R. T., and Chen, A. A., J. *Geophys. Res.*, Vol. 73, 1968, pp. 2513.

Birkan, M. A., "Arcjets and Arc Heaters: An Overview of Research Status and Needs," *Journal of Propulsion and Power*, Vol. 12, No. 6, Nov.-Dec. 1996, pp. 1011-1017.

Bohm, D., Burhop, E. H. S., and Massey, H. S. W., "The Characteristics of Electrical Discharges in Magnetic Fields," (A. Guthrie and R. K. Wakerling, eds.), Chapter 2, McGraw-Hill, New York, 1949.

Boyer, D. W., and Touryan, K. J., "Experimental and Numerical Studies of Flush Electrostatic Probes in Hypersonic Ionized Flows: I. Experiment," *AIAA Journal*, Vol. 10, No. 12, Dec. 1972, pp. 1667-1674.

Bredfeldt, H. R., Scharfman, W. E., Guthart, H., and Morita, T., "Boundary-Layer Ion Density Profiles As Measured by Electrostatic Probes," *AIAA Journal*, Vol. 5, No. 1, Jan. 1967, pp. 91-98.

Bufton, S. A., *Exit Plane Plasma Measurements of a Low-Power Hydrazine Arcjet*, Ph. D. Thesis, University of Illinois, 1996.

Burtner, D., Keefer, D., and Ruyten, W., "Low-Power Ammonia Arcjet: Numerical Simulations and Laser-Induced Fluorescence Measurements," *Journal of Propulsion and Power*, Vol. 12, No. 6, Nov-Dec. 1996, pp. 1123-1128.

Burton, R. L. and Bufton, S. A., "Exit-Plane Electrostatic Probe Measurements of a Low-Power Arcjet." ," *Journal of Propulsion and Power*, Vol. 12, No. 6, Nov.-Dec. 1996, pp. 1099-1106.

Burton, R. L., DelMedico, S. G., and Andrews, J. C., "Application of a Quadruple Probe Technique to MPD Thruster Plume Measurements," *Journal of Propulsion and Power*, Vol. 9, No. 5, pp. 771-777, 1993.

Butler, G. W., and Cassady, R. J., "Directions for Arcjet Technology Development," *Journal of Propulsion and Power*, Vol. 12, No. 6, Nov.-Dec., 1996, pp. 1026-1034.

Butler, G. W., Kull, A. E., and King, D. Q., "Numerical Simulations of Hydrogen Arcjet Performance," IEPC Paper 93-249, Sept. 1993.

Butler, G. W., Kull, A. E., and King, D. Q., "Single Fluid Simulations of Low Power Hydrogen Arcjets," AIAA Paper 94-2870, July 1994.

Cappelli, M. A., "Modeling of the Near-Electrode Regions of Arcjets I: Coupling of the Flowfield to the Non-Equilibrium Boundary Layer," AIAA Paper 92-3109, July 1992.

Cappelli, M. A., and Storm, P. V., "Interior Plasma Diagnostics of Arcjet Thrusters," AIAA Paper 94-2654, June, 1994.

Carney, L. M., and Keith, T. G., "Langmuir Probe Measurements of an Arcjet Exhaust," *Journal of Propulsion and Power*, Vol. 5, No. 3, May-June 1989, pp. 287-293.

Carrier, G. F., and Fendell, F. E., 1970, *Physics Fluids*, Vol. 13, pp. 2966.

Chang, K. W., and Bienkowski, G. K., "Effects of Electron Emission on Electrostatic Probes at Arbitrary Pressures," *Physics of Fluids*, Vol. 13, No. 4, April 1970, pp. 902-920.

Chen, F. F., "Electric Probes", Chapter 4 in *Plasma Diagnostic Techniques*, edited by R. H. Huddlestone, and S. L. Leonard, Academic Press, New York, 1965, pp. 113-200.

Chen, F. F., *Plasma Physics and Controlled Fusion*, second edition, Plenum Press, New York, 1983, pp.159.

Chung, P. M., Talbot, L., and Touryan, K. J., "Electric Probes in Stationary and Flowing Plasmas: Theory and Application", Springer-Verlag, New York, 1975.

Chung, P. M., Talbot, L., and Touryan, K. J., "Part 2. Continuum Probes," *AIAA Journal*, Vol. 12, No. 2, Feb., 1974, pp. 144-154.

Clayden, W. A., "Langmuir Probe Measurements in the R.A.R.D.E. Plasma Jet," *Rarefied Gas Dynamics*, 3rd Symposium edited by J. A. Laurmann, Vol. II, , Academic Press, New York, 1963, pp. 435.

Clements, R. M., "Plasma Diagnostics With Electric Probes," *Journal of Vac. Sci. Technol.*, Vol. 15, No. 2, March-April 1978, pp. 193-198.

Clements, R. M., and Smy, P. R., "Sheath-Convection Effects with Flush-Mounted Electrostatic Probes," *Canadian Journal of Physics*, Vol. 49, May 1971, pp. 2540-2546.

Clements, R. M., and Smy, P. R., *J. Phys. D*, Vol. 6, 1973, pp. 1253.

Coakley, P., Johnson, L., and Hershkowitz, N., *Phys. Lett.*, Vol. 70A, 1979, pp.425.

Cobine, J. D., *Gaseous Conductors*, 1st edition., McGraw-Hill, New York, 1941, Chapter VI.

Curran, F. M., Manzella, D. H., and Pencil, E. J., "Performance Characterization of a Segmented Anode Arcjet Thruster," IEPC Paper 90-2582, July 1990.

Curran, F. M., "An Experimental Study of Energy Loss Mechanisms and Efficiency Considerations in the Low Power dc Arcjet," AIAA Paper 85-2017, Sept. 1985.

Curran, F. M., and Haag, T. W., "Extended Life and Performance Test of a Low-Power Arcjet," Journal of Spacecraft and Rockets, Vol. 29, No. 4, 1992, pp. 444-452.

DelMedico, S. G., *Plasma Flow Measurements by a Quadruple Probe in a Quasi-Steady MPD Plasma*, M. S. Thesis, University of Illinois, 1992.

Diamant, K. D., private communication, Princeton University, Princeton, N.J., Oct. 1995.

Dinulescu, H. A., and Pfender, E., "Analysis of the Anode Boundary Layer of High Intensity Arcs," *Journal of Applied Physics*, Vol. 51, No. 6, 1980, pp. 3149-3157.

Dunn, M. G., and Lordi, J. A., *AIAA Journal*, Vol. 8, 1970, pp. 1077.

Felderman, E. J., MacDermott, W. N., and Fisher, C. J., "Near-Electrode Model for 100-Standard Atmosphere Arc Discharges," *Journal of Propulsion and Power*, Vol. 12, No. 6, Nov.-Dec. 1996, pp. 1084-1092.

Gallimore, A. D., Kelly, A. J., and Jahn, R. G., "Anode Power Deposition in Magnetoplasmadynamic Thrusters," *Journal of Propulsion and Power*, Vol. 9, No. 3, May-June 1993, pp. 361-368.

General Electric Company, RTV-110, McMaster-Carr, Chicago, IL, 708-833-0300.

Glocker, B., and Auweter-Kurtz, M., "Numerical and Experimental Constrictor Flow Analysis of a 10 kW Thermal Arcjet," AIAA Paper 92-3835, July 1992.

Godard, R., and Laframboise, J. G., "Total Current to Cylindrical Collectors in Collisionless Plasma Flow," *Planet. Space Sci.*, Vol. 31, No. 3, 1983, pp. 275-283.

Godyak, V. A., and Sternberg, N., *IEEE Trans. Plasma Sci.*, Vol. 18, 1990, pp. 159.

Goodfellow, K. D., and Polk, J. E., "Experimental Verification of a High-Current Cathode Thermal Model," AIAA Paper 95-3062, July 1995.

Hargus, W., Micci, M., and Spores, R., "Interior Spectroscopic Investigation of the Propellant Energy Modes in an Arcjet Nozzle," AIAA Paper 94-3302, June 1994.

Harris, W. J., O'Hair, E. A., Hatfield, L. L., Kristiansen, M., and Mankins, J. S., "Anode Arc Motion in High Power Arcjets," AIAA Paper 92-3838, July 1992.

Hayes, D.T., and Rotman, W., "Microwave and Electrostatic Probe Measurements on a Blunt Re-Entry Vehicle," *AIAA Journal*, Vol. 11, No. 5, May 1973, pp. 675-682.

Hershkowitz, Noah, "How Langmuir Probes Work", Chapter 3 in *Plasma Diagnostics*, Vol. I, edited by Orlando Auciello and Daniel L. Flamm, Academic Press, Inc., New York, 1989, pp. 114-183.

Hester, S. D., and Sonin, A. A., *Phys. Fluids*, Vol. 13, 1970, pp. 1265.

Hill, P., and Peterson, C., *Mechanics and Thermodynamics of Propulsion*, 2nd ed., Addison-Wesley, New York, 1992.

Holmes, J. C., and Szuszczewicz, E.P., "Versatile Plasma Probe", *Rev. of Sci. Instrum.*, Vol. 46, No. 5, May 1975, pp. 592-598.

Hoppman, R. F., *Physics of Fluids*, Vol. 11, 1968, pp. 1092.

Hoskins, W. A., Kull, A. E., Nesser, W. M., and Butler, G. W., "Measurement of Energy Deposition Modes in an Intermediate Power Hydrogen Arcjet," IEPC Paper 93-216, 1993.

Hutchinson, I. H., *Principles of Plasma Diagnostics*, Cambridge University Press, 1987.

Jahn, R. G., *Physics of Electric Propulsion*, McGraw-Hill, New York, 1968, pp. 56 - 57.

Jakubowski, A., "Effect of Angle of Incidence on the Response of Cylindrical Electrostatic Probes at Supersonic Speeds," AIAA Journal, Vol. 10, No. 8, Aug. 1972, pp. 988-995.

Johnson, B. H., and Murphree, D. L., *AIAA Journal*, Vol. 7, 1969, pp. 2028.

Keefer, D., and Semak, V. V., "Measurements of Radial and Axial Distributions of Ion Thruster Plasma Parameters Using a Langmuir Probe," AIAA Paper 96-2984, 1996.

Kim, S. W., Foster, J. E., and Gallimore, A. D., "Very-Near-Field Plume Study of a 1.35 kW SPT-100," AIAA Paper 96-2972, 1996.

Kirchoff, R. H., Peterson, E. W., and Talbot, L., *AIAA Journal*, Vol. 9, 1971, pp. 1686.

Kline, S. J., and McClintock, F. A., "Describing Uncertainties in Single-Sample Experiments," *Mech. Eng.*, Jan. 1953, pp. 3.

Kozlov, O. V., *Electric Probes in Plasma*, Atomizdat, Moscow, 1969.

Kushner, M. J., private communication, February, 1997.

Laframboise, J. G., "Theory of Spherical and Cylindrical Langmuir Probes in a Collisionless, Maxwellian Plasma at Rest," University of Toronto, Institute for Aerospace Studies, UTIAS Report No. 100, June 1966 (NTIS AD-634596).

Lam, S. H., "A General Theory for the Flow of Weakly Ionized Gases," *AIAA Journal*, Vol. 2, No. 2, 1964, pp. 256-262.

Langmuir, I., and Mott-Smith, H. M., *Gen. Elec. Rev.*, Vol. 26, 1923, pp. 731; Vol. 27, 1924, pp. 449, 583, 616, 726, 810; *Phys. Rev.*, Vol. 28, 1926, pp. 727.

Lederman, S., Bloom, M. H., Widhopf, G. F., *AIAA Journal*, Vol. 6, 1968, pp. 2133.

LEM USA., Inc., Milwaukee, WI., 414-353-0711.

Lichon, P., and Sankovic, J., "Development and Demonstration of a 600 Second Mission Average Arcjet," *Journal of Propulsion and Power*, Vol. 12, No. 6, Nov.-Dec., 1996, pp. 1018-1025.

Lieberman, M. A., and Lichtenberg, A. J., *Principles of Plasma Discharges and Materials Processing*, John Wiley & Sons, Inc., New York, 1994.

Martinez-Sanchez, M., and Miller, S. A., "Arcjet Modeling: Status and Prospects," *Journal of Propulsion and Power*, Vol. 12, No. 6, Nov.-Dec., 1996, pp. 1035-1043.

Meeks, E., and Capelli, M. A., "A Multi-Fluid Model of Near-Electrode Plasma Behavior," AIAA Paper 93-2103, June 1993.

Megli, T. W., Lu, J., Krier, H., and Burton, R. L., "Modeling Plasma Processes in 1 kW Hydrazine Arcjet Thrusters," AIAA Paper 96-2965, July, 1996.

Megli, T. M., *A Nonequilibrium Plasmadynamics Model for Nitrogen/Hydrogen Arcjets*, Ph.D. Thesis, University of Illinois, 1995.

Merinov, N. S., and Petrosov, V. A., "Existence Region for Arcing Conditions with Negative Anode Potential Drop," *Journal of Applied Mechanics and Technical Physics*, Vol. 17, No. 1, 1976, pp. 12-18.

Mertogul, A. E., *Modeling and Experimental Measurements of Laser Sustained Plasma*, Ph. D. Thesis, Department of Mechanical and Industrial Engineering, University of Illinois at Urbana-Champaign, 1993.

Mikoshiba, S., and Smy, P. R., *J. Applied Physics*, Vol. 44, 1973, pp. 1562.

Miller, S. A., and Martinez-Sanchez, M., "Two-Fluid Non-Equilibrium Simulation of Hydrogen Arcjet Thrusters," *Journal of Propulsion and Power*, Vol. 12, No. 1, 1996, pp. 112-119.

Miller, S. A., and Martinez-Sanchez, M., "Multifluid Nonequilibrium Simulation of Electrothermal Arcjets," AIAA Paper 93-2101, June, 1993.

Mitchner, M., and Kruger, C. H., *Partially Ionized Gases*, John Wiley & Sons, Inc., 1973.

Mi-Tech Metals Inc., Indianapolis, IN, 317-549-4290.

Morgan, W. L., and Penetrante, B. M., MacELENDIF Version 1.1, Kinema Software, 1994.

Morgan, W. L., and Penetrante, B. M., "ELENDIF: A Time-Dependent Boltzmann Solver for Partially Ionized Plasmas," *Computer Physics Communications*, Vol. 58, 1990, pp. 127 - 152.

Mosburg, E. R., Kerns, R. C., and Abelson, J. R., *Journal of Applied Physics*, Vol. 54, 1983, pp. 4916.

Myers, R. M., private communication, NASA-Lewis Research Center, Oct. 1995.

Oberth, R. C., and Jahn, R. G., "Anode Phenomena in High-Current Accelerators," *AIAA Journal*, Vol. 10., No. 1, Jan. 1972, pp. 86 - 91.

Oberth, R. C., *Anode Phenomena in High-Current Discharges*, Ph.D. Dissertation, Dept. of Mechanical and Aerospace Engineering, Princeton University, Princeton, N.J., 1970.

Peterson, E. W., "Electrostatic Probe Electron Current Collection in the Transition Regime," *AIAA Journal*, Vol. 9, No. 7, July 1971, pp. 1404-1405.

Poissant, G., and Dudeck, M., "Velocity Profiles in a Rarefied Argon Plasma Stream by Crossed Electrostatic Probes," *J. Appl. Phys.*, Vol. 58, No. 5, Sept. 1985, pp. 1772-1779.

Pollard, J. E., Jackson, D. E., Marvin, D. C., Jenkin, A. B., and Janson, S. W., "Electric Propulsion Flight Experience and Technology Readiness," AIAA Paper 93-2221, June, 1993.

Pollin, I., *Physics of Fluids*, Vol. 7, 1964, pp. 1433.

Rhodes, R. P., and Keefer, D., "Numerical Modeling of an Arcjet Thruster," AIAA Paper 90-2614, July, 1990.

Russo, A. J., and Touryan, K. J., "Experimental and Numerical Studies of Flush Electrostatic Probes in Hypersonic Ionized Flows: II. Theory," *AIAA Journal*, Vol. 10, No. 12, Dec. 1972, pp. 1675-1678.

Ruzic, D., private communication, April, 1997.

Ruzic, D. N., *Electron Probes for Low Temperature Plasmas*, The American Vacuum Society, 1994.

Sackheim, R. L., and Rosenthal, R., "Electric Propulsion: A Major Advancement in Space Transportation for Communications Satellites," AIAA Paper 94-1012, 1994.

Sankovic, J. M., "Investigation of the Arcjet Plume Near Field Using Electrostatic Probes," NASA Technical Memorandum 103638, Oct., 1990.

Schott, L., "Electrical Probes", chapter in *Plasma Diagnostics*, edited by W. Lochte-Holtgreven, John Wiley & Sons, Inc., New York, 1968, pp. 668-731.

Schultz, G. J., and Brown, S. C., *Physics Review*, Vol. 98, 1955, pp. 1642.

Segall, S. B., and Koopman, D. W., "Application of Cylindrical Langmuir Probes to Streaming Plasma Diagnostics," *Physics of Fluids*, Vol. 16, No. 7, July 1973, pp. 1149-1156.

Self, S. A., and Eskin, L. D., "The Boundary Layer Between Electrodes and a Thermal Plasma," *IEEE Transactions on Plasma Science*," Vol. P. S.-11, No. 4, Dec. 1983, pp. 279-285.

Sheridan, T. E., and Goree, J., "Collisional Plasma Sheath Model," *Physics of Fluids B*, Vol. 3, No. 10, Oct. 1991, pp. 2796-2804.

Smetana, F. O., "On the Current Collected by a Charged Circular Cylinder Immersed in a Two-Dimensional Rarefied Plasma Stream," *Rarefied Gas Dynamics*, 3rd Symposium (J. A. Laurmann, ed.) Vol. II, Academic Press, New York, 1963, pp. 65-91.

Smy, P. R., "The Use of Langmuir Probes in the Study of High Pressure Plasmas," *Advances in Physics*, Vol. 25, No. 5, April 1976, pp. 517-553.

Sonin, A. A., *J. Geophys. Res.*, Vol. 72, 1967, pp. 4547.

Sonin, A. A., *AIAA Journal*, Vol. 4, 1966, pp. 1588.

Soulas, G. C., and Myers, R. M., "Mechanisms of Anode Power Deposition in a Low Pressure Free Burning Arc," NASA Contractor Report 194442, IEPC Paper 93-194, Sept., 1993.

Spencer, Jr. F. E., and Phelps, A. V., "Momentum Transfer Cross Sections and Conductivity Integrals for Gases of MHD Interest," *Proc.* X^{vth} *Symp. Engineering Aspects of MHD*, Philadelphia, PA, pp. IX.9.12, 1976.

Sutton, G. P., *Rocket Propulsion Elements*, sixth edition, John Wiley & Sons, Inc., New York, 1992.

Sutton and Sherman, *Engineering MagnetoHydrodynamics*, McGraw-Hill, New York, 1965, pp. 148 - 190.

Swift, J. D., and Schwar, M. J. R., *Electrical Probes for Plasma Diagnostics*, New York American Elsevier Publishing Company, 1969, pp. 220-245.

Szuszczewicz, E.P., and Holmes, J. C., "Surface Contamination of Active Electrodes in Plasmas: Distortion of Conventional Langmuir Probe Measurements," *Journal of Applied Physics*, Vol. 46, No. 12, Dec., 1975, pp. 5134-5139.

Tan, W. P. S., "Transverse Cylindrical Probe in Plasma Diagnostics," *J. Phys. D: Appl. Phys.*, Vol. 6, 1973, pp. 1188-1205.

Thomas, T. L., and Battle, E. L., "Effects of Contamination on Langmuir Probe Measurements in Glow Discharge Plasmas," *Journal of Applied Physics.*, Vol. 41, No. 8, July 1971, pp. 3428-3432.

Thornton, J. A., *AIAA Journal*, Vol. 9, 1971, pp. 342.

Tiliakos, N. T., Burton, R. L., and Krier, H., "Energy Transfer to the Anode of a 1 kW Arcjet," AIAA Paper 96-2964, July, 1996.

Tiliakos, N. T., and Burton, R. L., "Arcjet Anode Sheath Voltage Measurement by Langmuir Probe," *Journal of Propulsion and Power*, Vol. 12, No. 6, Nov.-Dec., 1996, pp. 1174-1176.

Tilley, D. L., "Propellant Breakdown Mechanisms in an Arcjet," IEPC Paper 93-050, 1993.

Tseng, R. C., and Talbot, L., "Flat Plate Boundary Layer Studies in a Partially Ionized Gas", AIAA Paper 70-86, January, 1970.

Tseng, R.C., " Flat Plate Boundary Layer Studies in a Partially Ionized Gas," Univ. of Calif. Aero. Sci. Rept. AS-69-14, 1969.

Tseng, R. C., and Talbot, L., "Flat Plate Boundary-Layer Studies in a Partially Ionized Gas," *AIAA Journal*, Vol. 9, No. 7, July 1971, pp. 1365-1372.

Unit Instruments Inc., Orange, CA.

Vainberg, L. I., Lyubimov, G. A., and Smolin, G. G., "High-Current Discharge Effects and Anode Damage in an End-Fire Plasma Accelerator," *Soviet Physics-Technical Physics*, Vol. 23, No. 4, 1978, pp. 439-443.

Vesuvious McDanel Product Catalog, 1991, 412-843-5644.

Waymouth, J. F., "Pulse Technique for Probe Measurements in Gas Discharges," *Journal of Applied Physics.*, Vol. 30, No. 9, Sept. 1959, pp. 1404 - 1412.

Wehner, G., and Medicus, G., "Reliability of Probe Measurements in Hot Cathode Gas Diodes," *Journal of Applied Physics.*, Vol. 23, No. 9, Sept. 1952, pp. 1035-1046.

Wilbur, P. J., Jahn, R. G., and Curran, F. C., "Space Electric Propulsion Plasmas," *IEEE Transactions on Plasma Science*, Vol. 19, No. 6, Dec. 1991, pp. 1167-1179.

Winters, H. F., and Sigmund, P., *Journal of Applied Physics*, Vol. 45, 1974, pp. 4760.

Zube, D.M., and Myers, R.M., "Techniques for Spectroscopic Measurements in an Arcjet Nozzle," *Journal of Propulsion and Power*, Vol. 8, No. 1, Jan.-Feb. 1992, pp. 254-256.

Zube, D.M., and Auweter-Kurtz, M., "Spectroscopic Arcjet Diagnostic Under Thermal Equilibrium and Nonequilibrium Conditions," AIAA Paper 93-1792, June 1993.

Vita

Nicholas Tiliakos was born in Manhasset, New York on June 19, 1968 and is the first child of Theologos and Helen Tiliakos. He and his brother Michael were raised in Queens, New York and have also lived in Athens, Greece from 1980-1983. Upon his return to the United States Nicholas attended the Bronx High School of Science. After graduating in 1986, he attended Cornell University in Ithaca, New York where he received his Bachelor of Science degree in mechanical engineering. Nicholas then continued his education at the University of Illinois at Urbana-Champaign by pursuing advanced degrees in aeronautical and astronautical engineering. During his M.S. and Ph.D. research he was supported as a teaching assistant and research assistant. Throughout his graduate career Nicholas worked under the guidance of Dr. Rodney L. Burton in the field of electric propulsion. In May of 1993 he completed his M.S. thesis research on a computational study of propellant preionization in magnetoplasmadynamic thrusters. He continued his graduate studies as a doctoral candidate working on experimental research in the Electric Propulsion Laboratory. His dissertation work involved the application of electrostatic micro-probes to study the internal physics of low power arcjet thrusters, used on geosynchronous satellites for North-South stationkeeping. Throughout his Ph.D. work he has been supported as a research assistant with funding from the United States Air Force Office of Scientific Research. Nicholas has accepted a position as a Scientist at the General Applied Science Laboratories (GASL, Inc.) in Ronkonkoma, New York, and will be working on hypersonic propulsion technology development.